ABSTRACT

Title of Document: DEVELOPMENT OF MAGNETIC SHAPE MEMORY ALLOY ACTUATORS FOR A SWASHPLATELESS HELICOPTER ROTOR.

Ronald Newton Couch, Ph.D., 2006

Directed By: Professor Inderjit Chopra, Department of Aerospace Engineering

Actuator concepts utilizing NiMnGa, ferromagnetic shape memory alloy are investigated for potential use on a smart rotor for trailing edge flap actuation. With their high energy density, large dynamic stroke, and wide operating bandwidth, ferromagnetic shape memory alloys (FSMA) like NiMnGa, seem like attractive candidates for smart rotor actuators, potentially able to fulfill the requirements for both primary rotor control and vibration suppression. However, because of the recent discovery of the material, current experimental data and analytical tools are limited.

To rectify these shortcomings, an extensive set of detailed experiments were conducted on samples of NiMnGa to characterize the response of the alloy for a wide variety of mechanical and magnetic loading conditions. Measurements of the material performance parameters such as power density, damping properties, magneto-mechanical coupling, and transduction efficiency were included. Once

characterized, the experimental data were used to develop a series of analytical tools to predict the behavior of the material. A model, developed in parallel to thermal shape memory alloy models is proposed to predict the quasi-static stress-strain behavior. A simple, low frequency, parameter based model was also developed to predict the alloy's dynamic strain response.

A method for developing conceptual actuators utilizing NiMnGa as the actuation element was proposed. This approach incorporates experimental data into a process that down-selects a series of possible actuator configurations to obtain a single configuration optimized for volumetric and weight considerations. The proposed actuator was designed to deliver 2 mm of stroke and 60 N of force at an actuation frequency of 50 Hz. However, to generate the 1.0 T magnetic field, the actuator mass was determined to be 2.8 kg and required a minimum of 320 Watts of power for operation. The mass of the NiMnGa element was only 18.3 g.

It was concluded that although the NiMnGa alloy was capable of meeting the trailing edge flap actuation requirements, the material is not suitable in its present form for this application because of weight and power consumption issues. The magnetic field requirements must be reduced to improve the utility of the material for rotorcraft applications.

DEVELOPMENT OF MAGNETIC SHAPE MEMORY ALLOY ACTUATORS FOR A SWASHPLATELESS HELICOPTER ROTOR

By

Ronald Newton Couch

Dissertation submitted to the Faculty of the Graduate School of the
University of Maryland, College Park, in partial fulfillment
of the requirements for the degree of
Doctor of Philosophy
2006

Advisory Committee:
Professor Inderjit Chopra, Chair
Dr. Jayant Sirohi, Co-advisor
Professor Norman Wereley
Professor Alison Flatau
Professor Amr Baz
Professor Michael Coplan

Dedication

For Alexia, always.

The Lord replied, *"My precious, precious child,*
I love you and I would never, never leave you
during your times of trial and suffering.
"When you saw only one set of footprints,
it was then that I carried you."

- -"Footprints" by Mary Stevenson

Acknowledgements

If the devil is in the details, then the devil and I have become well acquainted over the years. Earning my Ph.D. was a tremendous commitment and though ultimately rewarding, at times, it was a tiresome burden indeed. Fortunately, there have been many people who have helped lighten the load throughout this undertaking. In their own unique way, each has made a rich contribution to the entire effort. Without a doubt, I am grateful to them all for receiving a truly rewarding and enjoyable experience at Maryland.

First, I would like to thank my advisor, Dr. Chopra for all of his guidance and support. I am grateful that he was always encouraging me to 'look down deep' into the material and for the high quality of excellence he always expected from his students. Furthermore, Dr. Chopra's insistence on regular weekly meetings served as a steady reminder to keep moving forward. Although I might deny it in person, I must admit that I came to appreciate the value of the regular 'Monday Morning Meeting.' I would also like to recognize the influence of my advising committee: Dr. Norman Wereley, Dr. Amr Baz, Dr. Michael Coplan, and Dr. Alison Flatau whose time and effort were greatly appreciated. A special thanks goes to Dr. Michael Coplan for his thorough review of my dissertation. His valuable input played an integral role in improving the quality of my work. In addition, I would also like to recognize Dr. Darryll Pines for remaining interested in my progress throughout my time at Maryland.

I am also deeply indebted to my ‘co-advisor’, Dr. Jayant Sirohi. Much of what I learned about experimental investigation I owe to him. His friendship and guidance were of great value to me and to my work.

Of course it goes without saying that I am especially thankful to my friends and colleagues at the Alfred Gessow Rotorcraft Center. Thanks to Paul Samuel, Jayant Sirohi, Harsha Prahlad and Ashish Purekar, the ‘Old-timers’ who took the time to take a naïve first year under their wing. Thanks to Matt Tarascio, Felipe Bohorquez, Jayasimha ‘Baby Blue’ Atulasimha, Shaju John, Josh Ellison, Jaye Falls, Justin Kearns, Dr. Taeoh Lee, and Dr. V.T. Nagaraj for all the numerous technical discussions, fond memories, and friendship. Without these relationships, my time at Maryland would have been dreary and short.

Dr. John Main and Dr. Suzanne Smith at the University of Kentucky also deserve special recognition. Even though I have long departed Anderson Hall, both of my former mentors have always been willing to lend a hand for one thing or another at just the right time.

I would also like to thank my family for all of their support and encouragement. To my parents, Mom, Pop, Dad, Karen, James I., and Nancy, thank you for making me the man I am today. Also, thanks to my big brother, Paul who supported my decision to study at Maryland, yet faithfully remained unafraid to take me down a peg when I needed it. Thanks to Grandmama, Aunt Jacque, Aunt Ruby, Frank and Sarah and all the rest of my family for all your thoughts and prayers.

I dedicate this work to my wife Alexia. She is my friend, my inspiration, the mother of my son, and the reason to finish my studies in a timely fashion. Her role in

my success cannot be contained in the brief space of a few sentences. I would need volumes. Thanks also to my son, Gavin. Although he arrived at the end, I sincerely hope that he will one day come to know the rejuvenating influence of someone who is always glad to see his dad.

And finally, thanks to Maclachlan, the Martensite Dog. He knows why.

Table of Contents

List of Tables

List of Figures

Chapter 1: Introduction

1.1 Project Overview

The helicopter main rotor is a complex, multi-functional system providing both the required lift and thrust forces for the vehicle. This is achieved by a large diameter, low disk-loading rotor which can provide enough thrust to for the vehicle to achieve both forward flight and stable hovering flight capabilities. In fact, no other vehicle has achieved such broad success as the helicopter in terms of hovering flight and vertical take-off and landing (VTOL) capabilities. This unique aptitude for stable, hovering flight allows the helicopter to successfully accomplish missions closed to fixed-wing, aircraft. Therefore, the helicopter occupies a very important niche in the aerospace domain and is well suited for a wide variety of mission profiles including reconnaissance, search and rescue, civilian transport to name just a few.

The versatility of the main rotor mechanism is the source of most all of the desirable qualities typically attributed to the helicopter. However, the main rotor system is also the source of many of the problems associated with this unique vehicle. One of the main problems associated with the main rotor is the generation of unacceptable levels of vibration and noise. As a result of the asymmetric aerodynamic environment, helicopters are susceptible to high vibratory loads and noise levels. The high vibratory loads negatively impact the overall performance, significantly limiting the helicopter's capabilities [1]. In the long-term, vibrations reduce the structural life of system components which results in increased maintenance and operating costs [2]. Not only are vibrations potentially damaging to

the vehicle itself, but when combined with the magnitude of generated noise, they tend to be cause pilot fatigue, and result in poor ride quality for passengers. Not surprisingly, the noise levels generated by the main rotor are a major barrier for the public acceptance of helicopters in the role of a short range civilian transport [3]. Each year, noise levels in civilian areas are becoming increasingly regulated forcing the rotorcraft community to focus on noise reduction strategies. Furthermore, the military is also concerned with the effects that vibration and noise levels have on crew fatigue and targeting systems in addition to the stealth capabilities of the aircraft in a combat environment.

Because of these challenges, the rotorcraft community has placed increased emphasis on developing a 'jet-smooth' flight capability in helicopters [4] to counteract the problems associated with vibrations and noise, in order to increase the appeal of rotary wing vehicles. Consequently, the development and implementation of both passive and active vibration reduction strategies has received much attention from academic and research communities. The most popular and arguable the simplest vibration reduction strategies involve passive systems. However, although passive systems perform well at attenuating narrow vibration frequency bands, they tend to incur substantial weight penalties and perform poorly in off-design conditions. Active systems, on the other hand, are generally more difficult to design and implement, but have the potential of offering broadband vibration attenuation for a variety of flight conditions. The success of these active systems depends on high power density, lightweight, compact actuators that can be seamlessly integrated into the vehicle's aerodynamic surfaces or other critical systems.

One novel active control strategy involves the development of a swashplateless rotor system. This system involves replacing the complex, aerodynamically inefficient, swashplate mechanism with a compact, system of distributed actuators, sensors, and control surfaces directly integrated into the geometry of the rotor blade. When combined with real-time control algorithms, this system of actuators, sensors and aerodynamic control surfaces comprise a 'smart rotor' system.

The smart rotor system achieves primary rotor control via deflections of on-blade control surfaces (i.e. flaps) or global shape changes in the blade structure. These deflections are accomplished by integrated actuators, receiving power transmitted from the fixed to rotating frame by means of an electrical slip ring unit. Vibration reduction can be achieved by utilizing the same control strategy. As a result, the smart rotor system has the advantage of multifunctionality, becoming the source of both primary rotor control *and* active vibration control. The dual function of the smart rotor system is one of the most attractive aspects of the concept.

As mentioned previously, the success of the smart rotor relies in part on the development of actuators capable of providing adequate control authority to the system. Active materials such as piezoceramics and magnetostrictives offer enormous potential for use in smart rotor actuators. When energized with the appropriate field (magnetic, electric, thermal, etc.) these materials produce various levels of strain and force making them ideal for use as solid state actuators. Although many of these materials are capable of fulfilling the necessary force requirements of the smart-rotor system, they are all limited in the magnitude of achievable stroke. Often, actuators involving these active materials require mechanically complex

stroke-amplification mechanisms in order to generate the required blade deflections. Unfortunately, this requirement diminishes the attractiveness of these materials because the increased complexity negates some of the inherent advantages of the materials. One new material, the ferromagnetic shape memory alloy (FSMA) offers the potential to circumvent the shortcomings of other active materials because it has the capability of producing enormous levels of strain (~6%) without requiring cumbersome, force-amplification mechanisms [5]. Furthermore, FSMA can deliver these levels of strain at high frequencies, reported well-into the kHz range [6, 7].

The research presented in this dissertation is directed primarily at the characterization of the NiMnGa magnetic shape memory alloy for a wide range of magnetic and mechanical loading conditions. The aim is to assess the capabilities of the material in terms of its potential use in smart-rotor actuators. Once characterized for both quasi-static and dynamic excitation, a series of analytical tools to predict the behavior of the material are proposed. Finally, a conceptual NiMnGa actuator is designed and compared to existing smart actuators to foster a discussion regarding the relative advantages and disadvantages of the material.

1.2 Sources of Vibration and Noise in Rotorcraft

Before discussing the specific vibration control strategies, it is necessary to expose the some of the sources of helicopter vibration and noise. Although briefly discussed here, a more detailed discussion regarding the sources of vibration and noise can be found in a variety of other sources [8, 9]. The primary source of vibration for any helicopter is the main rotor. The aerodynamic environment on the main rotor is asymmetric and three dimensional which leads to the generation of

unsteady forces, especially in a high-speed flight condition. In forward flight, rotor blades experience a number of conditions that induce vibration. These conditions include a 1/rev variation in angle of attack, compressibility effects such as transonic shock on the advancing side, retreating side blade stall, and finally, a circular region of reversed flow on the retreating side with a diameter proportional to the advance ratio.

During forward flight, nonuniform airflow through the rotor causes periodically varying air loads on the rotor blades, which in turn lead to periodic excitation forces and moments on the rotor hub. These vibrations are most pronounced for advance ratios greater than or equal to 0.1. Furthermore, the interaction of the complex aerodynamic environment with the elastic rotor blades also generates substantial vibratory loads. All of these loads are transmitted through the hub to the fuselage and hence, to the crew and passenger seats [10, 11, 12, 13]. Wake from the main rotor also interacts with the tail rotor and fuselage. For example, as the each rotor blade passes over the tail boom, a 1/rev forcing is generated. Blade dissimilarities arising from the unavoidable introduction of small imperfections within the blade structure during manufacturing or flight operations also generate large 1/rev loads. The dominate helicopter excitation frequency is the $N_b\,\Omega$, where N_b is the number of rotor blades and Ω is the rotational speed of the rotor. For a rotor with N_b identical blades operating in the perfectly tracked condition, the N_b/rev, N_b-1/rev, and N_b+1/rev vibratory forces are transmitted through the hub to the fuselage as N_b/rev vibratory forces and moments [8, 14]. In other words, for an identically tracked rotor, only harmonics at integer multiples of the blade passage frequency (pN_b/rev) are

transmitted through the hub. However, in reality, rotor blades are never identically tracked, therefore vibratory loads composed of all harmonics are transmitted to the fuselage.

The main rotor is not the only source of vibration in helicopters. Other less dominating sources include the tail rotor and airframe itself. Helicopters also suffer from vibrations originating from the transmission and power plant assembly. Typically, the gearbox assembly is mounted above the passenger/crew compartment and is responsible for generating high frequency vibration signals. These high frequencies result in large internal noise levels which can be uncomfortable to the occupants of the helicopter. The frequencies responsible for these noise levels are the fundamental meshing frequencies of the spiral bevel, and planetary gears. Efforts have been directed towards attenuating these vibrations in order to improve the ride quality of the vehicle. Developing methods to identify these fundamental frequencies and their associated harmonics, which are responsible for most of the transmission induced noise, is a critical step for developing noise reduction strategies [15].

1.3 Methods of Vibration Reduction

Clearly, the levels of vibration and noise are a significant problem for the rotorcraft community. Consequently, there has always been an enormous interest in developing efficient strategies to reduce or eliminate troublesome vibratory loads. In practice, the main target of vibration reduction is the N_b/rev harmonics transmitted to the fuselage from the main rotor. Vibration control methods typically fall into one of two categories: passive isolation and active control.

1.3.1 Passive Isolation Methods

Vibration suppression is usually achieved through passive methods that dynamically isolate the rotor and transmission system from the fuselage of the vehicle. Combinations of structural optimization, vibration absorbers, elastomeric dampers mounted between the transmission and fuselage, and nodal beams have all been employed to attenuate the vibrations generated by the main rotor. These passive systems commonly implement dampers and tuned masses to diffuse fuselage vibrations [16, 17, 18]. Cabin mounted systems are convenient in that many of them do not require a detailed knowledge of the vibration sources and may be installed as needed. Hub mounted systems are self tuning however they incur large parasitic drag penalties. Furthermore, although these passive methods are useful in isolating the forcing frequency, they are associated with large weight penalties and have reduced effectiveness when the vehicle is operated away from the tuned flight condition [13].

The Liquid Inertia Vibration Eliminator (LIVE) force isolator system is an example of a passive system that has enjoyed wide acceptance as an effective vibration suppression tool. Dynamically, the isolator is equivalent to a nodal beam currently in service on the 206L [19]. The LIVE isolator is composed of outer and inner cylinders joined by a coaxial rubber bushing that also functions as a spring. The inner cylinder is attached to the transmission, while the outer cylinder is connected to the fuselage. Cavities connected by a tuning port within the cylinders serve as reservoirs for hydraulic fluid. The hydraulic fluid is heavy, like mercury, and acts as the tuning mass of the isolator. By varying the diameter of the tuning port, the device may be calibrated to isolate the desired frequency. The advantages of the LIVE

isolator include: a reduced mechanical complexity, bearingless, linear response at high g's, and a low weight compared to other passive systems. With the advent of new fluids, LIVE isolators continue to improve in terms of performance and weight. These state-of-the art isolators have been shown to significantly isolate over 60% of the vertical 4/rev vibratory forces [20]. This system also provides vertical pitch and roll vibration attenuation.

Another successful passive vibration suppression system is the antiresonance force isolator. Similar in principle to the LIVE system, the antiresonance force isolator contains a passive hydraulic force generator. For a certain excitation frequency (the antiresonance frequency) the dynamic component of the spring force and the dynamic force produced in the passive force generator, are opposite and equal at the node between the isolator and fuselage. The relative motion between the fuselage and rotor transmission generates the hydraulic force. As a consequence, the net vibratory force (N_b/rev) acting on the fuselage is minimized, thereby minimizing the vibratory response of the airframe. The difference between this design and the LIVE actuator is the performance. While LIVE actuators are capable of isolating 64% of the vibratory vertical forces, the isolation efficiency of the antiresonance force isolators is 70% because of the low self-damping of the design [21]. The system is mechanically simple, and has a well-defined separation of the load paths.

1.3.2 Active Methods

Two of the main disadvantages of passive vibration isolation systems are poor off design performance and large weight penalties. Active control systems offer much more versatility than passive systems because they can suppress a broad range of

vibration frequencies. Furthermore, these systems are envisaged to be much lighter than similar passive control mechanisms. In general, active control methods can be grouped into two categories: fixed frame and rotating frame schemes.

Fixed frame active control utilizes a series of distributed actuators and sensors that are mounted at various locations throughout the fuselage to counteract the vibratory loads transmitted from the main rotor. One method, known as the Active Control of Structural Response (ACSR), utilizes actuators to apply control forces at various critical points on the fuselage and gearbox struts to counteract vibratory loads. This system is currently in production on the EH-101 [22, 23], and has been tested on the Sikorsky S-76 [24] and the BK 117-C [25]. A similar system, the Active Vibration Reduction System (AVRS), is currently being developed for the Sikorsky S-92 and the Boeing V-22. Similar in principle to the ACSR, the AVRS system is comprised of pairs of single point MOOG^{TM} actuators, each consisting of a pair of unbalanced, counter-rotating eccentric masses. Vibration reduction is achieved by controlling the phasing between actuator pairs. By determining the optimum location for these actuators, significant reductions in vibration can be obtained. These inertial force generators are adapted from passive reduction methods. For the S-92, the dynamic force output provided by the actuators is 500 lb. Currently, the system designed for the S-92 has seen a reduction of over 50% in the levels of vibration, and the optimum actuator location has yet to be determined. The weight penalty for the AVRS system is 20% less than a passive system installed to perform the same function [26, 27].

Although the principle of operation is relatively straight forward, the ACSR and AVRS systems require an enormous investment of resources in order to implement them. Determining the optimum actuator locations requires detailed analysis and modeling of the vehicle structure. Initially, the natural modes must be determined by NASTRAN or a similar finite element analysis. Once completed, the model must be validated by ground shake tests and the structural transfer matrix must be identified. The ground shake tests narrow the field to a few candidate actuator locations. Finally, once several possible actuator locations are determined, flight tests must be scheduled to validate the modeling and confirm the optimum actuator locations.

Rotating frame active control schemes are oriented toward suppressing vibrations at the source, the main rotor. Typically, this is accomplished by changing the rotor blade geometry or through the motion of blade mounted, active control surfaces. These systems influence the air loads on the blade and if correctly controlled, can be used to counter the vibration producing, unsteady air loads generated by the rotor. Several systems, including Higher Harmonic Control (HHC), Individual Blade Control (IBC), and active tracking tabs introduce rotating frame control.

HHC vibration control involves exciting the swashplate at higher harmonics of the rotational speed. These higher harmonics induce changes in the root blade pitch which result in new, unsteady air loads on the rotor blades. If the new air loads are correctly phased, then the fuselage vibration is reduced. For adequate vibration control, the pitch input requirements are approximately ±2°. The effectiveness of the HHC in reducing vibration levels has been shown both analytically [28, 29, 30, 31, 32], and experimentally [33, 34, 35, 36, 37]. But despite the success of the HHC

system, it also has several major drawbacks. First, the system imposes a considerable weight penalty and is limited to only N_b/rev excitations of the swashplate. Furthermore, the power requirements of the servo-actuators are quite high especially at extreme flight conditions. Additionally, the HHC system has been shown to also promote blade stall at extreme flight conditions [31].

Another rotating frame approach is Individual Blade Control (IBC). In this approach, actuators are installed in the rotating frame, located between the swashplate and rotor blades [38, 39, 40, 41, 42]. The goal of the IBC concept is to expand the capabilities of the HHC system by allowing blades to be excited over a wide range of frequencies, including frequencies that are not multiples of blade harmonics. Wind tunnel and flight test data have shown that both vibration reduction and noise suppression are possible with IBC [43, 44, 45, 46]. There are a few drawbacks associated with the IBC system however. First, the system requires a hydraulic slip ring unit that in addition to being complex, incurs a substantial weight penalty. Furthermore, the required actuation power has been shown to be up to 2% of the installed maximum sea level power at cruise speed [39]. However IBC research has expanded to other applications besides vibration reduction including: lag damping augmentation [41], gust alleviation [47], stall flutter suppression [48], and BVI noise reduction [49].

Helicopters often encounter vibratory loads that arise from rotor dissimilarities. These dissimilarities cause a tremendous increase in the 1/rev vibration level and hence the rotor encounters larger vibratory loads. To alleviate these dissimilarities, blades are periodically tracked by manipulating trailing edge tabs, adjusting pitch-link

lengths, or by adding masses near the blade root. These operations are performed manually in an iterative procedure, and are an integral part of ground maintenance. This process is both costly and time consuming, resulting in increased operating costs and maintenance downtime. An active, in-flight tracking system is another rotating frame approach that would allow a rotor system to be tracked in a matter of minutes instead of hours or days. This will result in a long term benefit of reduced operating costs, relaxed blade manufacturing tolerances, and increased fatigue life of structural components and instruments [50, 51]. The active tracking tab system adds both precision and speed to the tracking process.

1.3.3 Trailing Edge Flap System

The HHC and IBC control schemes are capable of successfully reducing main rotor vibration although both systems do require significant actuation power in addition to incurring substantial weight penalties. Fundamentally, both systems change rotor air loads by altering the blade pitch at the root. However, the inboard section of the blade does not have a major effect on blade air loads because the dynamic pressure of the region is relatively low. Therefore, systems involving blade root pitch change mechanisms are not optimal for changing the air loads on the main rotor. One solution to this problem is to install active control surfaces directly on the individual rotor blades. On-blade aerodynamic control surfaces, actuated by actuators in the rotating frame can significantly reduce the power requirements relative to a conventional IBC approach, and provide additional performance benefits [52, 53]. These control surfaces commonly take the form of trailing edge flaps, which are dynamically deflected as the blade traverses its azimuth. In general, there exist two

types of trailing edge flaps: servo flaps and plain flaps. Depending on the blade dynamics, the trailing edge flap operates as a direct lift or moment flap. The dominant effect of servo flaps is to generate aerodynamic moments about the elastic axis of the blade, resulting in a new twist distribution. On the other hand, the dominant effect of plain flaps is to increase the local lift on the blade section.

The Kaman helicopter utilizes on-blade servo flaps for primary flight control of its helicopters. Furthermore, one of the first investigations regarding the use of servo flaps for vibration reduction was conducted by Kaman on their Multicyclic Controllable Twist Rotor (MCTR) HHC research. This system utilized a combination of higher harmonic servo flap inputs with primary cyclic pitch control. A set of push-pull rods attached to the swashplate were used to drive the on-blade servo flaps. The higher harmonic servo flap inputs were then superimposed onto the flight control inputs. This system could achieve flap deflections of ±6° at frequencies of up to 4/rev which resulted in significant reductions of vibratory hub loads [54, 55, 56, 57].

An investigation of plain flap control surfaces was conducted by McDonnell Douglas Helicopter systems [58, 59, 60]. The Active Flap Rotor (AFR) project consisted of a 12 foot diameter rotor model, with on-blade plain flaps driven by a cam and cable linkage. Experiments were conducted using open loop multicyclic flap control inputs, whose phasing was adjusted by mechanical arrangement. The effectiveness of the plain flap in regards to vibration control, BVI noise reduction and power requirements was investigated.

Sikorsky has also been involved with trailing edge flap research as part of its Variable Geometry Rotor Technology (VGART) program. The Active Rotor Control

(ARC) tests involved driving trailing edge flaps with on-blade hydraulic actuators on a Mach scaled rotor [61]. A hydraulic slip ring unit consisting of state of the art, 4-way spool valves and custom electronics enabled the actuators to operate at frequencies of up to 50 Hz. The goal of this effort was to develop next generation rotors with both improved vibration and noise characteristics and enhanced performance.

A variety of analytical studies on active, trailing edge flaps for vibration reduction have been conducted by various research groups. Millot and Friedmann have conducted analytical studies regarding vibration reduction by using active servo flaps [62, 63, 64]. Milgram and Chopra [52, 65], and Shen and Chopra [66, 67] have conducted parametric studies for plain trailing edge flaps. The results indicate that significant vibration reduction was feasible with flap sizes ranging from 10-20% span, 25% chord and flap deflections of the order ±5°. A further important conclusion was that the optimum location of the flap midspan was related to the blade dynamics and is near the 75% span station. Furthermore, Shen and Chopra have also investigated the use of trailing edge flaps for primary rotor control on an ultra-light helicopter [68].

The concept known as the X-frame was developed by Prechtl and Hall [69, 70, 71, 72, 73] represented an innovative way to actively control trailing edge flaps. Basically, the X-frame is a piezostack stroke amplification mechanism that improves stroke via shallow angles. Hover tests on a $1/6^{th}$ Mach-scale Boeing CH-47 (Chinook) rotor with an integrated X-frame were conducted [71]. A slotted servo flap

with an 11.5% span, 20% chord and aerodynamic overhang 27.5% of flap chord was used. Flap deflections of ±3.9° were achieved during the test.

1.4 The Smart Rotor

Recent developments in rotorcraft technology have led to an emphasis on developing swashplateless rotor concepts. By incorporating on-blade active control surfaces such as trailing edge flaps (TEF), or active twist, primary rotor control can be achieved without the swashplate mechanism. There are several key advantages to this approach. First, elimination of the swashplate from the main rotor assembly will simplify the hub design. The reduction of the main rotor parts count both improves the reliability of the mechanism as well as reducing the production and maintenance costs of the system. Second, the swashplate and its associated pitch links are exposed to the free stream which results in a significant level of parasitic drag. The elimination of the swashplate would lead to an aerodynamically cleaner hub design, which in turn will improve overall performance.

The utilization of TEFs for primary rotor control demands a more stringent set of actuation requirements than those used for vibration control. But studies have shown that on-blade elevon type control surfaces can potentially provide adequate collective and cyclic pitch inputs to provide enough control authority to incur a smaller parasitic drag penalty than a similar, exposed servo flap control surface [74]. For sufficient control authority, the torsional frequency of the blade is reduced to between 1.5/rev and 2.5/rev. The rotor blade works at free-stream velocities well above the elevon reversal speed.

The success of on-blade control surfaces relies on the development of compact, high power density actuators that provide enough control authority to the TEFs for primary rotor control and vibration reduction. In the case of the MCTR and AFR systems, actuation is achieved by means of mechanical linkages originating from the fixed frame. However, these linkages tend to introduce an impractical level of complexity to the hub mechanism as well as incur unacceptable weight penalties. Furthermore, rotor blades impose severe volumetric constraints and weight limitations on potential on-blade actuator candidates. Conventional actuators also consist of large numbers of moving parts and are unsuitable for operation under the high centrifugal load operating environment inherent to helicopter rotors. But, recent advances in active materials and smart structures provide an array of opportunities for use in on-blade actuators [4, 75, 76]. Active materials, with coupled electo-, thermo-, or magneto- mechanical behavior introduce the possibility of combining the functions of sensor and actuator into a single package. This presents the opportunity to apply collocated control algorithms for maximum performance. With the advent of these technologies, the concept of a 'smart rotor' system may be realized. This smart rotor concept consists of a distributed set of embedded actuator and sensors integrated directly into the blade geometry, and combined with fixed frame, signal conditioning and controller units. Control inputs are sent from the controller/signal conditioner to the on-blade actuators in response to signals generated by the embedded sensors. This integration of sensors, actuators, electronics, and control surfaces into the rotor structure are what makes the rotor 'smart'. In contrast, the active rotor concept only includes the actuator component [4, 77, 78].

The smart rotor concept offers other benefits besides primary rotor control and vibration suppression. Other positive benefits include improved handling qualities, improved performance, stall alleviation, augmented aeromechanical stability, and rotor health monitoring. One project has looked at applying a trailing edge flap smart rotor to an interrogating rotor concept for the purpose of detecting rotor blade faults [79]. Clearly, a fully realized smart rotor system has the potential to provide revolutionary advances in rotorcraft, and may indeed be a key component in a next generation helicopter.

1.4.1 Active Materials and the Smart Rotor

A growing interest in smart structures and materials has expanded the possibilities of the smart rotor system [4, 80]. With smart material based actuation, plain flap configurations have the potential to outperform the servo flap by eliminating losses associated with the hinge gap and external support structure, reducing the power requirements, and providing better structural integrity. Of the wide range of active materials currently available, piezoceramics and magnetostrictive materials are particularly attractive actuator candidates. These materials are lightweight, possess high energy densities, and operate over large frequency bandwidths. Furthermore, these materials can be utilized in solid state actuator designs thereby reducing or eliminating moving parts. When incorporated into TEF smart rotors, these active material actuators enable the system to benefit from all the advantages of IBC, but require less power, and eliminate the need for a hydraulic slip ring. Instead, control inputs and sensor signals are transmitted between the fixed and rotating frame via a conventional, electrical slip ring unit.

1.4.2 Overview of Active Materials

One of the most common types of active materials is piezoelectrics. Because of their electro-mechanical coupling, deformation is induced in response to an electric field. Likewise, these materials generate an electric field in response to an external strain field. Many piezoelectric actuators consist of piezoceramic elements. These elements may be manufactured in variety of geometries including stacks, sheets, tubes, and rods. Piezoelectric actuators have a comparable stiffness to aluminum (~70 GPa) and can operate over a wide bandwidth, on the order of tens of kHz. Induced strain levels are about 1000$\mu\varepsilon$ (piezostacks). Many actuator configurations exist, including stacks, bimorphs, and C-block types [81], as well as a variety of advanced concepts such as the RAINBOW [82] and THUNDER [83, 84] types. In general, piezoelectrics are characterized as a moderate force, low stroke, solid state device. For actuation, excitation voltages required to energize these materials can be as high as 1-2 kV, although 100 V is typical. However, because piezoelectrics have high energy density, operate over wide bandwidths, and are easy to incorporate into structures, they are a good candidate for smart actuation. Furthermore, due to a strong electro-mechanical coupling, piezoelectrics can also be implemented as sensors.

Electrostictive materials share similar characteristics to piezoelectrics, generating the same levels of strain but with decreased hysteresis effects. However, electrostrictives tend to be highly sensitive to temperature. Furthermore, the materials have a highly non-linear response, and because the strain depends only on the magnitude of the magnetic field and not the polarity, only uni-directional outputs

are possible. Similar to electrostrictives materials, magnetostrictives, such as Terfenol-D generate induced strain levels due to applied magnetic fields. These magnetic fields are usually generated by coils located on or near the material. Like piezoelectrics, these materials generate high force over wide operating bandwidths, although the modulus of Terfenol-D is roughly half that of piezoceramics. The strain capability of Terfenol however, is much higher, on the order of 2000$\mu\varepsilon$ (microstrain). The main drawback of magnetostrictive based actuators is that they require a relatively large and bulky set of magnetic coils in order to produce the level of magnetic field sufficient for actuation. Furthermore, these coils often require an extensive array of power electronics for operation.

Shape Memory Alloys (SMA), like NiTi, have the ability to recover plastic strain levels of up to 6% as a result of a temperature induced phase change. By heating and cooling the alloy, actuation can be achieved. However, since heating and cooling processes are relatively slow, actuation can only be achieved at low frequencies (less than 1 Hz). As a result, these materials are unsuitable for primary rotor and vibration control which require much higher bandwidths. But, since these materials have high stroke and high force generation capabilities, they are suited for a variety of smart rotor applications. Research involving the use of SMA actuators in active trailing edge tab actuators for rotor tracking [85, 86] and in active twist mechanisms for tiltrotor blades [87] has been conducted. Furthermore, SMA torsional actuators have also been investigated for fixed wing control surface actuation as part of the Smart Wing Program [88, 89].

Recently, a new shape memory alloy activated by magnetic rather than thermal fields has been discovered. This material, known as the ferromagnetic shape memory alloy (FSMA) is well suited for use in TEF actuators. As mentioned previously, the primary drawback of SMA for use in the smart rotor is the low bandwidth. FSMA however, do not rely on a temperature dependent phase change for actuation but rather, a magnetically induced rearrangement of martensite twins. The most common type of FSMA, NiMnGa (Nickel-Manganese-Gallium), has the ability to generate enormous levels of dynamic stroke (~6%) [5, 90] at very high bandwidths, reportedly in the kHz range [6]. Effectively, FSMA combine many of the desired properties in SMA with those of piezoelectrics and magnetostrictives. Although piezoceramics have received a great deal of attention for TEF actuator applications because of their dual role as a sensor and an actuator, they are limited in their achievable stroke. As a result, piezoelectric based systems often require stroke amplification mechanisms in order to produce the deflections necessary for flap actuation. These mechanisms introduce additional mechanical complexity in addition to substantial weight increases, which can negate many of the advantages of this active material. But since NiMnGa produces significantly larger magnitudes of dynamic stroke, stroke amplification mechanisms are not required, thus creating the possibility of a simple and potentially lightweight actuator design.

1.5 Review of Smart Rotor Concepts

A substantial body of research has accumulated in regards to smart rotor technology. This section provides a review of some of the major developments in the smart rotor concept. While trailing edge flap concepts and on-blade actuator

configurations are the primary focus, other concepts such as those involving active twist are discussed.

1.5.1 Active Twist Concepts

An active twist rotor was first developed by Chen and Chopra [91, 92, 93] using direct twist actuation. An array of dual-layer monolithic piezo patch elements was embedded in the rotor blade at +45 on the upper surface and -45 on the lower surface. These elements were distributed from 17.5% to 70% span with a piezo to fiberglass skin thickness ratio of approximately 4:1. A net shear strain on the blade is induced by the in phase excitation of the piezo elements. The net shear strain on the blade in turn caused a global twist in the blade geometry. This active twist concept was tested on a 1.83 m (6ft) diameter, Froude scale rotor in both hover and in the forward flight. Open-loop wind tunnel tests demonstrated that it was possible to appreciably alter hub loads despite the low level of blade tip twist induced by the piezos.

Another active twist concept involving the integration of active piezo-fiber plies into a composite blade structure was developed by Hagood et. al. [94, 95, 96, 97]. Active plies consisting of piezoceramic fibers replace graphite fibers in the resin matrix. Interdigitated electrodes deposited on these active plies enable the utilization of the larger d_{33} effect in piezoelectric materials. Linear twist along the blade section is achieved when active layers cured in a +45/-45 orientation are actuated. This concept has been tested on a $1/6^{th}$ model of the CH-47 rotor by Rodgers et. al. [97]. The results of this test showed that for a 16% mass penalty, a ±4° tip twist was achievable at full rotor speed and 8° collective.

An analytic model for active fiber composites incorporated into active twist blades was developed by Cesnik et. al. [98, 99, 100]. This research effort was complemented by the development of a $1/6^{th}$ Mach scale active rotor blade designed and tested at the NASA Langley transonic wind tunnel [99]. The open-loop hover test was conducted in a heavy gas medium, and achieved oscillatory twist amplitudes of ±1° in the 3-5/rev frequency range.

1.5.2 Model Scale Trailing Edge Flap Concepts

A great deal of research has been conducted on trailing edge flap actuation by piezo-bender elements for both Froude and Mach scaled rotors. Because of problems associated with friction and actuator clamping, these early tests achieved flap deflections of less than ±2° at full speed [101, 102]. Koratkar and Chopra improved the actuator mechanism and hover tested the system using both Froude and Mach scaled model rotors [103, 104, 105, 106, 107, 108, 109]. Wind tunnel testing of the rotor was conducted at an advance ratio of 0.3 with rotor RPM up to 1800 and 6° collective pitch setting. The piezo-bender actuators were excited at frequencies up to 5/rev and were capable of generating flap deflections of approximately ±4°, effectively doubling the deflections from earlier attempts.

A concept consisting of an arrangement of piezoceramic sheet actuators bonded to a bending-torsion coupled composite beam was developed by Bernhard and Chopra [9, 110, 111, 112]. The piezo-ceramic actuators induce bending moments in the beam when energized. As a result of the bending-torsion coupling in the composite beam, the net bending moment is zero, however a net global twist is imparted to the structure. The tip twist was used to actuate a trailing edge flap. Froude and Mach

scale hover tests were conducted on rotors utilizing this actuation strategy. The Froude scaled rotor achieved flap deflections of ±2°, at 900 RPM, at frequencies in the 1-5/rev range, in hover. Mach scaled hover tests conducted at 2000 RPM, and 2° collective generated tip deflections of between ±1.7° to ±2.8° for the 1-4/rev frequency range and due to resonance amplification, up to ±5.3° for the 5/rev case.

Bothwell et. al. [113] investigated an actuation concept for trailing edge flaps consisting of an extension-torsion coupled composite tube and an interanal piezostacks or magnetostrictive actuator. Actuation of the internal actuator induces an extension in the tube. As a result of the extension-torsion coupling, the tube responds with a net global twist. However, to obtain sufficient levels of twist for trailing edge flap deflection, multiple tubes, connected in series were required.

Sirohi and Chopra [114] explored the possibility of developing a compact piezo-hydraulic pump for use on an active pitch link concept. A pump design was developed and fabricated according to the requirements for both vibration control and primary flight control. Bench top testing of the pump showed that the piezo-hydraulic actuator was capable of pumping frequencies up to 1 kHz, a three-fold increase above existing pump designs.

1.5.3 Full Scale Trailing Edge Flap Concepts

The smart rotor concept has already begun to transition to full-scale applications. A full-scale active flap rotor program and feasibility study at McDonnell-Douglas/Boeing for the MD900 Explorer was initiated for the purpose of developing the AFR rotor [115, 116, 117, 118]. The MD900 is an eight seat utility helicopter with a maximum total operating weight of 6250 lbs, and a 5-bladed, 34 foot diameter

bearingless rotor. The final actuator design consists of a 3 foot span trailing edge flap driven b a bidirectional version of an X-frame actuator. The actuator was scaled up from the model scale in order to meet full scale actuation requirements [119, 120].

Eurocopter conducted studies for a full-scale active TEF configuration utilizing a piezo stack actuator with a shallow angle flextensional amplification mechanism [121, 122, 123, 124]. This actuator configuration has also been proposed for use on a leading edge droop concept for the purpose of delaying dynamic stall [125]. Eurocopter has also investigated two candidate technologies for vibration reduction and BVI noise suppression using a trailing edge flap system [126]. The first technology involves the use of DWARF piezoceramic actuators driving a 15% chord flap integrated into a modified BK117/ATR rotor. The second technology utilizes COCE electromagnetic actuators which drive a 25% chord flap in a modified Dauphin blade section

Lee and Chopra developed a piezostacks driven, bi-directional flap actuator and lever arm amplification mechanism [127, 128, 129]. The flap actuator was designed to meet the requirements to drive a trailing edge flap on a blade section of a full-scale MD900 Explorer helicopter. Vacuum chamber spin and wind tunnel tests were conducted on the actuator at frequencies of up to 5/rev. Peak to peak flap deflections of up to 12° were measured at free stream velocities of 120 ft/sec and 12° collective. Analysis of the actuator performance over predicted the actuator capabilities as a result of the finite stiffness of the mechanism linkages.

Although most full-scale smart rotor research programs have centered around piezoelectric based actuator systems, there has been some work directed toward the

implementation of electromagnetic actuation systems. Eurocopter has looked at the possibility of COCE actuators for use on the Dauphin main rotor. Fink et. al. [130, 131] has conducted a study regarding an electromagnetic actuator used to drive an 11.3% span, 46% chord flap centered at the 91% blade radius of an OH-58D, Kiowa Warrior rotor blade. This actuator concept was to serve as a replacement for blade tip balance weights in an effort to reduce their associated weight penalty. Flap deflections of ±6° for tip Mach numbers of 0.48 (representing 81% of design speed) were achieved. The power requirement for this system represented less than 0.05% of the maximum installed power of the OH-58D.

Two trailing edge flap actuator design based on FSMA were proposed by Tarascio et. al. [132] and Pereira et. al. [133]. Both concepts were designed to replace the conventional swashplate mechanism and provide both primary rotor control and vibration suppression. Furthermore, both designs involved incorporating FSMA actuators into the blade structure in order to drive the trailing edge flaps. The design proposed by Tarascio focused on the development of a 5-bladed, search and rescue helicopter utilizing two TEFs on each blade. The system was designed to provide the required flap deflections of ±5° and hinge moments of approximately 3 lb-ft for trim. An electromagnetic coil used in conjunction with rare-earth permanent magnets was used to drive the NiMnGa elements. The permanent magnets were used to magnetically bias the material in order to both reduce the time-varying field requirements as well as enable the material to provide bi-directional actuation. Because of the utilization of the permanent magnets, the required magnitude of the differential magnetic field was 100 kA/m. The total power requirement for the

actuators was 210 W which corresponded to roughly 0.2% of the total installed continuous power of the vehicle. A feasibility study regarding the use of FSMA trailing edge flap actuators for use on a Bell 206 light helicopter upgrade program was conducted by Pereira et. al [133]. Although the feasibility study concluded that FSMA materials were not yet mature enough for use on a near-term upgrade program, the potential benefits of the material for use in a smart rotor concept were clearly evident.

1.6 Motivation and Objectives of Current Research

Based on the above discussion, it is clear that the smart rotor concept provides a unique solution to the problems of vibration reduction and noise suppression. It is also evident that active materials will play a large role in the success of this technology. Already, piezoceramics have proven to be quite capable of being successfully integrated into smart rotor systems. However, there are many inherent drawbacks associated with piezoceramics that suggest that other active materials may be better suited for driving trailing edge flap actuators. FSMA, like NiMnGa, have many desirable attributes that could be used to fulfill the demands of a successful trailing edge flap system.

1.6.1 Motivation of Research

The major barrier associated with using active materials for trailing edge flap actuators is the lack of available stroke. To make up for this shortcoming, many active material based actuators employ the use of mechanical stroke amplification mechanisms (levers, etc.) in order to achieve the required amplitude of stroke which

will produce the necessary flap deflections to provide sufficient control authority to the main rotor. Some examples of these mechanisms include the L-L actuator, X-frame actuator, and the flex-tensional actuator. Each of these devices exchanges force generation for larger stroke amplitudes, which consequently require high block force materials such as piezostacks. Furthermore, the deformations of the force amplification mechanism must be kept to a minimum in order to maximize the efficiency of the transmitted power. This requires very stiff structures, which increases the weight penalty of the device. The level of complexity and weight penalties associated with these mechanisms tends to counteract any advantages that active materials may provide.

Structural coupling mechanisms like the bending-torsion beam proposed by Bernhard and Chopra [9] or the extension-torsion beam proposed by Bothwell et. al. [113] are unique in that they transmit power through a passive structural element. Through structural coupling, the element converts one mode of deformation into another, (bending to torsion for example). However, the problem with this type of actuation is that much of the work performed by the active material is lost in the deformation conversion process of the structural element, which leads to low actuation efficiency. Furthermore, full scale versions of these types of systems still incur large weight penalties. What is needed is an active material that can produce the large levels of stroke without requiring a lever stage to boost the strain output.

With the discovery of FSMA, however, materials like NiMnGa may be the solution to these problems. Like thermal shape memory alloys, NiMnGa produces large levels of strain (~6%) and exhibits similar strain recovery behaviors. But unlike

thermal SMA, NiMnGa does not rely on heating and cooling processes for actuation. In fact, it has the potential to respond rapidly to changes in the magnetic environment, and is capable of delivering large levels of dynamic stroke. These qualities have already been utilized for a variety of non-aerospace applications including the control of a latching valve [134] and various general purpose actuator concepts [135].

Because NiMnGa is a relatively new material, its capabilities are still largely unexplored. There has been a great deal of work centered around measuring the properties of NiMnGa for thin films but a complete characterization of the bulk scale material is still lacking. Furthermore, current NiMnGa actuator designs have not yet been considered for use on rotorcraft. The complex dynamics, constrained volumes, and high centrifugal loadings associated with the main rotor offer a unique set of design challenges for FSMA based actuators.

The focus of the present research is to investigate the properties of bulk-scale NiMnGa for various magnetic and mechanical loading conditions. Quasi-static and dynamic loading conditions are considered along with a range of mechanical loads ranging from the free to blocked condition and magnetic loading up to saturation. In addition, new analytical tools are developed in order to predict the material response for a variety of magnetic and mechanical inputs. Furthermore, the feasibility of NiMnGa based actuators for use on TEF will be studied. Based on a previous aeromechanics analysis of a trailing edge flap rotor system conducted by Shen and Chopra [136, 137], a series of conceptual actuators are designed and evaluated in order to develop an understanding of the capabilities and performance of an FSMA based actuator.

1.6.2 Objectives of Research

There are three main goals regarding the present research:

1. Systematic characterization of bulk material specimens of NiMnGa ferro-magnetic shape memory alloys. The material response will be explored over a wide range of operating conditions. Actuation in both quasi-static and dynamic magnetic field environments will be studied. The effects of preload, strain rate, bias fields are also investigated and the performance characteristics of the material itself are measured.

2. Develop and implement a comprehensive set of analytical modeling tools to predict bulk NiMnGa behavior. The formulation of a phenomenological model developed in parallel to the Brinson model used for thermal SMA, adapted for quasi-static NiMnGa behavior is discussed. A new, low frequency, dynamic model based on physical, material parameters is also proposed and developed. Each model is also compared to experimental data for validation.

3. Develop actuator configurations for smart rotor applications. Based on existing requirements for a trailing edge flap system, a variety of conceptual FSMA based actuators are proposed. The actuator designs include the coupled material-field generator system and are geared toward developing coil designs which minimize the required power and maximize the actuator performance.

1.7 Outline of Dissertation

This dissertation is divided into seven chapters. Chapters 2-4 focus on the magnetic shape memory phenomenon and the quasi-static and dynamic characterization of the NiMnGa material. In Chapter 5 work detailing the modeling of FSMA behavior for both quasi-static and dynamic actuation is presented. Chapters 6 focuses on the development of conceptual NiMnGa actuators for trailing edge flaps on rotorcraft. Finally, Chapter 7 includes a summary of the major findings of the research as well as possible suggestions for future research directions.

A brief description of each chapter follows:

Chapter 1: The problem of vibration and noise in helicopters is introduced. The concept of smart rotor is proposed and a brief discussion of past research efforts is presented. Overall goals of the current research are outlined.

Chapter 2: This chapter focuses on the phenomenon of the magnetic shape memory effect. The process of deformation by magnetically induced twin boundary motion is explained. Basic strain recovery mechanisms are discussed and emphasis is placed on the similarities between FSMA and thermal SMA materials.

Chapter 3: This chapter is geared toward the quasi-static testing on NiMnGa samples. DSC measurements are included in order to determine the temperature range over which the magnetic shape memory effect exists. Also, basic actuator properties such as free strain and block force are measured. The effects of constant axial stress, constant magnetic fields, and constant strain are

investigated. A brief discussion regarding the sensor characteristics of the material is included.

Chapter 4: In this chapter, the response of NiMnGa to a time varying magnetic field is investigated. FSMA elements are exposed to a maximum 1.2 T amplitude, dynamic magnetic field under various loading conditions. The effects of constant stress, constant strain, strain rate, and bias fields are observed. In addition, the performance of the material is evaluated. Measurements of the power density, and damping properties of the material are included.

Chapter 5: The modeling of the response of NiMnGa to quasi-static and dynamic loading environments is the focus of this chapter. A quasi-static model is proposed to predict the stress-strain response of NiMnGa. This model is developed in parallel to the Brinson model, adapting it for magnetic rather than thermal field actuation. A new set of material parameters is defined and the model is validated with experimental data. A low-frequency dynamic model is also proposed. Based on a set of measured, physics based parameters, the model predicts the dynamic strain response as a function of recovery stress, and excitation frequency. This model is also compared to experimental data for validation.

Chapter 6: This chapter opens with a brief review of the concepts of magnetism, emphasizing theory relevant to actuator design. A first order actuator design code is developed to size the NiMnGa element for the required forces and deflection, and to generate an optimized magnetic circuit configuration. A series of actuator

configurations are generated and then down-selected in order to determine the optimum configuration in terms of power consumption, rotor blade volume constraints, and weight. The performance characteristics of the actuator are estimated and compared to other, existing active material actuator configurations.

Chapter 7: In the final chapter, the major findings of this work are summarized and important conclusions regarding the use of NiMnGa actuators in smart rotor applications are drawn. Recommendations for future research endeavors regarding NiMnGa actuators are also provided.

1.8 Contributions

Specific contributions of the present research are listed below:

1. Bulk scale testing and characterization of material properties. Various loading conditions were investigated including mechanical loading from free strain to the blocked condition, and magnetic fields up to 1.2 T. These conditions were tested for both quasi-static and dynamic magnetic excitation. The influence of strain rate on material behavior was also measured.

2. Performance measurements of NiMnGa. Energy and power densities as a function of material volume were measured. For quasi-static excitation, the energy loss per unit volume of the material mechanically cycled in constant magnetic field intensity was measured. This allowed the damping properties of the material to be estimated.

3. Recognition of similarities between NiMnGa and NiTi. NiTi and NiMnGa share similar strain recovery mechanisms both exhibiting shape memory and pseudoelastic effects. Because of the similarities in behavior, it is possible to utilize similar testing and modeling approaches for NiMnGa that are used for NiTi.

4. Formulation of a quasi-static phenomenological model validated by test data. A quasi-static model developed in parallel to the Brinson model was developed for NiMnGa. Concessions were made to accommodate a magnetic rather than thermal activation field. New material parameters were identified and measured. The stress-strain response of the material for a wide variety of conditions was predicted and then compared to experimental data for validation.

5. Formulation of an original, low-frequency dynamic model validated by test data. A low frequency model defined by physical, material parameters was developed. The analysis predicts the strain response of the material as a function of applied field, excitation frequency and stress. Several material parameters were identified and measured through a series of experiments. Model results were compared to experimental data for validation.

6. Development of a first stage FSMA actuator design code. Recognizing that NiMnGa actuators require carefully designed magnetic coils, a first order design code for FSMA sizing and coil design was developed.

7. Estimated performance of conceptual FSMA actuators and compared them to existing active material based actuator designs. A FSMA actuator design optimized for weight, power consumption, and volume was developed. Performance parameters such as electromechanical efficiency and power density were measured. The coupling coefficient, k, of the material was also determined through experiment. Based on these results, the NiMnGa based actuator was compared to similar piezoelectric and magnetostrictive configurations.

8. Design and fabrication of a FSMA quasi-static material test rig. The custom built test rig allows for precision material testing for a wide variety magnetic field and mechanical loading conditions.

Chapter 2: The Magnetic Shape Memory Phenomenon

Ferromagnetic shape memory alloys (FSMA) show enormous potential as a viable actuator material. Magnetic shape memory materials are especially suited for many actuator applications currently closed to other active materials such as SMAs and piezoelectrics because of limitations in either stroke or bandwidth. In general, when a magnetic field on the order of 2-4 kOe is applied to a FSMA specimen, an enormous level of apparently plastic strain can be recovered, typically on the order of 6-8% [138, 139, 140, 141]. Like thermal shape memory alloys, magnetic shape memory alloys have associated one-way magnetic shape memory effect and pseudoelastic behaviors that are implemented to achieve these levels of reversible strain. One of the most common types of FSMA is the NiMnGa alloy. Currently, three main varieties of NiMnGa are in use. These alloys are classified by their martensite structure and are known as non-layered, five-layered, and seven-layered martensite. Each of these varieties of NiMnGa martensite has its own level of maximum achievable strain. The five-layered martensite variety of NiMnGa alloy is characterized by a tetragonal, crystal structure which is capable of yielding reversible, magnetic field-induced strains of up to 6% [142, 143, 144, 145]. The seven-layered martensite, consisting of an orthorhombic crystal structure has been shown to be capable of even greater magnetically-induced strains of up to 10% [146, 147]. Furthermore, even though no magnetic field-induced strains have been detected, the non-layered martensite variety, composed of a tetragonal crystal structure has been reported to show reversible stress-induced strains of up to 20% [148, 149]. Although the properties of all three varieties depend heavily on alloy composition and

temperature, the seven-layered and non-layered martensite are especially sensitive to thermal effects [146]. Additionally, the seven-layered and non-layered varieties are also characterized by a low modulus of elasticity as compared to the five-layered variety. Although the potential for recoverable strain is greater in these types, the low modulus all but prohibits the seven-layered and non-layered versions for use as practical force generators [150, 151]. This study focuses exclusively on the five-layered martensite variety of NiMnGa because it can generate a practical level of force, it is capable of achieving induced strains comparable to thermal SMA and it is the most common type of NiMnGa.

As stated previously, a key advantage of magnetic shape memory alloys is that its enormous strain response also has a relatively wide bandwidth, reported to be well into the kHz range [139, 152]. In contrast, thermally driven SMA like NiTi, have a very narrow bandwidth, no more than 1 Hz in ideal conditions. This is primarily attributed to the time involved with heating and cooling processes. Since NiMnGa is magnetically rather than thermally reactive, heating and cooling processes do not directly restrict the material bandwidth. Because NiMnGa can achieve enormous, reversible strain at high frequencies, it seems to show great potential in various smart structures applications requiring a high dynamic stroke. A photograph of a set of NiMnGa samples is shown in Figure 2.1.

NiMnGa is not without limitations. The material requires a substantial magnetic field strength (3.5-10 kOe) to activate its strain recovery behavior, resulting in the need for a robust, and subsequently heavy, supporting magnetic circuit. In addition, sufficient supporting power electronics are also necessary, which further

adds to the size and complexity of the entire system. These issues will be revisited in following sections.

Current research suggests that the magnetic shape memory effect occurs as a result of the rearrangement of twin variants in the martensite crystal structure as a direct result of an applied magnetic field. Unlike the conventional, *thermal* shape memory effect, this twin rearrangement and the associated change in shape is not related to a diffusionless structural phase transformation from a high-temperature, high-symmetry austenite phase to a low-temperature, low-symmetry, martensite phase [142, 143, 144, 145, 146, 147, 153, 154, 155, 156]. This chapter discusses in detail these fundamental processes that support the magnetic shape memory phenomenon. An overview of the general principles related to the generation of magnetic shape memory strains is provided and used as a basis to compare with thermally induced shape memory strains. Once the principle of magnetic shape memory strains is established, correlations between magnetic and thermal SMA are provided to show the similarities in the general nature of these two classes of materials.

2.1 Fundamentals of Magnetic Shape Memory Strains

There are several key characteristics that make NiMnGa a unique and remarkable alloy, garnering it a high degree of research interest. First, it is the only known ferromagnetic intermetallic compound that undergoes a martensitic transformation from what is known as a cubic $L2_1$ structure to a complex tetragonal structure [157]. The second reason, which is of greater interest to the active materials community, is associated with the martensitic transformation in that it exhibits several

active properties including the two-way shape memory effect [158], pseudoelasticity [159, 160] and magnetic field-induced strain [154, 156, 161,]. Furthermore, these field-induced strain mechanisms present in NiMnGa do not appear to arise from conventional magnetostriction, i.e. rotation of the direction of magnetization in materials with an appreciable level of spin-orbit coupling [162]. Thus FSMA are distinguished from common magnetostrictive materials like terfenol and galfenol.

As previously stated, one of the key advantages of magnetic shape memory alloys is the ability to rapidly induce large cyclic strains. Unlike thermo-elastic shape memory alloys, such as NiTi, the strains generated by NiMnGa do not rely on thermal events, but rather on the mechanical rotation of the unit cell structure through the mechanism of twin boundary motion. The following discussion explains the fundamental principle of the magnetic shape memory effect by examining the behavior of the unit cell structure of the alloy.

2.1.1 Principle of Twin Boundaries

Before the influence of an external magnetic field on a bulk scale sample of NiMnGa is examined, a discussion of the events occurring at the micro-structure level is warranted. At present, magnetic shape memory strains are attributed to a mechanism of magnetic field-induced, twin boundary motion, a process initially suggested by Ullakko in 1996 [154]. The phenomenon of twin boundary formation and motion is a key issue in both structural and martensitic phase transitions. As a result, modeling the dynamics of interacting twin boundaries in martensitic materials has received much attention in the physics and materials science communities [163, 164, 165]. These effects occur primarily on the micro-structure level. Since the

approach of the present research is focused on macroscopic response of the bulk material, the details of the underlying physics of twin boundary interactions are omitted. However, in order to understand the magnetic field-induced strain recovery mechanisms in NiMnGa, a rudimentary understanding of the nature of twin boundaries is necessary. Therefore, a brief discussion of the fundamental issues relating to twin boundary motion in martensite is presented in this section.

A wide variety of materials including NiTi and NiMnGa show substantial crystallographic distortions when cooled from the high temperature, austenite phase to the low temperature martensite phase. This crystallographic distortion is referred to as martensitic transformation when it is both diffusionless and involves an atomic shear displacement [162]. At the high temperature, austenite state, NiMnGa has a cubic lattice unit cell structure. When cooled to the martensite phase, the unit cell reverts to a tetragonal configuration consisting of a long axis (*a*-axis) and a short axis (*c*-axis). For NiMnGa, as the material is cooled below the martensite start temperature (M_s), regions of martensite form causing a large build up of elastic energy at the austenite-martensite phase boundary. In materials which exhibit martensitic transformation, twins originate as stress relief mechanisms of the crystal through coherent motion of atoms, the net effect being to minimize the elastic energy at the phase boundary. The resulting crystal, or twin variant, is the mirror image of the parent material. The demarcation between the variants is referred to as the twin boundary [166, 167]. Or in other words, a twin is a pair of unit cells in a lattice that are oriented in such a manner that they are mirror images of one another. Figure 2.2

depicts a schematic of a twin variant in a two-dimensional lattice. In essence, a twin boundary is a planar defect in the crystal structure of a material.

To fully appreciate the effect of twin boundary motion as it pertains to the large magneto-strains attributed to NiMnGa, a brief description of the concept of twinning is necessary. Consider a twin pair of unit cells in a lattice. In Figure 2.3(a), a schematic representation of two-dimensional, twinned lattice is shown. The twin boundary within the lattice is represented by the line of atoms that appear to constitute the mirror image line of symmetry of the twin pair. As implied previously, the twin boundary is fundamentally a boundary between a change of orientation of unit cells within the lattice as opposed to an actual break in the lattice structure. In the simplified example shown in Figure 2.3a and Figure 2.3b, each two-dimensional unit cell has two preferred orientations. In reality, a three dimensional lattice contains many more than two distinct orientations. Figure 2.3b shows the same example lattice but in the fully detwinned martensite configuration, or in other words, a complete reorientation of the twin variants into a single, distinct orientation. The lattice has increased its length by an amount ΔL as the atoms have been forced to move over a larger distance to occupy their subsequently new orientation in the detwinned lattice structure. On the bulk scale, the net effect of every ΔL originating from a reoriented unit cell yields a large plastic deformation in the structure. This property can be utilized during manufacturing in order to produce specified deformation paths. In many cases, crystals can be grown and cut in such a manner as to align the lattice structure, producing a significant plastic strain along a specific axis during detwinning. In fact, NiMnGa single crystals can be oriented to produce

several types of motion on the bulk scale including extension, torsion, and bending [5, 140, 168].

Now assume an axial, tensile stress is applied to the twinned martensite lattice as shown in Figure 2.4a. The stress results in an initial elastic deformation, Δl_E of the lattice, after which above a certain critical value, σ_{tw}, the detwinning phenomenon begins to occur. As the stress is increased, the lattice structure approaches the condition of fully detwinned martensite which is depicted in Figure 2.4b. The lattice has undergone a total change in length, ΔL, equal to the sum of the elastic (Δl_E) and detwinning (Δl_{tw}) components. The level of stress required to detwin the martensite is relatively small because the bonds between the atoms are not broken in the process. Effectively, the entire detwinning process is basically a rearrangement of atoms within the martensite. It is important to note that at much higher levels of stress, the bonds between the atoms are broken causing new bonds to form. This behavior is known as slip and is illustrated in Figure 2.5. This type of deformation is permanent and irreversible. While many types of martensite form by slip, such is not the predominant cause of the magnetic shape memory effect in NiMnGa, but rather twin boundary motion in the martensite [169, 170].

Provided that a significant level of slip does not occur, the process of detwinning is reversible in NiMnGa. By alternating tensile and compressive axial stresses on a specimen, twin boundaries may be manually reoriented from tensile to compressive configurations, introducing and removing plastic strain in the process. In other words, materials like NiMnGa have the capability of incurring stress induced reversible strain almost entirely through the phenomenon of twin boundary motion.

Furthermore, in addition to axial deformation, strains associated with twin boundary motion in martensite are also capable of supporting relatively large, plastic, bending or shear deformations [162].

2.1.2 Magnetic Anisotropy

Ferromagnetic materials consist of smaller volumes, known as domains. The direction of magnetization varies from domain to domain so that the net vector sum of all the domains produces a total magnetization of zero. Two of the major factors contributing to the direction of magnetization in a material are the influence of crystal structure and shape of grains. Both of these factors affect the magnetic properties of the material. If the magnetic properties of a material are dependent on a preferred direction, then that material is magnetically anisotropic. Magnetic anisotropy has a strong influence on the shape of a material's hysteresis loops and affects magnetic properties such as the magnitudes of the coercivity and remanence magnetization. There are several types of anisotropy, including magnetocrystalline, shape, and stress anisotropy. Magnetocrystalline anisotropy is related to crystal structure, shape anisotropy is associated with the material's grain shape, and stress anisotropy deals with applied or residual stresses [171, 172]. On a practical level, anisotropy is often exploited when designing magnetic materials for commercial applications.

In the study of NiMnGa alloys, magnetocrystalline anisotropy is of great importance. Fundamentally, magnetocrystalline anisotropy is independent of grain size or shape. The effect of anisotropy can be readily illustrated by measuring the magnetization curves along different crystal directions [171] For example, consider the magnetization curves of a specimen of magnetite shown in Figure 2.6 [172].

Depending on the crystallographic orientation of the magnetite in an applied magnetic field, the magnetization reaches a saturated condition at different field strengths. Note that <111> is the 'easy' direction of magnetization, and <100> is the 'hard' direction of magnetization. Since the magnetite reaches saturation at different field strengths depending on the direction of applied field, the magnetite has an inherent level of magnetic anisotropy.

Specifically, magnetocrystalline anisotropy can be described as the energy necessary to deflect the magnetic moment in a single crystal from the 'easy' to 'hard' direction. The 'easy' and 'hard' directions arise from the interaction of the spin magnetic moment with the crystal lattice, also known as spin-orbit coupling [138, 171]. If a material having a large magnetocrystalline anisotropy is configured in such a manner that the uniaxial easy direction of magnetization changes across the twin boundary then an external magnetic field can be an effective way to induce changes in the material twin structure, and hence the shape of the bulk material [138, 162]. Since the material has a large magnetocrystalline anisotropy, it requires a relatively large amount of energy to rotate the magnetic moments to align with the applied field. The magnetic moments are effectively "locked" into their orientations within the unit cell. In this situation, it requires less energy to induce changes in the twin structure than to rotate the magnetic moments to become magnetized.

Attempts have been made to model the anisotropy in NiMnGa. O'Handley showed that it is possible to model the effect of strong, weak and intermediate magnetic anisotropy on magnetic shape memory alloys with a simple phenomenological model [138].

2.1.3 Magnetic-Field Induced Twin Boundary Motion

Current research has determined that there exists a strong field dependence of strain in the martensitic phase of NiMnGa single crystals [154, 173]. However, the strains are largely the result of twin boundary motion and not magnetostriction. In fact, observations of NiMnGa exposed to various magnetic loading, show a clear distinction between the magnetostrictive strain (strain quadratically proportional to the magnetization, M, below magnetic saturation) and strains due to twin boundary motion (strain linearly proportional to M below saturation) [138].

Like any ferromagnetic material, when NiMnGa is exposed to a magnetic field, the magnetic domains of the unit cell have a tendency to rotate; aligning themselves with the direction of the applied field. However, because NiMnGa exhibits a high level of magnetocrystalline anisotropy [138, 162], this process is not easily accomplished. It has been stated that the effect of this anisotropy is to rigidly fix the magnetic moments within the unit cell. Therefore, when a magnetic field is applied to the specimen, a pressure is exerted on each unit cell as the magnetic moments work against the anisotropic effects and try to align with the field direction. Subsequent twin boundary mobility in NiMnGa is attributed to this high degree of magneto-crystalline anisotropy. The external field induces the unit cell itself to undergo rotation which in turn, induces twin boundary motion in the lattice producing the associated large strains in the bulk specimen.

Current research suggests that the driving force of the Zeeman energy difference, $\Delta M \bullet H$, across the twin boundaries is responsible for the motion of twin variants and the subsequent large field-induced strains in specimens of NiMinGa

composed of the martensitic phase structure [138, 154, 173]. When a magnetic field is applied in a certain direction with respect to the martensitic twin boundary, a Zeeman pressure of an order equal to $2M_sH$ is exerted on that twin boundary. In the event that the magnetocrystalline anisotropy of the specimen is sufficiently strong, the unfavorably oriented twin variants are not easily able to rotate in alignment with the field direction. In this situation, the Zeeman energy is reduced and equilibrium is attained by twin boundary motion. This is the process responsible for the magnetic shape memory effect. In contrast to the thermo-elastic shape memory effect, the magnetic shape memory effect occurs only in specimens composed of the low-temperature, martensitic phase. The material therefore has the potential to be faster and more efficient than thermo-elastic shape memory processes [138, 162]. This is because the mechanism for magnetic shape memory does not rely on slower heating and cooling processes.

Now that it has been established that the magnetically induced plastic strains in NiMnGa alloy are the direct result of the rearrangement of the martensite twin structure of the material [5, 174, 175, 176 177], it necessary to consider the effect on a bulk specimen. For simplicity, the martensite phase in bulk specimens can be considered to be subdivided into two primary variants: a field preferred and a stress preferred configuration. The c-axis is aligned parallel to the axis of magnetization, and is also known as the ‘easy’ axis. Just as the case of the micro-scale behavior, and like any ferromagnetic material, the axis of magnetization in the bulk specimen will align itself with the direction of an applied external field. This process of unit cell realignment causes the material to grow field preferred twin variants at the expense of

stress preferred twin variants. When the NiMnGa bulk specimen transforms from a stress preferred to field preferred configuration, a change in dimensions occurs. This change in actuator dimension is known as the magnetic shape memory (MSM) induced strain, otherwise known as the magnetic shape memory effect (MSME). In the present study, the direction of strain within the NiMnGa sample is oriented perpendicular to the direction of the applied field. NiMnGa samples may also be oriented to produce strain along the direction of the applied field [178, 179]. However, the maximum strain capability of specimens of this configuration is greatly reduced, reported to be no more than 6300 $\mu\varepsilon$ [178].

Applied stresses also affect the magnetic shape memory properties of NiMnGa by raising the activation field requirements. If a specimen is subjected to an external stress field along the direction of strain then the applied magnetic field must first overcome the elastic energy associated with the applied stress in order to induce twin boundary motion. The activation fields increase proportionally to the level of applied stress. A limiting case is reached when the elastic energy becomes greater than the energy associated with the magnetic anisotropy. In this situation, once the applied field reaches a critically high level, the magnetic anisotropy of the material is overcome before the elastic energy. This causes the sample to spontaneously magnetize rather than inducing the twin boundary motion. In essence, it becomes energetically preferable for the magnetic domains to overcome the magneto-anisotropy and detach themselves from their relative positions within the unit cell, so that they can rotate to align themselves with the direction of the applied field without inducing a twin boundary rearrangement of the unit cell. In this

instance, the material is in a blocked condition and cannot generate magnetically induced strains, regardless of the applied field.

2.1.4 Temperature Dependence of MSM Strains

It is has been established that the Zeeman energy difference between adjacent twin variants is the driving force behind the magnetic shape memory effect and the associated large, field-induced strains. However, this statement is only true for single crystal, martensite samples of NiMnGa in field intensities below saturation [180, 181]. This means that the magnetic shape memory effect is only present in specimens of NiMnGa in the low temperature, martensite phase. A transition from martensite to austenite removes the magnetic shape memory properties of the material. However, the effect of temperature has a significant impact on the magnetic shape memory strains of martensite single crystals. Specifically, the magnetic shape memory effect (MSME) depends on the tetragonality, or lattice distortion of the unit cell [138, 181, 182, 183]. Since tetragonality is sensitive to changes in temperature, it is important to examine the thermal effects on the magnetic field-induced strains.

In Glavatska [181], the effect of temperature of the martensitic structure and the magnetic field-induced strains in single crystal NiMnGa alloy is observed for temperatures ranging from room temperature (16° C) to the A_s, 63 °C , to the martensite to austenite transformation temperature. Glavatska's research documented several important findings. First, the research showed that the lattice distortion (1-*c*/*a*) of the martensite decreased linearly with increasing temperature. Lattice distortion of the martensite is important because it defines the theoretical limit of the available magnetic field-induced strain. A linear decrease in the lattice distortion

implies a linear decrease in the available magnetic field-induced strain. It was shown that the linear decrease in the field-induced strain is indeed proportional to the lattice distortion parameter, (1-*c*/*a*) [181]. Second, it was shown that the critical value of magnetic field required for the activation of twin boundary motion also decreased with increasing temperature.

When designing smart systems utilizing NiMnGa, the effect of the ambient temperature cannot be ignored. In carefully controlled conditions, temperature can be used to reduce the magnetic field requirements of the actuator which subsequently reduces the power requirements at the cost of a modest decrease in the available MSME strain. However, since the A_s temperature is very close to room temperature it is easy to envision a real-world scenario in which the operating conditions of the actuator raise the temperature of the NiMnGa above A_s, completely removing the MSME capability and causing a system failure. It is essential to carefully consider thermal effects when designing NiMnGa based active structures.

2.1.5 Effect of Composition on Transformation Temperatures

Both the magnetic shape memory effect and the mechanical properties of single crystal NiMnGa alloy specimens vary significantly due to strong dependence on crystal structure, material composition, initial microstructure, and variant volume fraction [147, 151 184, 185, 186]. Material composition is especially critical in the determination of the martensite to austenite transformation temperatures, or the M_s, M_f, A_s, and A_f, for the martensite start, martensite finish, austenite start, and austenite finish respectively. In particular, it has been observed that the M_s temperature of NiMnGa is especially sensitive to composition [158]. Generally, it has been shown in

recent studies that the partial substitution of Mn for Ni results in both an increase in the M_s temperature and the decrease in the Curie temperature of the alloy [180, 187, 188].

In Wu [189], the effect of material composition on the transformation temperatures, in particular the M_s temperature, of NiMnGa was observed. It was demonstrated that the off-stoichiometric Ni_2MnGa have a M_s temperature that is significantly affected by individual Ni and Ga content and that their effects are opposed [189]. In addition to the transformation temperatures, the martensitic transformation enthalpy, ΔH, was also studied. It was discovered that the effect of Mn on phase transformation temperatures is relatively small, while Ni and Ga have a major impact on M_s, M_f, A_s, and A_f. The effects were also shown to be opposed to one another, meaning that increasing the Ni content at the expense of Ga content increases the M_s, M_f, A_s, and A_f temperatures as well as the transformation enthalpy, ΔH. In contrast, reducing the Ni and increasing the Ga content tends to decrease the transformation enthalpy and the M_s, M_f, A_s, and A_f temperatures. Wu and Yang further developed a simple set of equations using linear regression techniques, which allow the M_s and ΔH to be predicted. Simply stated, for a specimen having a fixed concentration of Mn, the addition of Ga will lower the M_s temperature. Similarly, for a specimen with a constant Ni concentration, the addition of Mn will cause the M_s temperature to increase dramatically. Finally, for a specimen having a constant Ga concentration, the substitution of Mn for Ni will significantly lower the M_s temperature [189].

For practical applications of NiMnGa, it is necessary to use material compositions that place the austenite to martensite transformation temperatures well above the expected operating temperature. This is necessary because the effects of martensite crystal structure, temperature, and maximum strain capability are all interrelated. When fabricating NiMnGa specimens for practical applications, material composition must be considered in order to produce a robust design that minimizes thermal effects on the magnetic shape memory performance.

2.1.6 Thermal Shape Memory Effect in NiMnGa

It is well known that the Heusler-type alloy Ni_2MnGa exhibits a structural martensitic phase transition from the high-temperature cubic austenite phase to a low temperature tetragonal martensite phase, implying that there exists the possibility of thermo-elastic shape memory behavior in addition to ferromagnetic [180, 190]. Furthermore, the relationship between M_s and the transformation enthalpy, ΔH, is very important with respect to the thermo-elastic shape memory behavior of NiMnGa. It has been determined that the linear relationship between these two quantities also suggests that NiMnGa SMAs undergo thermo-elastic shape memory martensitic transformation [189, 191]. As a result, NiMnGa ferromagnetic shape memory alloy martensite specimens are classified as both thermo-elastic and ferromagnetic [192, 193]. This means that in addition to generating large magnetically induced strains, NiMnGa can also be used as a conventional, thermally driven shape memory alloy, like NiTi. In principle, the thermo-elastic shape memory behavior present in various forms of NiTi is also present in NiMnGa [189, 194, 195]. Plastic strain is recovered by introducing the sample to a thermal event sufficient to raise the temperature of the

specimen above the austenite finish (A_f) boundary. As the specimen undergoes a phase change from martensite to the austenite, or parent phase, the plastic strain is recovered. For thermo-elastic SMAs, the mechanism for strain recovery is driven by a phase transformation in the material [169, 170, 196].

The thermoelastic behavior of NiMnGa was closely observed and reported by Cherechukin, [180]. It was shown that the one-way shape memory effect in polycrystalline $Ni_2MnFeGa$ occurred as a result of the martensite to austenite structural phase transition close to the crossover of M_s and the Curie temperature, T_C. The subsequent plastic strains are accounted for by the change in phase volumes. The plasticity of the alloy was improved, without sacrificing both the magnetic and thermoelastic properties, by a low doping of Fe. Furthermore, it was shown that during cooling, samples subjected to external loading and strongly deformed in the martensite phase, recover their initial shapes in the austenite phase during heating while working against the external force. This result implies that the specimens exhibited a one-way, thermo-elastic shape memory effect. The restored deformation was measured to be 2-4% in the most favorable case. A two-way shape memory effect with a transformation strain magnitude of about 0.2% has also been detected in NiMnGa [158, 160, 180].

2.2 Magnetic Shape Memory Deformation Mechanisms

Recent experiments have shown that the magnetically induced twin boundary motion in NiMnGa produce considerably larger strains than magnetostrictive materials such as $(Tb, Dy)Fe_2$. Unlike magnetostrictive materials, FSMA utilize the a strong magnetic anisotropy of the martensite twin variants which have the easy axis

aligned with the *c*-axis to produce a reversible twin boundary motion capable of generating large strains [138, 154, 157, 161, 180, 197, 198, 199, 200, 201]. This phenomenon although fundamentally different shows remarkable qualitative similarities to behaviors exhibited in thermal SMAs. Specifically, ferromagnetic shape memory alloys, like NiMnGa, exhibit strain recovery mechanisms similar in nature to conventional, SMAs, such as NiTi. Both materials exhibit a one-way shape memory effect and pseudoelasticity. The main difference between the two materials is that NiTi requires a thermal field and NiMnGa requires a magnetic field to activate the shape memory effect.

The following section defines the one-way shape memory effect and pseudoelasticity as they are related to magnetic shape memory alloys. Details of the expected changes in the stress-strain behavior of the material as a function of magnetic field are provided. In a qualitative manner, the critical points of the stress strain curves are tracked as a function of external magnetic field intensity.

2.2.1 The Magnetic Shape Memory Effect

For a typical bar shaped NiMnGa specimen, an external magnetic field induces axial strain perpendicular to the direction of the applied field. However, some research has been focused on NiMnGa specimens that have collinear orientations of applied field and strain [178, 179, 186]. Provided that the magnetic anisotropy is large, application of the magnetic field induces twin boundary mobility, converting the specimen to a field preferred condition. This conversion results in an induced strain that remains when the field is removed. The induced strain is apparently plastic in nature and may be removed by applying an axial, compressive stress on the order

of 3 MPa to the actuator along the direction of strain. The axial stress manually induces twin boundary motion, reorienting the specimen into a stress preferred condition. Or in other words, applied stress can re-twin the martensite structure of the specimen.

The one way shape magnetic shape memory effect in NiMnGa is defined as follows. When an FSMA in the field preferred configuration is axially loaded (>3 MPa) in compression at zero magnetic field, twin boundary motion occurs causing the actuator to become "twinned" martensite. The level of resulting plastic strain introduced into the sample is approximately 6%. The theoretical limit of the induced strain associated with twin boundary motion is based on the lattice distortion parameter, (1-*c*/*a*), where *c* and *a* are lattice parameters representing the "easy" and "hard" directions of magnetization respectively. The resulting twinned martensite configuration is known as the stress preferred configuration. To recover the induced strain, an external magnetic field on the order of 2-3 kOe is applied to the bar at zero applied stress, reordering the martensite twin variants, and converting the actuator to its original, field preferred configuration. This phenomenon is the magnetic shape memory effect (MSME). A schematic of the one-way magnetic shape memory effect appears in Figure 2.7.

The one way magnetic shape memory effect can also be explained by examining the stress-strain curve. In the first case, NiMnGa under tension is examined. A typical FSMA stress-strain curve at zero magnetic field under a tensile loading is shown in Figure 2.8. For zero applied field, and for a specimen of the material existing in the stress preferred configuration, an axial, tensile stress is

applied along the direction of strain. As the stress increases, there is a region of elastic deformation (region 1) where the strain increases linearly with stress. At a critical stress level, the martensitic twin boundaries become mobile and the NiMnGa begins to de-twin. Because these twin boundaries are easily moved relative to the elastic deformation, the slope of this region (region 2) of the stress-strain curve is very small. The material is undergoing an apparent plastic deformation in this region. However, this deformation due to twin boundary motion can be recovered by applying a compressive stress along the direction of strain to reinitiate twin boundary and compress the specimen back to its original length. The stress levels that define the second elastic region are called critical stresses, $\sigma_{cr,s}$ and $\sigma_{cr,f}$, the start and finish stresses respectively. At the completion of detwinning, the slope of the stress-strain curve in region 3 increases and becomes larger than that of region two. Eventually, if a limiting value of strain is reached, slip begins to occur and the material deforms plastically. This event occurs in region 4. The plastic strain in this region is permanent and cannot be recovered by twin boundary motion. Thus, there are two distinct yield points in the stress-strain curve. The first occurs just before twin boundary motion is activated and the second occurs at the onset of slip long after the material has completely detwinned.

In the second case, NiMnGa under compression is considered. In Figure 2.9, a typical stress-strain curve for a NiMnGa specimen under compression is shown. For a specimen initially in the field preferred configuration, subjected to a zero applied field, a compressive load is applied along the direction of strain. Just as in the previous case, as the stress increases, there is a region of elastic deformation

where the strain increases linearly with stress (region 1). At the first critical stress level, the martensite twin boundaries become mobile, reconfiguring the specimen into the stress preferred configuration (region 2). As the stress is increased beyond the second critical level, the specimen is composed of stress preferred twin variants and the slope of the stress-strain curve once again increases (region 3). If the stress is removed at this point, the material will recover a small amount of elastic strain, ϵ_e, however, a residual strain, ϵ_r, on the order of 6% remains. Although this strain is apparently plastic, it can be recovered by applying a sufficient external magnetic field ($H > 2$ kOe). The applied field induces twin boundary motion, converting the specimen to a field preferred configuration and allowing it to fully recover the strain. This process is known as the one-way magnetic shape memory effect.

2.2.2 Magnetic Pseudoelasticity

NiMnGa also exhibits pseudoelastic behavior. When the material, initially in the field preferred state, is subjected to increasing, axial, compressive stress while exposed to a large magnetic field, on the order of 4 kOe, the actuator will undergo a transformation from field to stress preferred martensite, inducing a large plastic strain. As the stress is brought to zero, the strain is completely recovered in a hysteresis loop.

In thermal SMAs pseudoelasticity is a phenomenon involving the formation of stress induced martensite for a specimen initially in the austenite phase. This is a stress dependent behavior in which the material completely recovers plastic strain upon the removal of stress in a hysteresis loop. NiMnGa also exhibits a similar stress dependent pseudoelastic behavior. For NiMnGa, pseudoelastic behavior is defined as

the formation of stress preferred twin variants in a specimen exposed to an external magnetic field, for a specimen initially in the field preferred configuration. Note that there is no change of phase in this process. The NiMnGa remains in the martensite phase over the course of the entire process. In Figure 2.10 a schematic of a specimen of NiMnGa undergoing pseudoelastic deformation is shown. In this case, of a NiMnGa bar, initially in the field preferred configuration, subjected to an axial, compressive stress. At this point (region 1) there exists a linear relationship between stress and strain. When a critical stress is reached, stress preferred twin variants begin to appear and the material begins to re-twin (region 2). Region 2 is defined by a significant reduction in the slope of the curve, indicating mobile twin boundaries. As the stress is increased beyond the second critical point, (region 3) the material has been fully converted to the stress preferred configuration and the slope of the stress-strain curve once again increases significantly. When the stress is removed, the applied magnetic field causes the stress preferred martensite to become unstable and revert back to the field preferred martensite configuration. If the applied magnetic field H is greater than a critical value H_f, then the plastic strain in the material is fully recovered in a hysteresis loop. Because the hysteresis loop in the loading-unloading cycle is significantly large, the magnetic pseudoelastic behavior of FSMA has the potential to be used in a wide variety of damping applications. The origin of this large hysteresis can be traced to the frictional losses incurred by twin boundary motion in the martensite.

2.2.3 Partial Magnetic Pseudoelasticity

NiMnGa also exhibits an interesting behavior at low magnetic fields. At low fields ($1 < H < 3$ kOe), the NiMnGa can exhibit partial pseudoelastic recovery. If the applied magnetic field is between the critical values H_s and H_f, then there will only be a partial recovery of strain during the unloading cycle. However, the residual strain ϵ_r is fully recovered upon the application of additional magnetic field above H_f at zero stress. Figure 2.11 shows a schematic representation of partial pseudoelastic behavior. In this case, a specimen, initially in the field preferred configuration, is subject to a small applied magnetic field of about between H_s and H_f. While the applied field remains constant, an increasing, compressive, axial stress is applied to the actuator. As in the case of the magnetic shape memory effect and magnetic pseudoelasticity, regions 1 and 2 characterize the elastic deformation of detwinned martensite and the phenomenon of twin boundary motion respectively. During unloading, when the stress is removed, a portion of the strain ϵ_p is recovered in the resulting hysteresis loop while a residual strain ϵ_r remains. Under these conditions, the magnetic field is insufficient to induce full twin boundary mobility along the entire length of the actuator. Therefore, only a partial amount of strain is recovered. The remaining, residual strain can be recovered by raising the level of the field to beyond H_f to activate twin boundary motion along the entire length of the actuator.

2.2.4 Effect of Sample History and Heat Treatment

The magnetic shape memory effect in NiMnGa is sensitive to other factors besides magnetic field and temperature. The mechanical loading history and prior heat treatments of a specimen can also influence the behavior of the material.

Although the fatigue life of NiMnGa has yet to be fully determined, NiMnGa specimens have the capability to undergo millions of cycles before failure.

Cheng [153] has shown the effects of heat treatment and sample history in specimens of NiMnGa. It was determined that mechanical cycling of NiMnGa has two main effects. First, subjecting a NiMnGa sample to a series of compressive loadings has the effect of increasing the volume fraction of the major twin variants while reducing the minor variants. This is very important to the performance NiMnGa because the magnitude of the strain of the bulk specimen is the sum of the strain produced by the major variants. Therefore, to maximize the achievable strain for a given direction, it is necessary to also maximize the number of major variants within the sample. It was also shown that mechanical cycling improves the mobility of the twin boundaries by unpinning them from pre-existing defects. Essentially, mechanical cycling streamlines the inherent twin boundary motion of the material, working out any 'kinks'. Further research demonstrated that prior mechanical history could have strong influence on the magnitude of twinning start strain and the total twinning strain.

Cheng [153] also investigated the effect of heat treatment on NiMnGa samples. Specifically, heat treatment of the material tends to improve the ordering of the high temperature, cubic, austenite phase. This results in an increase in the magnitude of thermal shape memory strain that can be achieved. Although, heat treatment can improve the level of induced strain, it cannot increase it above the theoretical limit which is not affected by heat treatment processes. Although not

directly quantified, it was indicated that prior heat treatments also affect the martensite structure of NiMnGa formed during cooling.

Figure 2.1 Photograph of NiMnGa Specimens

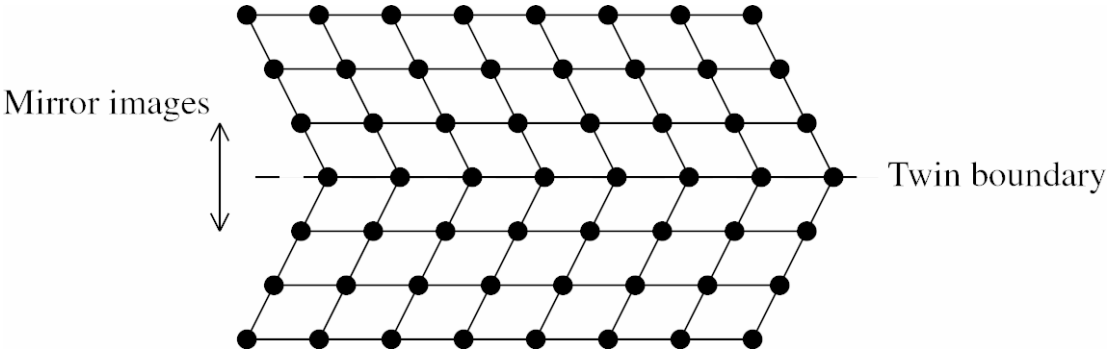

Figure 2.2 Schematic of two-dimensional, twinned lattice

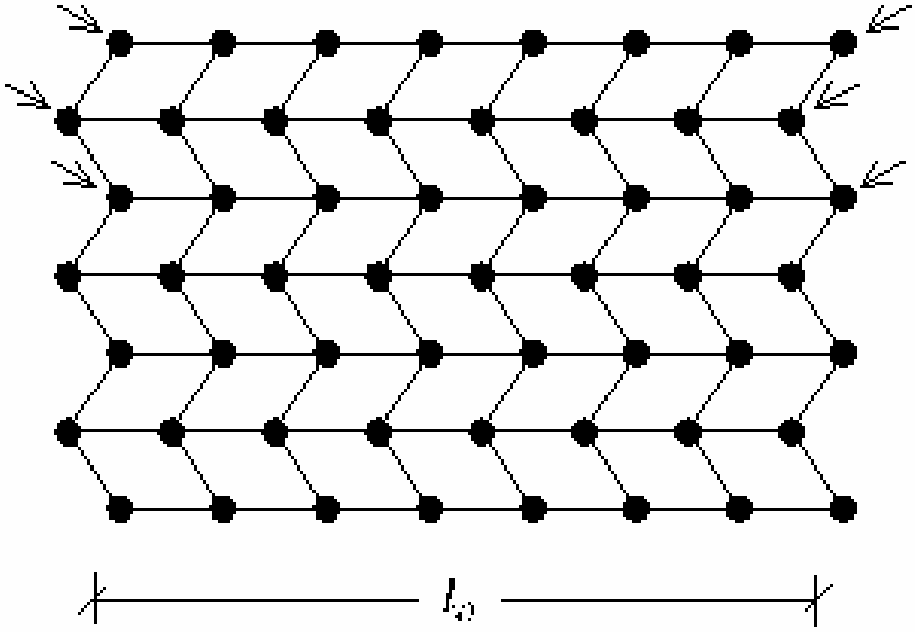

a) Twinned martensite

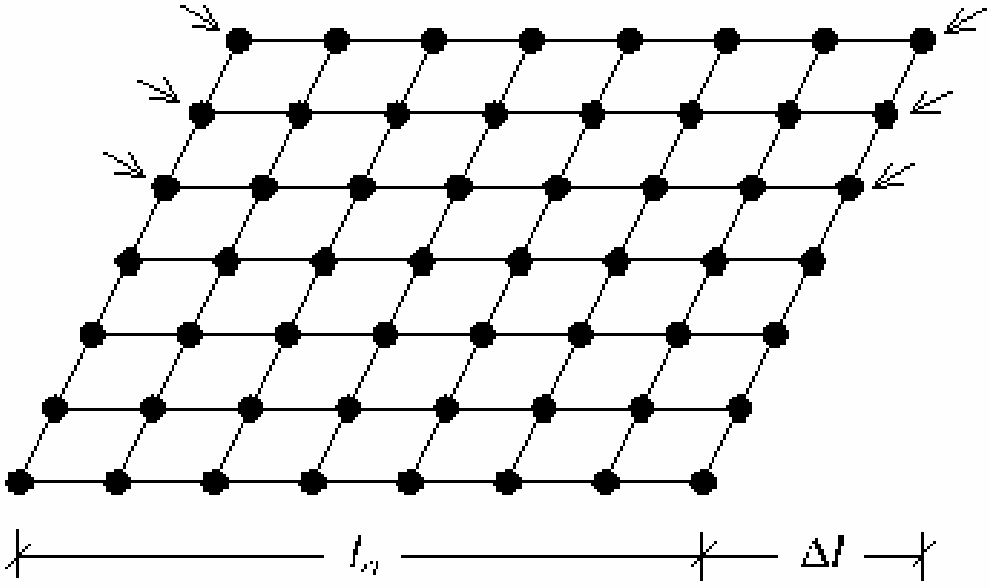

b) Detwinned martensite

Figure 2.3 Schematic of twin variants in a two-dimensional lattice

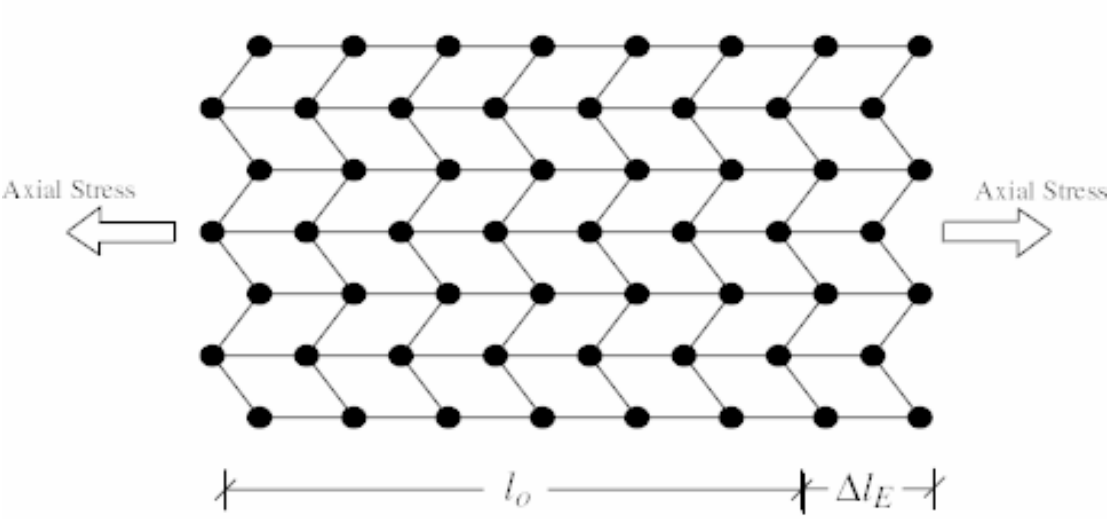

a) Initial elastic lattice deformation and onset of twinning

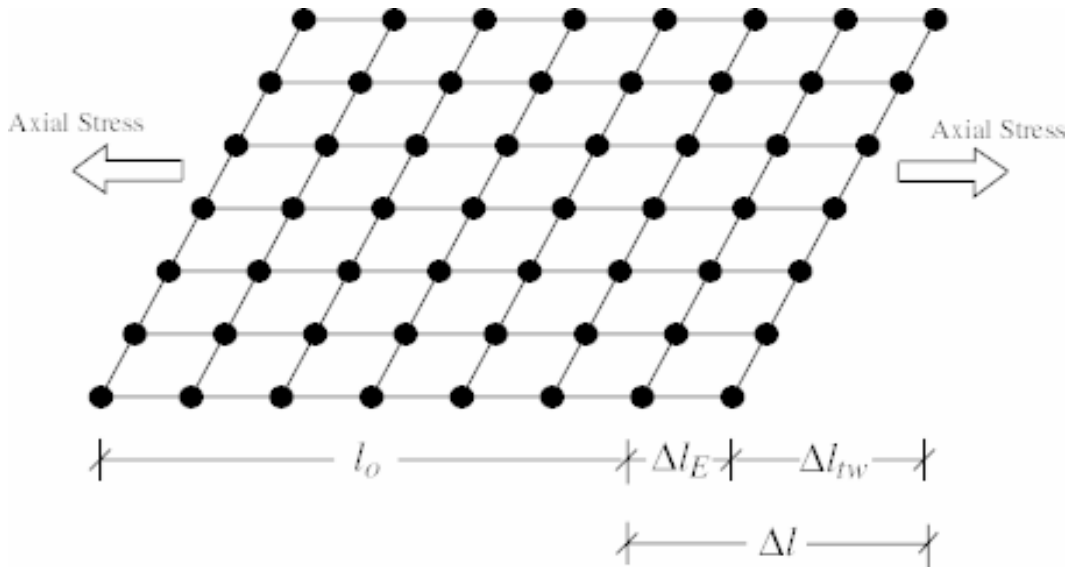

b) Stress-induced detwinned martensite

Figure 2.4 Effect of applied stress twinned lattice structure

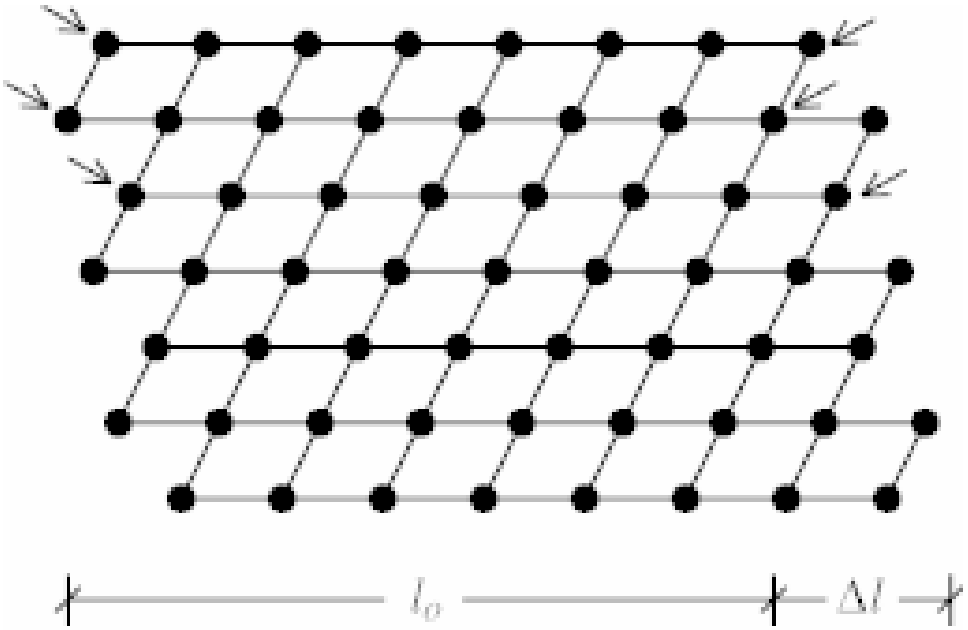

Figure 2.5 Deformation by slip

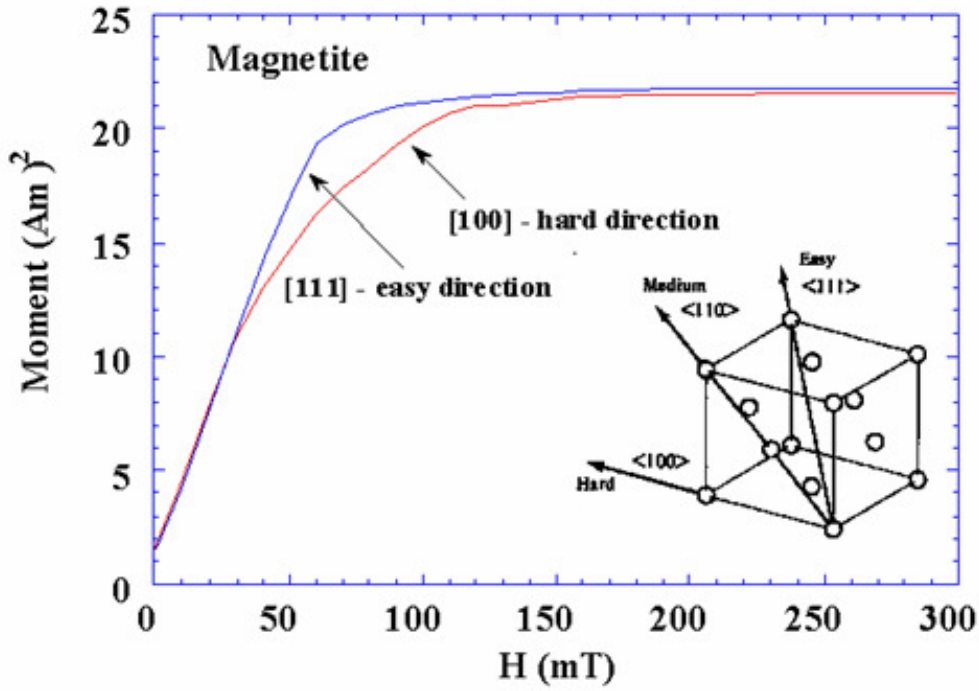

Figure 2.6 Magnetization curves for magnetite [202]

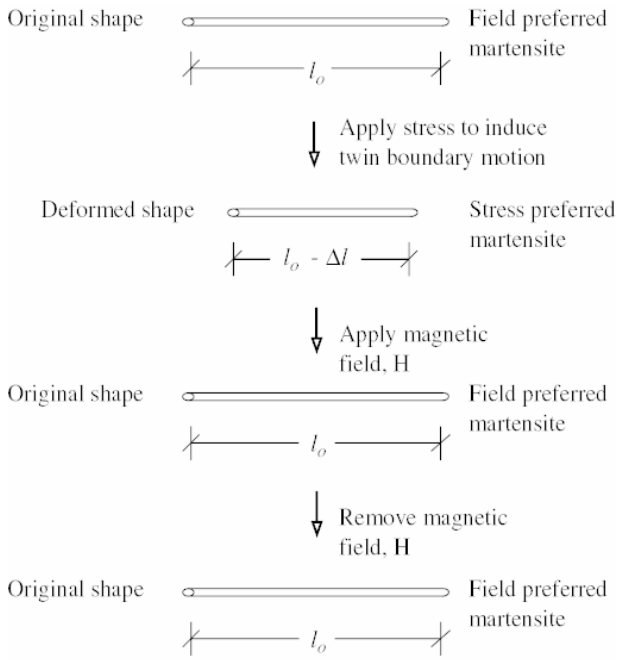

Figure 2.7 Schematic of the magnetic shape memory effect (MSME)

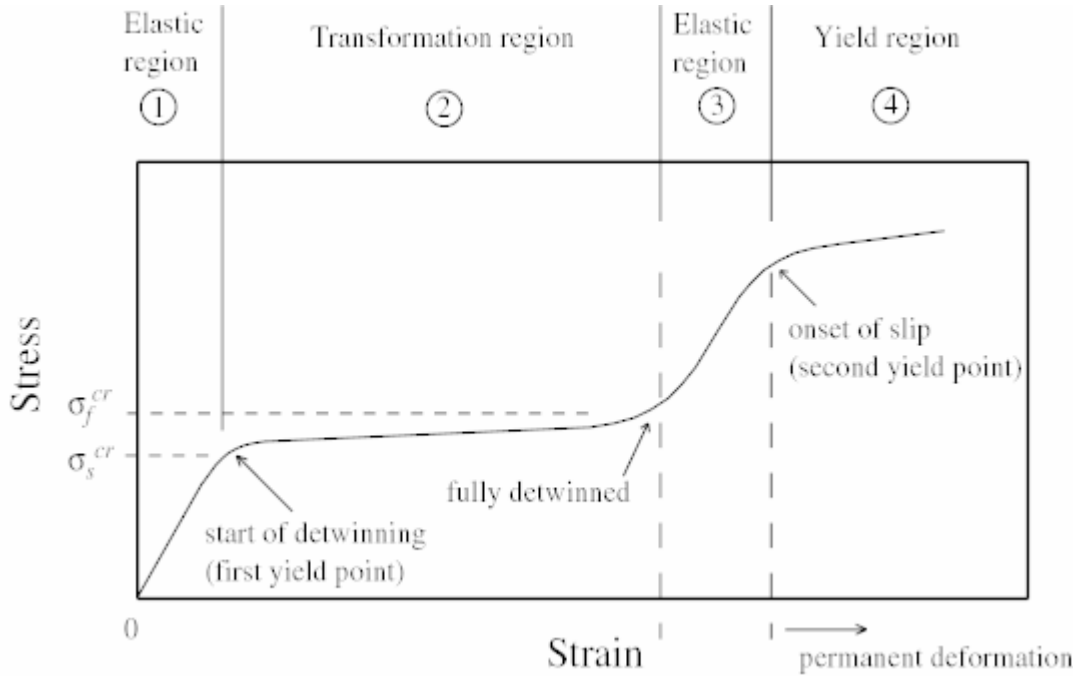

Figure 2.8 Stress strain curve for FSMA in tension under zero magnetic field

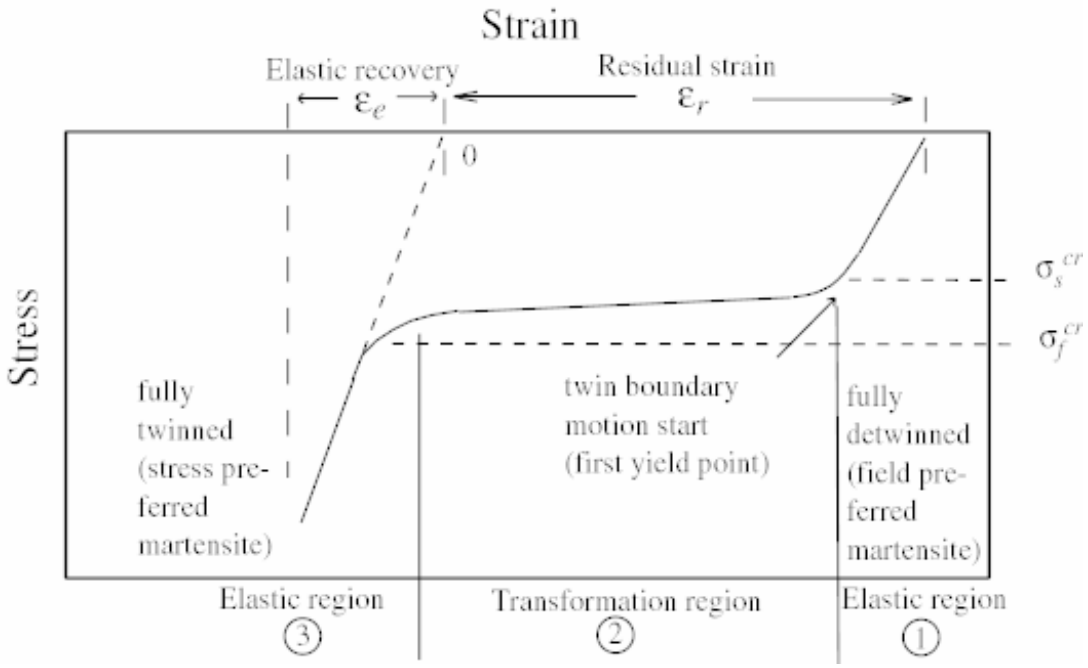

Figure 2.9 Stress-strain curve for FSMA in compression under zero magnetic field

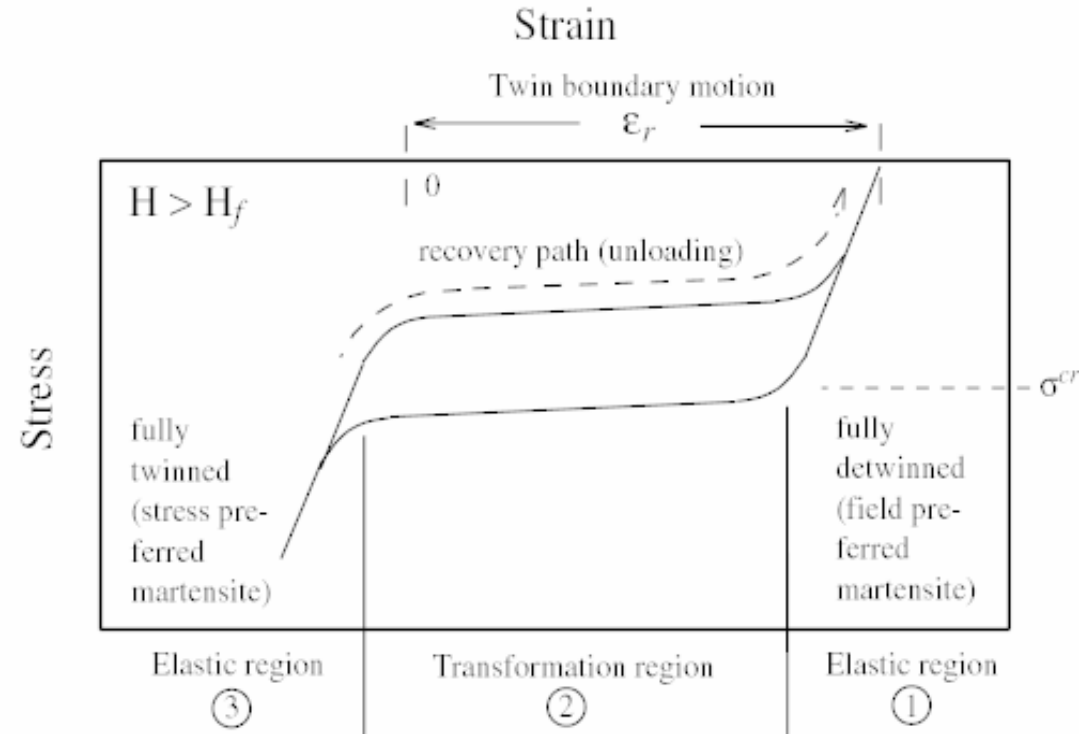

Figure 2.10 Schematic of stress-stain behavior for FSMA pseudoelasticity in compression

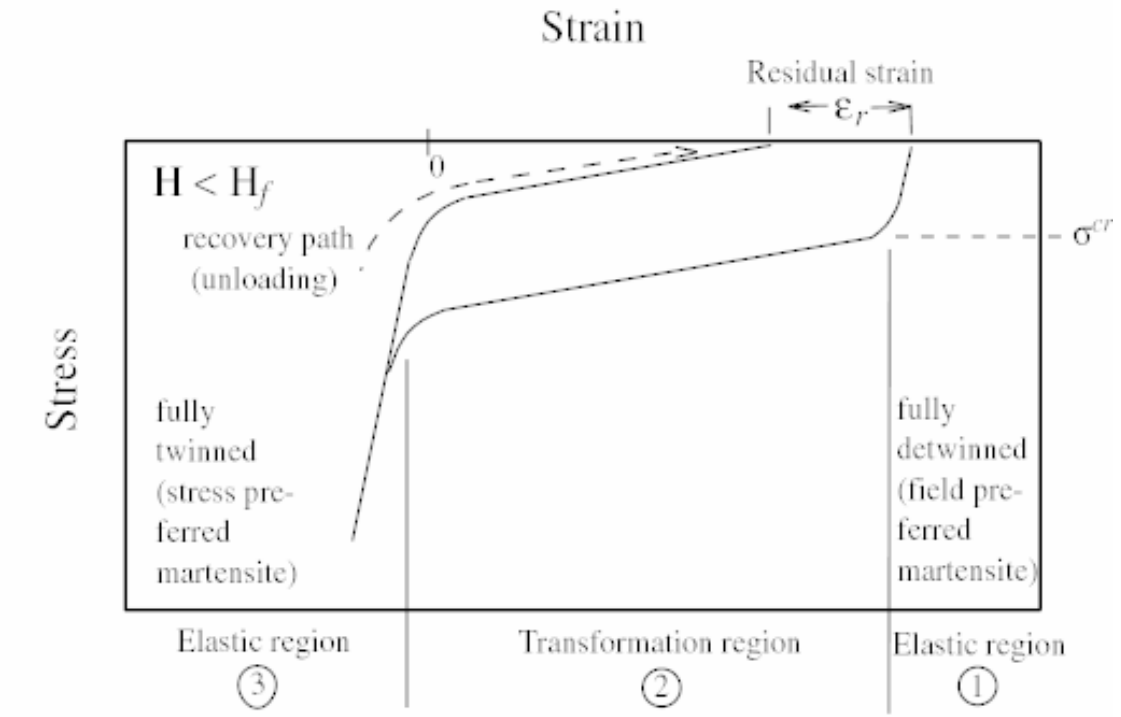

Figure 2.11 Schematic stress-strain curve for FSMA partial pseudoelastic behavior under compressive stress

Chapter 3: Quasi-Static Testing of NiMnGa

Materials exhibiting the magnetic shape memory effect have several desirable attributes that make them a potentially actuator material. The combination of a large induced strain potential and wide operating bandwidth present a strong argument for the use of NiMnGa in actuator applications. But in order to design actuators incorporating FSMA, it is first necessary to develop an extensive understanding of the characteristic magnetomechanical behavior of these materials. Thus this chapter focuses on the measurement of the quasi-static, uniaxial behavior of NiMnGa by testing bar specimens in compression. Tensile testing is not included because of inherent material limitations. However, since many smart material based actuators are operated in compression and to safeguard the actuator material from failure, the available NiMnGa specimens were configured to operate in response to compressive loading. Thus, the actuator material can be adequately characterized without exploring tensile tests.

This chapter discusses the behavior of NiMnGa magnetic shape memory alloy bar actuators under various mechanical and magnetic loading conditions. Testing is geared toward the quasi-static, or low strain rate, response of the NiMnGa to external magnetic and mechanical stimuli. A series of tests including constant stress, constant coil drive current, constant induction and constant strain are conducted to fully explore the material response. The data obtained from these test is necessary for the formulation of an initial design method for FSMA based, smart actuators. In addition, the phase transformation temperatures of the material, basic performance characteristics, and sensor characteristics are also determined.

This chapter is organized into three main parts. The first part details the initial transformation temperature tests, the determination of basic performance characteristics, and other various preliminary issues before systematic axial testing. The second part consists entirely of uniaxial testing related issues involving the constant stress, constant drive current, constant induction and constant strain tests. Each test is presented separately in detail. Finally, a brief discussion of the sensor characteristics and evaluation of the FSMA element as a practical sensor is included.

3.1 Differential Scanning Calorimeter Tests

In order to characterize the material behavior, it is important to identify the regions where the NiMnGa exists in the martensite phase. The magnetic shape memory effect is only present in regions consisting of stable martensite. These regions of stability however, are temperature dependent. Temperatures over which the phase transformation begins and ends are called transformation temperatures. Like thermal SMA, the transformation temperatures of FSMA are commonly denoted in the literature as A_s, A_f, M_s, and M_f for austenite start, austenite finish, martensite start, and martensite finish temperatures respectively [203, 204, 205]. These temperatures represent the stress free, phase transformation temperatures of the material.

Since the magnetic shape memory effect is observable only in martensite specimens, it is necessary to determine the temperature phase boundaries in order to establish a practical operating temperature range. To ensure that the specimen was in the complete martensite phase during quasi-static testing, the phase transformation temperatures were determined experimentally. If the A_s and A_f temperatures are

sufficiently higher than room temperature, then it can be guaranteed that the specimen is in the complete martensite phase and that the large strains produced in the presence of magnetic fields are the direct result of the magnetic shape memory effect.

To determine the transformation temperatures of the bar under zero stress, a Perkin-Elmer Pyris 6 Differential Scanning Calorimeter (DSC) was used. A photograph of the DSC is shown in Figure 3.1. To determine the start and finish temperatures for the phase transformation, the DSC determines the change in heat capacity of the material. When a phase transformation occurs in the material being tested by the DSC, it absorbs, or emits, heat over a small change in the specimen temperature. This effectively constant temperature heat emission or absorption is indicative of any type of phase transformation. Phase transformation refers to for example, a change in the various phases of water (i.e. steam, liquid, ice). The phase transformation appears as a peak in the plot of heat flow vs. temperature. The DSC allows the sample to be heated and cooled between given temperatures at a specific temperature rate controlled by an onboard temperature controller. Under normal operation, the thermal chamber is heated and cooled through a mixture of regulated helium and liquid nitrogen and a heating element attached to the bottom of the thermal chamber. However, since a supply of liquid nitrogen was unavailable for these tests, a mixture of ice and water was used for cooling instead. The ice-water mixture, although not as effective as the liquid nitrogen, allowed for specimen cooling to 10 degrees Celsius. Despite this limitation, this level of cooling was more than adequate for this particular experiment. Further details on this apparatus can be obtained from the Perkin-Elmer website [206].

Two separate material compositions were studied in this test. Both material compositions are derived from samples produced by the Adaptamat company. Composition #1 was manufactured before composition #2. Furthermore, composition #2 represents a significant advance in the metallurgical properties of the material.

3.1.1 DSC Sample Preparation

With the aid of a precision, water-cooled, diamond tip saw, small pieces of NiMnGa were shaved off of a parent specimen. These tiny NiMnGa chips were then placed in a small aluminum envelope and sealed using an aluminum cover plate and tabletop press. The result was a 30-35 gram NiMnGa specimen, completely enclosed in a tiny aluminum casing. To deduce the mass of the FSMA enclosed within the aluminum envelope, the empty mass of the pan is subtracted from the empty mass of the pan with the NiMnGa chips. For consistent, high quality results, the mass of the material tested with the DSC should be between 20 and 40 grams. A small, non-zero stress in the FSMA sample may be introduced as a result of the sample preparation process. However, since multiple specimens of varying mass tested in the DSC yielded nearly identical results, the effect of any small, pre-existing, non-zero stress is assumed to be negligible.

The first step in the DSC testing procedure consists of preparing baseline aluminum test pans. One test pan containing FSMA chips and two test pans without FSMA chips were prepared. The pans are weighed in a digital balance to determine, precisely, the mass of each. First, the two empty baseline pans were placed inside the thermal chamber of the DSC and subsequently sealed from the ambient environment. Next the temperature of the chamber was raised from 10°C to 100°C and then

lowered from 100°C to 10°C at a rate of either 2°C/min or 5°C/min, while the baseline heat flow rate vs. temperature was recorded by the data acquisition computer. After a complete thermal cycle, one of the baseline pans was removed and substituted with the pan containing the FSMA chips. Then, the temperature cycling procedure was repeated and the resulting heat flow that included the effect of the presence of the NiMnGa specimen was recorded. To obtain the quantitative, temperature-varying rate of heat flow for the FSMA, the heat flow from the baseline case was subtracted from the heat flow of the case containing the NiMnGa specimen. The result was a heat flow difference equal to the heat flow of the NiMnGa material. To ensure repeatability, this procedure was repeated 2-3 times for each sample. It was observed that the baseline heat flow was nearly constant and displayed no peaks, which suggested that the subtracted heat flow is important only for quantitative specific heat and latent heat measurements. Since these properties aren't necessary for the characterization of the magnetically induced actuation of NiMnGa, the unsubtracted heat flow rate of the FSMA is sufficient to determine the transformation temperatures of the material. Therefore, in this case, the baseline heat flow tests were not strictly necessary.

3.1.2 Determination of Transformation Temperatures

The transformation temperatures of the NiMnGa (A_s, A_f, M_s, M_f) were determined by heating the specimen pan at rates of 2°C/min and 5 °C/min. Both heating rates were slow enough to capture all of the important features of the transformation temperature behavior. However, it was observed that both heating rates yielded identical results. Furthermore, the results at each rate were highly

repeatable showing a difference of no more than 0.4°C between transformation temperature measurements. Since the transformation temperatures of the NiMnGa were adequately determined for low heating rates, heating at higher rates was unnecessary and not investigated.

The unsubtracted heat flow rates yielded from the DSC tests for two compositions of NiMnGa are plotted in Figures 3.2(a) and 3.2(b). Composition #1 is depicted in Figure 3.2(a) while composition #2 is shown in Figure 3.2(b). As stated previously, since the objective of this test is to determine transformation temperatures and not specific or latent heat properties, obtaining the unsubtracted heat flow rate vs. temperature plot was sufficient. The sharp peaks in the heat flow rate indicated a phase change in the material. Qualitatively, the magnitude of the heat flow rate during heating was approximately the same as the magnitude of the heat flow rate during cooling. The direction of the peak indicates the direction of heat flow either into (endothermic) or out of (exothermic) the sample during thermal cycling. The direction of the peak indicating an endothermic reaction is denoted on Figures 3.2(a) and 3.2(b). Transformation temperatures are determined by identifying temperatures that mark the start and finish of the heat flow rate peak. For example, during heating, the beginning and ending of the spike in the heat flow indicates the corresponding A_s and A_f temperatures of the material respectively. Likewise, during cooling, the beginning and ending of the spike in the heat flow indicate the M_s and M_f transformation temperatures. Transformation temperatures are denoted by circular markers in Figures 3.2(a) and 3.2(b).

The results of the DSC tests indicate that the martensite to austenite transformation for composition #1 occurred between 24 °C and 28 °C, very close to room temperature. However, for composition #2, the martensite to austenite transformation occurred between 56 °C and 61 °C, well above room temperature. In fact, all the transformation temperatures for composition #1 were significantly lower than those of composition #2. Since the A_s and A_f transformation temperatures of composition #1 are very close to room temperature, it can be argued that its usefulness in practical actuator applications is limited. Because the transformation temperatures are so close to room temperature, any increase in the temperature of the ambient environment would result in a degradation of the magnetic shape memory capabilities of the material and possible failure of the device. Since the most common method of FSMA actuation involves current carrying coils which typically produce significant amounts of heat, the ambient temperature is likely to be higher than room temperature. Therefore, composition #2 has more potential as an actuator grade of NiMnGa because it is less sensitive to small temperature changes in the environment. Table 3.1 lists the four experimentally determined transformation temperatures for both compositions of the NiMnGa, providing a comparison of both grades of the alloy. Since composition #2 has a higher martensite to austenite boundary all of the NiMnGa rods used in the quasi-static characterization tests utilize this composition. Furthermore, with regard to the present work, because all quasi-static tests were conducted at room temperature (~23°C), utilization of composition #2 ensures that the actuator remains completely in the martensite phase. As a result,

it was assumed that the full magnetically induced strain capability of the material was observed for all testing conditions.

3.2 Variable Stiffness Testing

The goal of the variable stiffness tests was to determine some basic actuator characteristics of the NiMnGa, such as block force, free strain and energy density. Not only do these parameters provide a general idea of the capabilities of the material as an actuator but they also provide a means to quickly compare NiMnGa to other smart materials such as Terfenol and piezoelectrics.

3.2.1 Variable Stiffness Test Hardware

The variable stiffness tests were carried out using a custom built test rig. A photograph and schematic of this test rig appears in Figure 3.3. The bar shaped specimen of NiMnGa was gripped between the poles of a laminated steel core electromagnet capable of producing inductive fields on the order of 1.0 Tesla. Between the tapered electromagnetic poles, a uniform, transverse magnetic field could be applied across the entire length of the specimen. Further details on the electromagnet are provided in following sections (section 3.3.2). The specimen was glued onto special aluminum grips using a high shear stiffness, cyanoacrylate adhesive. One end of the specimen was attached to an adjustable pushrod assembly. During tests, the adjustable pushrod remained immobile, effectively providing an infinite stiffness for the actuator to act against. Attached to the other end of the specimen was a moveable pushrod assembly consisting of an aluminum rod, variable stiffness spring, load cell, and advance screw. The preload on the NiMnGa specimen

could be adjusted by simply turning the advance screw. A set of Polysorb®, polymer disk spring washers manufactured by the Igus company [207] were used to construct the variable-stiffness spring. These disk washers were chosen because of several desirable properties including:

1. Constant spring coefficient: Spring force and deflection remain linearly related even for very small displacements. Deviations from linearity at large deformations occur only when the washer begins to "bottom-out." This event occurs beyond 90% of the washers total deflection.

2. Electrically insulated: Enabled the load cell to be insulated from electrical noise generated from the electromagnet.

3. No lubrication of the spring washers was necessary.

4. Adjustable: Spring stiffness and total deflection could be adjusted by placing stacks of washers in parallel and series combinations. Spring deflection increases proportional to the number of springs used while spring stiffness increases in proportion to the number of parallel combinations used.

A variable-stiffness spring was necessary in order to observe the behavior of the NiMnGa specimen as it was actuated against a wide variety of recovery springs. The use of the disk spring washers provided a simple design solution for developing a system that required the accommodation of a wide variety of recovery springs. With just 20 to 30 washers, hundreds of recovery springs combinations were possible. Forces generated by the FSMA element were measured by a 10 lb load cell accurately measuring loads to within 0.005 lb. An aluminum tab attached to the moveable pushrod provided a reference point for a laser sensor to measure the global deflection and subsequently the induced strain of the NiMnGa bar. The laser sensor could accurately detect deflections of 0.01 mm. The moveable pushrod was supported by a

low-friction, linear bearing that was lubricated before every test to ensure that frictional losses were minimized. Inductive fields applied to the FSMA element were measured by Hall Effect sensors located in the air gap between the electromagnetic poles and NiMnGa bar. Coil current was measured by tracking the voltage across a 1 ohm, 25W, precision resistor connected in series between the coil and ground. The current measurements were precise to within 5 mA. During the fabrication of the test rig, special care was taken to align the NiMnGa specimen, pushrods, load cell, and recovery spring to ensure that all applied loads were axial in nature and to minimize the impact of off-axis loads and moments. The alignment was precise to within 0.002 inches.

Power to the coils was provided by a programmable 20V/10A, DC power supply. Due to the high electrical power requirements of the electromagnet, a thermocouple was attached to the coils to monitor temperature, providing a safeguard to protect against overheating. Four parameters were measured including force, strain, magnetic field (induction), and coil current. Each signal was acquired by a 16 channel, computer controlled data acquisition system running on a MATLAB script.

3.2.2 Experimental Method: Variable Stiffness Tests

The variable stiffness tests were carried out using the following experimental procedure: first, a recovery spring stiffness was chosen and the disk washers comprising the recovery spring were appropriately configured. To simulate the limiting case of the blocked condition, the spring washers were removed and the specimen was allowed to push directly against the load cell through the moveable pushrod. The free strain condition was obtained by removing both the load cell and

the recovery spring so that the NiMnGa element could be allowed to reach the maximum induced strain in a zero stress environment. After the stiffness of the recovery spring was set, an axial load was applied to the specimen via the advance screw until the FSMA was fully converted into the stress preferred martensite configuration. If a recovery spring was being utilized, then a small preload of approximately 1N was applied to the specimen. This small preload was necessary in order to ensure a 'just-tight' packing of the spring washers on the test rig. Once the preload was set, the electromagnetic coils were energized and a magnetic field of 0.8 Tesla was applied to the FSMA element. While the field level was maintained constant, force and deflection data were recorded. Then, power to the coils was removed and the magnetic field was brought to zero. If necessary, the electromagnet was allowed to cool at this point. This step is essential not only to protect the coils from damage but to prevent changes in coil resistance as a result of wire heating, and the subsequent magnitude of magnetic field between tests.

3.2.3 Determination of Basic Actuator parameters

The primary goal of the static testing of the NiMnGa rod was to determine the force deflection behavior of the material. Once determined, the actuator stiffness can be calculated and then through a process of impedance matching, the energy density of the FSMA material can be calculated.

Determination of the actuator stiffness of the NiMnGa requires an accurate assessment of the force-deflection behavior of the material. This relationship was determined by exposing a sample of NiMnGa to a magnetic field approximately 0.8 T in magnitude to induce the magnetic shape memory effect and observe the aggregate

force and strain response as the material acted against a series of recovery springs. A total of twelve separate spring stiffnesses were examined including the blocked (significantly large stiffness) and free (effectively zero stiffness) conditions. Each spring stiffness constitutes one data point on the force-deflection curve. Furthermore, in an effort to minimize experimental error, each data point is the averaged result of three trials. Table 3.2 shows the averaged results of all twelve data points as well as the recovery stiffness of all twelve springs. Then the data shown in Table 3.2 were plotted to determine and evaluate the force-deflection behavior of the actuator. Figure 3.4(a) shows the experimentally determined force-deflection curve for NiMnGa endpoints on force-deflection curve. According to the data, this NiMnGa element has a block force (zero-strain load) of approximately 9.3 N and a free strain (zero-force strain) of 5.02%. These results were highly repeatable, with a variation of only 0.014 N in the block force measurement and a variation of only 0.08% around the free strain measurement. Judging by the results presented in Figure 3.4(a), the deflection of the actuator material increases linearly as the induced force decreases. The slope of this curve is equivalent to the spring stiffness of the actuator material. This spring stiffness was determined to be 10 N/mm. Using the cross-sectional dimensions of the FSMA element (2mm x 3mm) and the original length of the specimen (16.4 mm), the data in Figure 3.4(a) can be re-plotted in terms of stress and strain. The slope of this curve is equivalent to the modulus of the material as it is undergoing twin boundary motion. The region twin boundary motion encompasses the material behavior when the crystal structure is reorienting itself from a stress to field preferred configuration under the influence of an external magnetic field. The

experimentally determined stress-strain behavior observed in the variable stiffness tests appears in Figure 3.4(b). Based on the experimentally determined curve shown in Figure 3.4(b) the modulus of the twin boundary motion region was calculated to be 26.3 MPa.

Once the force-deflection behavior of the NiMnGa specimen was determined, the energy density of the material was calculated next. Using the principle of impedance matching, the optimum energy output of the material was calculated. Since it was determined that the actuator stiffness of the material was approximately 10 N/mm the NiMnGa spring can be matched to recovery spring #7 on Table 3.2 which has a similar spring stiffness of 10.21 N/mm. Based on the force-deflection data for this spring, the optimum available work output for this NiMnGa actuator was calculated to be 2.73×10^{-3} J. Dividing the optimum available work output by the material volume and mass yields the energy densities by volume and weight respectively. The energy density of the NiMnGa element was calculated to be 28.34 kJ/m^3 by volume, and 3.39 J/kg by weight. Given the fact that the energy density of most commercially available piezostacks varies between 0.12 and 5.85 J/kg, this finding suggests that at least superficially, NiMnGa is comparable with piezoelectric stacks [129]. Qualitatively speaking, a piezoelectric stack is a high-force, low-displacement, solid state device while a NiMnGa can be considered a low-force, high displacement, solid state device. Essentially, NiMnGa trades the force generation capability of a piezoelectric stack for a large induced strain capability.

One important point must be mentioned regarding the calculation of the energy density of NiMnGa. These calculations were based on the material alone and

did not include the presence of the electromagnetic coils. Unlike piezoelectric materials, in order to actuate the NiMnGa, it must be contained within a relatively massive magnetic circuit. Therefore, to more accurately compare NiMnGa to other active materials, the mass of coils, optimized for both mass and performance, should be included in the FSMA power density calculations. The main reason that this was not done at this point was that the laboratory electromagnet used for this set of tests was unnecessarily massive. Therefore, power densities calculated using the parameters of this particular magnetic circuit would result in an unintentionally misleading data. Because this study of NiMnGa was still in its initial stages, a set of coil optimization parameters had not yet been developed. Instead, the magnetic circuit was designed for its, in terms of magnetic field generation, brute strength without consideration of optimizing its weight or volume. In proceeding chapters, the issue of designing an optimized coil will be revisited enabling the calculation of a more accurate material power density.

3.3 Uniaxial Quasi-Static Testing

A series of quasi-static tests focused on subjecting the NiMnGa bars to a series of magnetic and mechanical loading conditions was conducted. By systematically testing bars of NiMnGa, the material behavior is characterized and its feasibility for use in smart actuators is evaluated. Several categories of test procedures were developed and implemented. These tests included determining the strain response for a constant axial stress, evaluating the stress-strain behavior for a constant coil drive current, observing the stress-strain response for a constant induction, and finally, investigating the force response of the material under a

constant pre-strain. Not only do these tests provide an assessment of the actuator capabilities of the FSMA, but they will be very useful in determining appropriate parameters for use in a constitutive model designed to predict material behavior.

3.3.1 Sample Preparation and Composition

The specimens used for the quasi-static testing were all manufactured by the Adaptamat company based in Helsinki, Finland. Commercial grade, single crystal NiMnGa specimens are first grown in production furnaces into 30 cm long 'billets'. Next, smaller FSMA sticks, or bars, are cut from these billets. Depending on the customer's specifications, the size of these sticks generally runs between 0.1 and 40 mm. Furthermore, the type of motion (extension, torsion, or bending) can be controlled by the orientation of the crystal structure of the stick as it is cut from the larger billet. After undergoing a series of proprietary magnetic and surface polishing treatments, the specimens are ready for use in actuators. Further information on NiMnGa production procedures can be obtained from the Adaptamat website [135].

The current study involves the use of eight, single-crystal, martensite, NiMnGa bars obtained from Adaptamat. These specimens were oriented for extensional strain resulting from an orthogonally applied magnetic field. Specimen dimensions in the stress preferred configuration (configuration after an applied axial stress at zero field) were 2 x 3 x 16.4 mm, and the magnetic easy, or c axis, is oriented parallel to the direction of the long axis. Therefore, magnetic strain is induced when a field is applied perpendicular to the long axis of the NiMnGa Rod. Specimen dimensions in the field preferred configuration (configuration after an

applied orthogonal field at zero stress) were 2 x 3 x 17.4 mm. Furthermore, the density of the material was measured to be 8.36 g/cm^3.

3.3.2 Test Hardware

The quasi-static, uniaxial tests were carried out on three different test rigs, each one accommodating the demands of a specific magnetic and/or mechanical testing environment. Two of the test rigs were custom designed and developed at the University of Maryland, while the third was purchased from a commercial manufacturer of material testing equipment.

The first category of testing, the constant axial stress tests, utilized a custom built test rig. A labeled photograph and schematic of the constant stress test rig is shown in Figures 3.5(a) and 3.5(b). A NiMnGa specimen is oriented vertically (perpendicular to the ground), and gripped between a stationary lower grip and a moveable upper grip. Because of potential mechanical interference between the specimen grips and electromagnetic circuit, an alternate method of gripping the material was employed. Instead of mechanical grips, the NiMnGa specimen was glued into the aluminum 'grips' using a high shear stiffness, low viscosity, cyanoacrylate adhesive. Special care was taken in order to ensure that only small amounts of the adhesive were used to minimize the effect of the bond layer on the twin boundary motion of the NiMnGa. This method allowed the specimen to be located between the poles of the electromagnet without any mechanical interference. The specimen was supported by a stationary, lower rod so that when an external field was applied to the FSMA element, the resulting induced strain is restricted to the vertical direction only. When an orthogonal magnetic field was applied, the specimen

pushed against the moveable, upper pushrod. This upper pushrod was attached to a low-friction, linear bearing to minimize the effect of friction on the material response. Above the upper pushrod, another support rod attached to the upper end of the linear bearing connected the bearing-pushrod combination to a linear potentiometer and weight pan. Global, induced strains were measured by the linear potentiometer, which was precise to within 0.002 mm, and the level of constant stress was regulated by adding and subtracting weights to the weight pan. The mass of the weight pan, linear potentiometer and support rods was measured to be 100 grams. The maximum mass acceptable to the weight pan was determined by the maximum force rating of the linear bearing. The maximum allowable mass in the weight pan was restricted to 2 kg to minimize the effect of friction as a result of overloading the bearing. The NiMnGa specimen itself is situated between the two poles of a laminated steel core electromagnet. Applied magnetic field measurements were obtained by two Hall Effect sensors located in the air gap between the magnetic pole and NiMnGa bar. The electromagnet in this rig was powered by two 30V/5A power supplies connected in series. To control the decay of the magnetic field after the power supply was switched off, a rack of capacitors was connected in parallel with the coils to obtain a sufficient RC time constant in the electrical circuit. Two sets of capacitors were used over the course of the constant stress testing. For preliminary constant stress testing, the rig utilized one 20 volt / 50,000 μF and two, 50 volt / 10,000 μF capacitors in the RC circuit. The time constant of this configuration was acceptable but the maximum voltage applied to the electromagnet was limited to 20 volts which resulted in an unacceptable level of applied magnetic field (less than 0.8 Tesla). The capacitor bank

was upgraded to include ten 50 volt / 10,000 μF capacitors. This configuration improved not only the RC constant of the circuit, but raised the maximum applied voltage to 50 volts instead of 20 volts. In addition, this change allowed more current to pass through the coils and therefore produce a larger magnetic field. The upgraded RC configuration allowed the electromagnet to generate a maximum magnetic field of 1.2 Tesla when the NiMnGa specimen was present in the magnetic circuit. As mentioned previously, a high RC constant is necessary to have a slow decay in the magnetic field when the power was removed so that the quasi-static behavior of the material could be observed. Current in the electromagnetic coils was monitored by measuring the voltage across a 1 ohm, 25W, precision resistor connected in series, between the coil and ground. In Figure 3.6, a schematic of the electrical circuit is provided.

The experimental rig used in the constant drive current tests was also designed and developed at the University of Maryland. A photograph and operational schematic of the constant field test rig appears in Figures 3.7(a) and 3.7(b). Within this rig, the NiMnGa specimen was gripped between a stationary, 25 lb load cell and a moveable carriage. Similar to the constant applied stress test rig described above, the specimen was glued into the 'grips' using small amounts of a high shear stiffness, low viscosity, cyanoacrylate adhesive. To ensure that the specimen was entirely exposed to a uniform magnetic field and to minimize the effects of magnetic fringing at the boundaries of the magnetic poles, the FSMA was carefully situated within the center of the air gap in the magnetic circuit. Loads were applied to the NiMnGa bar via a motorized, moveable carriage assembly. The carriage was supported by two,

precision linear bearings attached to two parallel bars in order to minimize the effects friction. The carriage, itself was driven by a computer controlled, NEMA-23 precision, stepper motor and screw assembly. Axial loads were applied to the specimen by energizing the stepper motor and allowing it to compress the FSMA rod against the load cell at a prescribed strain rate. For this set of tests, the NiMnGa bar was compressed at a rate of 0.02 mm/sec, to simulate quasi-static actuation. The precision of the load cell was within 0.0045 N and was used to measure the compressive loads on the FSMA specimen. As in the case of the of the constant stress tests, the magnetic field, B, was measured by a set of Hall sensors placed in the air gap between the specimen and pole face. Applied magnetic field intensity, H, was determined by calibrating the electromagnet with the level of current in the coils without the specimen present in the magnetic circuit. Coil current was determined by measuring the voltage across a 1 ohm, 50W, precision resistor in series with the coil. Typical levels of current varied between 0 and 3.5 amps. To protect the instrumentation, the precision resistor was connected between the coil and ground to prevent creating electrical short between the resistor and data acquisition system. Power to the coils of the electromagnet was provided by a 5V DC excitation signal from the data acquisition card routed to an amplifier connected in series with the coils. A schematic of the electrical circuit appears in Figure 3.8. To determine the induced strain of the FSMA material, the global displacement of the carriage was measured by recording the angular deflection of the stepper motor using a rotary potentiometer. The accuracy of the strain measurement is within 0.01 mm or 0.062 % strain.

Data acquisition for the custom rigs was handled by a computer and a multi-socket-type National Instruments data acquisition board. Signals from the Hall Effect sensors, precision resistors, load cell, and potentiometers were routed through 10 V analog feed-through modules. Data was acquired at a sampling rate of 1000 samples per second which was more than adequate for a quasi-static test. A simple MATLAB script was written for both test categories to acquire and process the data.

For the final two categories of tests, the constant induction and constant strain tests, and to validate the data obtained from the custom test rigs, a Fasttrack 8840 series DynaMight, tabletop, axial test machine was purchased from the Instron corporation. A photograph of the DynaMight rig appears in Figure 3.9. The DynaMight consists of a high stiffness, single column load frame configured in a vertical orientation. Axial loads are measured by a 1 kN load cell mounted directly below the lower grip on the load frame. The accuracy of the load cell is within 0.01 N. Strain measurements are obtained by measuring the global displacement of the servo-hydraulic actuator mounted above the upper grip on the load frame. Global displacement of the servo-hydraulic actuator was measured by a LVDT and accurate to within 0.001 mm. Using a built-in, user defined PID controller, the DynaMight rig was capable of maintaining either a prescribed position or a prescribed load. For further details on 8840 series axial test machine, consult the Instron website [208]. To supply a uniform magnetic field to the FSMA specimen, the electromagnet coils were mounted on aluminum struts to position the pole faces so that they would fully enclose the test section. Power to the coils was provided by computer controlled output module fed through a series LVC623 AE Techron Inc, current amplifier.

Connected to a single channel, the amplifier was capable of continuously supplying 145 W or 4 amps to the electromagnet coils.

Data acquisition for the DynaMight system was handled in a manner similar to that of the custom test rigs. The onboard data acquisition system of the DynaMight rig was capable of handling only two channels of data. One channel acquired load cell signals while the other channel acquired LVDT signals. However, since additional channels were needed for magnetic field and coil voltage/current measurements, an auxiliary data acquisition system was employed. Signals from the load cell and LVDT were routed through the onboard data acquisition system and then sent to a National Instruments data acquisition card via two 10V analog feed-through modules. Since the maximum voltage of the LVDT exceeded 10V, it was necessary to add a simple voltage divider circuit to step the voltage of the LVDT signal down to a level that the data acquisition card could accept. Signals from the Hall Effect sensors were routed through two full-bridge, isolated strain gage input modules. The excitation voltage from these strain gage modules was fixed at 3.3V. This presented a problem because the input impedance of the Hall Effect sensors was low (approximately 50 ohms) and the maximum allowable control current was 30 mA. At this level of excitation voltage, the control current was approximately 70 mA, more than twice the allowable limit. The effect of the resulting excitation current passing through sensor was to saturate the data acquisition card (i.e. generate a Hall voltage signal in excess of 10 volts in response to the magnetic field) or cause the sensor to 'burn out.' To solve both of these problems, a small resistor network was connected in series between the excitation voltage terminals supplied by the

strain gage module and the Hall Effect sensor. The resistor network effectively raised the input impedance of the Hall Effect sensor from 50 to 2000 ohms, subsequently dropping the control current to 16 mA, well within the allowable limit. As a result, the peak Hall voltage sensed by the data acquisition card dropped below the 10V saturation voltage. The Hall Effect sensors were calibrated using a F.W. Bell model 5080 Gauss/Tesla meter. Each sensor was taped to the field probe of the gaussmeter to ensure that both devices were measuring the magnetic field at the same reference location. Then, using the magnetic coils to generate a field in response to a known level of drive current, readings from the gaussmeter and Hall effect sensor were recorded. Calibration factors for the Hall effect sensors were determined from a series of these measurements. The resolution of the gaussmeter measurements was 0.01 mT. The accuracy of the DC measurements from the gaussmeter was within 1% of the reference value and the device was capable of accuracy to within 3% for AC measurements. The sensitivity of the Hall voltage detected by the Hall effect sensor was 12 mV. Coil current and coil voltage were obtained from the current and voltage monitors on the current amplifier. Both signals were routed through 10V analog feed-through modules on the data acquisition board. A 5V isolated voltage output module connected to the current amplifier was used to energize the electromagnetic coils. Figure 3.10 shows a block diagram of the data acquisition hardware. A brief LABVIEW script was written to handle the data acquisition, data pre-processing and function generation.

DC magnetic fields for all the test rigs, including the variable stiffness test rig, were applied to the NiMnGa by a laminated, transformer-steel core electromagnet

capable of producing field intensities on the order of 10 kOe. Inductive fields on the order of 1.2 Tesla were achievable in the coupled FSMA-field generator system. The magnetic circuit was built around a laminated core divided into two, E shaped halves, each consisting of 50 transformer steel layers. The halves are joined together by an aluminum frame and an air gap was machined out of the center bars of the E-frame to create magnetic poles. The dimensions of the pole faces were 27 mm thick by 24 mm in length. These dimensions were deliberately chosen so that the effects of magnetic fringing at the edges of the pole faces could be neglected. Magnetic fringing can significantly reduce the magnetic field at the boundaries and is therefore not desirable when attempting to create a uniform, magnetic field environment. Since the FSMA element achieves a maximum length of 17.4 mm when exposed to a sufficient magnetic field, a margin of 3.3 mm (or 20% of the specimen length) from the edge of the actuator to the edge of the pole face in the lengthwise direction, is left at either end of the specimen. As a rule of thumb, a margin of only 10% is required to be able neglect the influence of fringing. The two, 500 turn, 24 gage, copper wire coils, connected in parallel, were fixed to the poles of the laminated core by interchangeable Delrin bobbins. The copper wire was carefully wound, by hand, around the bobbins in even rows to maximize the flux linkage. Once completed, the inductance of the coil was measured to be 0.45 H, with a standard deviation of 5.4 mH. NiMnGa specimens were situated in between the two tapered poles of the electromagnet where a uniform, transverse field could be applied to the entire specimen. A 25% taper along the length of the electromagnetic poles was introduced in order to focus the magnetic flux into a smaller area at the pole faces. Tapering is an effective method of

passively increasing the flux density across the NiMnGa specimen. When the NiMnGa specimen is present, an air gap of approximately 0.030" exists between the specimen and the two pole faces. Reluctances of each component of the magnetic circuit were then calculated. The approximate reluctance values of the laminated steel core, air gap and FSMA element were 15000 A/Wb, 97000 A/Wb, and 2028000 A/Wb respectively. It should be noted that these reluctances are not constant but functions of the magnetic permeability which is a field dependent parameter. However, these component values do provide insight into the relative magnitude of the magnetic circuit parameters. A generalized schematic of the magnetic circuit of the coil appears in Figure 3.11.

As mentioned previously, uniformity of the applied field was necessary in order to increase the accuracy of induced strain and force measurements observed in the NiMnGa specimen. A non-uniform field environment will introduce additional uncertainty into the measurements of induced force and strain. Also, one of the main assumptions in the magnetic circuit modeling (see Chapter 6) is that the applied magnetic field is uniform. Testing in a uniform magnetic field environment improves the correlation between experiment and analysis. To ensure that a proper field distribution was applied along the length of the specimen, Hall Effect sensors were used to characterize the uniformity of the field between the poles. The sensors were placed at 11, regularly spaced, intervals along the entire length of the magnetic poles, coinciding with the location of the FSMA element. At each station, the magnetic induction was measured for a constant voltage supplied to the coils. Using this data, a profile of the magnetic field applied was developed to evaluate the uniformity of the

field across the pole faces. This profile appears in Figure 3.12. Based on the profile shown in Figure 3.12, the applied magnetic field varied less than 2% along the plane of the pole face. Therefore, the applied field was assumed to be uniform for the purpose of these tests. Furthermore, since the magnetic field showed little variation at the pole edges (stations 1 and 11), it can be concluded that magnetic fringing at the boundaries was not a significant issue for this coil configuration.

3.3.3 Unique Measurement Challenges Involving NiMnGa

Most magnetostrictive materials, terfenol and galfenol for example, are configured to produce actuation in the presence of a collinear field. In contrast, none of the NiMnGa samples observed in this study were configured for a collinear field and strain actuation. In the case of the specimens used in the current study, the direction of the magnetically induced strain in NiMnGa is instead, *perpendicular* to the direction of applied field. The orthogonal field and strain actuation configuration presents a problem when trying to determine the field and magnetization *inside* the alloy (specifically, the quantities $H_{internal}$ and M). For the purpose of comparison, first consider the case of collinear field actuation for another magnetic smart material such as Terfenol. Figure 3.13 shows a schematic of collinear field actuation of a terfenol rod. The terfenol specimen is gripped between two poles of the flux return path (S and N). A magnetic field is applied to the terfenol via the primary coil. A secondary, pickup coil is wound within the primary coil to measure the total flux density, B, passing through the specimen. Using continuity assumptions, a Hall Effect probe can be used to determine the field intensity, $H_{internal}$, inside the specimen. Since B and $H_{internal}$ are now known, the magnetization vector, M, can be calculated. In the

example of collinear field actuation, the geometry of the configuration is convenient for the measurement of the magnetic vectors B, $H_{internal}$, and M [209]. In contrast, for the case of perpendicular field actuation, the geometry of the configuration is inconvenient for measuring these quantities. Figure 3.14 shows the a schematic of the perpendicular field actuation of a NiMnGa rod. In this case, the pick-up coil must be wound around the long axis of the specimen in order to measure the total flux passing through the FSMA. Furthermore, the Hall Effect probe must be placed on the face perpendicular to the long axis of the specimen in order to take advantage of continuity assumptions. Since the direction of strain in the NiMnGa specimen is perpendicular to the applied field in this configuration, the necessary locations for the Hall Effect sensor and pickup coil cause mechanical interference with the material actuation. In order to take advantage of continuity, the Hall Effect sensor must be placed within the load path of the specimen which, over time, can damage the sensor. Furthermore, the geometry of the pickup coil not only creates a problem with gripping the specimen but, due to its location, causes a physical constraint to the actuation of the NiMnGa bar. Other configurations are possible, however, given the limited space available within the air gap of the magnetic circuit and mechanical constraints involved with gripping the specimen, it is difficult to determine the B and $H_{interenal}$ for this configuration. Instead, the material is characterized with respect to the induction in the complete magnetic circuit (flux return, air gap, and NiMnGa bar) and the level of drive current within the coils, without the NiMnGa specimen (applied field intensity without the presence of the FSMA element). Although it does not provide a complete picture of what is happening inside material, these parameters are

very useful for characterizing actuators containing NiMnGa elements because they are simple to measure and because they include the effects of the magnetic circuit. For practical actuator applications, the design of the magnetic circuit is critical, often providing the most stringent limiting factors in the actuator design. Since the focus of this study is to evaluate the FSMA material as an actuator material, it is necessary to include the effect of the entire magnetic circuit in the characterization. The obvious drawback to this choice of measurement parameters is that the magnetic behavior inside the specimen cannot be completely determined, therefore material specific effects such as the magnetization vector, internal field intensity, and the influence of the demagnetization field cannot be decoupled from the magnetic circuit.

3.4 Constant Axial Stress Tests

The three goals of the constant axial stress tests were to determine, as functions of applied stress, the induced strain, the residual strain, and the behavior of critical transformation fields. The first two goals are geared toward developing an understanding of the capabilities of the material itself, while the third goal was directed toward the identification of model parameters.

3.4.1 Experimental Method: Constant Stress Testing

The constant stress tests were carried out using the following procedure. After the NiMnGa rod was properly situated in the grips, 2 kg of mass was added to the weight pan above the actuator material in order to provide enough compressive force to fully configure the NiMnGa specimen into the stress preferred state. After a few seconds of exposure to the influence of the load, the specimen reverted to the

stress preferred state. At this point, the 2 kg mass was removed. Next, mass was added to the weight pan until the axial stress acting on the specimen reached the desired level for the current testing scenario. As mentioned previously, any mass between 100 grams (empty pan weight) and 2100 grams (empty pan weight plus 2 kg of additional mass) could be used. Once the desired mass was added to the weight pan, the FSMA element was ready to be magnetically cycled. Next, the power supply to the electromagnet was switched on to energize the coils and charge the capacitors. As this process was occurring, the magnetic field applied to the specimen was also increasing. Eventually, the level of magnetic field was sufficient to induce the magnetic shape memory effect in the material and subsequently produce an induced strain. In each case, the coils produced a magnetic field that varied from 0 to 1.1 Tesla over an interval of 40 seconds. Halfway through the test, and once the capacitors were fully charged and the maximum magnetic field level of 1.1 Tesla had been reached and sustained for a few seconds, the power to the coils was removed and the field was allowed to decay. The rate of this decay in the magnetic field was prescribed by the RC constant of the circuit as the capacitors discharged through the coils. Time histories of the magnetic field, B, the magnitude of current in the coils, and the actuator displacement were recorded over the entire test duration.

3.4.2 Determination of Critical Stress Behavior

One of the key goals in the characterization of NiMnGa as an actuator material was to observe the capabilities and behavior of the specimen for different loads. In the present study, only axial loads were considered. Currently, commercial grade NiMnGa samples are configured to generate extensional strain as a result of an

external, transverse magnetic field. Although theoretically possible, specimens configured to operate in the bending and torsion modes are not commercially available at this time. However, NiMnGa specimens configured for extensional actuation provide the potential for a wide variety of actuator applications. Direct measurements of the induced strain and threshold fields of the FSMA for a complete range of axial loads are needed to define the actuation capabilities of the material.

Consider for a moment, thermally reactive SMA materials such as NiTi. For this class of materials, constant stress testing is used to develop a profile of the stress vs. temperature behavior [170, 210, 211]. Generally, this behavior is determined by identifying the temperatures at which the transformation between martensite and austenite occurs (M_s, M_f, A_s, A_f) for a constant stress and then plotting these points over the entire range of stresses tested. This profile is a very valuable tool because it can be used to predict the state of the material for virtually any set of thermal or mechanical loading conditions. Furthermore, the profile is useful for determining parameters that can be utilized in a phenomenological model. Likewise for NiMnGa, one of the main goals was to develop a similar, experimental profile. In this set of tests, the goal was to determine as a function of axial stress, the magnetic fields signifying the transformation between stress and field preferred martensite during magnetic loading and the magnetic fields signifying the transformation between field and stress preferred martensite as the magnetic field was removed. These critical transformation fields could then be plotted over the entire range of stresses to assemble a profile of the stress vs. magnetic field behavior of the NiMnGa material. For this set of tests, inductive fields between 0 and 1.1 Tesla and stresses between

0.17 and 2.5 MPa were applied. Critical transformation fields were identified in each case and the results were plotted on the stress vs. magnetic field profile. Once completed, the profile was evaluated for its potential use as a tool for predicting material behavior. Differences in the quality results between 'low' and 'high' levels of applied stress were noted.

In Figure 3.15, the material behavior acting against a constant stress of 0.4 MPa (250 grams) is shown. The data is meant to showcase a typical result for a characteristically 'low' level of applied compressive stress. As the magnetic field is increased, a rapid increase in the induced strain occurs after increment 1 (0.24 T). This increase in the strain response indicates the onset of twin boundary motion in the FSMA element as the material begins to convert from a stress preferred martensite variant to a field preferred martensite variant. After increment 2 is reached (0.68 T) the strain response levels off indicating that the material can no longer yield additional induced strain. This behavior signifies that the twin variants have been completely reoriented into the field preferred martensite variant and that the material has produced the maximum amount of induced strain for this particular magnitude of axial loading. The magnetic fields corresponding to each station are known as threshold fields and signify the start and finish of the twin boundary motion in the material. During this phase of the test, the maximum induced strain of the FSMA element was observed to be 6.5%. Comparing this result to the maximum induced strain observed during the variable stiffness tests (5.02% strain, see section 3.2) it is clear that there exists a significant difference in the actuator capabilities between specimens. After the magnetic field was allowed to reach 1.1 T and dwell at that

level for approximately 10 seconds, the power to the coils was removed and the behavior of the material subjected to a constant axial stress in a decaying magnetic field environment was observed. As the field decreased, the level of strain in the actuator began to decay at increment 3 (0.55 T). Increment 3 represents the beginning of the reverse transformation from the field preferred martensite variant to the stress preferred martensite variant. As the field was decreases below increment 3, the twin boundaries became mobile under the influence of the applied compressive stress. The magnetic field associated with increment 3 represents another threshold field, this time signifying the transformation back to the stress preferred configuration. However, because the level of applied stress is 'low' in this case, the material is never completely reverted back to the stress preferred condition when the level of magnetic field returns to zero. Instead, a residual strain of approximately 1.5% remains in the NiMnGa bar, supporting the assertion that the magnitude of constant stress is not sufficient to entirely compress the actuator back to its original, stress preferred condition. The residual strain is proportional to the volume fraction of field preferred twin variants remaining in the FSMA element after the removal of the magnetic field. This residual strain is recoverable and may be removed by applying additional axial force to the actuator. In the limiting case where the minimum amount of axial stress is applied to the material (0.17 MPa) there is no reverse transformation from the field preferred to stress preferred martensite variants. The stress level for this case is simply to low to induce any twin boundary motion in the material. Figure 3.16 shows the results for a constant stress of 0.17 MPa (100 grams). The residual strain in this case was 6.5% and two critical threshold fields

were identified. Generally, for cases where a 'low' level of axial stress is applied to the NiMnGa element, only 2 or 3 threshold fields can be identified.

One important issue associated with 'low' stress level testing is the quality of the data, specifically the certainty of the location of the threshold fields. Consider again the case where an axial compressive stress of 0.4 MPa is applied to the NiMnGa specimen (Figure 3.15). During the forward transformation from stress to field preferred martensite, stations 1 and 2 are relatively easy to identify. At a specific point, or threshold field, a sharp change in the strain response occurs. After station 1, a sharp increase in the strain response occurs continuing until, at station 2, the induced strain abruptly levels off. The distinct changes in the threshold fields during magnetic loading enable them to be easily identified. In contrast, when the magnetic field is decreased to zero, the strain response did not show characteristically abrupt changes, but instead displayed a gradual, smooth decay. The consequence of this behavior is that since the threshold fields are less distinct, it becomes exceedingly difficult to identify the exact location where twin boundary motion begins during the unloading of the magnetic field. This subsequently introduces a significant level of uncertainty in the measurement of threshold fields for the reverse transformation. Furthermore, this level of uncertainty will be transferred to the stress vs. magnetic field profile, limiting its use as an indicator of quasi-static material behavior.

In Figure 3.17, the FSMA specimen subjected to a constant compressive stress of 1.3 MPa (800 grams) is shown. This set of data is meant to showcase a typical result for a characteristically 'high' level of applied stress. As in the case of the 'low' level of constant applied stress, station 1 (0.42 T) was characterized by a sharp

increase in the strain response, indicating the onset of twin boundary motion, while station 2 (0.88 T) was characterized by an abrupt plateau in the induced strain. Stations 1 and 2 denote the boundaries of the forward transformation from stress preferred to field preferred martensite and their corresponding threshold fields are substantially larger in magnitude then those identified in the 'low' stress case (Figure 3.15). A maximum induced strain of 6.3% was observed for this level of applied stress. Once again, the magnetic field was allowed to reach and dwell at 1.1 T for 10 seconds, before being quasi-statically reduced to zero. The beginning of the reverse transformation from the field preferred to stress preferred martensite variant began at station 3 (0.61 T) and ended at station 4 (0.12 T). In the 'high' stress case, the applied load was significantly large enough to fully reconfigure the twin structure of the material to its original, stress preferred state upon removal of the magnetic field, unlike the previous, 'low' stress case. Subsequently, for high stress residual strain in the material is completely recovered once the magnetic field has been reduced to zero. Furthermore, the threshold fields associated with stations 1, 2 and 3 (0.42 T, 0.88 T, and 0.61 T respectively) were each higher in magnitude than their corresponding 'low' stress counterparts (0.24 T, 0.68 T, and 0.55 T respectively). Therefore, it was concluded that the threshold fields have a strong dependence on the level of applied axial stress. Essentially, the applied compressive stress opposes the magnetically induced twin boundary motion, effectively delaying the onset of the magnetic shape memory effect as stress is increased. Although not determined in this set of experiments due to limitations in the test apparatus, it can be assumed that eventually, after the axial stress has been increased to a significantly large enough

level, the twin boundary motion will be completely impeded, indicating a block-force condition. Additionally, it was observed that for characteristically 'high' levels of applied stress, 4 critical threshold fields could be identified. This means that both the forward and reverse transformations of the martensite variants could be observed over the course of one magnetic cycle.

As in the case of the 'low' stress level, the quality of the data was a necessary consideration when evaluating the level of certainty associated with the location of the threshold fields. Unlike the data obtained from the 'low' stress case (Figure 3.15) the 'high' stress case (Figure 3.17) shows four, clearly delineated threshold fields over the course of the magnetic cycling. As a result, it was concluded that as stress is increased, the accuracy associated with the identification of threshold field was improved.

Once the behavior of the material was observed for each level of applied stress, the profile of stress vs. magnetic field was developed. This profile is shown in Figure 3.18. Although there seems to be a clear linear relationship between applied stress and the magnetic threshold fields, the profile raises some difficult questions regarding the data obtained using this type of experiment. First, because of the high degree of uncertainty associated with the threshold fields for 'low' levels of stress, the slope of the curve associated with the fields at station 3 is highly suspect. Second, the slope of the curve resulting from the fields associated with station 2 increases sharply after 2 MPa. This indicates that the electromagnetic could not deliver a sufficient level of inductive field to fully convert the NiMnGa element to the field preferred state. The result of this effect was that when the field is removed, the twin structure

of the FSMA bar was in an intermediate and unknown state. As a result, the state of the material at higher levels of stress as the magnetic field is being removed could not be reliably predicted. Because of these issues, the stress vs. magnetic field profile obtained from the constant axial stress testing must be rejected as a tool for material behavior prediction. However, this profile can be obtained by alternate means. Specifically, it was determined that characterizing the material in terms of constant magnetic fields and threshold stresses was a more effective method of generating this profile than through constant axial stress testing. This process is discussed in detail in a proceeding section (section 3.5). Despite the seemingly inherent limits of the results obtained from constant stress testing, they do provide very valuable information regarding the critical issues of residual strain and magnetic circuit limitations.

3.4.3 Residual Strain

As discussed previously, the phenomenon of residual strain occurs when the recovery force is insufficient to fully convert the NiMnGa element from a field preferred to a stress preferred configuration as the magnetic field is reduced to zero. For low levels of recovery force, the FSMA element is composed of both field and stress preferred martensite variants. In Figure 3.19, the residual strain as a function of applied stress is shown. Qualitatively, the data displays a characteristic bell-shaped curve indicating a nonlinear relationship between recovery force and residual strain. For very small levels of applied stress, < 0.3 MPa, the residual strain remains at approximately 6.3%. Given the fact that the maximum attainable strain determined for this specimen was 6.5%, the recovery of 0.2% strain seems to be purely elastic in

nature. Up until 0.3 MPa, the applied stress in insufficient to induce a complete variant reorientation in the specimen. Beyond this stress level, the magnitude of residual strain sharply decreases until when at 0.73 MPa, the residual strain becomes zero. Between 0.3 MPa and 0.73 MPa, the applied stress is only capable of inducing twin boundary motion in a portion of the specimen. In this stress region, the NiMnGa material is in an intermediate state, composed of both stress and field preferred variants after the applied magnetic field has been removed. Beyond 0.73 MPa, the applied load is sufficient to fully induce twin boundary motion within the entire NiMnGa element, reverting the specimen back to its original, stress preferred martensite.

It is necessary to understand the occurrence of residual strain in NiMnGa because it highlights several important material behaviors. First, tracking residual strain essentially characterizes the nature of the phenomenon of twin boundary motion within the specimen as it transitions between field and stress preferred configurations. Clearly, this transition is not a linear phenomenon, and is dependent upon many factors including applied stress, crystal structure, and material composition. Second, the existence of residual strain within a material emphasizes the stress dependence of the magnetic shape memory effect. Since the test apparatus was capable of applying a magnetic field in a single direction only, introduction of a recovery force was the only way to induce twin boundary motion in the specimen after the applied field has been removed. Furthermore, if the recovery force is below the threshold stress for complete twin variant reorientation (< 0.73 MPa), the magnitude of residual strain can be used to determine the maximum achievable,

induced strain after the next magnetic cycle. For example, consider once again the data presented in Figure 3.15. For an applied stress of 0.4 MPa, the residual strain is 5.5% recovering only 1% strain after the magnetic field is removed. If the specimen was magnetically cycled a second time, the FSMA would only be capable of generating 1% of induced strain. Because the recovery force was capable of inducing only a small amount of stress preferred variants when the field was removed, the number of strain generating twins (stress preferred twins) for the next magnetic cycle was significantly decreased. In summary, the phenomenon of residual strain demonstrates the stress dependence of the magnetic shape memory effect and the necessity of recovery force in FSMA based actuator applications.

3.4.4 Effect of Limited Magnetic Field

It has been shown that the magnetic shape memory effect is a both a field and stress dependent phenomenon [212, 213]. Up until now, tests have focused on the stress dependent aspects of the phenomenon. As pertaining to this study, the effectiveness of the external magnetic circuit to deliver a sufficient level of magnetic field has not been considered. Applied magnetic fields have been characterized as either on or off, in other words, either zero, or suitably large enough to induce complete variant reorientation in the specimen regardless of the applied loading. The question of what happens to material behavior in situations where the magnetic field is not large enough to induce complete variant reorientation within the specimen during magnetic loading has not been examined. This is of critical importance because like the phenomenon of residual strain, it affects the magnitude of the maximum achievable induced strain in the material. Constant stress testing provided

insight into this aspect of material behavior by determining, at least qualitatively, the effect of magnetic fields on the maximum strain capability of the actuator material.

As described previously, the magnetic shape memory effect is both a stress and field dependent phenomenon. For a constant level of applied magnetic field, the applied stress opposes the effect of the field, effectively raising the requirement necessary to induce twin boundary motion in the FSMA element. As the magnitude of the axial stress is increased, the magnitude of the applied field must also be increased to compensate and initiate twin boundary motion. This behavior has been verified by the constant axial stress testing. But from the perspective of the material, the level of magnetic anisotropy essentially limits the magnitude of applied field that can be applied in order to overcome the influence of the applied stress. At some point, the energy associated with the applied stress becomes larger than the energy associated with the magnetic anisotropy. In this limiting case, when the magnetic field is supplied, it becomes energetically preferable to reorient the magnetic domains of the unit cell through conventional magnetic domain rotation rather than a mechanism of twin boundary motion (i.e. the MSME). Provided that the magnetic circuit can deliver enough magnetic energy to overcome the applied stress and that the elastic energy associated with that applied stress is less than the energy associated with the magnetic anisotropy, twin boundary motion will occur and the FSMA material will be fully converted into the field preferred martensite variant. In this scenario, the limiting factor for producing the magnetically induced strain is the energy associated with the magnetic anisotropy of the material. However, if the magnetic circuit is unable to deliver at least as much magnetic energy as the inherent

magnetic anisotropic energy of the NiMnGa element, then the limiting factor for induced strain is the magnetic circuit itself. This idea is of critical importance when designing FSMA actuators. Harnessing the full potential of the FSMA material, requires a well designed, and sufficiently powerful magnetic circuit.

To illustrate the effect of the magnetic circuit on material behavior, we consider the case of field generator providing a 7.5 kOe field. This magnetic field represents half of the total magnitude of field that it can generate. The field is applied to a NiMnGa specimen under constant stress. In Figure 3.20(a), the results of this test are shown. The maximum strain as a function of the applied stress for an applied magnetic field cycled between 0 kOe and 7.5 kOe is shown. For stresses below the critical value $\sigma_{cr,H}$ = 2 MPa, the maximum induced strain remains between 6.5% and 6.3% decreasing slightly as a result of pure elastic deformation. As stress is increased beyond the critical value of 2 MPa, the maximum achievable induced strain decreases in a sharply linear fashion. For stresses above $\sigma_{cr,H}$, the maximum external field intensity, $H_{ext,max}$, of 7.5 kOe is not strong enough to overcome the load and completely convert the actuator to field preferred martensite. Based on this trend, the actuator will be blocked at 2.75 MPa for the electromagnet delivering a maximum field intensity of 0.75 kOe. However, this behavior is not an inherent property of the material but occurs due to the lack of availability of magnetic field. If the electromagnet was capable of delivering a magnetic field less than 7.5 kOe, for instance 4.5 kOe, the value of $\sigma_{cr,H}$ would shift to the left as a result of a decreased field availability. Likewise, it the electromagnet was generating a field above 7.5 kOe, 12 kOe for instance, the value of $\sigma_{cr,H}$ will shift to right up until the theoretical

limit as determined by the magnetic anisotropy of the material is reached. Figure 3.20(b) summarizes this principle.

The total induced strain available over an entire magnetic loading cycle can be determined from the plots of residual strain (Figure 3.19) and maximum induced strain (Figure 3.20(a)). Considering both plots, the total strain that the FSMA actuator element undergoes for one magnetic cycle at a constant stress is equal to twice the maximum strain predicted in Figure 3.20(a) minus the residual strain predicted in Figure 3.19.

3.5 Constant Drive Current Tests

Constant Drive Current tests are included to provide an understanding of the material as it would behave in an actuator. From an electronics perspective, it is a relatively simple matter to measure and regulate drive coil current. Therefore, it is reasonable to assert that most practical actuator applications for this material will rely on regulated drive current. These tests show how the NiMnGa behaves in a coupled actuator material-field generator environment. Specifically, the following set of tests focuses exclusively on the effect of external magnetic fields, by exposing the NiMnGa specimens to a series of constant external field intensities, to observe the stress-strain behavior of the material.

3.5.1 Experimental Method: Constant Drive Current Tests

Constant drive current tests (CDCT) were carried out on both the custom, CDCT test rig (shown in Figure 3.7(a)) and on the DynaMight axial test machine (shown in Figure 3.9). First, the electromagnet was calibrated by determining the

relationship between the field intensity generated by the coils as a function of drive current for the case where the NiMnGa element is removed from the magnetic circuit. This calibration curve is shown in Figure 3.21. It is important to clarify that all field intensities were measured across the air gap, between the two poles, with the specimen removed from the magnetic circuit. The field intensity within the air gap was calibrated with respect to the magnitude of current inside the coils. This was done so that the response of the material could be directly related to the capabilities of the coil as a separate entity, thus providing a set magnetic circuit performance requirements for coil design. As explained earlier, (section 3.3.3), the field intensity *inside* the specimen could not be determined with the present instrumentation. Once the specimens were situated in the grips between the magnetic poles, the magnetic field was cycled to 12 kOe, while the specimen was maintained at zero stress, to induce twin boundary motion and convert the element to the field preferred configuration. After magnetic cycling, the level of current in the coils was raised until the desired DC field intensity was reached. While the coil drive current was held at a constant level, the NiMnGa bar was subjected to a quasi-static, compressive loading along the long axis of the specimen to induce twin boundary motion and reorder the martensite twin variants into the stress preferred configuration. To maintain a quasi-static loading condition, the specimen was strained at a rate of 0.04 mm per second. Once the compressive stress reached a level where post twin boundary motion material behavior could be observed (about 9-10 MPa) it was removed at the same, quasi-static rate. Still in the presence of the magnetic field, the twin structure of the FSMA element was allowed to reach equilibrium so that

recovery behavior could also be determined. Stress and strain responses during the complete cycle were recorded and critical transformation stresses were measured for each level of applied field. These stresses were then compiled into a critical stress vs. applied magnetic field profile. Each data point on the stress vs. applied field profile represents the average of at least three separate tests, so that the repeatability of the measurements could be assessed. The effectiveness of the profile as a tool to predict material behavior was then evaluated.

3.5.2 Obtaining Critical Stresses

One of the key goals for constant drive current testing was to determine threshold stresses as a function of applied magnetic field. These threshold stresses, or critical transformation stresses, denote the onset of twin boundary motion in NiMnGa. For this set of tests, the FSMA elements were exposed to constant applied fields ranging from 0 kOe to 12 kOe. At each level of applied field, the critical transformation stresses were identified. All three strain recovery mechanisms, including the magnetic shape memory effect, magnetic pseudoelasticity, and partial magnetic pseudoelasticity were observed. Figures 3.22(a) and 3.22(b), show the stress strain behavior for the magnetic shape memory effect and magnetic pseudoelasticity respectively, while Figures 3.23(a), and 3.23(b) show the stress-strain behavior for two cases of partial magnetic pseudoelasticity.

The first case, represented in 3.22(a) illustrates the magnetic shape memory effect for a zero field condition. Initially, the compressive stress is linearly related to the strain indicating elastic deformation. When the axial stress reached a critical value of $\sigma_1 = 0.3$ MPa in magnitude the twin boundaries in the martensite became mobile

and the stiffness of the material sharply decreased. While the twin boundaries were mobile, subsequent small increases in stress were accompanied by large increases in strain. The strains induced in this region were effectively plastic in nature, remaining in the material after the compressive stress was removed. When the level of stress exceeded a second critical value, σ_2 = 0.8 MPa, the twin boundaries in the material were completely reordered into the stress preferred configuration and a sharp increase in material stiffness occurred. Further application of stress in this configuration yielded only purely elastic strain. This trend will continue until either the material crumbles or column buckling of the specimen occurs. Well below both of these failure events, the maximum stress applied to the material for any case observed in this test was 6 MPa. The stress was then removed, which produced a small amount of elastic recovery, approximately 0.2% in this case. For this specimen a residual strain of 5.8% remained in the specimen. This apparently plastic strain could be recovered however, by the introduction of a magnetic field greater than 3.5 kOe at zero stress. To be sure that all the martensite twin variants were reverted to the field preferred configuration, a magnetic field of 12 kOe was then applied to the specimen at zero stress before commencing any test case, resulting in a complete recovery of the stress induced strain. The magnetic shape memory effect is characterized as having two critical stresses, σ_1 and σ_2 which denote the beginning and end of the transformation from field preferred to stress preferred martensite. Over the entire range of magnetic field intensities tested, the magnetic shape memory effect strain recovery mechanism was observed only for applied fields between 0 kOe and 1.5 kOe.

Figure 3.22(b) shows the second strain recovery behavior of the NiMnGa material, magnetic pseudoelasticity. In this case, the external applied field intensity was 5 kOe. Just as in the case for a zero applied field, stress is initially linearly related to strain, an indicator of elastic deformation. When the magnitude of stress reached 2 MPa, the stiffness sharply decreased as the twin boundaries within the material became mobile. Once the compressive stress reached 3.9 MPa, the twin variants were completely reordered into the stress preferred configuration. At this point, the stiffness increased sharply and the material resumed its elastic deformation. Essentially, the loading behavior of the material followed the same pattern as that in the zero field behavior except that the first two critical transformation stresses were larger in magnitude. So, for a 5 kOe external field, the critical stresses σ_1 and σ_2 were 2 MPa and 3.9 MPa respectively. After a maximum stress level of approximately 6 MPa was achieved, the stress was removed. Initially, the FSMA material recovered strain elastically. However, because the material was exposed to a 5kOe magnetic field, the material began a hysteretic recovery of strain when the stress level decreased below 2.2 MPa. At that point, the magnetic field induced a reverse transformation from stress preferred to the field preferred martensite variant. Therefore a third critical stress, σ_3 = 2.2 MPa was identified. As stress was further decreased below σ_3, twin boundary motion within the specimen occurred until a fourth critical transformation stress, σ_4 = 0.72 MPa was reached. At that point, the twin variants were completely reordered into the field preferred configuration and the material resumed conventional, elastic deformation. The remaining 0.4% strain was recovered elastically as the compressive stress level was reduced to zero. All of the

strain introduced into the NiMnGa upon loading was completely recovered in a hysteresis loop upon unloading. Since this is the main characteristic of pseudoelastic behavior, it can be concluded that the FSMA element was demonstrating magnetic pseudoelasticity at a 5 kOe applied field. The width of the hysteresis loop throughout the loading cycle was approximately 1 MPa. The phenomenon of magnetic pseudoelasticity is characterized by four critical transformation stresses. The transition from field preferred to stress preferred martensite occurs between σ_1 and σ_2, during compressive loading. The reverse transition from stress preferred to field preferred martensite occurs between σ_3 and σ_4 during unloading. The magnetic pseudoelastic behavior in NiMnGa was observed for applied fields between 3.5kOe and 12 kOe.

The third type of strain recovery involves a combination of both the previous behaviors at an intermediate applied field. The phenomenon of partial pseudoelasticity is shown in Figures 3.23(a) and 3.23(b) for the cases of 2 kOe and 3 kOe fields. As in the two previous cases, when the material was compressively loaded, it showed elastic deformation for stresses below σ_1 and above σ_2. Twin boundary motion, and a substantial decrease in material stiffness, occurred at stress levels between σ_1 and σ_2. Likewise, when the compressive stress was decreased, the material behaved pseudoelastically, exhibiting elastic deformation for stresses above σ_3 and twin boundary motion deformation for stresses below σ_3. However, the magnetic field was not sufficiently large enough to fully reconfigure the martensite twin variants into the field preferred state. Therefore, the mechanism of twin boundary motion recovered only a portion of the stress induced strain. Thus, when

the stress level reached zero, a residual strain remained present in the NiMnGa specimen. However, this residual strain could be removed by applying a larger magnetic field to the specimen at zero stress. For the case of the 2 kOe applied field, during loading, σ_1 = 0.53 MPa and σ_2 = 2.1 MPa. During unloading, pseudoelastic recovery began as stress was decreased below σ_3 = 0.87 MPa. However, when the stress level reached zero, a residual strain of approximately 3% remained within the material. As mentioned previously (section 3.4.3), the residual strain was recovered by supplying a larger field (> 4.0 kOe) at zero stress. For a 3 kOe applied field, σ_1, σ_2, and σ_3 were 1.1 MPa, 2.7 MPa, and 1.4 MPa respectively. The difference in this case was that the residual strain had been reduced to approximately 0.5%, clearly indicating a dependence of residual strain on applied field. As in the case with the 2 kOe applied field, the residual strain was completely recovered by introducing a larger magnetic field (> 4.0 kOe). This behavior of partial pseudoelasticity was observed for applied fields between 1.5 kOe and 3.5 kOe.

3.5.3 Effect of Applied Field

In order to study the effect of the applied field on the behavior of NiMnGa, the tests were conducted over a range of magnetic field intensities (0 kOe to 12 k0e). The main effects of an increasing applied field on the stress strain behavior of NiMnGa elements are shown in Figure 3.24. Stress-strain curves for compressive loading of specimens exposed to 3.5 kOe, 6.0 kOe, and 10 kOe are shown. Based on the trend shown in Figure 3.24, the main effect of increasing the field intensity was to raise the level of the critical transformation stresses that determine the start and finish of twin boundary motion. Therefore, the critical transformation stresses showed a

pronounced dependence on the applied magnetic field intensity. However, after 7 kOe, the material began to experience magnetic saturation and at 9.5 kOe, critical transformation stresses became insensitive to increasing magnitudes of magnetic field intensity. In contrast, the slopes of each stress-strain curves of the purely elastic regions (stresses below σ_1, and above σ_2) did not appear to be affected by the change in applied field magnitude. This led to the conclusion that the elastic modulus of the field preferred (region below σ_1) and stress preferred (region above σ_2) martensite variants were unaffected by the level of applied field intensity. The modulus of the field preferred region and the stress preferred region are denoted on Figure 3.24 as E_H and E_σ respectively. The moduli of both variants appeared to be roughly equivalent to 1 GPa. However, it was determined that the slope of the post-σ_2 stress-strain behavior was slightly larger than the slope of the pre-σ_1 stress-strain behavior. This indicated that the modulus of the stress preferred variant was slightly higher than that of the field preferred variant. It was speculated that the reason for this difference in modulus may have been the result of a slight strain hardening phenomenon that occurred during the formation of stress preferred martensite variants.

In the regions of partial pseudoelastic and magnetic shape memory behavior (0.0 kOe < H <3.5 kOe), the effect of the applied field on the residual strain was observed. In Figure 3.25, the residual strain as a function of applied field intensity is shown. As mentioned previously, the residual strain is defined as the induced strain remaining in the specimen when the compressive stress has been reduced to zero, while the FSMA bar is exposed to constant, applied field intensity. Similar to the results presented in the constant axial stress testing, the residual strain is related to the

applied field intensity in a nonlinear fashion. In this instance, the presence of a residual strain indicates an incomplete conversion from the stress preferred to field preferred configuration. In other words, when the stress is brought to zero, the volume fraction of field preferred twins is less than 1.0. For applied fields below 1.0 kOe the level of residual strain remained constant at approximately 5.8%. Then, the residual strain appeared to decrease with increasing applied field intensity, in an apparent bell-curve-like manner, tapering to zero at 3.5 kOe. This characteristic bell-curve shape of the data can be used to provide a straightforward estimation of the proportions of field and stress preferred martensite variants within the material for applied fields within the partial pseudoelastic boundary.

Finally, the level of hysteretic stress in the pseudoelastic region (3.5 kOe < H <12 kOe), was also measured. Hysteretic stress is dissipative in nature and arises from the internal friction associated with twin boundary motion [170]. The hysteretic stress for a particular applied field was determined from the difference in magnitude between the stress levels in the specimen occurring in the region of twin boundary motion during loading and unloading. An example of hysteretic stress for the case of a constant, 7 kOe applied field is shown in Figure 3.26. The hysteretic stress was measured for each applied field. In Figure 3.27 the hysteretic stress as a function of applied field is shown. Based on this set of data, the hysteretic stress appears to remain constant at a level of approximately 1 MPa for all levels of applied field. Therefore, it was concluded that the hysteretic stress is a constant and independent of the applied field. Furthermore, since the area bounded by the hysteresis loop on the stress-strain curve is indicative of the energy dissipated during a mechanical cycle,

the hysteretic stress can be used as a means to estimate the damping behavior of the material.

3.5.4 Experimental Critical Stress vs. Applied Field Profile

Once the constant drive current tests were conducted over the entire range of applied field intensities (0 kOe < H < 12 kOe), and the critical transformation stresses identified in each case, a critical stress vs. applied field profile was developed. This profile, shown in Figure 3.28, is a useful tool for determining material behavior for various sets of mechanical and magnetic loading conditions. The profile clearly allows the relationship critical stress as a function of applied magnetic field to be determined. Looking at Figure 3.28, the curves associated with the critical stresses that define the twin boundary motion for the FSMA specimen during compressive loading are denoted as σ_1 and σ_2. As mentioned previously, these critical stresses mark the beginning and end respectively, of the transition from stress field to stress preferred martensite. For the transition from stress preferred to field preferred martensite during unloading, the curves associated with these critical stresses are similarly defined and denoted as σ_3 and σ_4. Generally, each curve of the critical stress profile followed the same fundamental pattern. For applied fields below 7 kOe, the critical stress appeared to be linearly related to the applied field intensity. For fields greater than 7 kOe, the critical stresses began to level off, indicating the onset of magnetic saturation. The curves associated with the initiation of twin boundary motion, σ_1 and σ_3 appeared to be collinear, and roughly equivalent. In this instance, σ_1 represents the beginning of stress-induced twin boundary motion during compressive loading and σ_3 represents the beginning of field-induced twin boundary

motion during unloading. Also, for applied magnetic fields below 1.5 kOe, the first critical stress, σ_1 did not tend to zero but remained effectively constant at approximately 0.34 MPa. Likewise, σ_2 was always non-zero and was a strong function of the applied magnetic field. This observation suggests that even for a zero field input, there are still at least two threshold stresses associated with the twin boundary motion of the material during compressive loading.

As previously mentioned, the critical stress vs. applied field profile can be used to predict NiMnGa behavior for various loading conditions. As long as the mechanical and magnetic history of the specimen is known, consultation of the profile enables the prediction of both the strain recovery mechanism and material state at any point. For example, the region above σ_2 curve always indicates a specimen completely in the stress preferred martensite variant, while the region below σ_4 always indicates a specimen completely in the field preferred martensite configuration. Likewise, if a constant magnetic field test is conducted at 8 kOe, the strain recovery will be pseudoelastic while an iso-magnetic test conducted at 1 kOe falls within the boundaries of the magnetic shape memory effect. In other words, regions where both the full, and partial pseudoelastic effects and where the standard magnetic shape memory effects occur can be predicted using this critical stress vs. applied field profile. Finally, even though the strain recovery mechanism is pseudoelastic in nature, iso-magnetic tests conducted for applied fields between 8.5 kOe and 12 kOe will yield similar results due to magnetic saturation. Figure 3.29 illustrates these concepts.

Even though this profile was constructed using data from constant applied field testing, constant axial stress behavior can also be predicted from the profile. One of the main difficulties with constant stress testing was the identification of critical transformation fields. However, threshold fields can be determined from the critical stress vs. applied field profile by considering lines of constant stress and noting the intersections with the σ_1, σ_2, σ_3, and σ_4 curves.

3.6 Constant Induction Tests

While constant drive current testing provided a clear insight into the coupled field generator-actuator material behavior as a function of the external field H, it did not offer much insight into the behavior of the actuator material itself. As explained previously (section 3.3.3), this was due in large part to the difficulty in measuring the field intensity *inside* the specimen. Due to difficulties associated with both the actuator geometry and the material requirement of an orthogonal actuation field, the magnetization and field intensity inside the NiMnGa could not be measured. The compromise in that case was to characterize the behavior of the material with respect to a magnetic circuit that did not contain the FSMA element. The goal was to determine the coupled actuator material-field generator behavior while simultaneously providing a set of magnetic circuit design requirements. However, by maintaining a constant level of flux density in the magnetic circuit with the specimen and evaluating the stress-strain response, a degree of the actuator material behavior can be decoupled from the field generator. The limitation of course, is that in order to maintain a constant flux density, either the field intensity inside the specimen, the magnetization vector, or some combination of both must vary. As stated above, it

was not possible to record these quantities. The following set of tests focuses on the characterization of the material as a function of the level of inductive field within the magnetic circuit containing an FSMA element. Furthermore, the effect of the direction of the magnetic field was also considered. For the purpose of clarity, unless otherwise noted, the terms "applied magnetic field" and "magnetic field" refer to inductive, B fields in this section.

3.6.1 Experimental Method: Constant Induction Tests

A series of constant inductive field tests were carried out using the DynaMight, tabletop axial testing machine (Figure 3.9). Each test involved the compressive loading of a NiMnGa bar in which the inductive, B-field was maintained constant as the specimen was compressively loaded along the long axis of the specimen. As in the case of the constant drive current tests, the specimen was strained at a rate of 0.04 mm per second to maintain the quasi-static condition. After the specimen was situated in the grips between the magnetic poles, the sample was magnetically cycled in a 1.2 Tesla field at zero stress to ensure that the specimen began the test fully in the field preferred condition. Next, the magnetic circuit was energized to provide a user-defined inductive field environment for the FSMA element. The flux density was measured by a Hall Effect sensor situated between the specimen and the electromagnet poles. The signal from the Hall Effect sensor was connected to a programmable PID controller tuned to the system using the Ziegler-Nichols method. The PID controller was able to maintain a constant flux density by regulating the drive current in the coils. Then, while the flux density was held constant, the axial compressive load was increased until the martensite twin variants

of the material were completely reordered into the stress preferred configuration. While the NiMnGa was still in the presence of the constant magnetic field, the stress was removed and the twin structure of the actuator was allowed to reach equilibrium. Stress and strain responses during the complete cycle were recorded while the flux density was monitored to validate the assumption of a constant magnetic field environment. Next, the stress-strain behavior of the material was analyzed and transformation stresses were identified. This test was repeated for fields ranging from -1.0 Tesla to 1.0 Tesla. Once the entire range of fields was tested, the transformation stresses were then compiled into a critical stress vs. applied inductive field profile. The effectiveness of the profile and the dependence of field direction on material properties were then evaluated.

3.6.2 Effect of Flux Density and Directional Dependence

Figure 3.30 shows the effect of flux density on the stress-strain response of the material for an increasing, inductive field. The stress-strain curves for constant inductive fields of 0.2 T, 0.4 T, and 0.8 T are shown. Critical transformation stresses ($\sigma_{B,1}$, $\sigma_{B,2}$, $\sigma_{B,3}$, $\sigma_{B,4}$) for the 0.8 T case are denoted with circular markers. As in the case of constant drive current testing, critical transformation stresses appeared to be directly related to the level of flux passing through the FSMA element. Furthermore, the material stiffness for both the stress and field preferred configurations appeared to be independent of the level of flux density in the circuit, similar to the behavior observed in the constant drive current testing (section 3.5). As the level of flux density was increased, the transformation stresses also increased until the onset of magnetic saturation which occurred at approximately 0.8 T. Beyond 0.8 T the

transformation stresses could no longer be increased by additional inductive field. One feature of note resulting from this set of tests was the existence of 'kinks' in the stress-strain curves for low to intermediate flux densities (0.0 T < B < 0.7 T). Because the internal field intensity and magnetization vectors of the material are not known, it is difficult to explain this behavior. This shortcoming suggests that constant inductive testing is not as useful for actuator characterization because of the difficulty in measuring several key parameters, namely $H_{internal}$ and M. Because these quantities were left unknown, further analysis of material specific behavior was not possible.

By plotting the transformation stresses against their respective flux densities, a profile of the transformation stresses vs. the inductive field was developed using the data from these tests. This profile, shown in Figure 3.31, can be used to evaluate the effect of flux density on material behavior. For any value of applied magnetic field, the first two critical stresses, $\sigma_{B,1}$ and $\sigma_{B,2}$ were always present and represented the beginning and end of the compressive stress-induced twin boundary motion during the loading cycle. As before, once the stress level was increased beyond $\sigma_{B,2}$ the twin structure of the martensite had been completely reordered into the stress preferred variant. For the reverse transition occurring during unloading, the critical stresses $\sigma_{B,3}$ and $\sigma_{B,4}$ were not present for all values of the applied magnetic field. The first critical stress, $\sigma_{B,1}$, saturates at a magnitude of 2.2 MPa for flux densities greater than 0.9 Tesla. A saturation of the second critical transformation stress, $\sigma_{B,2}$, was not observed due to the limitations in the available power delivered to the magnetic circuit. However, based on the trends exhibited in both this set of tests and the

constant drive current tests, it can be assumed with a fair degree of certainty that eventually, magnetic saturation will begin to affect the magnitude of $\sigma_{B,2}$. The third and fourth transformation stresses, $\sigma_{B,3}$ and $\sigma_{B,4}$ respectively, were not present for all values of applied field. The stress $\sigma_{B,3}$ was present only for applied fields greater than 0.1 T while the fourth transformation stress $\sigma_{B,4}$, was only present for applied fields greater than 0.7 T.

One property that can be evaluated from constant induction testing is the dependence of field direction on material behavior. The constant induction tests were carried out over a range of fields from -1.0 to 1.0 Tesla. For each level of magnetic field, the critical stresses were plotted to extend the profile shown in Figure 3.31 to cover all of the experimentally observed values of field. This complete profile is shown in Figure 3.32. Qualitatively, the critical stress behavior for negative applied fields appeared to be identical to that for the positive oriented fields. Based on these data, it can be argued by reasons of symmetry about the origin that the critical transformation stresses were unaffected by the direction of the applied field. This argument holds true only for fields applied across the long axis of the specimen.

3.7 Constant Strain Tests

Up until this point, tests have been directed at determining the induced strain for either a constant axial stress or magnetic field input. However, a complete characterization of the material behavior requires that in addition to examining the potential induced strain available in an FSMA element, the force generation capabilities must also be examined. In this section, the ability of the NiMnGa specimens to be used as a force generation device is considered. One method of

determining the force generation potential of the active material is to measure the induced force generated for a particular magnetic field input while the material is constrained to a specific geometry. Since these tests deal with axial loading, the specific constrained geometry is translated as a prescribed, constant pre-strain. In other words, these tests involve measuring the force response for the magnetic cycling of an FSMA element at a constant strain. A series of these tests was conducted on specimens of NiMnGa to determine the effect of pre-strain.

3.7.1 Constant Strain Test Method

Constant strain experiments were conducted on the Instron DynaMight, tabletop, uniaxial test system. First, a bar specimen of NiMnGa was gripped between the two poles of the electromagnet and the electromagnet was energized to expose the specimen to a 1.2 Tesla, DC inductive field at zero applied load. The field was large enough to induce the magnetic shape memory effect causing the specimen to completely revert to the field preferred configuration. Next, with the field set to zero, the specimen was then compressed to a prescribed pre-strain. Pre-strains ranging from 0.5% to 5% were examined over the course of the experiment. The test rig was then set to maintain a constant global position by activating the rig's onboard PID controller. At this point, the FSMA material was completely constrained in the axial direction. While the pre-strain was kept constant, the applied, inductive field was then incrementally increased from zero to 1.2 Tesla. For each increment of magnetic field, the material was allowed a few seconds to stabilize before data were recorded in order to remove any transient effects. After the material was allowed to reach equilibrium, axial force, magnetic field, and position were recorded for that magnetic

increment. This process was repeated over the entire range of magnetic field (0.0 to 1.2 Tesla). To ensure that a constant global strain in the FSMA element was maintained, strain was plotted against the inductive field for the cases of 1%, 2%, 3%, 4%, and 5% pre-strain. These data, depicted in Figure 3.33, shows the global strain in the NiMnGa over the entire range of applied fields, indicating that the constant strain condition was maintained. After removing the magnetic field, the specimen was set to the next level of pre-strain and the test was repeated.

3.7.2 Effect of Pre-Strain on NiMnGa Behavior

The results of the constant pre-strain tests are shown in Figure 3.34. Five levels of pre-strain, ranging from 1% to 5% in increments of 1% are shown. Judging by the trends shown in Figure 3.34, the main effect of increasing pre-strain is to increase the force generation potential of the FSMA. Furthermore, the activation field required by the material to generate force and the saturation field also appear to be affected by pre-strain.

For each level of pre-strain, the behavior of the material follows the same fundamental pattern. Initially, for low levels of magnetic field, the force generated by the specimen was independent of the applied field, and remained constant. For the case of 1% pre-strain, the stress level in the material was initially zero. In contrast, for the case of 5% pre-strain, the stress level in the material was initially 0.9 MPa. The initial stress in the NiMnGa arises from elastic deformation introduced in the specimen as a result of the applied pre-strain. When the pre-strain is applied to the specimen, twin boundary motion is initiated along its length. However, before twin boundary motion occurs, the material undergoes a small elastic deformation until the

first critical transformation stress, σ_1, is reached. This result was demonstrated in the constant drive current, stress-strain curves shown in Figure 3.22. In essence, the elastic stress acts as a DC bias. However, the DC bias stress is not necessarily related to the first critical transformation stress due to the significant level of hysteretic stress inherent to the material behavior. Since the pre-strain was the parameter held constant, the stress acting on the material during the initial pre-straining procedure was partially dissipated through as a result of hysteresis during unloading. Therefore, because of the material hysteresis, a degree of stress relief occurred and the bias stress was completely dissipated for the 1% pre-strain test. In this case, the initial stress level reached an equilibrium level of 0 MPa. However, as pre-strain was increased, nonzero values of bias stress were observed. This indicated that the inherent material hysteresis had a less pronounced effect on the level of bias stress when the magnitude of pre-strain was increased. Next, the applied field was increased incrementally to 1.2 T. For each pre-strain, when a certain field level was reached, the material "activates" and the force generated by the NiMnGa specimen appeared to vary directly proportionally to the magnitude of the applied magnetic field. This activation field is noted as B_{act}. This relationship continued until the onset of magnetic saturation where the generated force began to level off. According to the data presented in Figure 3.34, magnetic saturation occurred at different fields depending on the level of pre-strain. Due to limitations in the available electrical power for the electromagnet, an extensive study of magnetic saturation in the material was not possible. However, when magnetically saturated, it can be expected that the material can no longer produce additional force by increasing the magnitude of the inductive

field. The level of applied field where magnetic saturation begins is referred to as B_{sat}.

As mentioned above, when the level of pre-strain is increased, the magnitude of force generation was also increased. The reason for this behavior is related to the volume fraction of stress preferred twins in the FSMA. When pre-strain was introduced in the sample, the volume fraction of stress-preferred twins was also increased. From the perspective of the material composition, a mechanical bias toward the stress preferred twins was introduced. Force is generated from these stress preferred twins as they attempt to reorient themselves into the field preferred configuration due to the influence of the external magnetic field. Because the level of strain was being held constant in this experiment, these twins were prevented from reorienting themselves into the field preferred configuration and as a result, they exerted a pressure on adjacent twin variants, essentially becoming local, internal force generators. The aggregate effect of these internal force generators was to allow the bulk material to produce a global force. Field preferred twin variants do not become local force generators because they are already in the preferential orientation, they do not exert pressure on surrounding variants as a result of a magnetic field. As the pre-strain is increased, more twin variants are biased toward the stress preferred configuration, therefore increasing the number of twin variants available to be recruited for force generation. Consequently, the force generation capability of the material was also improved by the introduction of pre-strain. Consider the case of 1% pre-strain. For fields less than 0.4 Tesla, the stress was zero, but once the applied field became greater than B_{act}, (B_{act} = 0.4 T) the NiMnGa was 'activated' and the

stress increased to a maximum of 2.8 MPa at 1.2 Tesla. In the case of 5% pre-strain, the stress was initially 0.9 MPa. As the field was increased, the NiMnGa activates once B_{act} = 0.1 T was exceeded. The maximum stress reached in this case was 3.8 MPa at 1.2 Tesla. Because the volume fraction of stress preferred twins was much larger for 5% pre-strain than for 1% pre-strain, it contained more twins available for generating force. For fields between B_{act} and B_{sat} the magnitude of stress generated by the specimen was linearly related to the level of applied field. Regardless of the pre-strain, and despite the apparent changes in B_{act} and B_{sat}, the slope of this relationship remained nearly constant.

As mentioned above, another effect of pre-strain in NiMnGa was to lower both the apparent activation and saturation fields of the material. As stated earlier, the activation field for 1% pre-strain was approximately 0.4 Tesla. The apparent activation field decreased to roughly 0.28 Tesla at 3% pre-strain, to 0.1 Tesla at 5% pre-strain. The saturation field, B_{sat}, was also affected. For the 1% pre-strain case, magnetic saturation began to occur at approximately 1.0 T while in the case of 5% pre-strain, magnetic saturation occurred at approximately 0.84 T. The magnetic field band, $\triangle B$, ($\triangle B = B_{sat}-B_{act}$) over which the linear relationship between stress and applied field remained at a constant level, approximately 0.6-0.7 Tesla. It is difficult to determine exactly the reason behind these behaviors due to lack of knowledge of the field intensity and magnetization inside the NiMnGa element. However, two clear trends were evident from the data. First, both the activation fields and saturation fields decreased with increasing pre-strain. Second $\triangle B$ remains constant as the pre-strain was increased. Figure 3.35 summarizes these trends.

3.8 Sensor Characteristics

Many active materials, such as piezoelectrics for example, utilize the converse effect in order to produce actuation [214, 215,]. In general, the converse effect is defined as follows. For a given input (i.e. electrical, thermal, magnetic) the active material produces a strain field. On the other hand, sensor applications use the direct effect. The direct effect states that for a given stress field, the material generates an associated electric, thermal or magnetic field. By utilizing the direct effect, active materials such as piezoelectrics and magnetostrictives have been implemented in a host of sensor applications including load cells, accelerometers and acoustics [216, 217, 218].

A number of similar sensor applications have been proposed for NiMnGa. Specifically, NiMnGa velocity and position sensors have been proposed and developed [219]. Currently, a MSM position sensor has been patented for use in a joystick application [220]. This device utilizes the soft bending stiffness and prodigious use of field sensors to determine the change in permeability at different sides of a bent NiMnGa element. Another potential sensor application proposed for NiMnGa is that of a position sensor. Position can be measured by examining the axial strain as a function of the inductance of the material. However, the possibility of implementing NiMnGa in a load cell has not been fully explored. According to the direct effect, a NiMnGa based load cell would have to be held in a constant H environment. If the specimen was then exposed to a non-zero stress field, the resulting change in the flux density may be directly correlated to the level of force

applied to the specimen. This section explores the potential of NiMnGa for use in sensing applications by evaluating this sensor characteristic.

3.8.1 Obtaining the Senor Characteristics of NiMnGa

The sensor characteristics of NiMnGa were obtained in a manner similar to those used for other magnetostrictive materials like Terfenol and Galfenol [209, 221, 222]. While the material was exposed to a constant magnitude of field intensity (constant H), a bar of NiMnGa is subjected to an axial, compressive stress while the flux density, B, was measured by a Hall Effect senor. Constant H was maintained by regulating the drive coil current. This was accomplished by utilizing a 1 ohm precision, 'sense' resistor connected in series between the coils and ground. A PID controller was implemented to regulate the drive current in the coils. The PID controller accomplished this task by maintaining a constant voltage across the 'sense' resistor which therefore regulated the level of current within the electromagnetic coils. A series of constant field intensities were tested ranging from 0.5 kOe to 12 kOe.

3.8.2 Evaluation of NiMnGa as a Practical Sensor

The sensor characteristics of the NiMnGa are shown in Figure 3.36. If the constant applied field intensity is known and the flux density is measured by a Hall Effect sensor or using some other device, then the magnitude of stress applied to the NiMnGa can be determined by cross referencing the data with the correct curve in Figure 3.36. Consider the case where the flux density is monitored for a NiMnGa element exposed to a known field intensity of 3.5 kOe. Using this information, the

appropriate curve is located on Figure 3.36. This curve is denoted as '1'. As the compressive stress is increased, the flux density, initially at 0.7 T, is monitored. The stress remains constant until approximately 1.5 MPa. At this point, the flux density begins to decrease and at approximately 2.3 MPa, the flux density once again becomes constant at 0.54 T. So to measure stress between 1.5 and 2.3 MPa, the magnitude of flux density is matched with its corresponding level of stress. For example, if the flux density in this case was measured to be 0.6 T, the corresponding stress in the actuator would be approximately 2 MPa. However, due to the large level of hysteresis in B vs. σ curve (approximately 1 MPa), the same level of stress does not correspond with the same level of flux density when the load is removed. Although there does exist a correlation between the level of axial force applied to the NiMnGa bar and the flux density of the material, the large amount of hysteresis indicates that this material is a poor force sensor. To be used as an effective force sensor, the device should have low hysteresis curves. In this event, the flux density would correspond to a specific stress regardless of the loading history. But as a result of the substantial hysteresis, a high degree of uncertainty is introduced in the force measurements, thereby rendering it impossible to determine the level of force acting on a specimen with an unknown loading history.

Other drawbacks to the use of NiMnGa force sensors are associated with both the physical size and the magnitude of power required to maintain the large applied field intensity across the material. For practical sensor applications, it is best to minimize both the required power and the physical size of the device. To apply large magnetic field intensities to the specimen, a relatively bulky set of coils, requiring

significant support electronics (amplifiers, etc.) is required. Thus it would be difficult to design a practical NiMnGa force sensor even if hysteresis were not a concern.

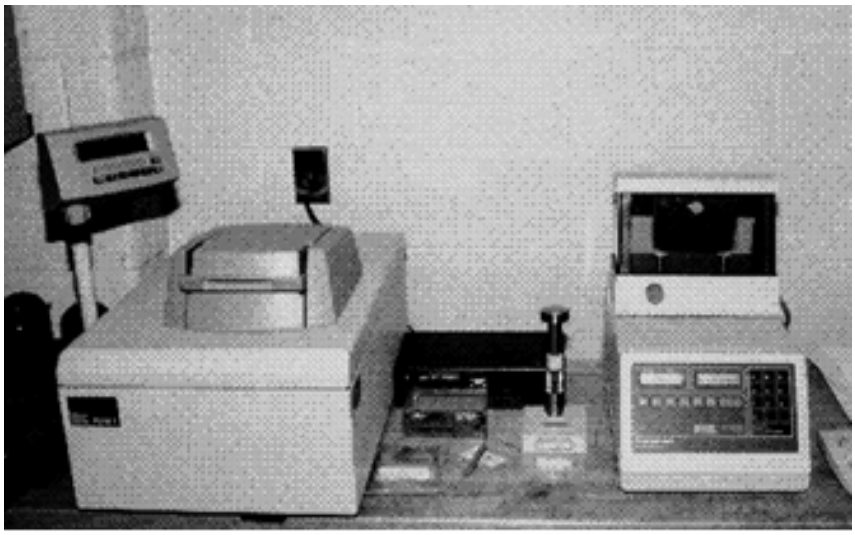

Figure 3.1 Differential Scanning Calorimeter (DSC)

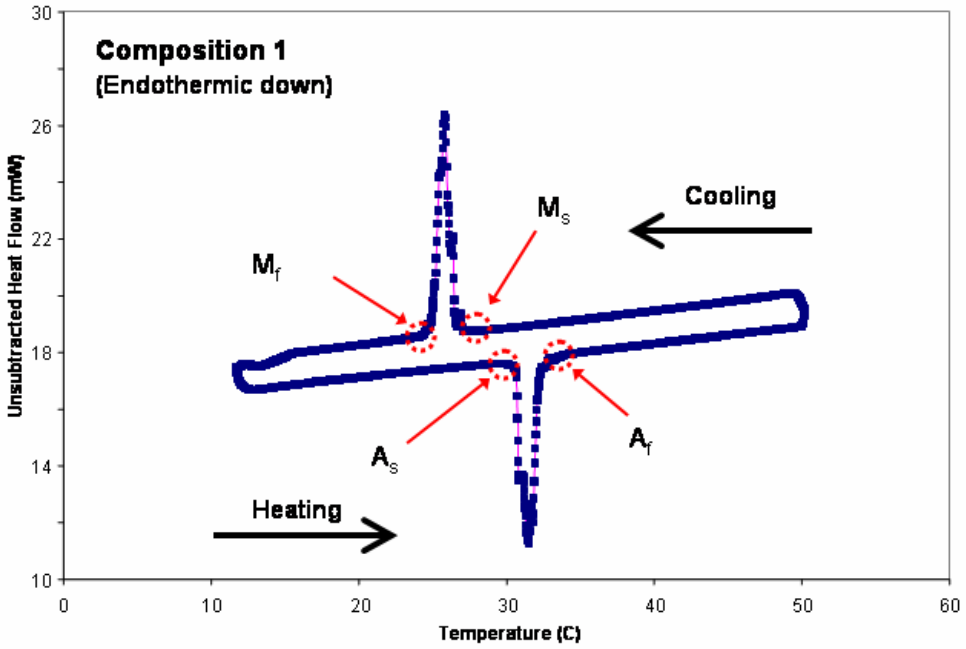

a) Identification of transformation temperatures for composition #1

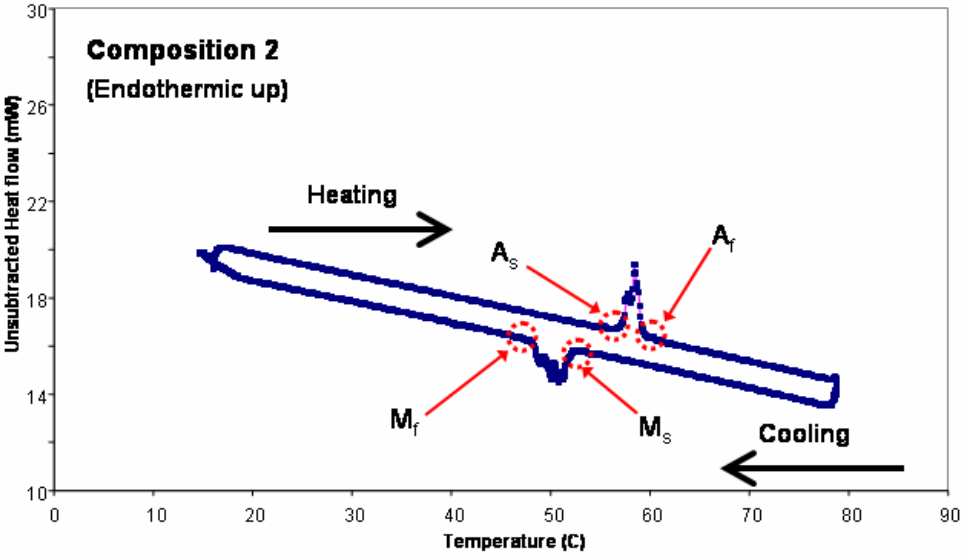

b) Identification of transformation temperatures for composition #2

Figure 3.2 NiMnGa DSC testing results

	COMPOSITION #1	COMPOSITION #2
	°C	°C
M_f	24	47
M_s	28	52
A_s	30	56
A_f	34	61

Table 3.1 Transformation temperatures of NiMnGa bars in degrees Celsius

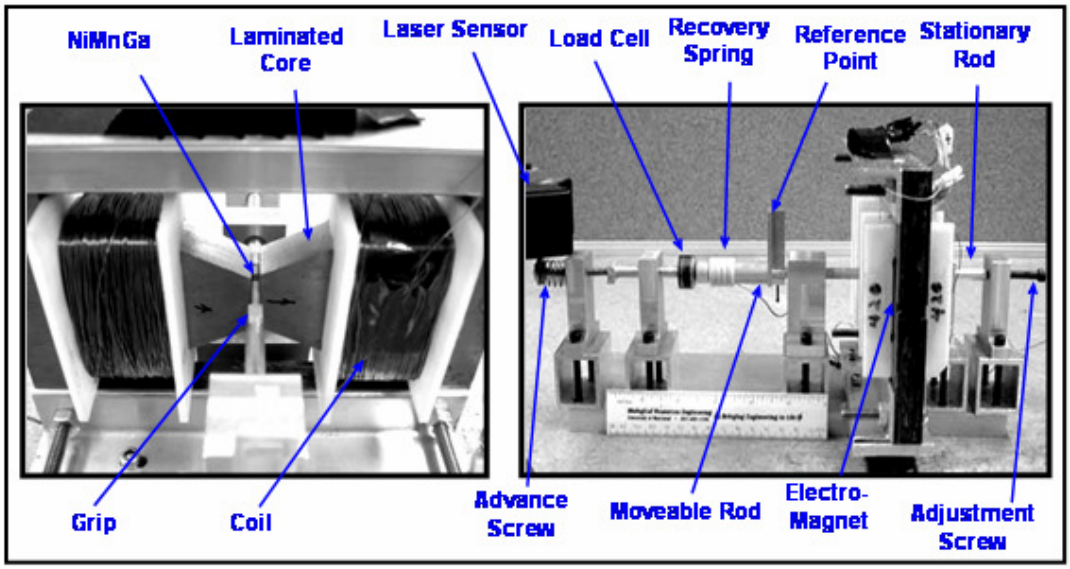

Figure 3.3 Photograph of the variable stiffness testing rig

SPRING	*K*	FORCE	DEFLECTION
	N/mm	*N*	*mm*
1	702.77	9.28	0.01
2	61.04	7.87	0.13
3	30.66	8.01	0.26
4	19.60	6.51	0.33
5	16.26	5.68	0.35
6	13.18	5.72	0.43
7	10.21	5.27	0.52
8	6.62	3.55	0.54
9	6.26	4.06	0.65
10	6.77	4.41	0.65
11	3.50	2.62	0.75
12	0.00	0.00	0.80

Table 3.2 Variable stiffness test data points (peak field 0.8 T) and recovery spring stiffness values

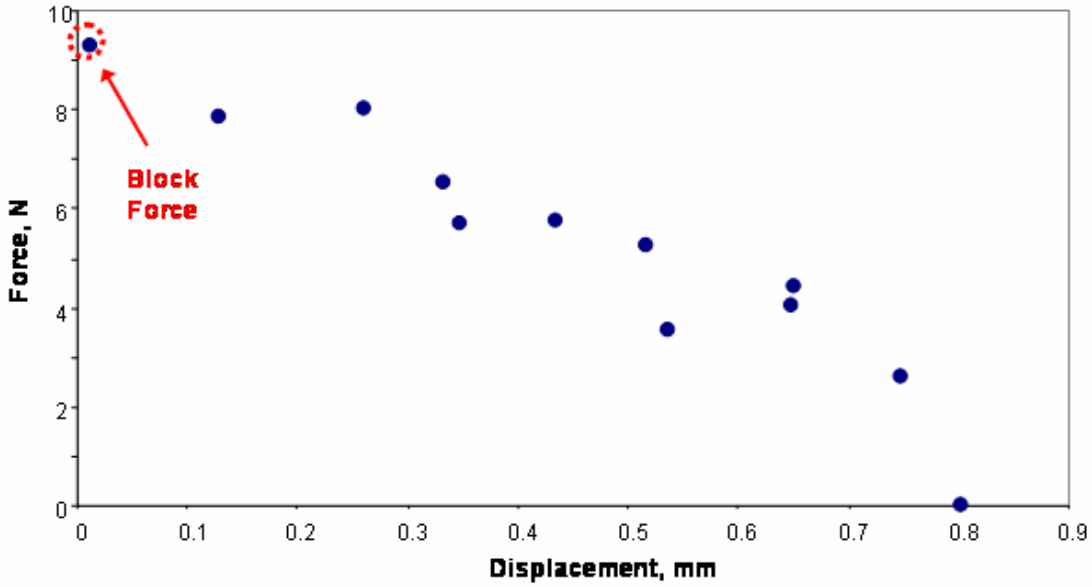

a) Force-deflection behavior

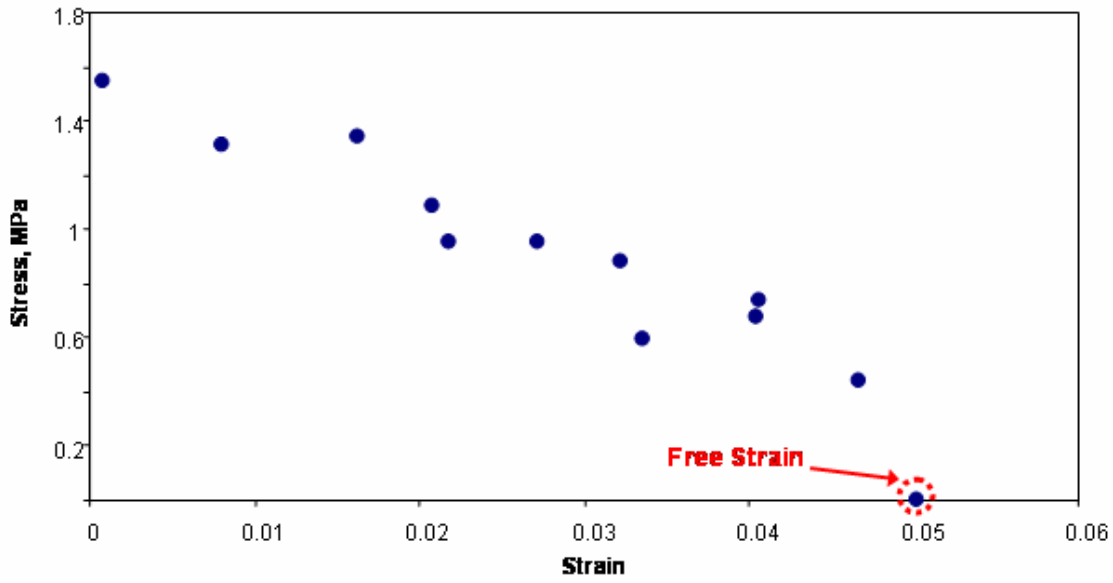

b) Stress-strain behavior

Figure 3.4 Variable recovery stiffness test results for NiMnGa

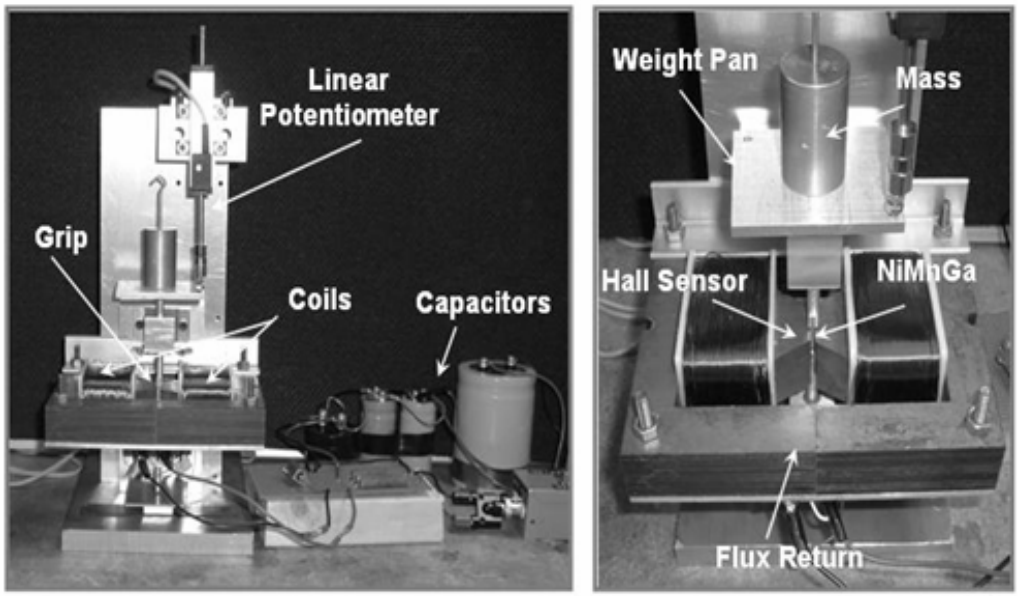

a) Photograph of constant stress test rig

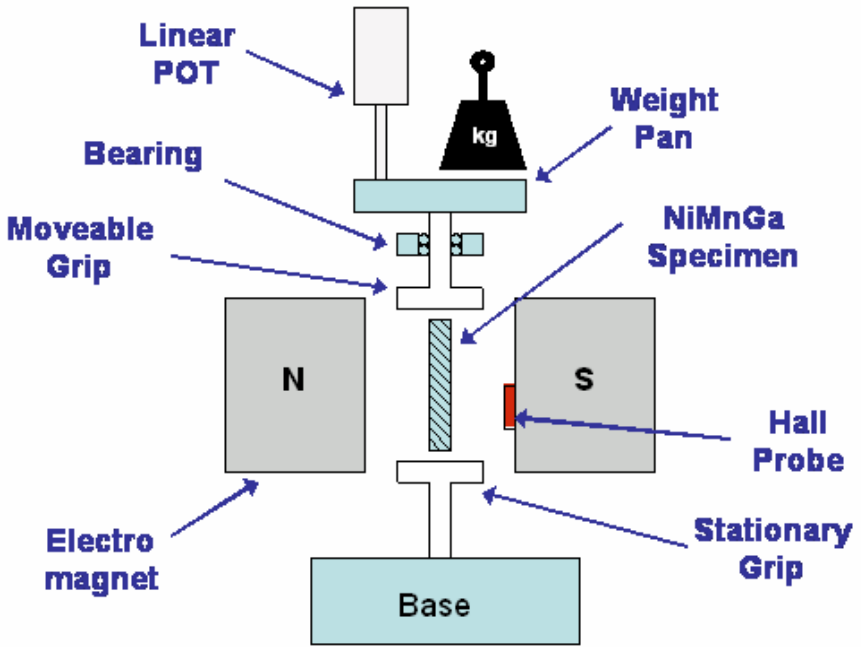

b) Schematic of constant test rig

Figure 3.5 Constant axial stress test rig

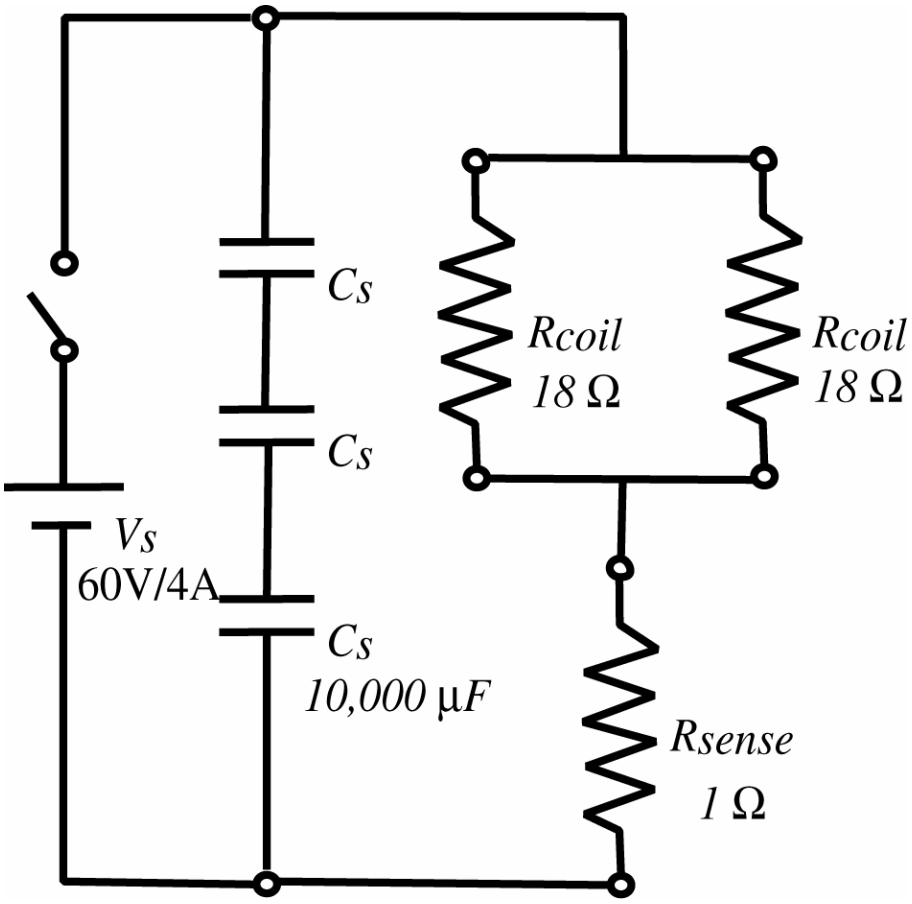

Figure 3.6 Circuit diagram for constant stress test rig

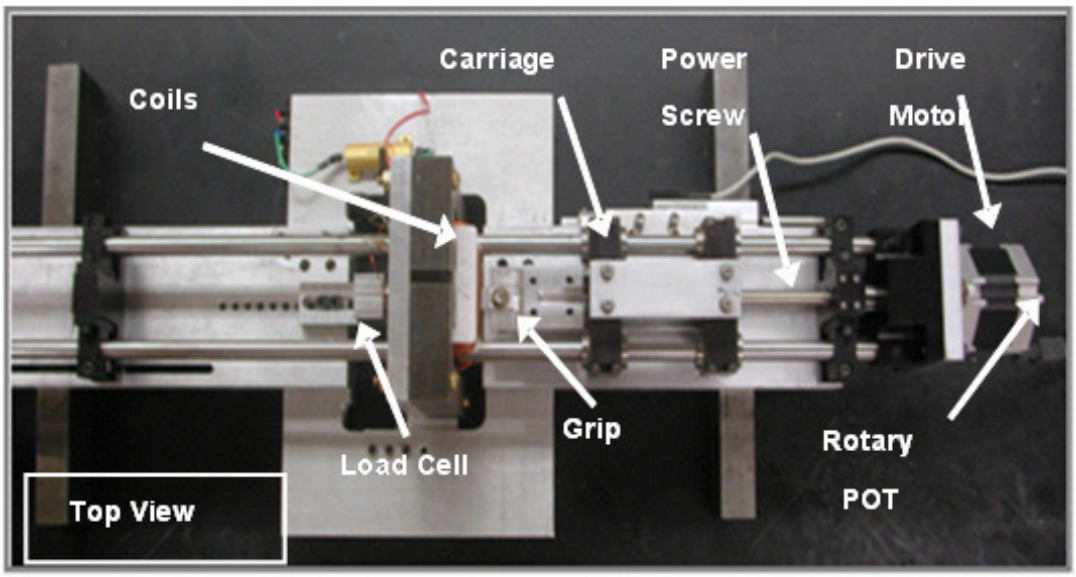

a) Photograph of constant drive current test rig

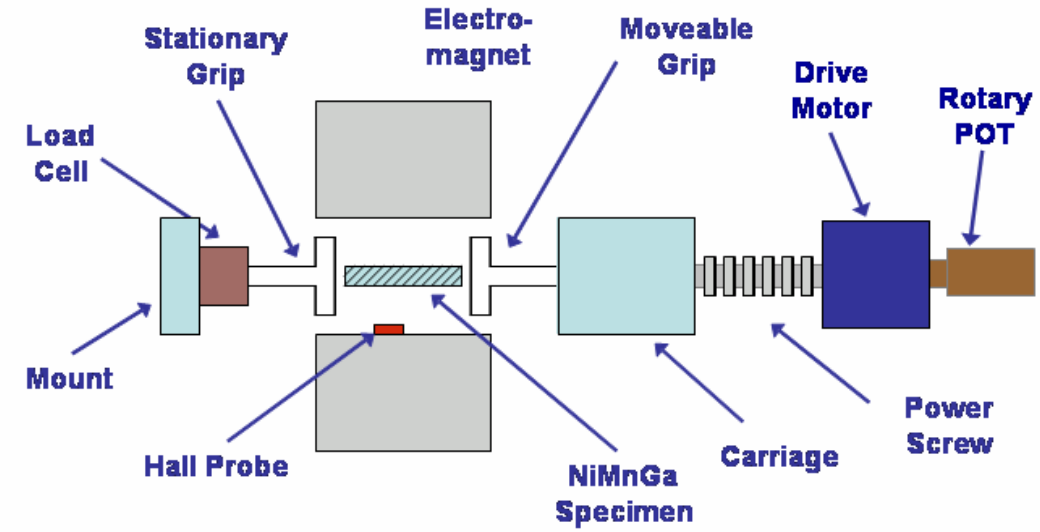

b) Schematic of constant drive current test rig

Figure 3.7 Constant drive current test rig

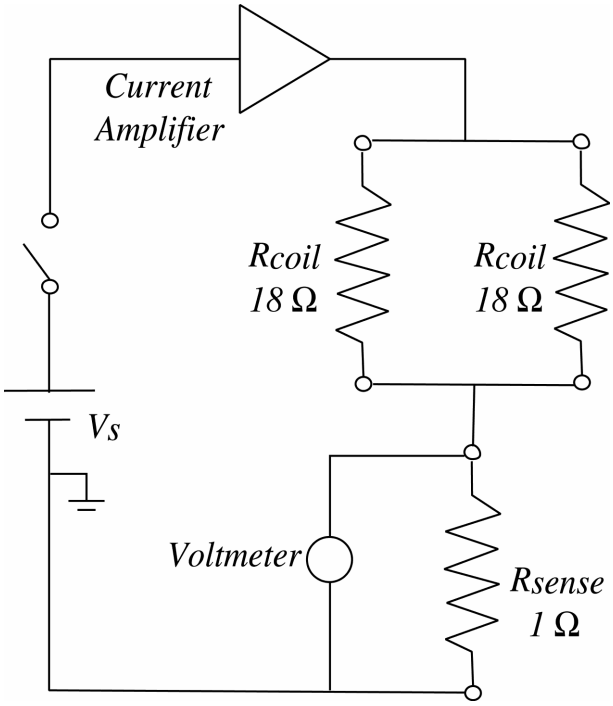

Figure 3.8 Circuit diagram for the constant drive current test rig

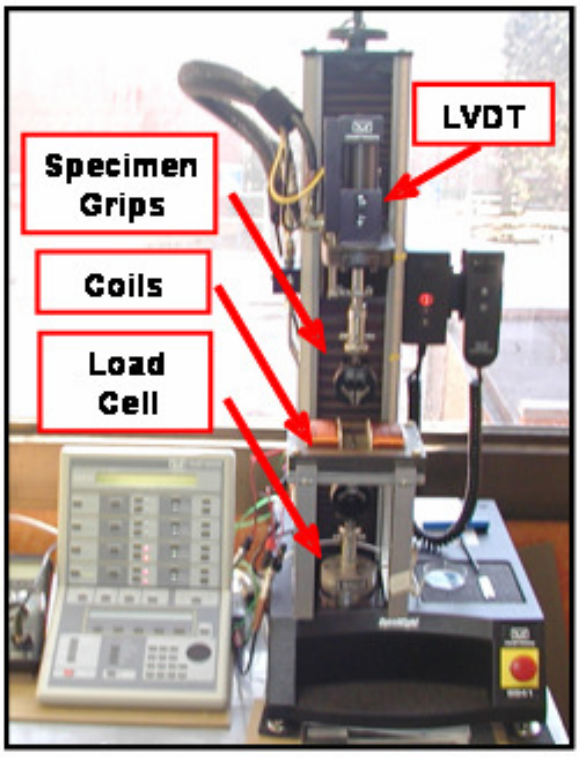

Figure 3.9 Photograph of the Instron DynaMight axial material tester

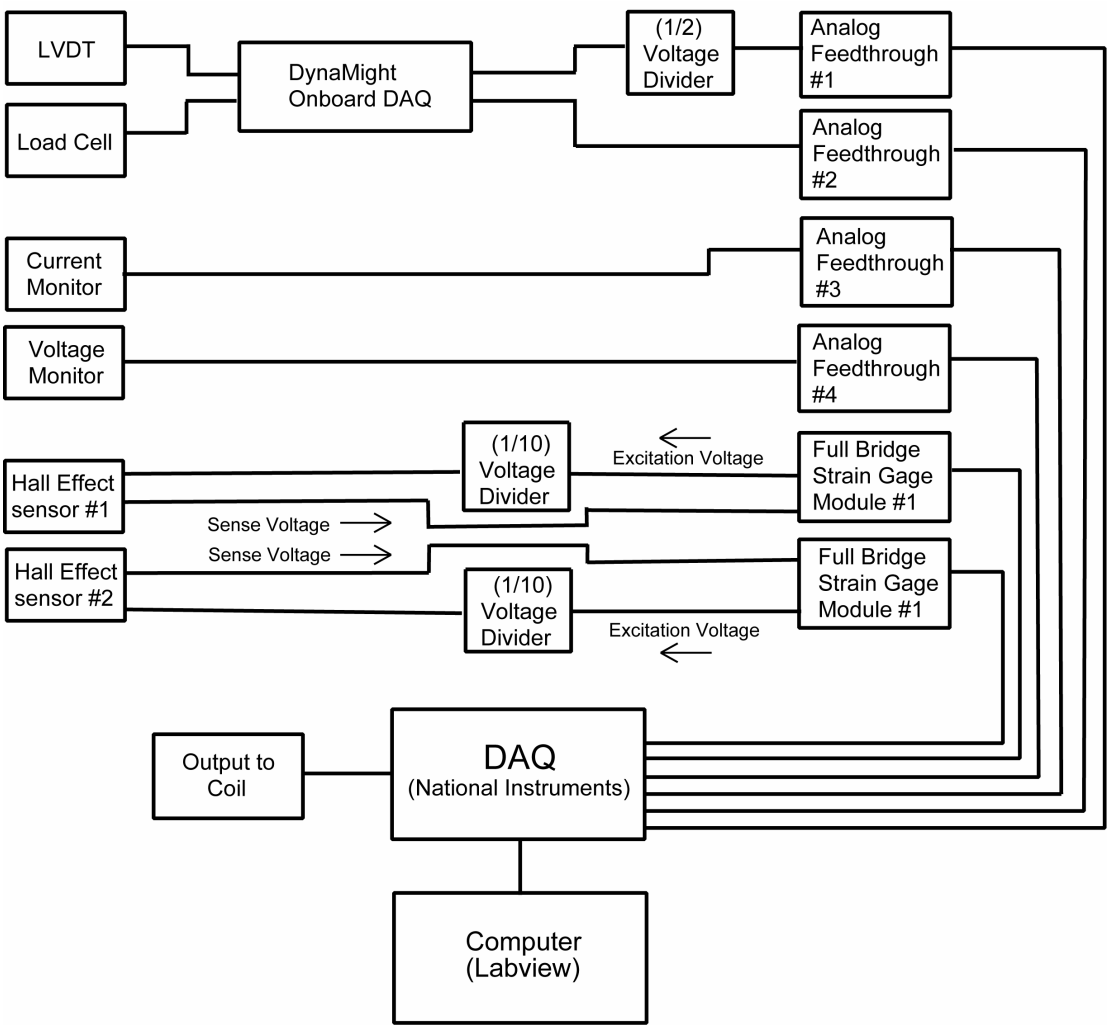

Figure 3.10 Block diagram of data acquisition hardware

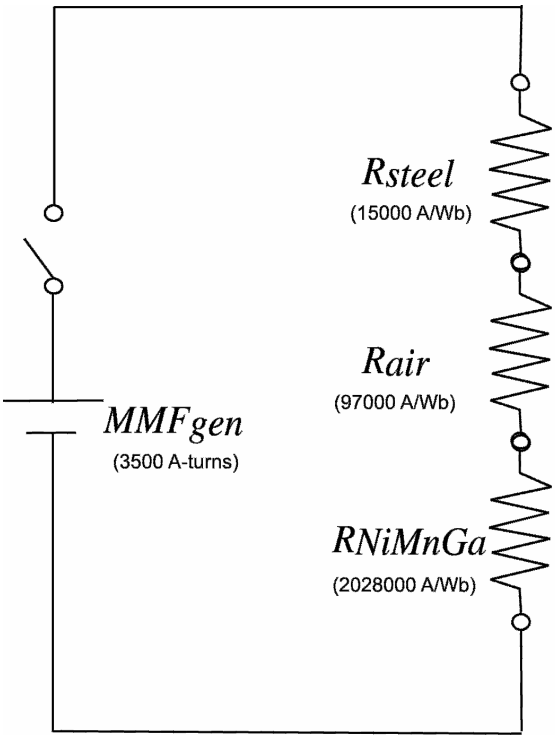

Figure 3.11 Magnetic circuit diagram for electromagnet

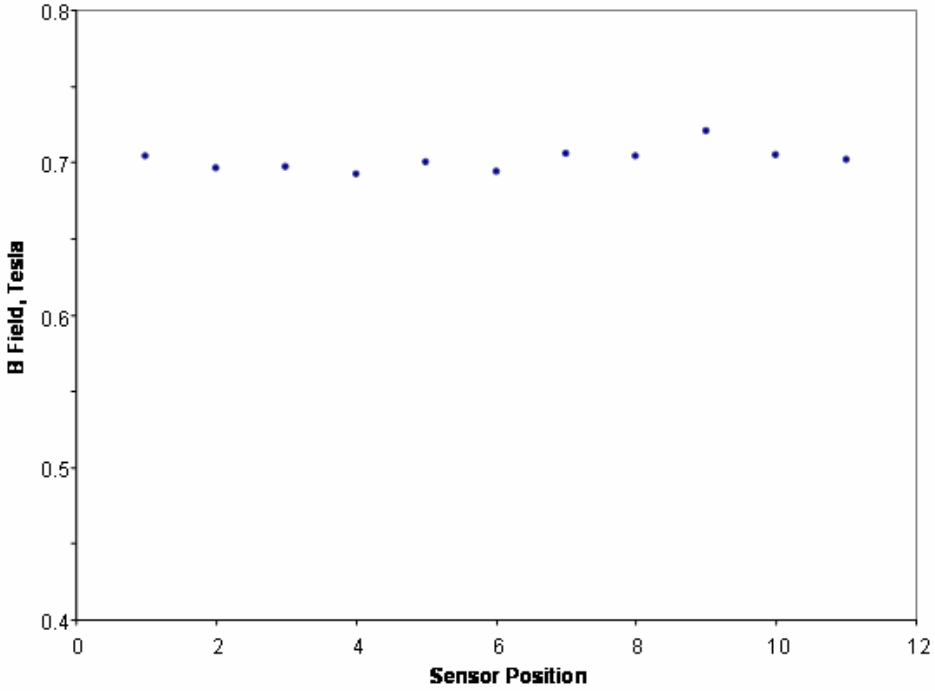

Figure 3.12 Profile of magnetic field between the pole faces

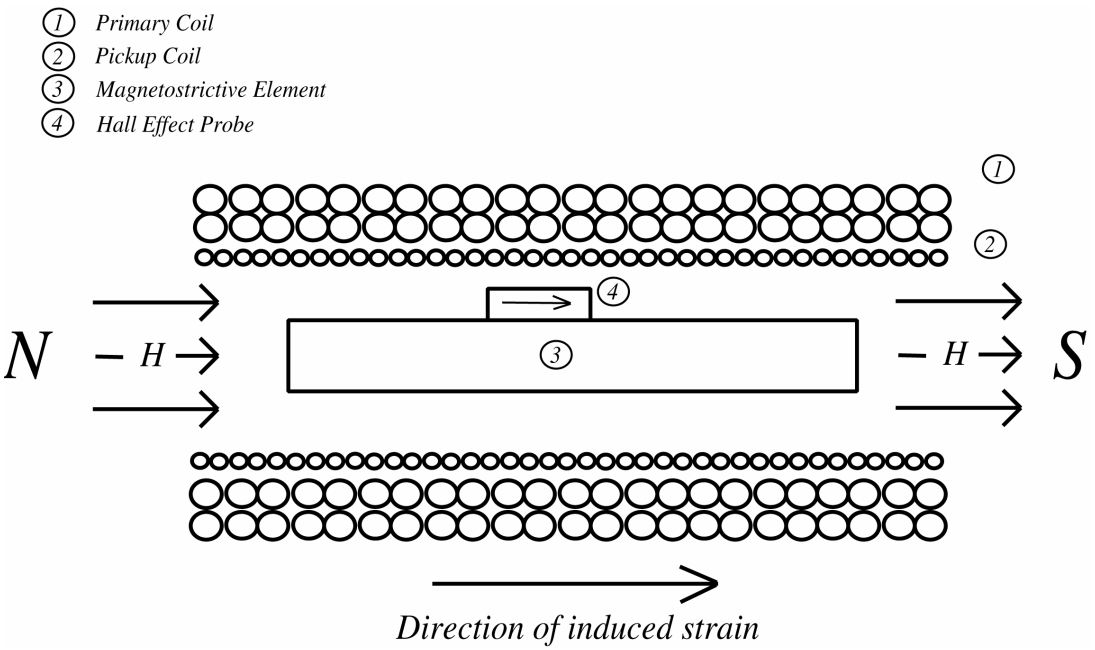

Figure 3.13 Schematic of collinear actuation instrumentation

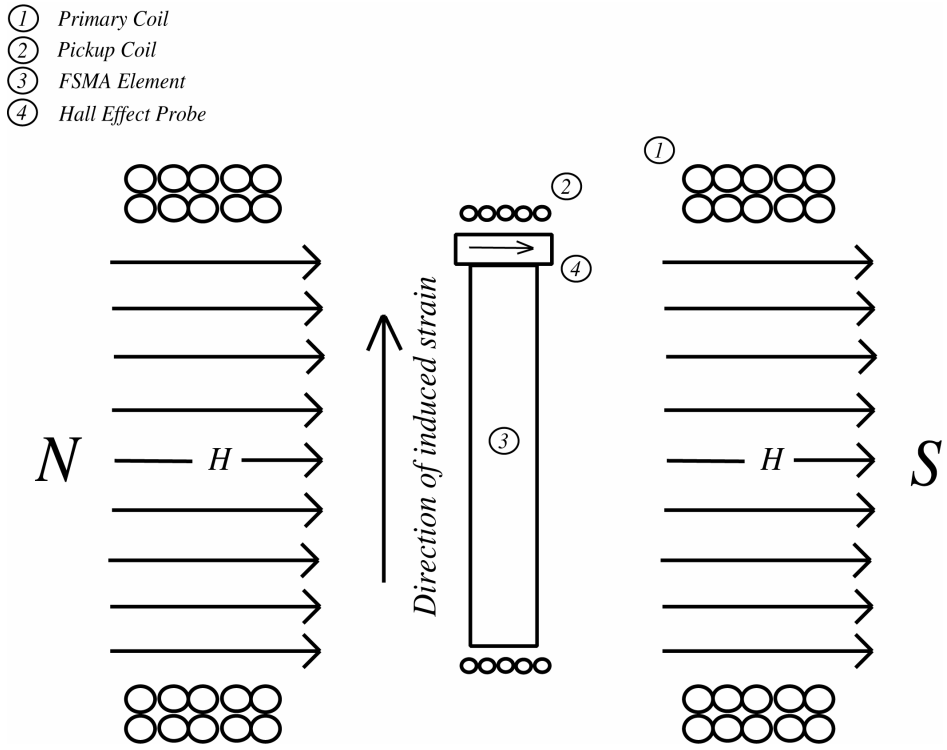

Figure 3.14 Schematic of orthogonal actuation instrumentation

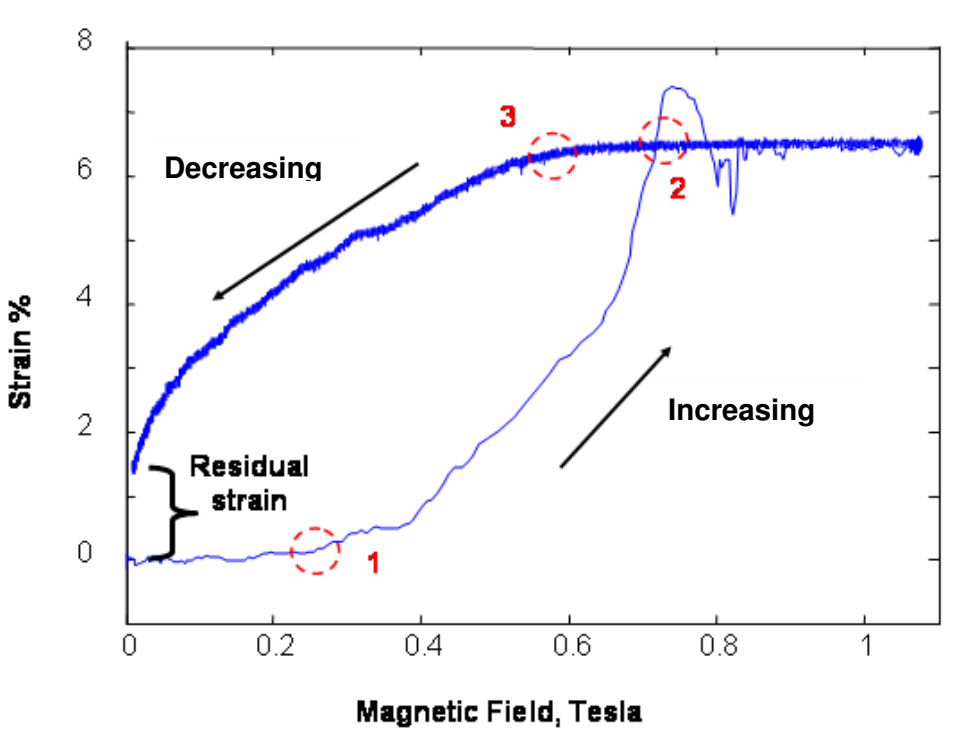

Figure 3.15 Constant Stress Data at 0.4 MPa (compressive)

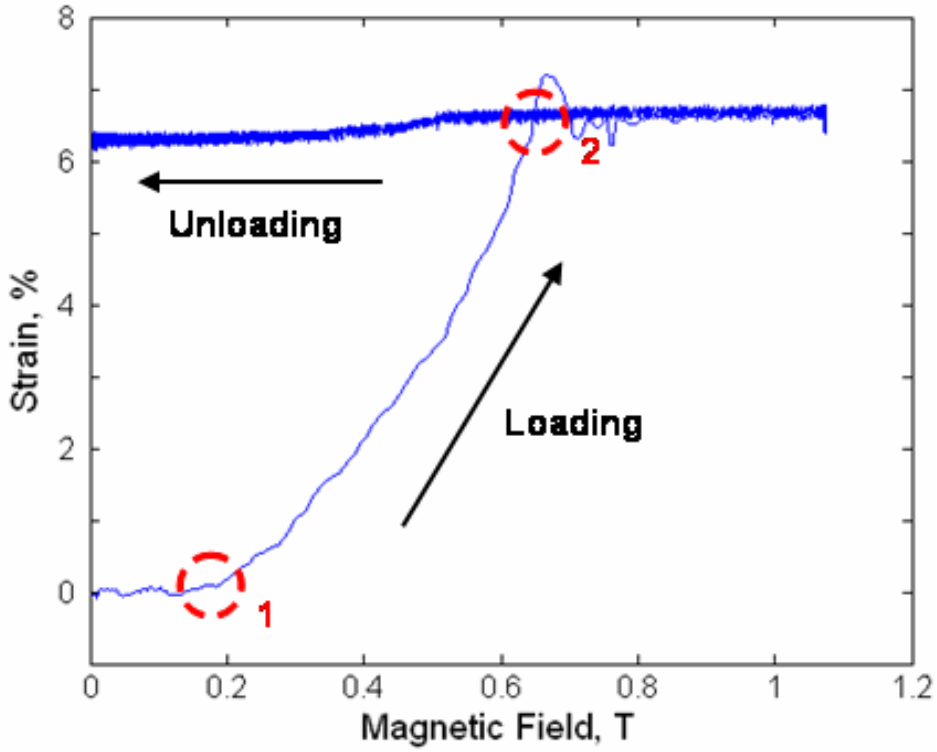

Figure 3.16 Constant axial stress data at 0.17 MPa (compressive)

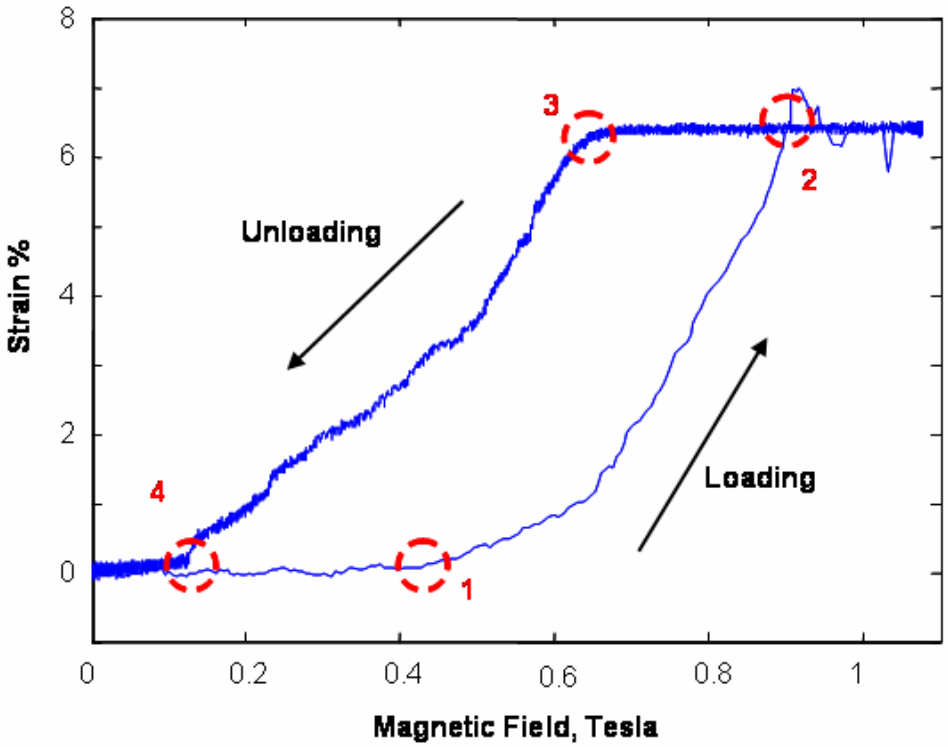

Figure 3.17 Constant axial stress data at 1.3 MPa (compression)

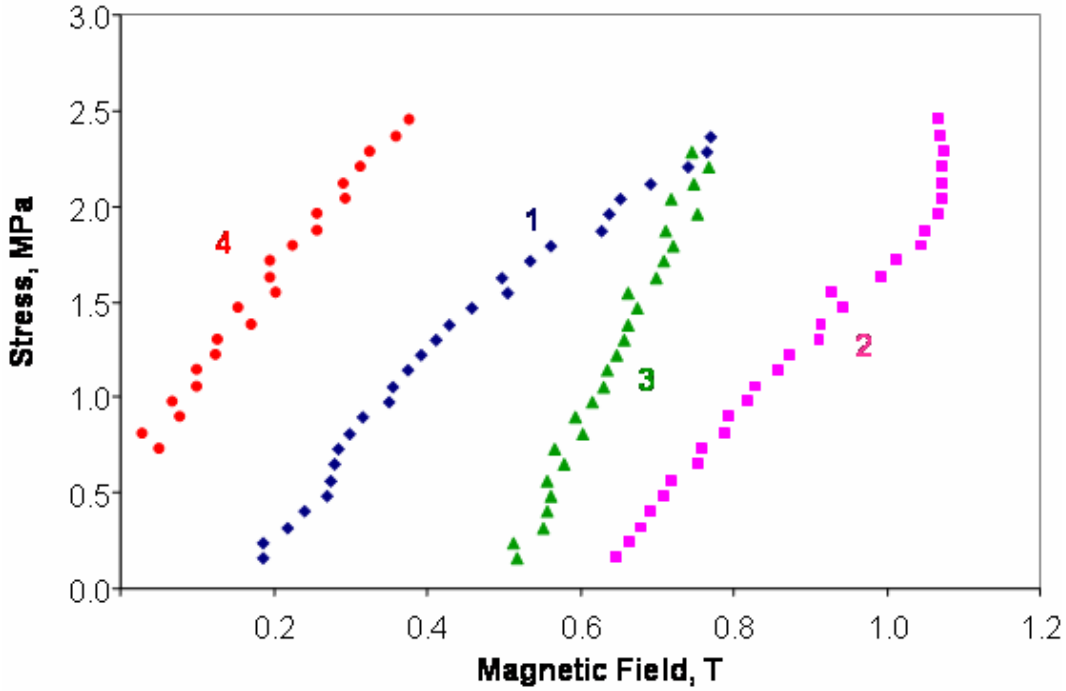

Figure 3.18 Stress vs. Magnetic Field profile obtained from constant axial stress experiments

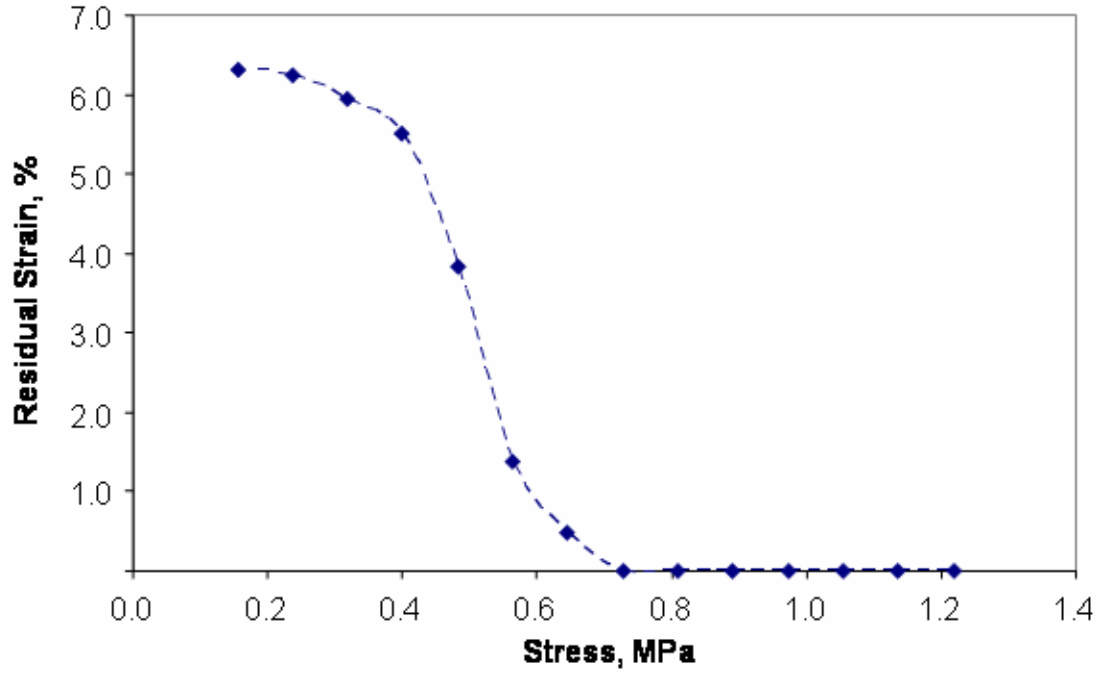

Figure 3.19 Residual strain vs. applied stress

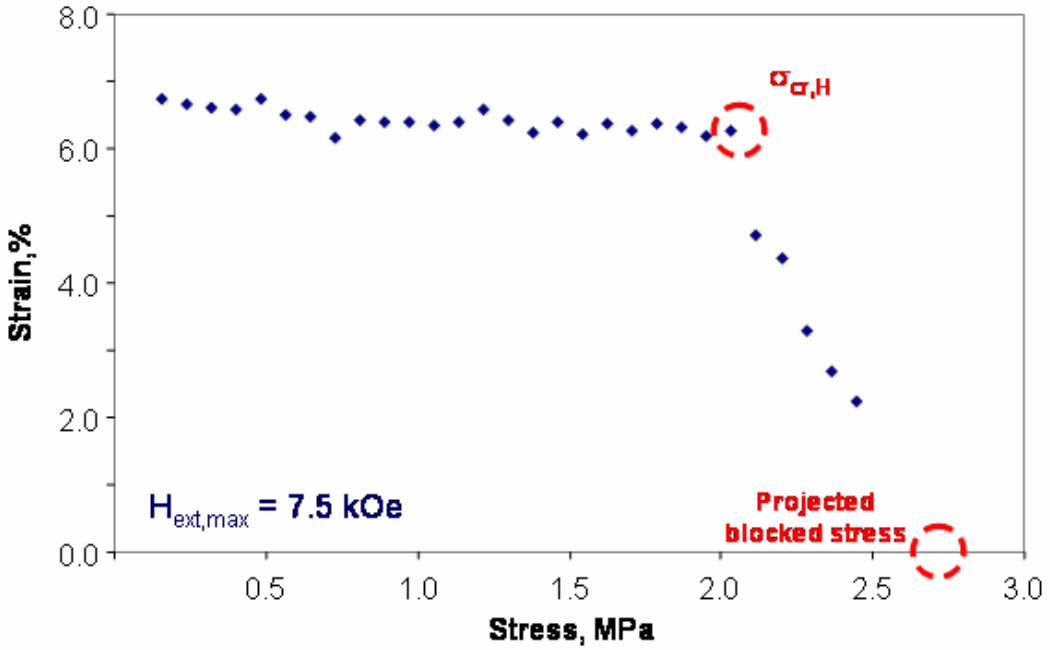

a) Maximum induced strain vs. stress for electromagnet operating at 50% of its maximum strength

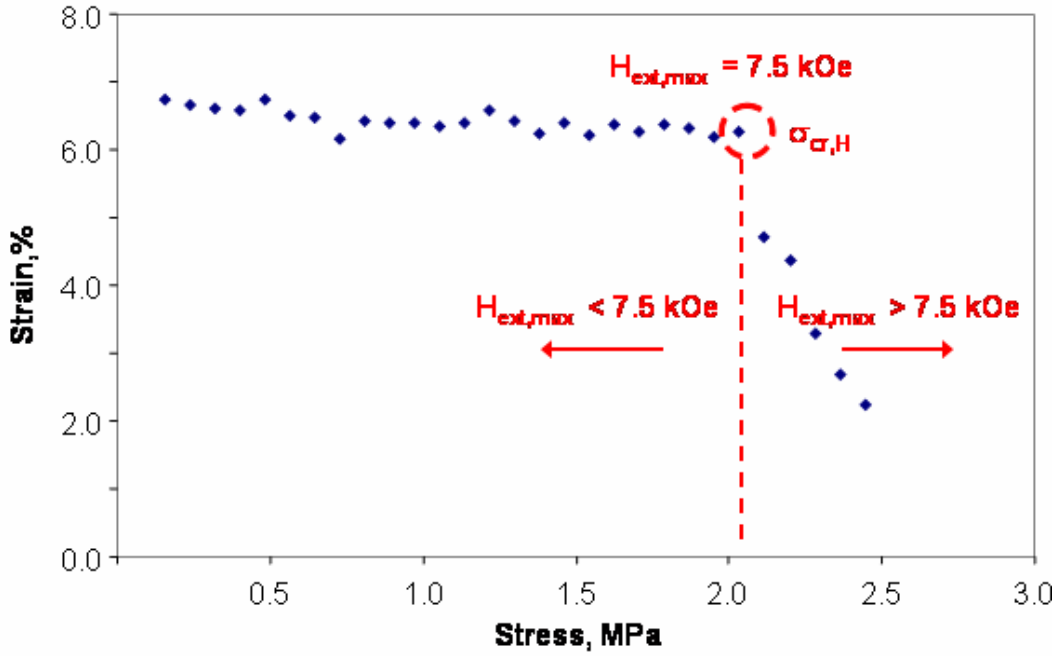

b) Dependence of $\sigma_{cr,H}$ on capability of external magnetic field generator

Figure 3.20 Constant axial stress results: maximum induced strain

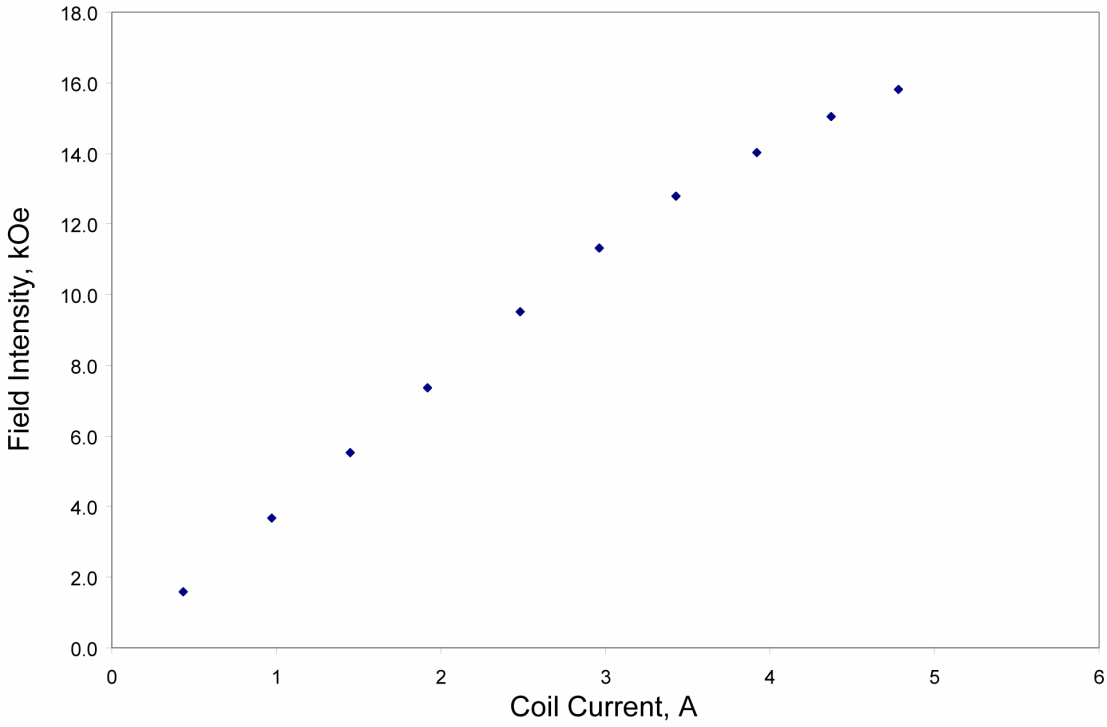

Figure 3.21 Coil calibration curve: Constant drive current tests (precision to within 0.008 kOe)

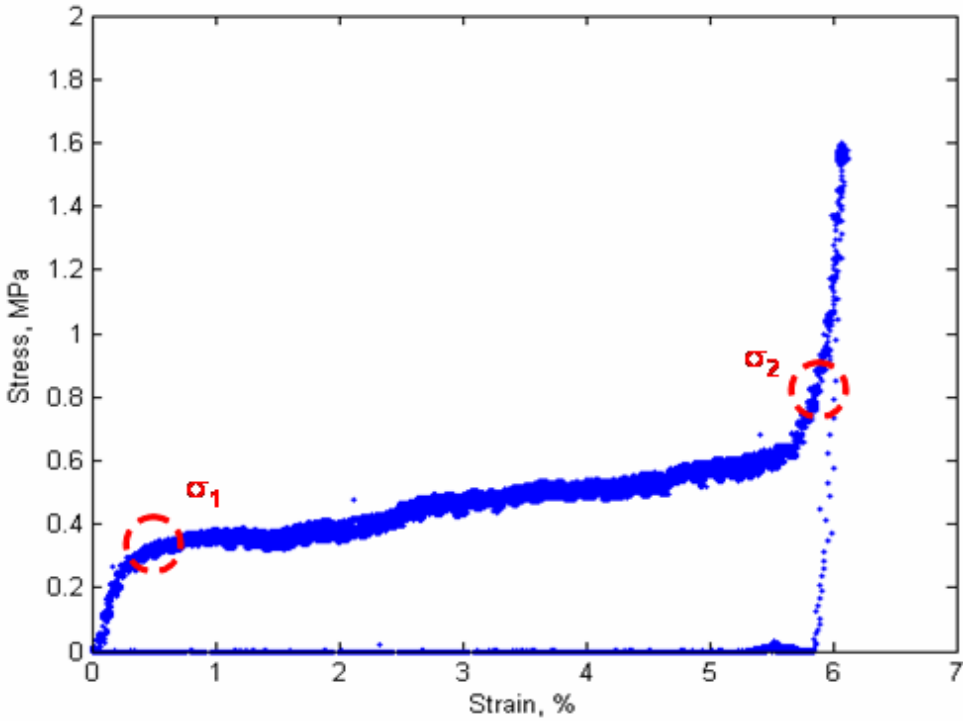

a) Magnetic shape memory effect at zero applied field

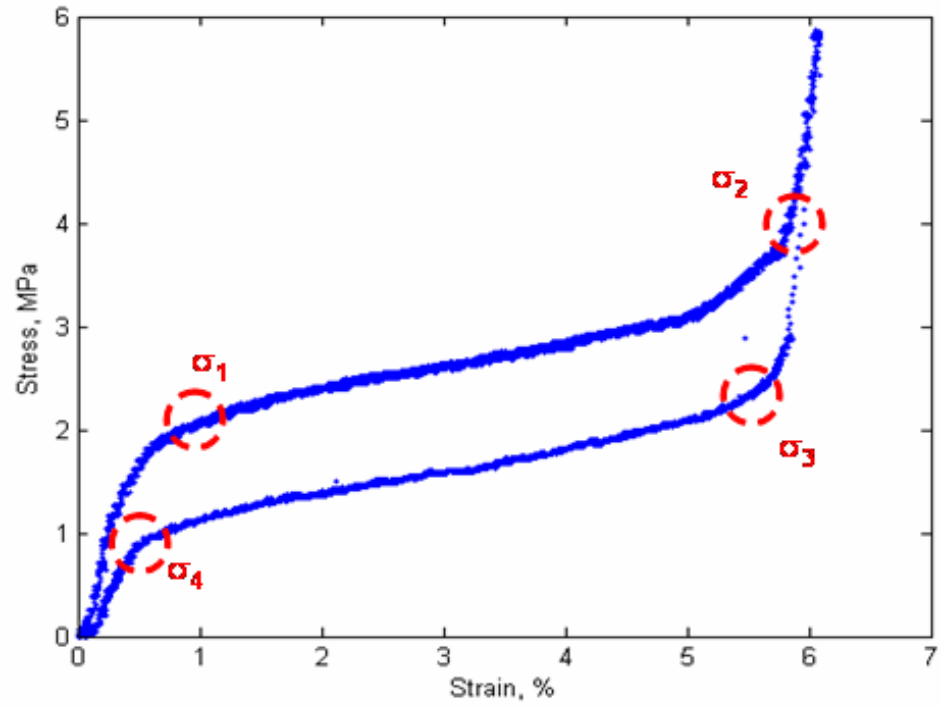

b) Magnetic pseudoelasticity for 5 kOe applied field

Figure 3.22 Constant drive current test results

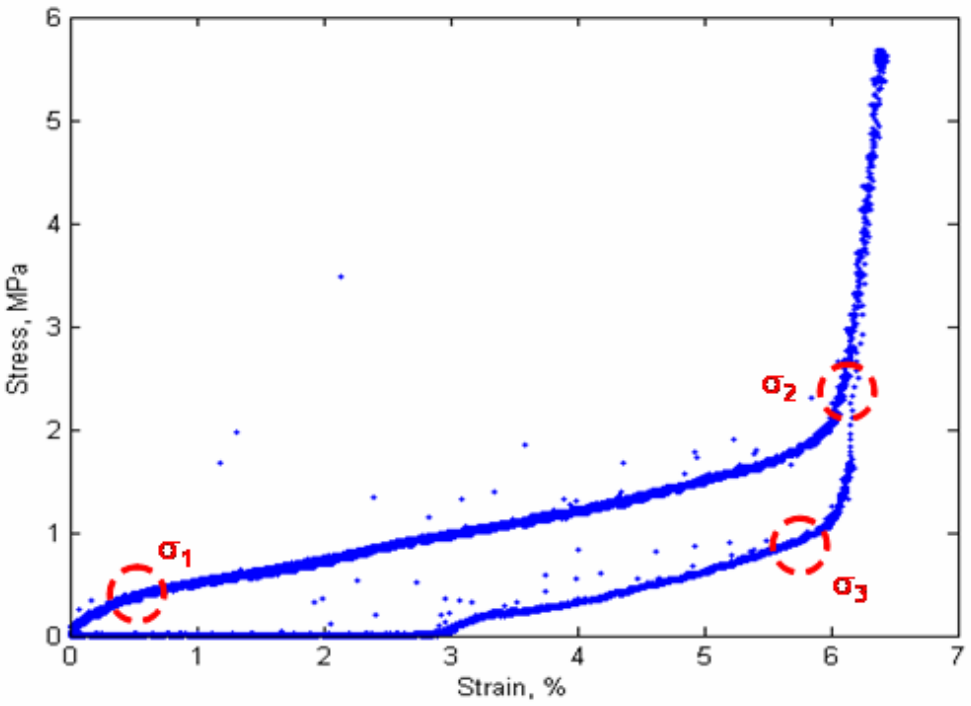

a) Partial pseudoelasticity for 2kOe applied field

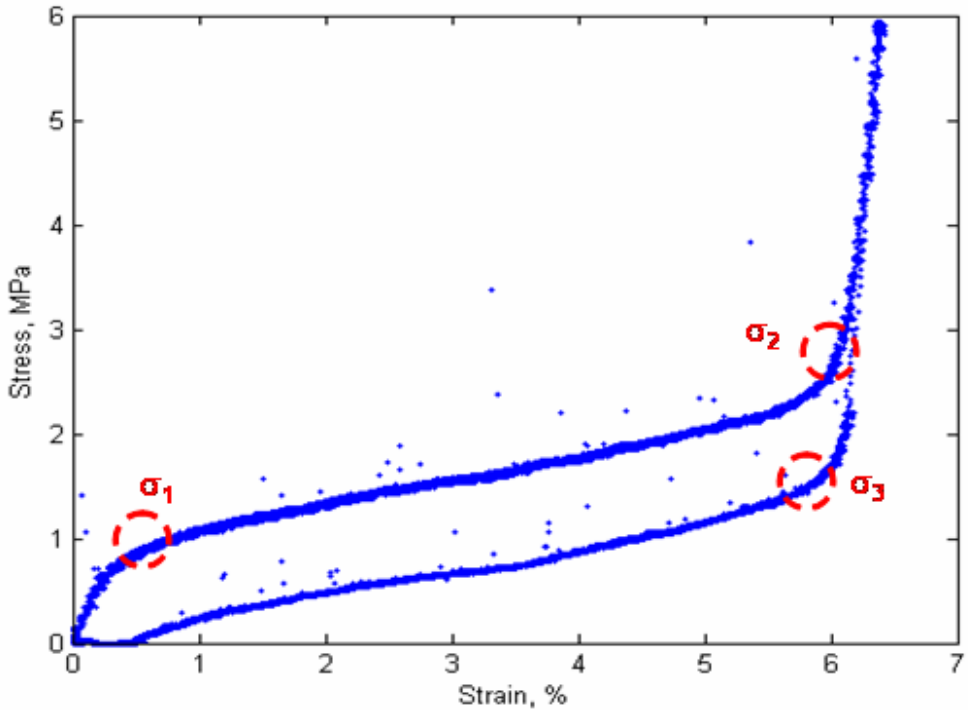

b) Partial pseudoelasticity for 3kOe applied field

Figure 3.23 Partial magnetic pseudoelasticity

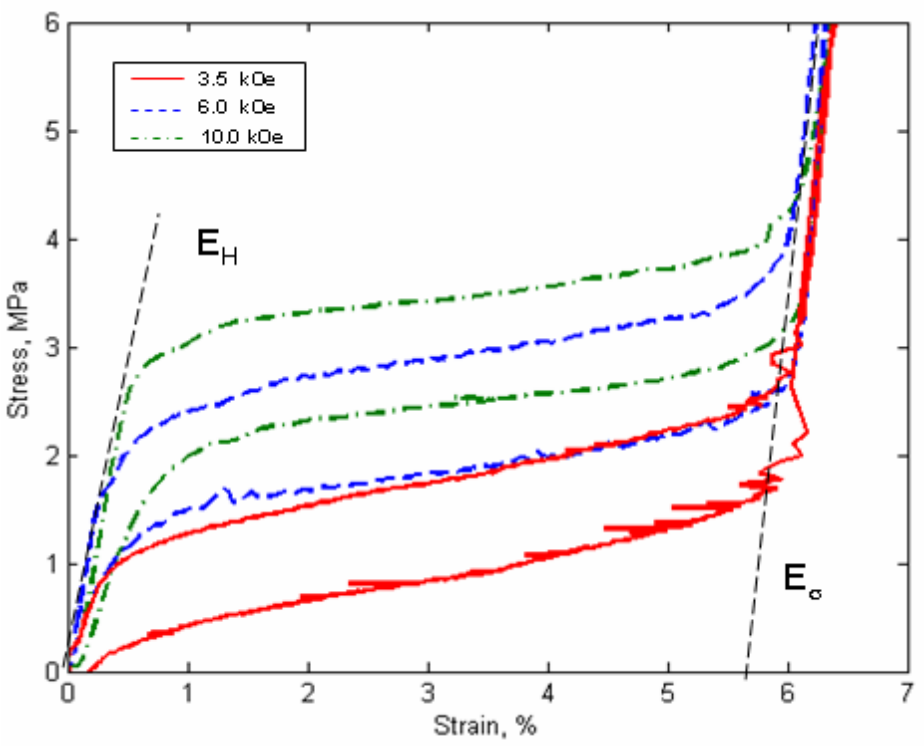

Figure 3.24 Effect of applied field

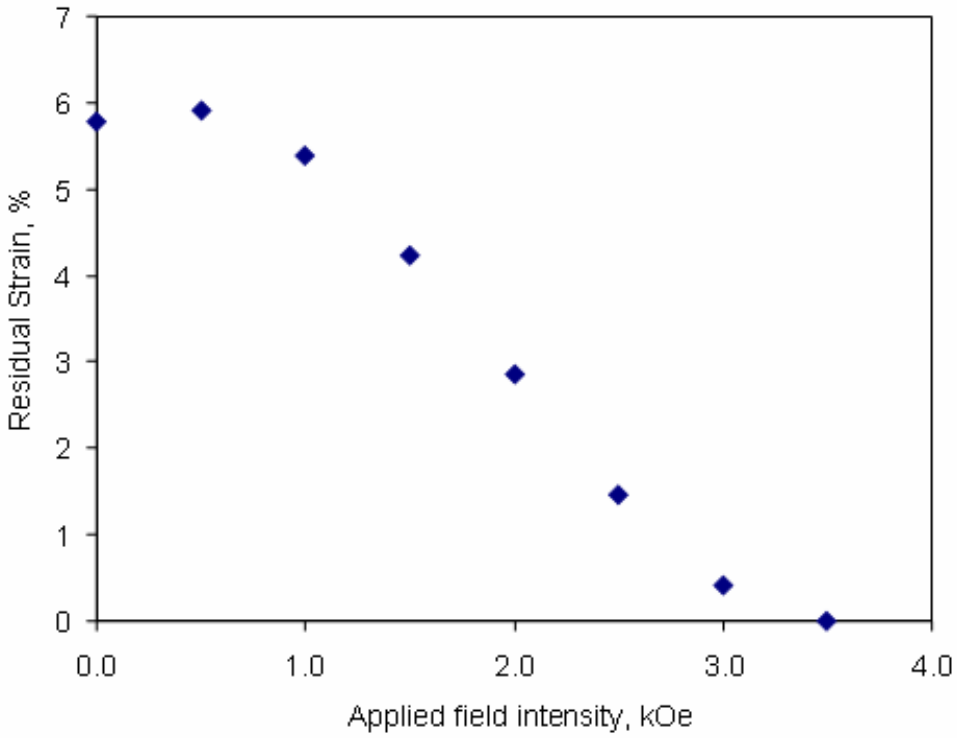

Figure 3.25 Residual strain (zero stress) measured from constant drive current testing

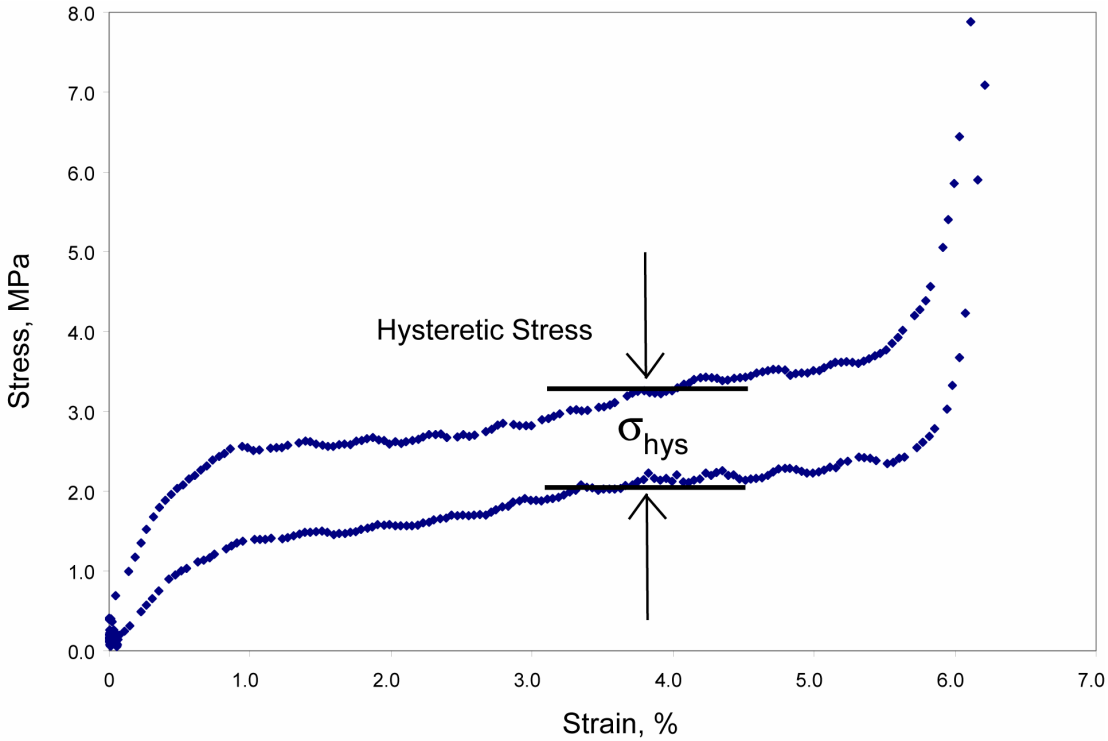

Figure 3.26 Hysteretic stress for 7 kOe applied field intensity

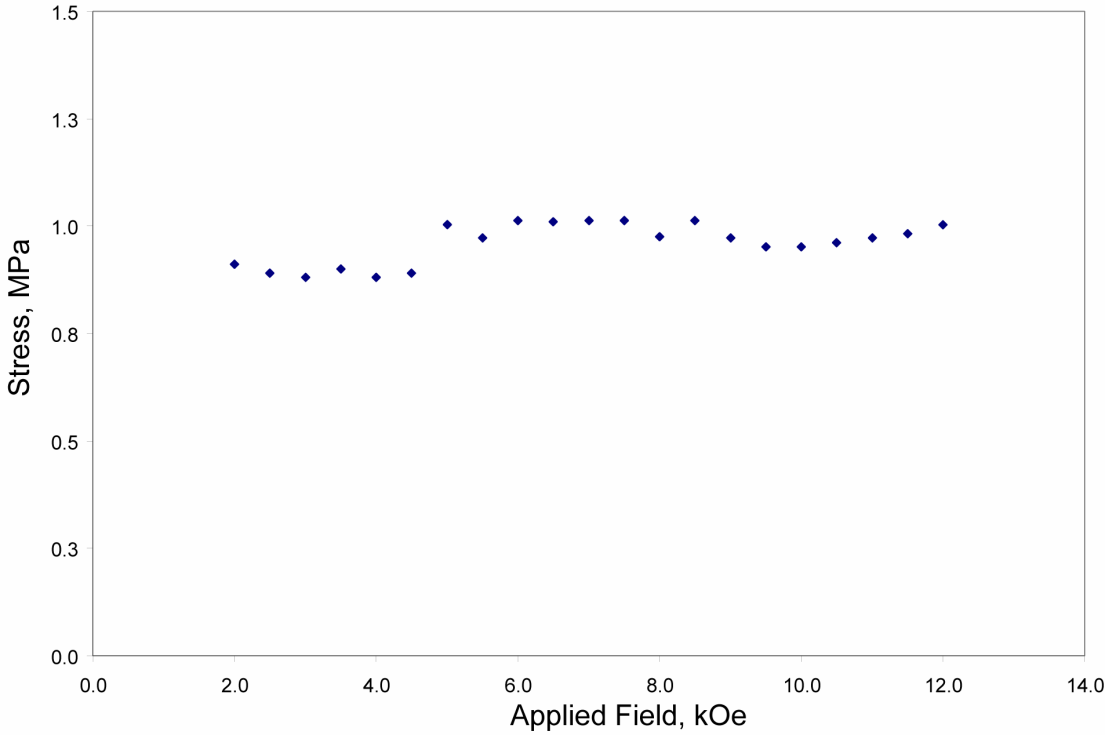

Figure 3.27 Hysteretic stress as a function of applied field intensity

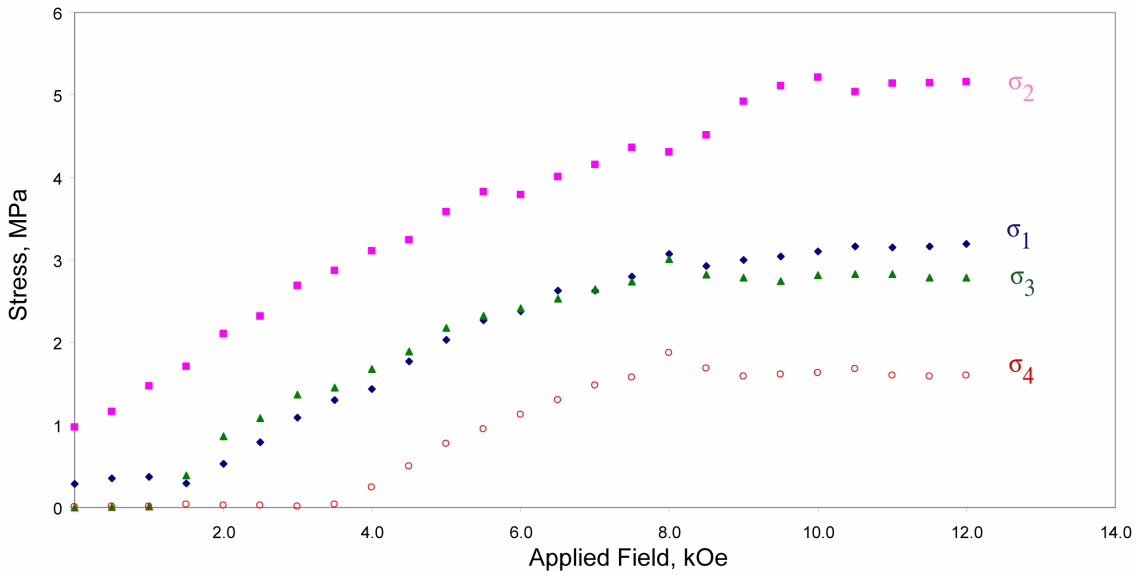

Figure 3.28 Critical stress vs. applied field (H) profile

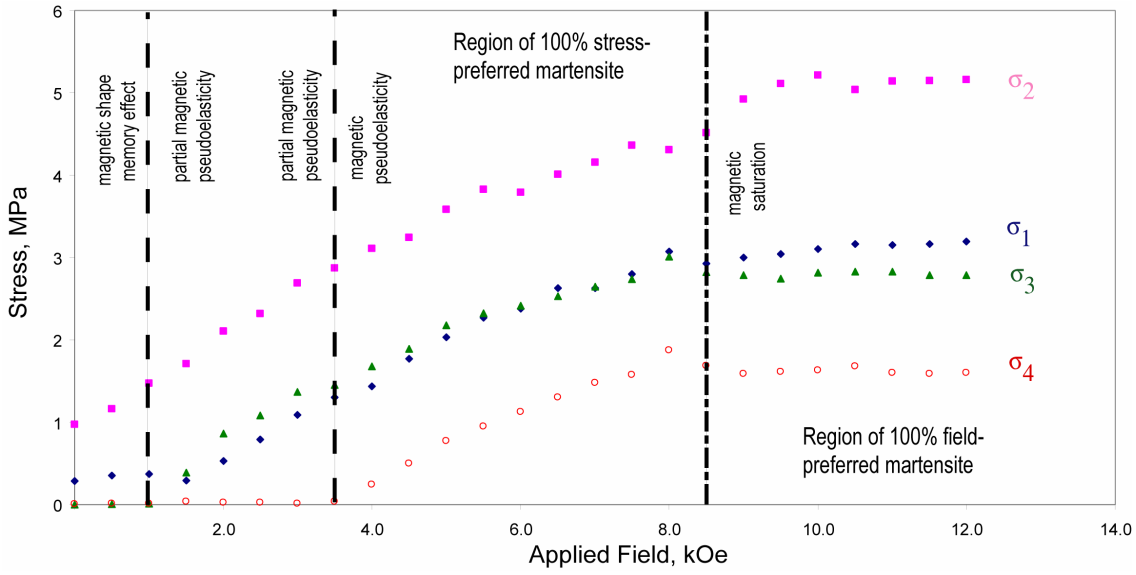

Figure 3.29 Prediction of material state using the critical stress vs. applied field (H) profile

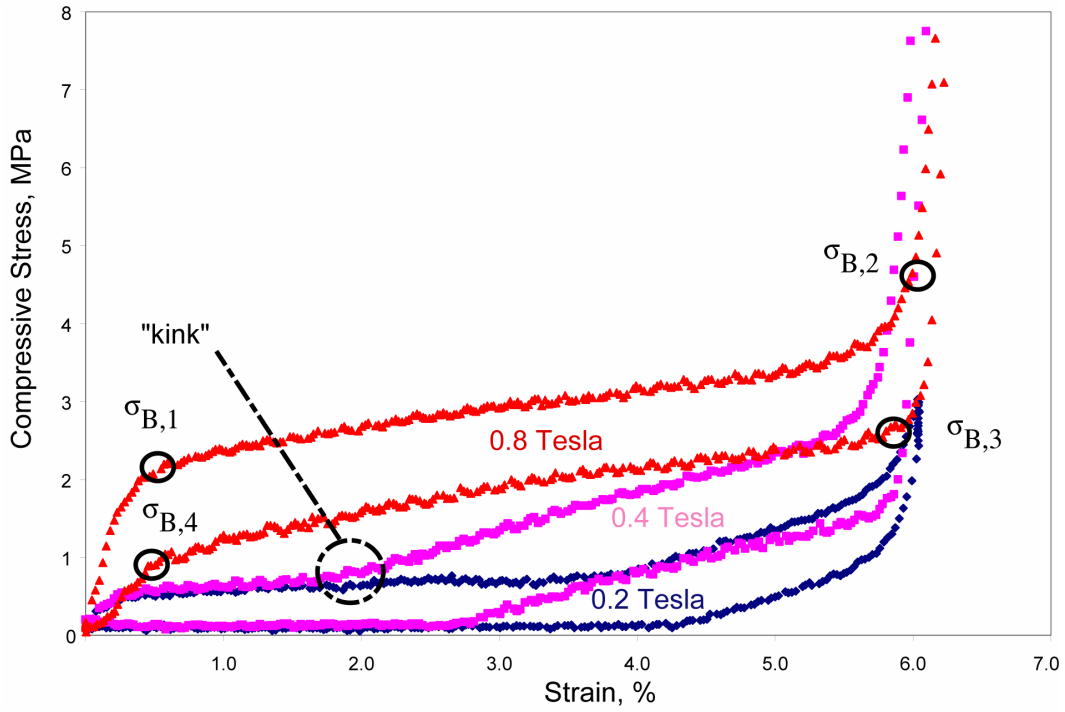

Figure 3.30 Effect of inductive magnetic fields

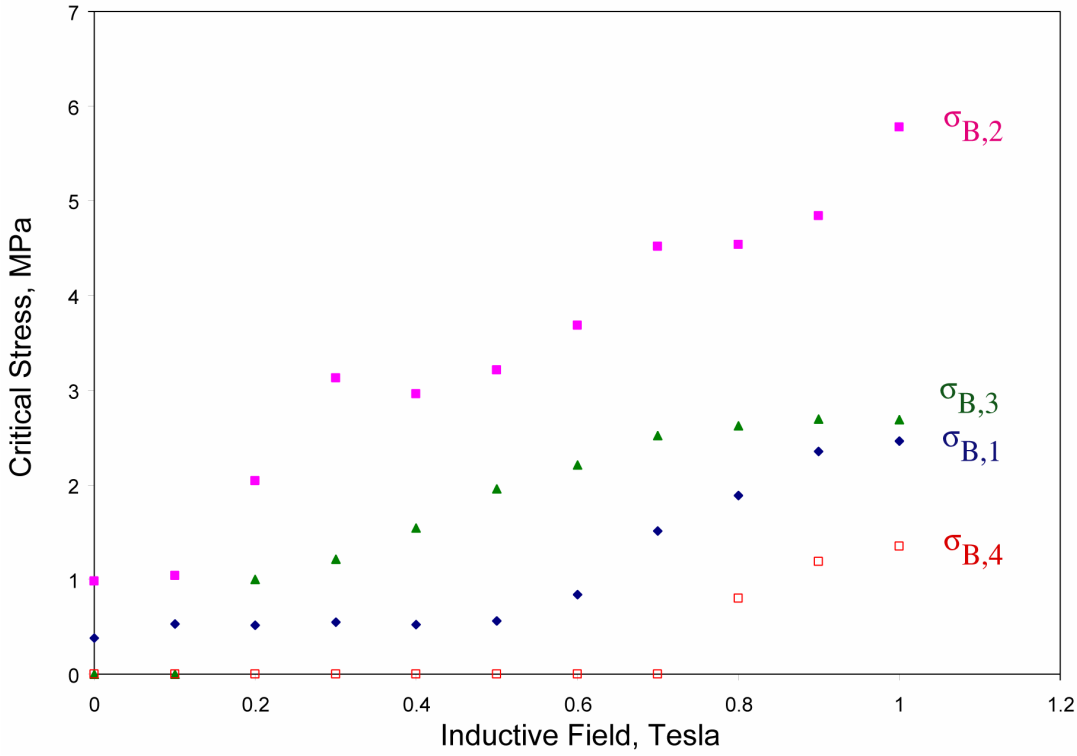

Figure 3.31 Profile of critical stress vs. inductive field

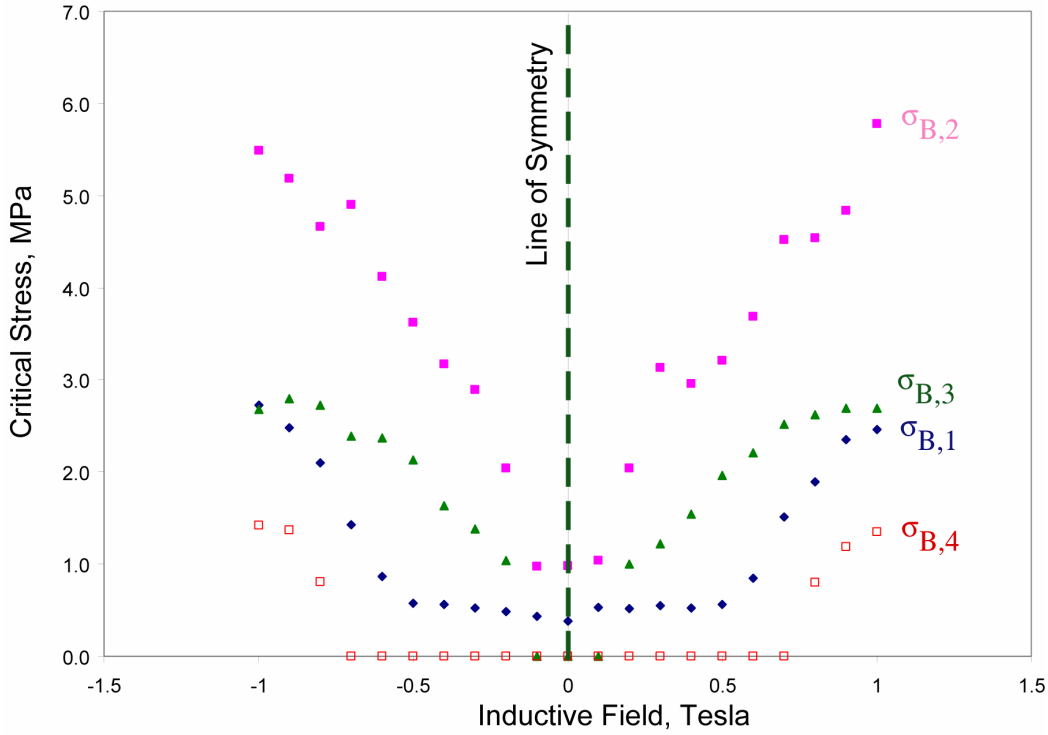

Figure 3.32 Effect of field orientation on critical transformation stresses

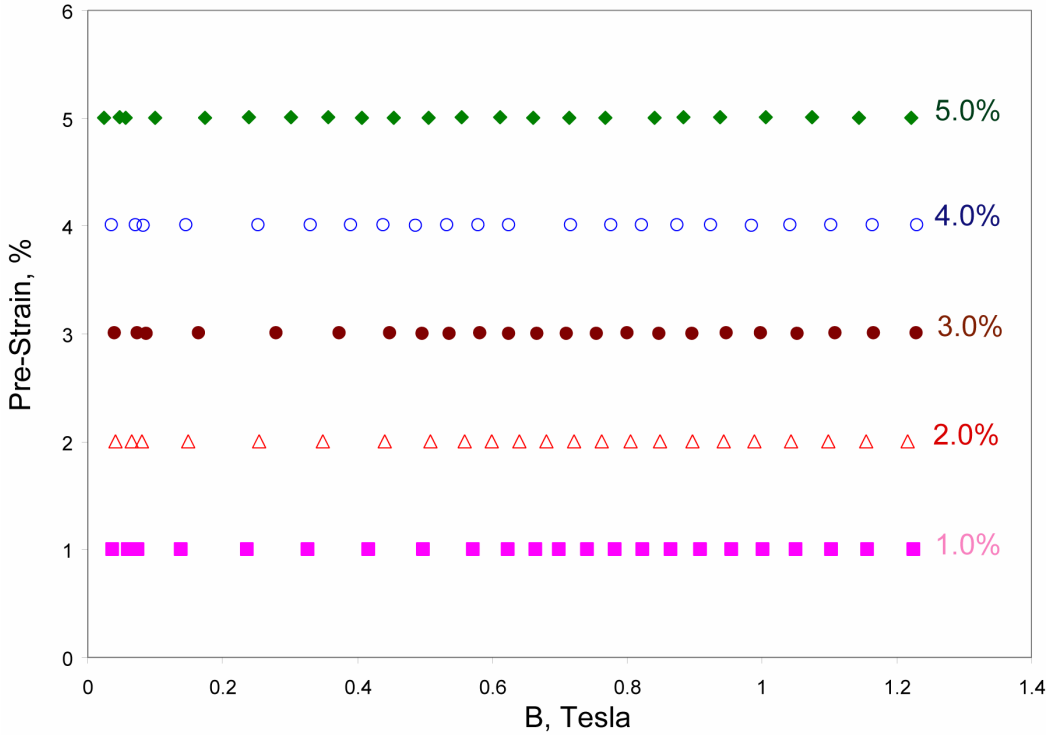

Figure 3.33 Global strain in the NiMnGa element over the range of inductive fields tested in the constant pre-strain experiment

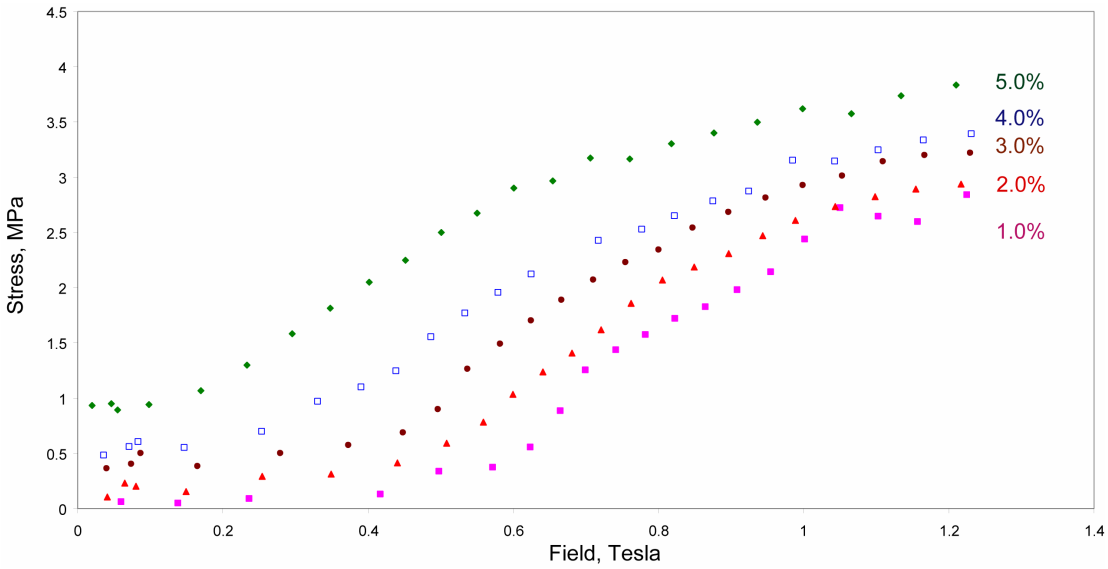

Figure 3.34 Effect of constant pre-strain in NiMnGa

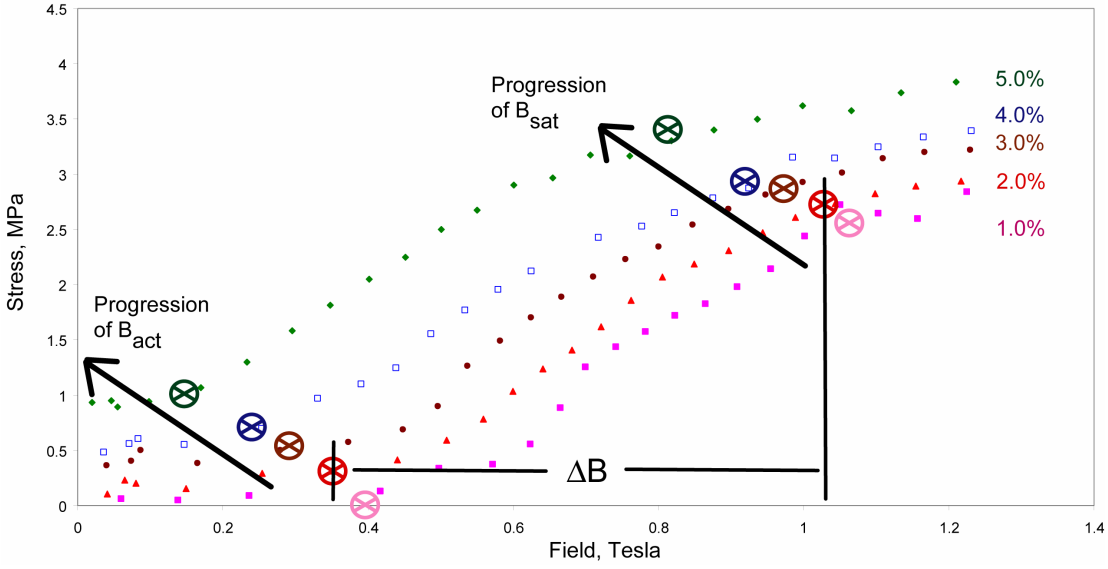

Figure 3.35 Activation and saturation field behavior in NiMnGa for constant pre-strain experiments

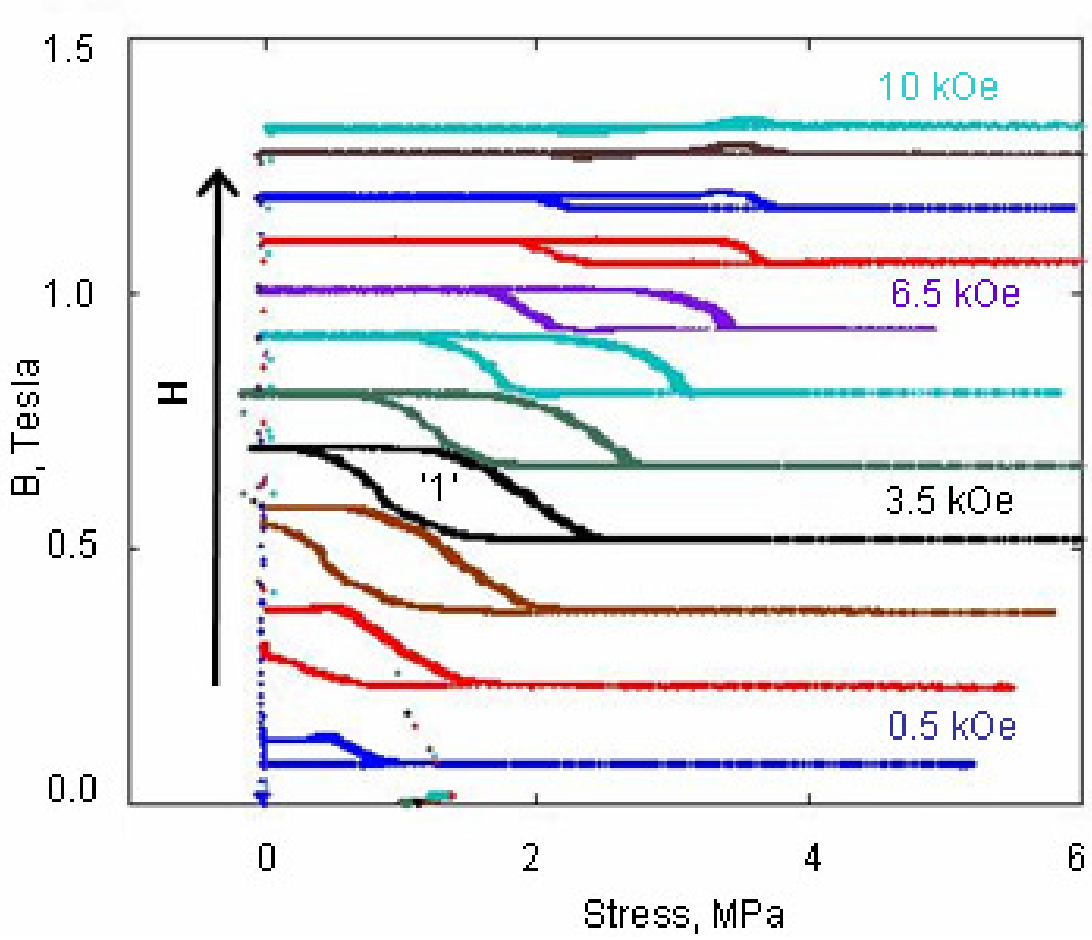

Figure 3.36 Sensor characteristic for NiMnGa element

Chapter 4: Non Quasi-Static and Dynamic Behavior of NiMnGa

Because of their large energy output, FSMA show enormous potential in high-stroke, dynamic, actuator applications [168, 219, 223]. A complete, experimental characterization of both the static and dynamic response of bulk specimens of NiMnGa is necessary before the material can be successfully utilized in practical actuator applications. Up until now, research has been directed mainly on the static and quasi-static characterization of the FSMA. This chapter expands the focus to include dynamic behavior by examining the response of NiMnGa specimens to dynamic, magnetic excitation fields. A characterization of material behavior to a wide range of loading conditions was conducted. Non quasi-static effects such as the effect of strain rate were examined. A series of tests in which NiMnGa elements were exposed to constant load and constant strain conditions was conducted. Finally, based on these results, performance characteristics including damping, energy, density, power density, and electromechanical efficiency were measured.

4.1 Preliminary NiMnGa Dynamic Testing

For the first stage of dynamic testing, experiments were carried out on the test rig described in section 3.2.1. Based on the results presented in section 3.2, for optimum material performance, a recovery spring of 10.21 N/mm was chosen to generate the recovery forces for dynamic actuation.

A function generator connected in series with a 2450 Watt amplifier provided power to the electromagnet. NiMnGa specimens were energized by a 0.85 T peak, field at excitation frequencies ranging from 1 to 50 Hz. Because of limitations in

power generation, higher excitation frequencies were not capable of being generated by this magnetic circuit configuration. Although a 1.0 T peak field was desired, the electromagnet was capable of generating inductive fields large enough to induce twin boundary motion in the material so that the dynamic behavior of the material could be observed qualitatively.

NiMnGa specimens were glued into the grips of the test rig and situated between the poles of the electromagnet so that a uniform exposure to the magnetic field was guaranteed. Next, a preload was applied to the specimen via a mechanical advance screw system. Then the coils were energized and the NiMnGa element was exposed to a dynamic excitation field and allowed to act against the recovery spring. Excitation frequencies between 1 and 50 Hz were tested. Preloads ranging from 2 to 10 N were tested at each excitation frequency. Measurements of the induced force, deflection, and magnetic field were taken for each test case. From these measurements, axial stress, and strain generated by the NiMnGa element were calculated.

4.1.1 Dynamic Strain Response

When a NiMnGa actuator is subjected to an AC field of sufficient magnitude, the induced strain and force generated may be divided into two components, mean and dynamic. The mean strain is the maximum amount of strain achieved by the actuator from the zero strain condition to a static mean point. Dynamic strain is the value of strain generated about a static mean point and is the direct result of the recovery spring acting against the MSM effect. Figure 4.1(a) and 4.1(b) show the strain and force generated by a NiMnGa element reacting to a 20 Hz, 0.85 T peak

inductive excitation field with an applied preload of 4.3 N. In this case, the mean strain was 1.2% (Figure 4.1(a)) and the mean force was 3.3 N (Figure 4.1(b)). Likewise, the dynamic components of induced strain and force were 1.15% and 2.2 N respectively. Finally, absolute strain and force produced by the actuator are defined as the mean component plus the one half the dynamic component. The absolute strain and force measurements provide insight into the magnitude of the maximum strain and force generated by the material during magnetic excitation. One of the main goals of the preliminary study was to examine the effect of preload and excitation frequency on the mean and dynamic components of the induced strain and force.

For dynamic actuation of the NiMnGa specimen, the presence of a recovery force is essential. Consider a case in which the material is exposed to a sufficient AC transverse field, but with the recovery spring removed. Because the force generated by the recovery spring is out of phase with the magnetic forces responsible for inducing twin boundary motion, its effect is to "reset" the twin boundaries every cycle. In fact, dynamic strain can only occur when a recovery force is present. For dynamic actuator applications, the magnitude of the dynamic strain is important for determining actuator performance.

In Figure 4.2, the absolute strain of the material for excitation frequencies between 18 and 50 Hz acting under 2.1, 4.3 and 6.4 N preloads is shown. For this set of tests, it was not possible to produce excitation fields below 18 Hz due to limitations in the frequency response of the amplifier. Based on these results, it was concluded that despite some scatter, the maximum level of induced strain remained relatively constant over the frequency range for each preload. For the case of the 2.1

N preload, the absolute strain was approximately 2.25% over the entire frequency range. As the preload was increased, the average value of absolute strain steadily dropped to 1.6% for a 4.3 N preload and 0.8% for the 6.4 N preload. Based on this trend, a preload of about 9 N would completely block the induced strain response of the material. This behavior is expected as the block force determined in the static testing occurred at approximately 9.2 N (Figure 3.5(a)).

In Figure 4.3, the effect of preload on the dynamic strain component of the material is shown. Unlike absolute strain, the maximum dynamic strain can increase with preload. Figure 4.3 shows the strain response of the material over the frequency range for 2.1 and 6.4 N preloads. The dynamic strain for the case of 6.4 N preload begins at 0.5% at an actuation frequency of 18 Hz and reaches a plateau of 0.8% at 30 Hz excitation. Likewise, the dynamic strain for the 2.1 N preload begins at 0.2% at 18 Hz and reaches a plateau at 30 Hz of 0.45% strain. It is important to point out that the dynamic response in this case will be influenced by the dynamics of the combined test rig and NiMnGa element system. The location of the plateau on the frequency spectrum could be shifted by alteration of the stiffness of the recovery spring or the mass of the FSMA material. What remained unaffected, however, was the trends present in the dynamic strain results. In other words, the magnitude of dynamic strain was determined to be a function of the recovery force. So, between the range of 0 to 6.4 N preload, the dynamic strain appears to increase in magnitude. Although not observed in this set of tests, it can be asserted that for some level of preload beyond 6.4 N, the dynamic strain response should begin to decrease. This would indicate that the level of preload has reached a magnitude sufficiently large enough to introduce a

stress preferred bias in the material. In other words, the preload will eventually introduce a volume fraction of stress preferred twin variants that are mechanically restricted and unable to generate induced strain.

It was concluded that the magnitude of the dynamic strain was dependant upon the stiffness of the recovery spring, the magnitude of an applied preload or some combination of the two. This was expected because both factors influence the magnitude of the recover force. In general, it was determined that the dynamic strain response of the NiMnGa could be optimized for a given recovery spring by adjusting the applied preload.

4.1.2 Optimization of Dynamic Response

In section 4.1.1, it was determined that the magnitude of the absolute and dynamic strain components of the response was directly related to the level of preload acting on the FSMA specimen. Based on these results, it was proposed that components of the dynamic force generated by sinusoidal excitation fields would behave similarly. To test this assertion, stress-strain curves of the NiMnGa element for several excitation frequencies were generated and compared.

In the previous dynamic tests, limitations in the frequency response of the amplifier prevented low frequency testing. As a result, excitation frequencies below 18 Hz were not capable of being generated. To resolve this problem, a new amplifier was obtained. However, in this case, the new amplifier was limited to excitation frequencies below 10 Hz due to its lower power rating compared to the amplifier used in the previous tests. However, in each case, the peak excitation field was held

constant at 0.85 T so that the material response could be compared at any excitation frequency.

Stress-strain curves were generated for 1 Hz, 5 Hz, and 10 Hz excitation field. In Figure 4.4, results for 1 Hz (4.4(a)) and 10 Hz (4.4(b)) excitation fields are shown. The stress-strain curves yield a clear representation of the trends associated with the main components of the dynamic response of the FSMA element for a given frequency. Mean, dynamic and absolute components of the induced strain and force are all present and were readily determined from the stress-strain curves. For example, consider the case in which the NiMnGa was subjected to a 6.4 N preload. In Figure 4.4(a), the mean, dynamic and absolute components of the induced strain for 1 Hz excitation are denoted. Likewise, the components of the induced force for 10 Hz excitation could be determined from stress levels marked for the 6.4 N preload case shown in Figure 4.4(b).

Several clear trends can be identified from the data presented in Figure 4.4. Clearly, regardless of the excitation frequency, absolute and mean strain decrease as preload was increased while in contrast, absolute and mean force increase as preload was increased. Furthermore, the area enclosed by the stress-strain curve for a particular level of preload also appeared to be a function of preload. In other words, the magnitude work done by the FSMA element seemed to be directly related to the magnitude of recovery force. Judging by the data presented in Figures 4.4(a) and 4.4(b), the magnitude of work done by the NiMnGa increased from a minimum at 2.1 N preload to a maximum occurring at 6.4 N preload. Beyond the 6.4 N preload level the work began to decrease, indicating the onset of a permanent stress preferred bias

proposed in section 4.1.1. Clearly, for preloads above 6.4 N, the dynamic strain of the element began to decrease, which subsequently reduced the area bounded by the stress-strain curves. In terms of NiMnGa actuator design, this result indicates the importance of the recovery force on the actuator performance. In order to maximize the energy output of the actuator, it is necessary to determine the optimum recovery force.

There were a few limitations in the preliminary tests that must be addressed. First, subsequent dynamic tests revealed that a minimum of a 1.0 T peak inductive field was required to completely induce the magnetic shape memory effect along the entire specimen for the range of preloads tested. However, as mentioned previously, constraints in the support electronics, mainly the power amplifier, limited the peak value of the inductive field to 0.85 T. As a result, the most meaningful results from the preliminary testing were the trends in material behavior. Although, the magnitude of the response will undoubtedly change for different levels of magnetic excitation, the trends established in regards to the components of induced strain and force will remain the same. Second, because of the presence of a recovery spring, the magnitude of the recovery force was not held constant over the excitation field. Therefore, it was not possible to directly determine the effect of recovery force on material behavior. Changes in either the stiffness of the recovery spring or the level of preload directly impact the magnitude of recovery force acting on the FSMA element. Because it has been established that recovery force plays a major role in the dynamic performance of the material, it is necessary to determine exactly its effect on

the response of the material. Subsequent testing will include measuring the material response as a function of recovery force.

4.1.3 Frequency Doubling

Like magnetostrictive materials such as terfenol and galfenol, NiMnGa is insensitive to the polarity of the applied field. In the case of NiMnGa, the magnetic field has the effect of reorienting twin boundaries. The subsequent change in length is the same irrespective of the polarity of the applied field. Consequently, the induced strain is treated as having a quadratic dependence on the applied magnetic field. Furthermore, the quadratic relation between strain and applied field indicates that it is not possible to obtain a bipolar output strain with a bipolar magnetic excitation field. However, this quadratic relation does produce a frequency doubling effect. For AC excitation fields, both the positive and negative half cycles of the excitation field produce identical unidirectional pulse in the material. So, for a 1 Hz excitation field, the material response will be 2 Hz. Figure 4.5 shows the frequency doubling effect for a specimen of NiMnGa exposed to a 1 Hz excitation field. The amplitude of the sinusoidal excitation field was 1.2 T. For both the positive and negative half cycles of the excitation field, the material responded with a unidirectional, 5.2% strain pulse.

4.2 Non Quasi-Static Behavior

The conclusion of the preliminary dynamic testing showed that a more careful experimental approach was required. Before conclusions could be drawn in regards to the dynamic behavior of the NiMnGa material, non quasi-static excitation of the FSMA elements should be examined. Observation of non-quasistatic behaviors in

FSMA provides a bridge between static and dynamic behavior. One important non-quasistatic effect is strain rate. Determination of the effect of strain rate on the stress-strain response of NiMnGa provides insight into the response time of the material and effectively maps the material capabilities over the transition region between quasi-static and dynamic behaviors. Therefore, knowledge of the behavior of the NiMnGa material in this region allows for a seamless transition between the static and dynamic behaviors. In the following section, the effect of strain rate in NiMnGa is studied.

4.2.1 Strain Rate Testing Procedures

This set of tests involved studying the effect of strain rate on the stress-strain behavior of the NiMnGa material behavior. A series of experiments were conducted in which the NiMnGa specimen was subjected to a constant magnetic field and then mechanically cycled in compression at different strain rates. A constant applied magnetic field environment was created by regulating the level of current in the coils of the electromagnet. Initially, the NiMnGa specimen was induced into the field preferred configuration by applying a large, magnetic field at zero stress. Then, while the material was still exposed to the DC magnetic field, the specimen was mechanically cycled in compression at a specified strain rate. Stress and strain responses over the complete mechanical cycle were recorded. Strain rates ranging from 1220 $\mu\varepsilon$/sec to 61000 $\mu\varepsilon$/sec (0.02 mm/sec to 1.00 mm/sec) were tested. Once each strain rate was tested, the results were compared to determine the effects of strain rate on the stress-strain behavior of the material.

4.2.2 Effect of Strain Rate

Specimens of NiMnGa were exposed to a constant magnetic field of 8 kOe and then mechanically cycled from 0 to 11 MPa at varying levels of strain rate. The stress-strain response for each strain rate was recorded. The total stroke of the actuator for one cycle was 1.0 mm. Beginning at a rate of 1220 $\mu\varepsilon$/sec and then repeating the test in increments of 1220 $\mu\varepsilon$/sec (0.02 mm/sec) to a maximum strain rate of 61000 $\mu\varepsilon$/sec (1.0 mm/sec), the effect of strain rate on material behavior was observed. The 61000 $\mu\varepsilon$/sec rate is equivalent to actuation at 0.5 Hz. Figure 4.6 shows the results of this test for 2440, 9760, 39000, and 61000 $\mu\varepsilon$/sec.

Based on the results in Figure 4.6, each strain rate produces the same stress-strain curve indicating that strain rates below 0.5 Hz, have a small impact on material behavior. The difference in the data between each strain rate was less than 6.9%. For each strain rate, essentially the same stress-strain curve was generated. Critical transformation stresses and Young's modulus appear to be unaffected by strain rates below 0.5 Hz. Furthermore, hysteresis in the stress strain curve also appears similarly unaffected by strain rate. Qualitatively, these results suggest that the material has a fast response time. Given that the bandwidth of the material has been reported to be well in the kHz region [6], this result is not surprising. In fact, the response time of the material allows for the alloy to quickly respond to changes in the magnetic environment. The material is more than capable of responding to changes in its environment effectively providing a seamless transition from DC to AC behavior.

4.3 Controlled Dynamic Testing

Once the quasi-static and non quasi-static behaviors of NiMnGa have been established, the next stage of tests focused on the dynamic behavior of the FSMA. Preliminary testing (section 4.1) results indicated that the response of the NiMnGa specimens showed a pronounced dependence on the level of recovery force and magnetic field magnitude. In fact, the two primary limitations in the preliminary tests were derived from these two qualities. The inability to isolate and control the level of recovery force prevented drawing quantitative conclusions in regards to its influence on the material response. Furthermore, limitations in the magnetic drive circuit (specifically, power limits of the amplifier and EM coil combination) prevented adequate availability of magnetic field. The preliminary tests seemed to indicate that larger excitation field magnitudes were required.

This section presents research directed towards addressing the shortcomings of the preliminary dynamic tests. The aim of this next stage of dynamic testing was to characterize the dynamic response of NiMnGa to a variety of mechanical and magnetic loading conditions in a tightly controlled manner. Specifically, sets of constant recovery force, and constant strain tests were conducted in order to more accurately define the relationship between recovery force and the material response. The magnetic circuit and supporting electronics were reconfigured to accommodate larger dynamic fields. Larger magnetic fields ensured that the FSMA elements reached magnetic saturation thereby maximizing the response and leading to increased confidence in the data. Finally, the effect of DC bias fields on both constant force and constant strain tests was also studied.

4.3.1 Dynamic Testing Procedure

Constant preload and constant pre-strain tests were carried out on the tabletop, servo-hydraulic, axial material test machine obtained used in the quasi-static tests detailed in section 3.3.2. A photograph of the Dynamight test rig is shown in Figure 3.9. Load or position control for the test rig was handled by an on-board, programmable PID controller. For dynamic excitation of the material, it was necessary to tune the load cell to the stiffness of the NiMnGa element. As a safeguard during the tuning process, a simple compression spring of matched stiffness to the NiMnGa was substituted for the actual element. In this way, NiMnGa specimens were protected from catastrophic failures incurred as a result of PID tuning errors. A Ziegler-Nichols tuning method was used to tune the controller according to the stiffness of the specimen. A set of gains was determined for each excitation frequency. Power to the coils was provided by computer controlled output module routed through a LVC623 AE Techron Inc, current amplifier. Connected to a single channel, the amplifier was capable of continuously supplying 145 W with a maximum drive current of 4 amps delivered to the electromagnetic coils.

The constant preload tests were carried out in the following manner. First, the specimen was mechanically loaded to compress the specimen fully into the stress preferred configuration in a zero applied field environment. After the load was removed, a specified axial pre-stress was applied to the NiMnGa. Pre-stresses ranging from 0.33 MPa to 1.5 MPa were investigated. A minimum of 0.33 MPa was required in order to keep the specimen from slipping out of the grips as a result of the magnetic field. Pre-stresses beyond 1.5 MPa were not tested because the PID

controller was unable to handle the change in material stiffness associated with pre-stresses beyond this level. After the preload was applied, the material was exposed to an AC magnetic field on the order of 1.2 T in magnitude while the magnitude of axial stress was held constant. Excitation frequencies of 1, 2 and 5 Hz were tested. However, the results from the 5Hz tests were ultimately discarded due to the inability of the servo-valve to adequately respond to the level of material stroke at this frequency. Several quantities were measured including, axial force, displacement, magnetic field, coil current, and coil voltage. This test was repeated for each combination of excitation frequency and preload.

The second category of dynamic tests was focused on measuring the force response of the material as a result of a constant pre-strain. Initially, the specimen was subjected to a 1.4 T magnetic field at zero stress, to convert the specimen into the field preferred condition. Then, after the field was removed, a compressive load was applied until the desired level of pre-strain was reached and was held constant throughout the entire test. Pre-strains ranging from 1% to 5% were examined. Once the pre-strain was introduced, the material was exposed to an AC magnetic field on the order of 1.2 T in magnitude and the force response was recorded.

To study the effect of bias fields on both categories of testing, the above procedures were repeated with a simultaneous application of an AC and DC magnetic field. This field was generated by the output module of the data acquisition system and consisted of a small, sinusoidal excitation superimposed on a DC voltage. The signal was then passed on through the LVC623 amplifier and the electromagnetic

coil. Data acquisition and excitation signal generation were handled by a LABVIEW script.

4.3.2 Constant Load Tests

The first category of dynamic tests focused on the strain response of the FSMA while acting under the influence of a constant, axial pre-stress. NiMnGa specimens were subjected to axial, compressive pre-stresses ranging from 0.33 MPa to 1.5 MPa for excitation frequencies of 1, 2, and 5 Hz. The axial stress field acting on the specimen was held constant throughout the magnetic excitation cycle using the test rig's programmable PID controller. Figure 4.7 shows the results of this test for the case of 1 Hz and 2 Hz excitation.

For both excitation frequencies, the magnitude of the induced strain appeared to be a strong function of the applied stress. The minimum induced strain occurred at the 0.33 MPa level for both excitation frequencies. The magnitude of strain for this case was approximately 0.5% and 0.8% for 1 Hz and 2 Hz excitation respectively. As the pre-stress was increased, the magnitude of the dynamic strain was also increased. The maximum induced strain of 5.5% at 1 Hz excitation and 5.2% at 2 Hz excitation occurred at 1.5 MPa of pre-stress. Furthermore, the data suggests nonlinear relationship between peak strain and stress. For each test, the constant pre-stress was increased in increments of 0.17 MPa. Each incremental increase in stress did not yield a constant increase in the subsequent peak strain. In fact, Figure 4.7(a) shows that for the same increase in constant stress, the change in the magnitude of peak strain was closely spaced for both low and high levels of stress ($\sigma < 0.67$ MPa & $\sigma >$ 1.17 MPa) and widely spaced for intermediate levels of stress (0.67 MPa $> \sigma >$ 1.17

MPa). This effect appeared to be most pronounced in the 1 Hz excitation case (Figure 4.7(a)).

The maximum stroke of the material during this test was 1 mm. At a 5 Hz excitation frequency, this level of stroke exceeded the capabilities of the test rig's servo-valve which led to a 'clipping' of the strain response. As a result, strain data from the 5 Hz test was discarded. Although this choice limited the scope of conclusions drawn regarding dynamic test results, the frequencies tested were sufficient to highlight the underlying physics of dynamic FSMA actuation. One effect that was expected but not observed was that beyond a certain magnitude of constant pre-stress, the level peak strain should begin to decrease. Preliminary dynamic testing (section 4.1) showed that the energy output of the material could be optimized by adjusting the preload. Both high and low preloads produced lower levels of work output. Therefore, in regards to the constant load tests, it was expected to see the strain response increase with applied load, reach a peak level and then decrease as the level of force continued to rise. Although the data presented suggests that the peak strain had reached its maximum value at or near 1.5 MPa, no decrease in peak strain was observed. Unfortunately, it was not possible to test the NiMnGa elements beyond 1.5 MPa for this set of experiments. The embedded, test rig PID controller was tuned to the stiffness attributed to the twin boundary motion of the material. Quasi-static tests (section 3.5, 3.6) showed that as the twin boundaries become mobile, the stiffness of the material was significantly reduced. However, once the material was converted to the stress preferred condition, the stiffness of the material sharply increased. For stress levels beyond 1.5 MPa, the material became

initially biased to the higher stiffness region which meant that the material would experience large shifts in stiffness over each excitation cycle. The PID controller could not be programmed to handle this abrupt change in material stiffness and as a result, high levels of 'ringing' were detected which led to large, uncontrollable overshoots as the test rig tried to compensate and in one instance catastrophic failure of the material specimen.

Constant stress testing was essential for developing an understanding the relationship between recovery force and induced strain. As mentioned previously, in order to produce a dynamic strain, the presence of a recovery force is required. During a magnetic excitation cycle, as the field was reduced to zero from the positive half cycle, the recovery force begins to dominate, and as a result, induces a reverse transition, effectively reconfiguring the specimen from the field preferred to stress preferred state. The effect of recovery force was to reset the material for another pulse occurring during the negative half-cycle. Without a recovery force, field preferred variants are not reoriented during the excitation cycle; therefore the NiMnGa cannot produce dynamic stain. In fact, in the absence of a recovery force, a FSMA element initially in the stress preferred configuration will only pulse once during dynamic excitation. In this case, provided that the level of field is sufficient, the material will respond to the first half cycle of the excitation by achieving its free strain value and then become effectively inert over the next and subsequent half cycles. Furthermore, in order to achieve the maximum peak strain, the restoring force must be optimized for the NiMnGa specimen. Small amounts of recovery force produce small amounts of dynamic strain and likewise large amount of recovery force produce small amounts

of strain. The maximum dynamic strain occurs for some level of force in between these two extremes.

4.3.3 Constant Strain Tests

The second type of dynamic testing involved observing the effect of constant pre-strain on the force response of the NiMnGa. Pre-strains ranging from 1% to 5% in increments of 1% strain were tested. While the level of strain was kept constant throughout the magnetic cycle, the NiMnGa bar was exposed to an AC magnetic field 1.2 T in magnitude and the force response was measured. Excitation frequencies of 1Hz, 5 Hz, 10 Hz were tested. Figure 4.8 shows the result of the 1 Hz test.

The main effect of introducing pre-strain in the NiMnGa specimen was to raise the mean level of force generated as a result of the magnetic field. In the case of 1% pre-strain, the mean force was approximately 10.3 N while in the case of 5% pre-strain, the mean force was observed to be approximately 18.1 N. Pre-strain incurs a global bias toward stress preferred twins in the bulk material. Since the strain in the bulk specimen is kept constant, these twins are blocked and therefore produce a force in response to magnetic excitation. When exposed to a magnetic field, these stress preferred twins act as local force generators as they attempt to align themselves in the field direction. Each of these stress preferred twins contribute to a global net force generated by the FSMA. Larger levels of pre-strain increase the number of stress preferred twins available for force generation. As a result, an increase in the mean force for increasing levels of pre-strain is expected.

Figure 4.9 shows the effect of pre-strain on the amplitude of the force response in NiMnGa. Although the mean force generated by the specimen increases

with pre-strain the amplitude of the dynamic force response decreases with additional pre-strain. For 3% pre-strain, the amplitude of the response was approximately 18-19 N while the amplitude of the 5% case was reduced to 14-15 N. This result can also be explained by considering the behavior of the material on the unit cell level. As pre-strain was increased, the internal stress acting on each unit cell in response to the magnetic excitation was also increased. As the AC field was applied to the specimen, the internal stresses acting on the unit cell become large enough to overcome the effect of the magnetocrystalline anisotropy. For these unit cells, the axis of magnetization effectively became mobile, freely rotating to align with the direction of the applied magnetic field. Consequently, no magnetic pressure developed on the unit cell. As a result, these twins become temporarily unavailable for force generation, which in turn reduced the amplitude of the force response. Although not experimentally observed, it was expected that for some value of constant pre-strain, the amplitude of the force response will be reduced to zero, indicating that the internal stresses acting on the unit cells of the entire specimen are great enough to completely overcome the magnetocrystalline anisotropy. In this case, the entire specimen would be unavailable for force generation.

Based on these results, it did not appear that the excitation frequencies tested in this experiment had a measurable effect on material behavior. However, given that the bandwidth of the material has been reported to be well into the kHz range [6], the bandwidth studied in this study was too narrow to draw meaningful conclusions regarding the effect of excitation frequency on material behavior.

4.3.4 Effect of Bias Fields

One important quality of the NiMnGa response to a dynamic field is that the material yields a unidirectional output regardless of the polarity of the excitation field. The phenomenon is explained in detail in section 4.1.3. This quality is important in terms of actuator design because it means that it is not possible to design a bidirectional actuator with a simple AC field. In order to obtain a bidirectional response, it is necessary to utilize a DC bias field.

A set of tests was carried out to study the effect of a bias field on the dynamic response of NiMnGa for constant load and strain conditions. For each case, the element was exposed to a 1 Hz, 1.0 Tesla peak AC magnetic field superimposed on a DC field ranging from 0 to 8 kOe. The main goal of this set of tests was to determine qualitatively the effect of the bias field on the material behavior.

Consider the case of constant load testing. Figure 4.10 shows the effect of bias fields on a 6.5 N (1.08 MPa), constant load test. The peak strain from the 0 kOe bias was approximately 5.2%. As the bias field was increased from 0 kOe to 2 kOe, the peak strain on the negative side of the excitation field dropped from 5.2% to 4.5%, while the peak strain on the right hand side remains at 5.2%. This trend continues when the field was increased to 4 kOe. In that case, the left hand peak strain dropped to 1.5%. For an 8 kOe bias field the polarity of the field never changes and the dynamic strain oscillates between 0 and 5.2%. At this point, the material pulsed only once per cycle indicating that the frequency doubling property of the material had been removed. Furthermore, the bias field did not appear to have any effect on the hysteresis of the response.

Figure 4.11 shows the effect of bias fields on the constant strain tests. The effect of the bias field very closely followed the same trends observed in the constant load tests. A FSMA element was given a 3% pre-strain and then dynamically excited with a 1 Tesla, AC field superimposed on a varying level of DC bias field. The peak load on the positive side of the excitation field was 18.1 N for the 0 kOe bias field. As the bias field was increased from 0 kOe to -2 kOe, the right hand peak value decreased to 14.4 N. Likewise, when the bias field was increased from -2 kOe to -4 kOe, -4 kOe to -6 kOe, and then from -6 kOe to -8 kOe, the right had peak dropped to 10.4 N, 5.4 N and 0 N respectively. It was noticed that for the -8 kOe bias field, the material response between -0.25 T and -0.85 T was linear.

There are several advantages to using bias fields. First, they enable the material to be used for bi-directional actuation. Consider the results in Figure 4.10. By introducing a 0.6 T bias field and a 0.6 T peak dynamic field, the material response will yield approximately 5.2% strain centered about the bias field effectively providing 2.5% magnitude of bi-directional strain. Furthermore, the AC field requirement has been significantly reduced from 1.0 T to 0.6 T. This means that a smaller coil, which in turn translates into a smaller inductance, is required for producing the dynamic field. Since the inductance is a frequency dependant component of the circuit's electrical impedance, a reduction in the inductance reduces the impedance at higher frequencies. As a consequence, the power required to drive that coil, especially at high frequencies, is reduced when compared to the case where a bias field is not used. This notion is very important in applications where power and actuator volume are premium. Furthermore, if permanent magnets are used to

generate the bias field, the DC excitation voltage can be removed which eliminates the DC drive current in the magnetic circuit, subsequently providing another significant reduction in required power. However, introduction of permanent magnets into the system is not a trivial matter, requiring an extensive magnetic FEM analysis to determine their optimum location within the magnetic circuit. Although introducing permanent magnets into the system increases the complexity of the magnetic circuit, it represents a possible solution for generating a bias field.

4.4 NiMnGa Performance Characteristics

One of the main issues determined from the dynamic testing results was the effect of recovery force on material behavior. Once the dynamic behavior of the FSMA was determined, the performance characteristics of the material were evaluated. Since it was observed that the strain response of NiMnGa specimens was largely dependent on the recovery force acting in opposition to the material actuation, it must be assumed that the performance of the material is also similarly affected. In this section, performance characteristics of the material were studied. Qualities such as damping, energy density, power density, total power output and electromechanical efficiency were investigated and addressed. The effect of recovery force on these performance characteristics was also determined.

4.4.1 NiMnGa Damping Properties

Quasi-static testing (section 3.5) showed that a large level of hysteresis occurred during the mechanical cycling of NiMnGa specimens exposed to a magnetic field controlled by a constant drive current coil. The area of the enclosed loop on the

stress-strain curve represents the energy loss during one mechanical cycle of the material. Consequently, measurement of this energy loss provides insight into the damping capabilities of the NiMnGa alloy. This is especially important for dynamic actuation because the energy loss per cycle is a key component to the required power of the material. Furthermore, it provides a lower bound to the power required for actuation. To measure the energy dissipation, a series of constant applied field, quasi-static loading tests were conducted. In each instance, the area enclosed by the stress-stain curve for each set of mechanical cycling at a constant applied field was calculated using a simple trapezoid rule, numerical integration technique.

Measurement of the damping characteristics of the FSMA material was carried out in a manner similar to that described in the strain rate tests. First the specimen was induced to its field preferred configuration by applying a large magnetic field at zero stress. Then the applied magnetic field was set to a specified level and held constant throughout the remainder of the test. The effects of applied fields ranging from 0 to 9.5 kOe were observed. After the level of DC magnetic field was introduced, the specimen was mechanically cycled in compression between 0 and 11 MPa. This compression was quasi-static in nature and occurred at a strain rate of 0.02 mm/sec. Over the course of the mechanical cycle, several quantities were measured including axial load, displacement, magnetic field, and coil current.

Figure 4.12 depicts an example data set for the case of a quasi-static, mechanical cycle at a constant applied field of 7 kOe. Once the area enclosed by the stress-strain curve was determined, the result represented one point on the plot shown in Figure 4.13. In Figure 4.13 the effect of applied field on the volumetric energy

dissipation of the NiMnGa specimens over the entire range of fields tested is shown. The magnitude of energy dissipation, or damping, for the quasi-static condition appears to be a function of the recovery stress for fields below 4 kOe. For applied fields below 4 kOe, the energy dissipation appeared to be linearly related to the applied field. However, for applied fields 4 kOe or greater the energy dissipation becomes effectively constant. Previous research showed that the NiMnGa exhibited a magnetic pseudoelastic behavior for applied fields greater than 3.5 kOe [224, 225]. Therefore it was concluded that NiMnGa specimens exhibiting a magnetic pseudoelastic strain recovery behavior effectively have the same level of material damping independent of the applied field. The maximum volumetric energy dissipation, occurring in the magnetic pseudoelastic region, appeared to be between 75-80 kJ/m^3. Given the relatively small volume of the material, this meant that the FSMA specimen was dissipating approximately 7.4-7.9 mJ of energy per cycle. Furthermore, these results are repeatable as shown by the close correlation between the two data sets illustrated in Figure 4.13.

4.4.2 Energy and Power Density Measurements

One of the main aims of the current research was to determine the power density of NiMnGa because it is a useful metric for assessing the performance of an actuator material. A quantitative determination of power density will enable the NiMnGa alloy to be compared and evaluated with other active materials. In the following section, the power density of NiMnGa and the major factors that influence its behavior are determined.

From the series of constant load tests, section 4.3.2, the energy density of the NiMnGa elements for dynamic magnetic excitation was determined. The volumetric energy density was calculated according to the following equation,

$$\rho_E^v = \sigma_a \varepsilon_{peak} \tag{1}$$

where σ_a is the actual recovery stress applied to the specimen and ε_{peak} represents the peak value of strain. It is important to note that this equation yields results that are normalized with respect to the volume of the material. Until the magnetic circuit has been properly optimized, its volume was considered separate from that of the material itself. However, when NiMnGa-based actuators are compared to other active materials, the volume of the magnetic circuit should be included to provide the most accurate picture of the actuator performance. In chapter 6, the effects of the magnetic circuit on the performance of the actuator will be considered.

Figure 4.14 shows the energy density of the NiMnGa as a function of the applied, constant preload. Two excitation frequencies, 1 Hz and 2 Hz are shown. The range of constant stress tested was between 0.33 MPa and 1.5 MPa. Generally, the magnitude of the energy density appears to be a strong function of the applied stress. The energy density sharply increases after 0.667 MPa reaching a maximum value of approximately 8000 kJ/m^3 at 1.5 MPa. In fact, since the energy density and the peak strain only differ by a constant, both have the same characteristic shape and both are functions of the recovery stress. One effect that was not determined, but predicted from the preliminary tests, was a stress-induced decrease in the energy density beyond an optimum recovery stress. At some value of recovery stress beyond 1.5 MPa, the twin boundary motion should begin to become mechanically constrained

thereby reducing the magnitude of peak strain and subsequently reducing the magnitude of the energy density. Further testing beyond 1.5 MPa is required to determine this optimum.

Properties such as the volumetric power density and total power output of the NiMnGa were also calculated from the data obtained by the dynamic constant pre-stress experiments. To determine power density, the following equation was used,

$$Q^v = \sigma_a \varepsilon_{peak} f_{ex} \tag{2}$$

or,

$$Q^v = \rho_E^v f_{ex} \tag{3}$$

where f_{ex} represents the excitation frequency in Hz. Just as in the calculation of energy density, the effect of the coil volume was not included at this time. The volume of the field generator and its effect on the actuator performance will be included in chapter 6.

In Figure 4.15 (a) and 4.15 (b), the effect of stress on the volumetric power density and total power output is shown. The peak power output for one excitation cycle was determined to be 3 W for a constant recovery stress of 1.5 MPa and 2 Hz excitation frequency. Both the power density and the power output showed a pronounced dependence on the applied stress and excitation frequency. Since power density is usually a linear function of excitation frequency, a strong dependence on excitation frequency was expected. However, a dependence of power density on applied stress clearly shows the importance of recovery force on material performance. Therefore, as the stress approached zero, the power density and power output also tend toward zero. Consequently, maximum values of power density and power output occur at a stress level of 1.5 MPa at 2 Hz excitation frequency. As

stated previously, this behavior was expected and is the result of the necessity of a recovery force for dynamic actuation. Since the constant stress acts as the restoring force, its removal will completely eliminate dynamic actuation of the FSMA. It has also been shown that the peak strain capability of NiMnGa is reduced at high levels of stress [7]. Although not observed in the data presented here, higher levels of stress should negatively impact the magnitude of both the volumetric power density and the power output.

4.4.3 Electromechanical Efficiency

Electromechanical efficiency is a key parameter of consideration for the design of actuators, motors and other mechanical or electrical devices. It provides a measure of the energy conversion capability of the device and is frequently used as a general measure of performance. However, estimation of the electromechanical efficiency of the NiMnGa material itself was not a straightforward task. The reason for this difficulty originates from the materials dependence on a field generating device for actuation. One of the main issues related to FSMA actuator design involves the necessity of optimizing the magnetic field generator. To generate the required level of magnetic fields for this study, a large, power consuming electromagnet was utilized. Since the laboratory electromagnet was designed to accommodate a wide range of NiMnGa specimens, an optimization procedure was not implemented, but instead a 'brute force' approach involving a maximization of coil turns and input current was utilized. As a result, the power required to generate the 1.2 T magnetic fields was enormous. However, the power requirements could be reduced if the magnetic circuit were optimized for required power with respect to a

specific specimen geometry. Until an optimization procedure is performed on the driving electromagnetic circuit, an estimation of the electromechanical efficiency that provide a meaningful comparison to other active materials can not be quantified. This topic will be revisited however, in chapter 6 where NiMnGa actuator design is discussed. At this stage, optimized coil-material systems are presented and compared to other smart material systems.

Despite these limitations, a few, qualitative assumptions regarding the electromechanical efficiency and performance of the coupled field generator-NiMnGa system can be made. First, for NiMnGa based actuators employing a coil for field generation, it can be reasonably assumed that the power density, including the volume of the field generator, will be several orders of magnitude less than what was presented in section 4.4.2. The main reason for this assumption is based on the fact that the weight of the flux return (typically iron or steel) and coils will dominate the total weight of the system. Also, coil based systems typically require large amounts of current to generate the required fields. Especially for dynamic excitation, the ohmic power losses alone will be quite significant due to the quadratic dependence on the magnitude of current. Impedance also becomes an issue because as the excitation frequency increases, the effect of the inductance begins to dominate which further increases the ohmic power losses. Furthermore, other frequency dependent power losses such as the effect of eddy currents contribute to additional power requirements. Some of these effects can be reduced by using permanent magnets to reduce the level of AC field requirement or utilizing laminated flux return structures to minimize eddy current losses. However, since the required magnitude of magnetic field required for

actuation is very large, the effect of these power-saving measures is limited. In section 4.4.2, the power density of the material was determined. For the 2 Hz case, a maximum power output of 3 W was measured. The required power in this case was 40 W which indicates an electromechanical efficiency of 7.5%. Due to the frequency dependence of the required power, however, it can be assumed that this efficiency will be reduced at higher excitation frequencies. In general, it can be assumed that NiMnGa actuators will be low-efficiency devices.

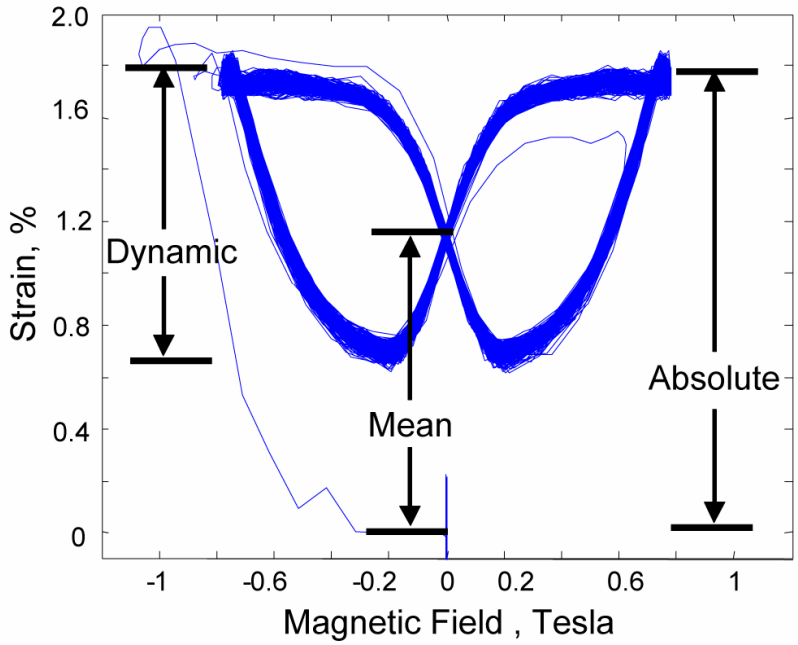

a) Components of induced strain, 20 Hz excitation, 0.85 T peak field

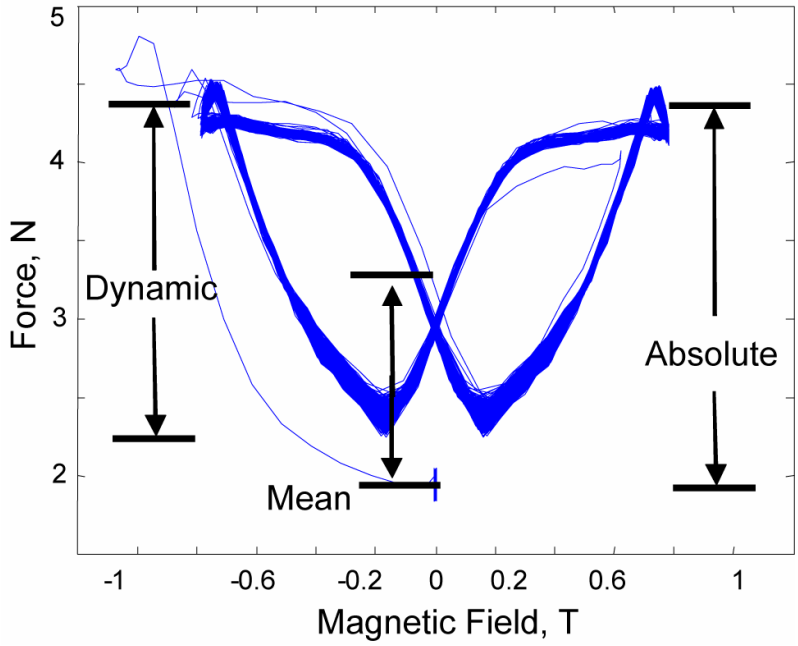

b) Components of induced force, 20 Hz excitation, 0.85 T peak field

Figure 4.1 Typical dynamic strain and force response for NiMnGa

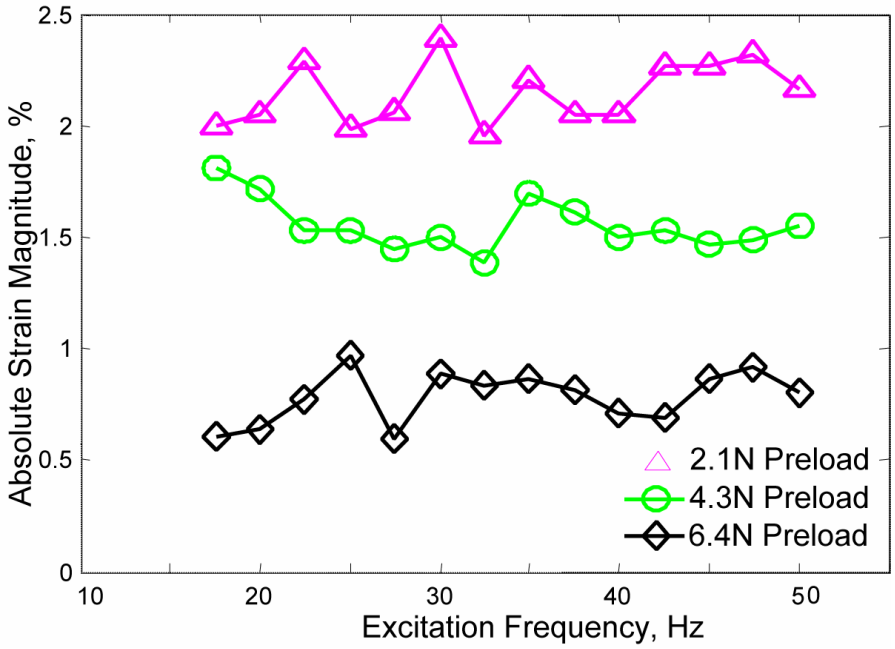

Figure 4.2 NiMnGa strain magnitude, 0.85 T magnetic field

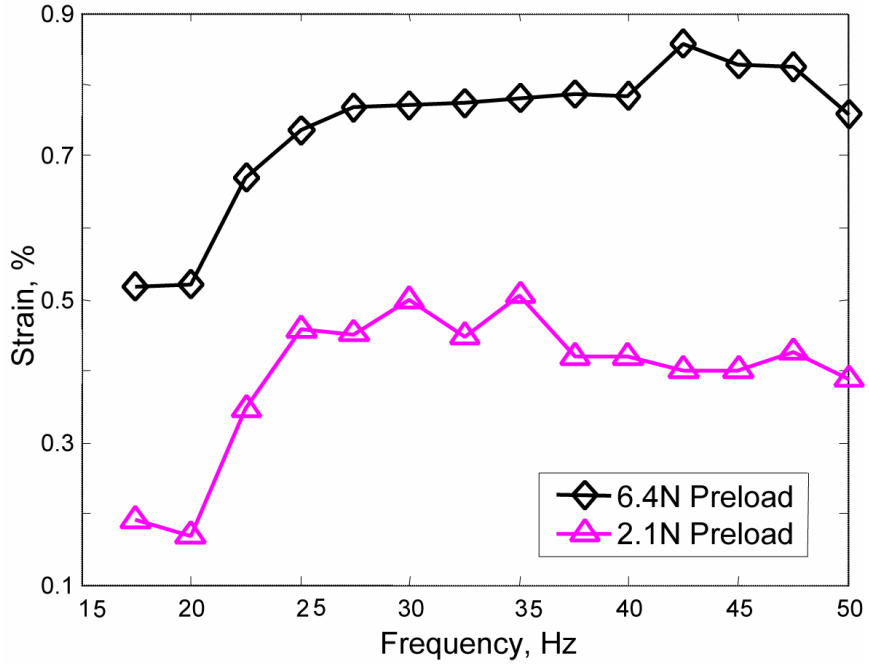

Figure 4.3 NiMnGa dynamic strain, 0.85 T magnetic field

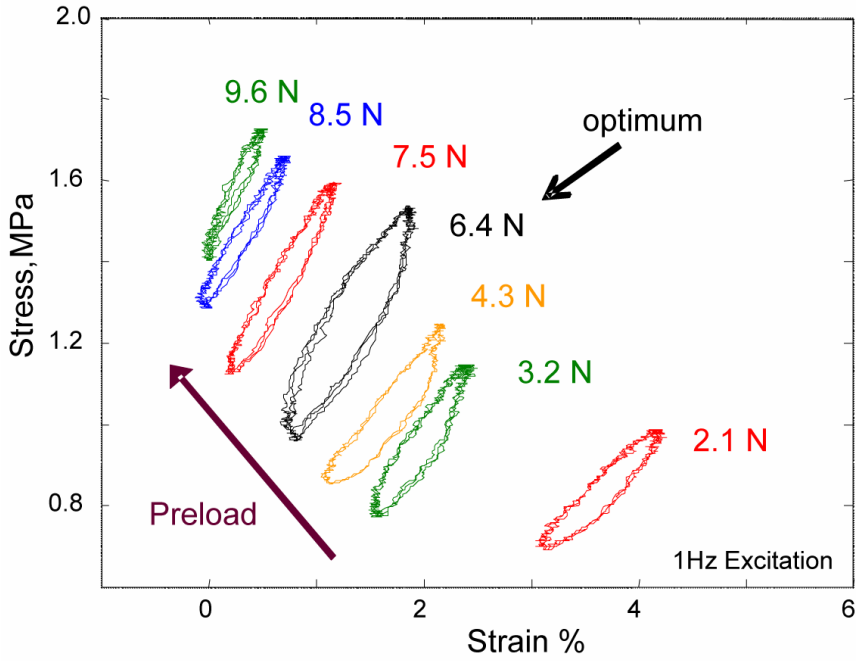

a) 1 Hz excitation, 0.85 T peak magnetic field

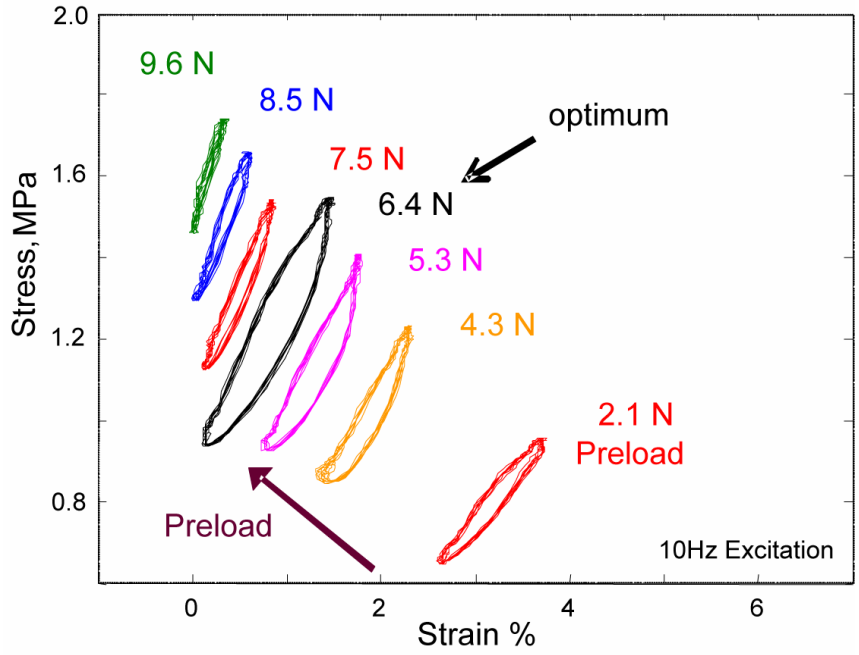

b) 10 Hz excitation, 0.85 T peak magnetic field

Figure 4.4 Effect of preload on dynamic stress-strain curves for NiMnGa

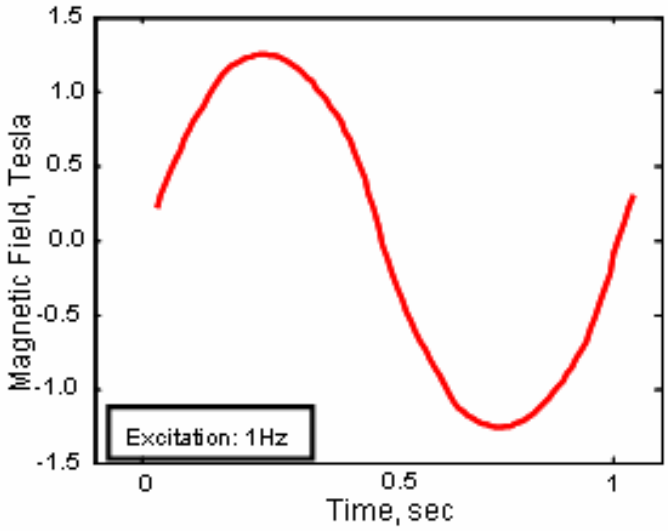

a) Sinusoidal magnetic excitation, 1.2 Tesla peak field

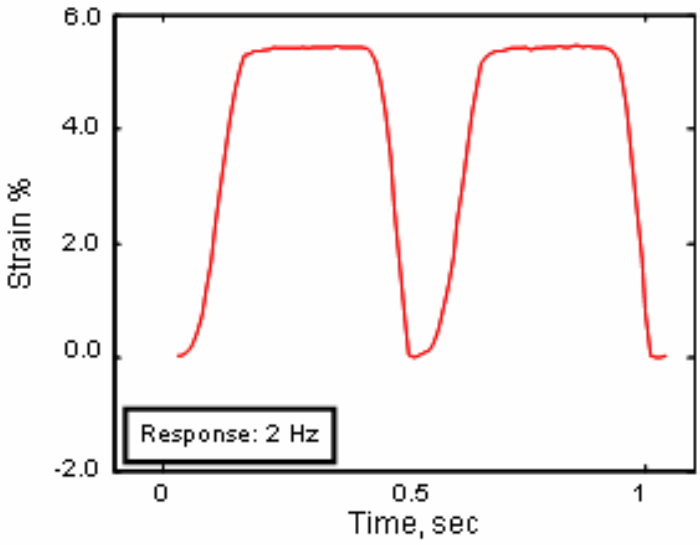

b) NiMnGa strain response

Figure 4.5 Frequency doubling effect in NiMnGa

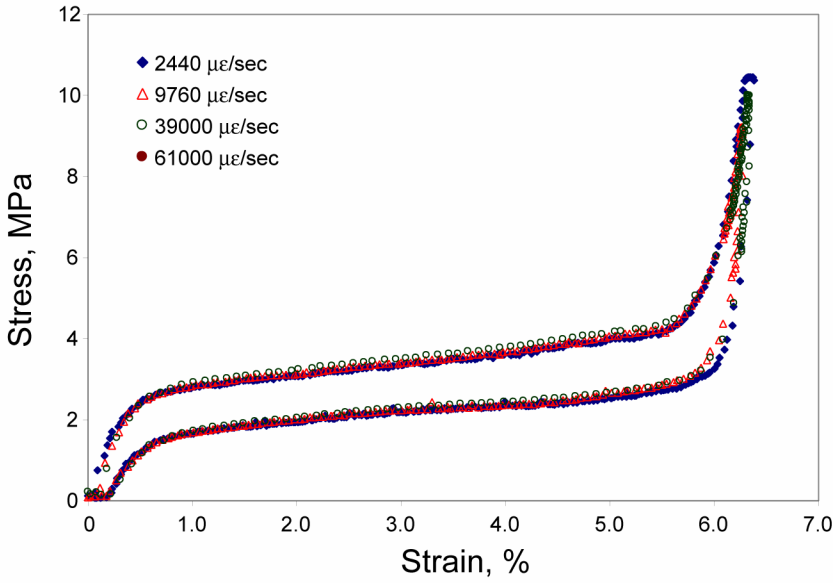

Figure 4.6 Effect of strain rate on NiMnGa stress-strain behavior

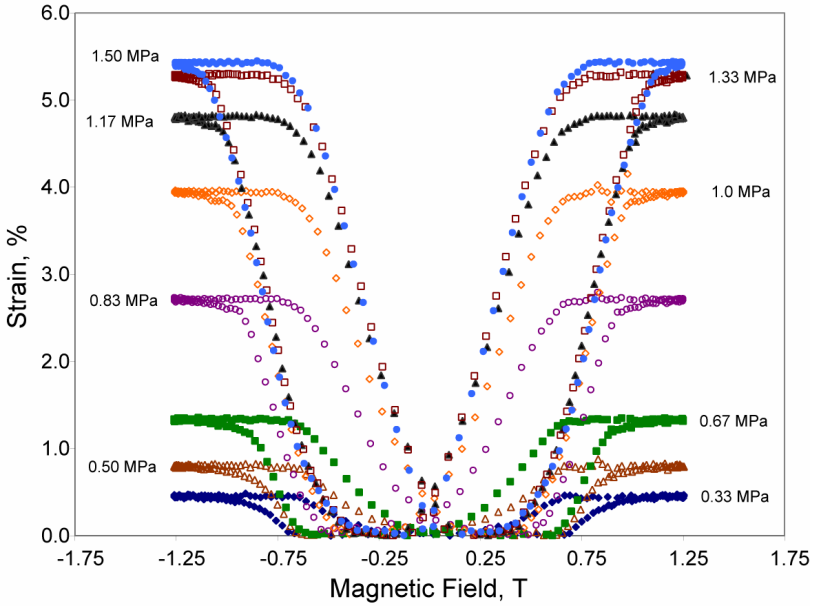

a) 1 Hz excitation

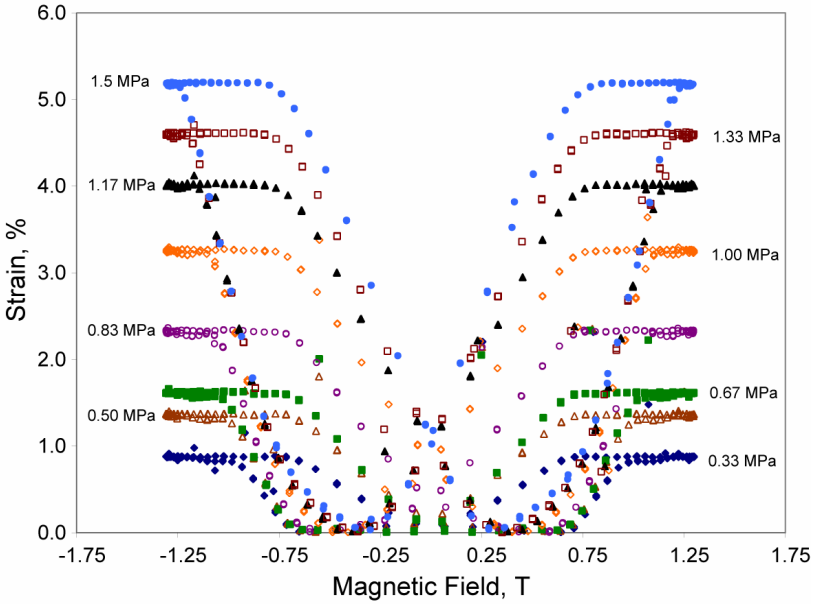

b) 2 Hz excitation

Figure 4.7 Effect of constant recovery stress on NiMnGa dynamic strain response

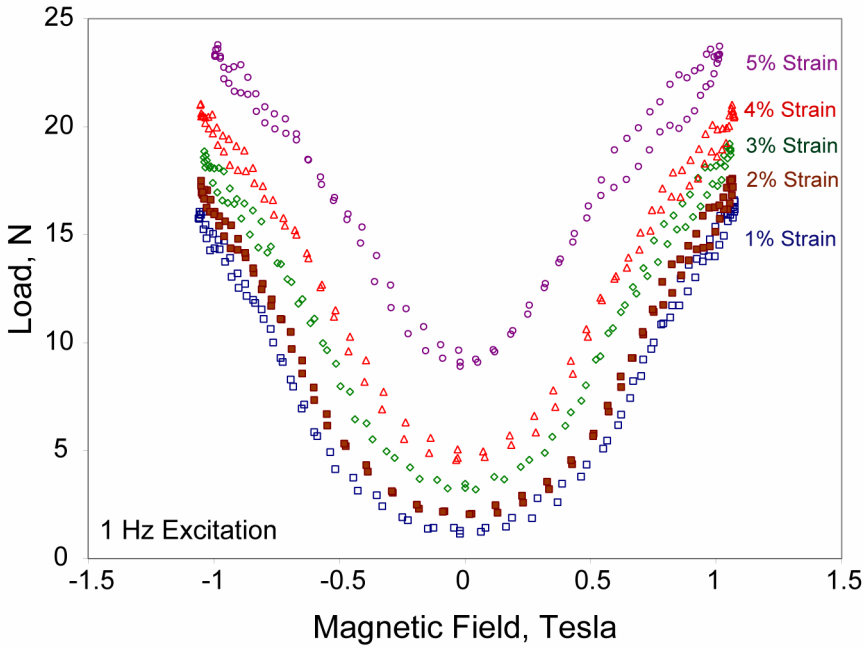

Figure 4.8 Effect of constant pre-strain on NiMnGa force response

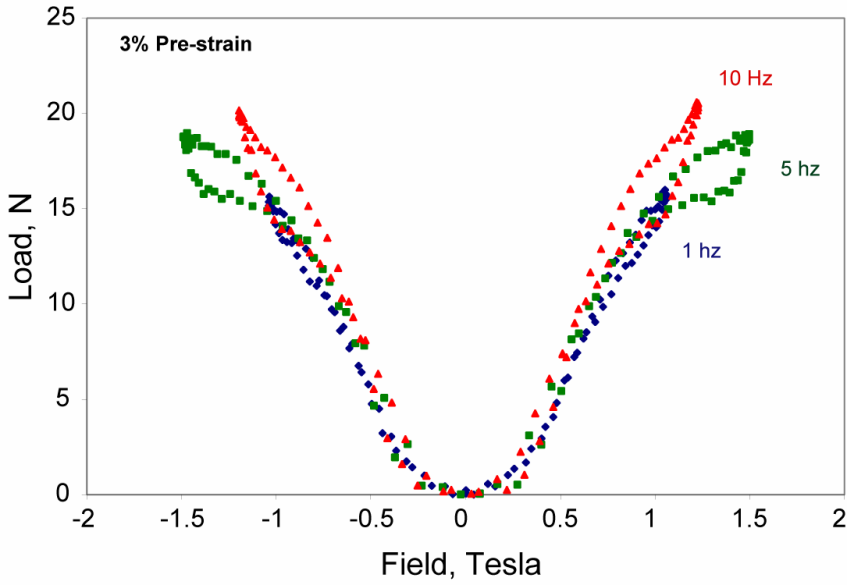

a) Force response: 3% Pre-strain

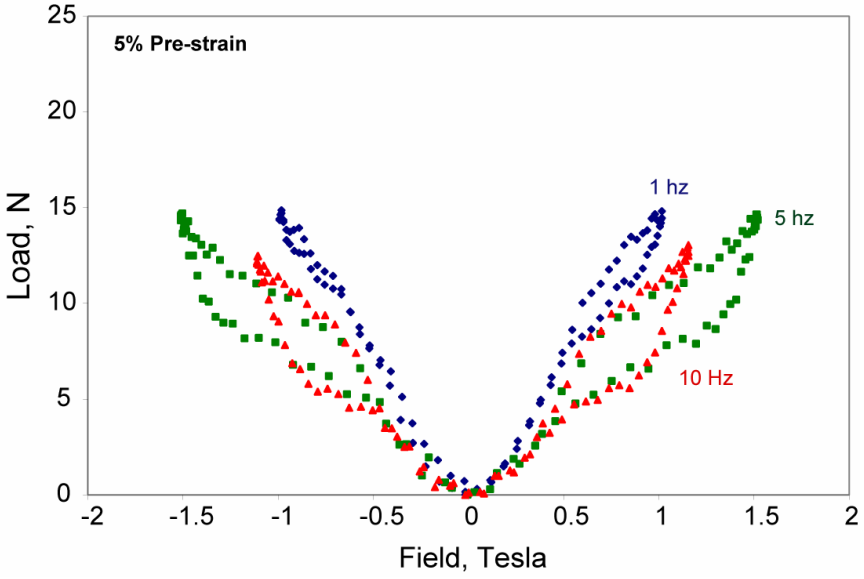

b) Force response: 5% pre-strain

Figure 4.9 Effect of pre-strain on the amplitude of force response

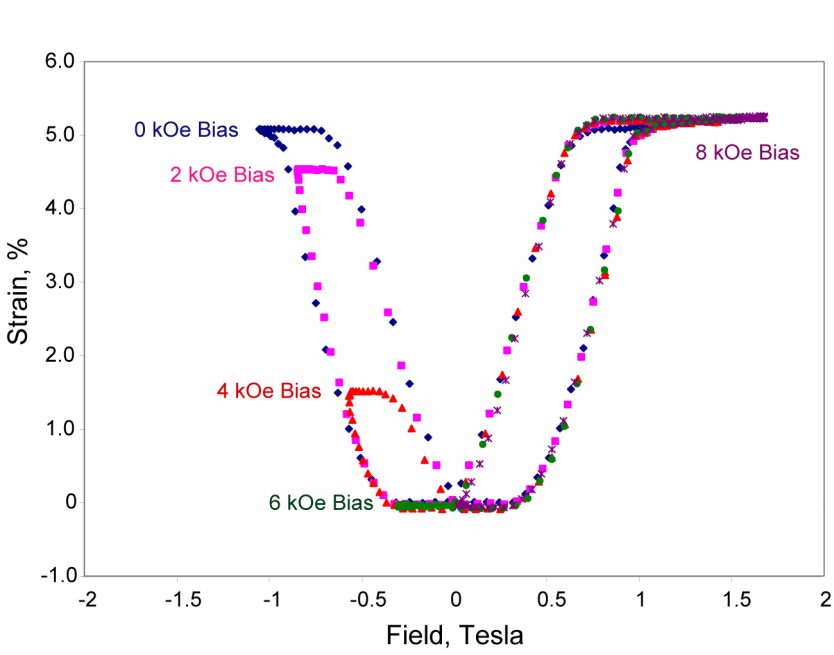

Figure 4.10 Effect of bias field on NiMnGa strain response, 1 Hz excitation and 1.1 MPa constant recovery stress

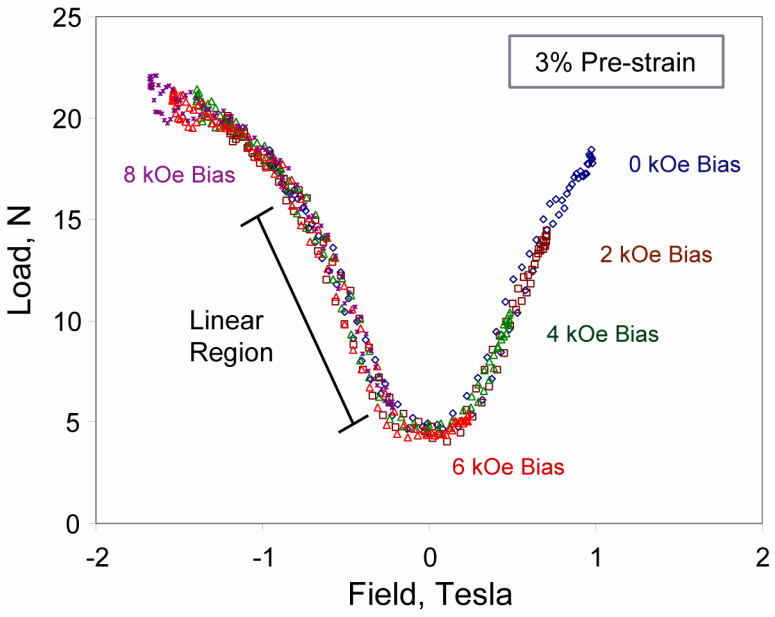

Figure 4.11 Effect of bias field on force response, 1 Hz excitation

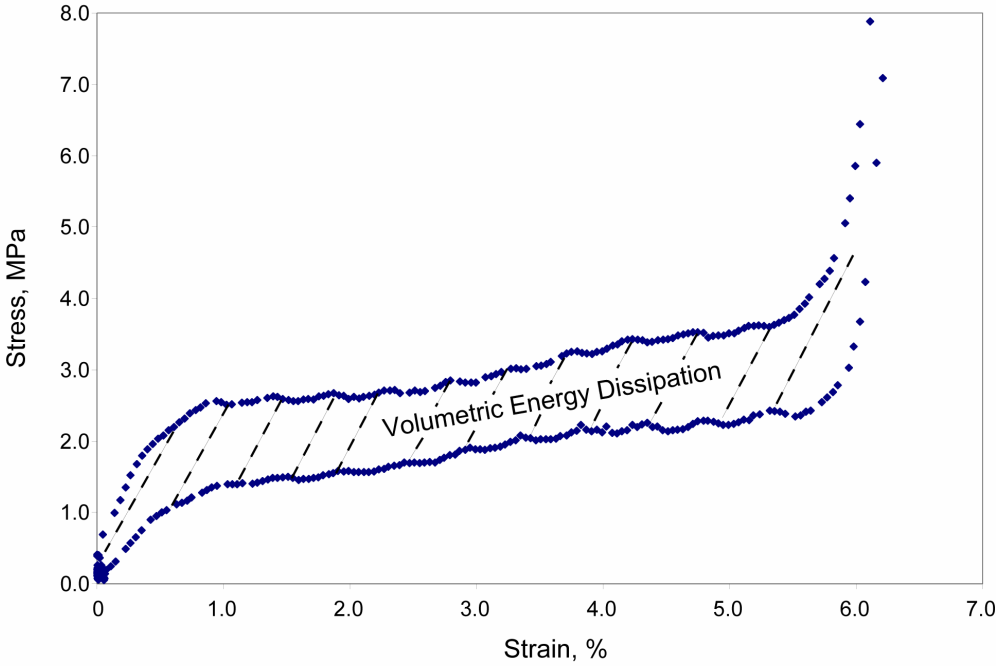

Figure 4.12 Volumetric energy dissipation for quasi-static mechanical cycling in a 7 kOe constant applied field

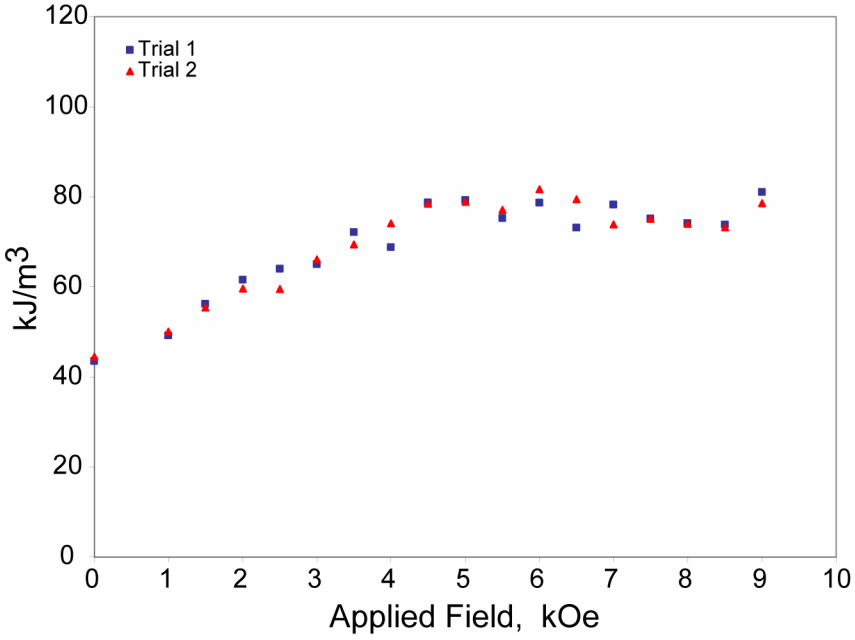

Figure 4.13 Effect of applied magnetic field on volumetric energy dissipation of NiMnGa

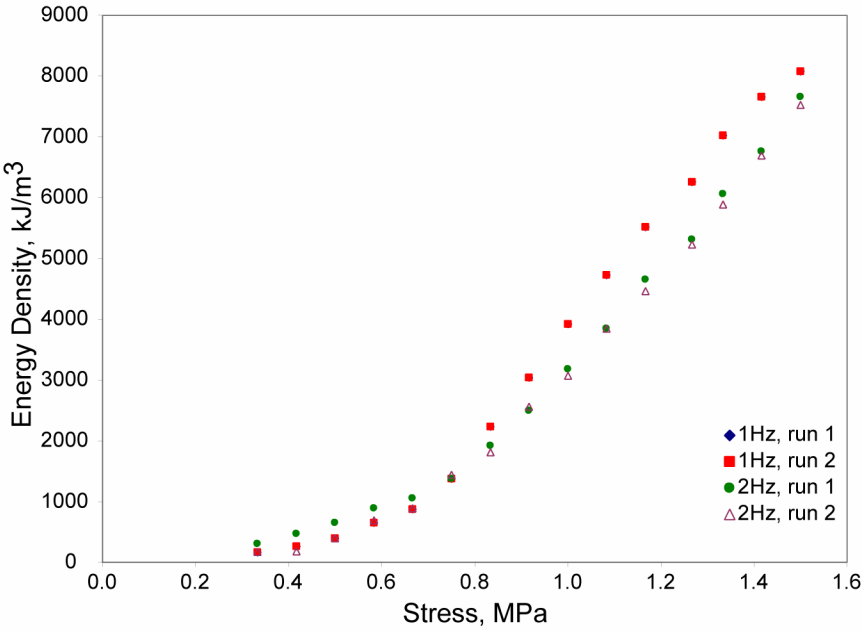

Figure 4.14 Volumetric energy density of NiMnGa

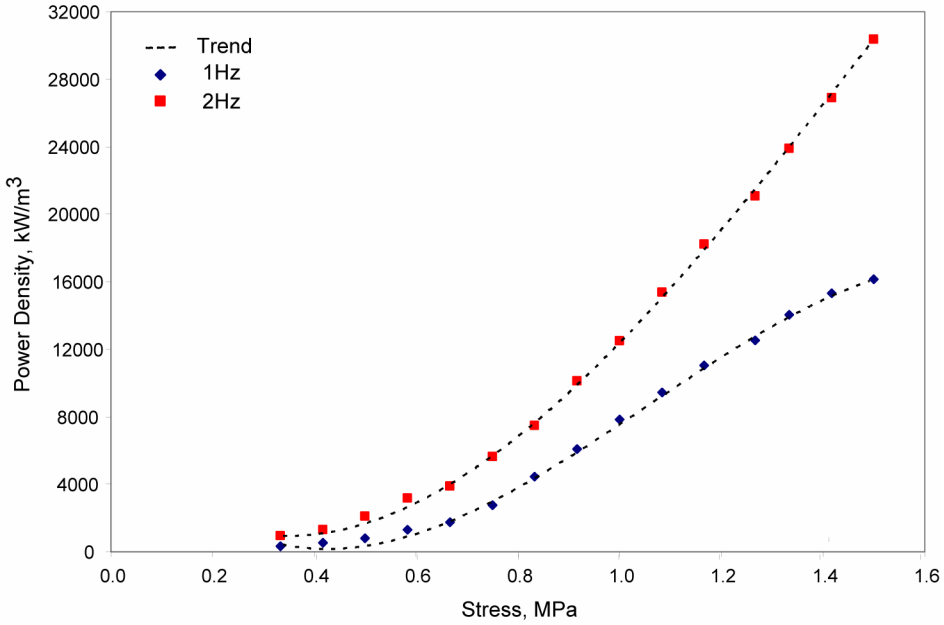

a) Volumetric power density

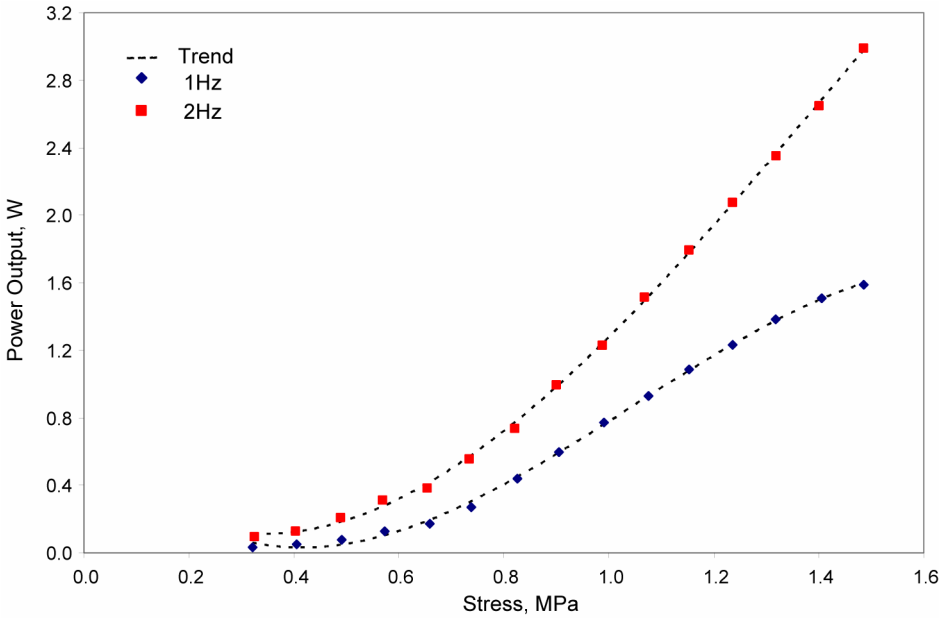

b) Total power output

Figure 4.15 Effect of constant recovery stress on power density and total power output of NiMnGa

Chapter 5: Modeling of NiMnGa Behavior

In order to effectively design FSMA based actuators, it is important to acquire both an understanding of the magneto-mechanical behavior of the material itself, and a set of reliable, analytical tools that effectively predict material behavior. Chapters 3 and 4 are devoted exclusively to the quasi-static and dynamic behavior of NiMnGa for a variety of magnetic and mechanical loading conditions. One of the over-arching goals of this testing was to develop a set of criteria that would be directed toward the development of analytical tools for NiMnGa behavior. In addition, these data are useful for both the formulation and validation of the behavioral models. Two models are presented in this chapter. The first model focuses on the quasi-static behavior of NiMnGa and was developed in parallel to existing *thermal* SMA models. A parameter-based dynamic model for low frequency actuation was also developed. Both models are compared to experimental data to validate their accuracy and effectiveness at predicting material behavior for various sets of magnetic and mechanical loading conditions.

This chapter is organized into three main parts. First, an overview of existing FSMA analytical models is presented to provide a background of current FSMA modeling capabilities and to review the state of the art of NiMnGa analysis. Key developments and shortcomings of the existing tools are expressed. Because of their importance in the development of the quasi-static modeling of NiMnGa, a review of the main NiTi, SMA models is also included. The second part is devoted to the formulation and validation of a quasi-static, model for NiMnGa. Comparisons between the experimentally obtained data and the phenomenological model are

presented for a broad range of magnetic and mechanical loading conditions. A discussion of the ability of the model to capture the unique strain recovery mechanisms of NiMnGa is provided. Finally, the third part covers the development of a low-frequency, dynamic model based on an experimentally determined set of physical parameters to predict the strain response of the alloy for a time varying magnetic field. A discussion of the capabilities of the model and its comparison to experimental data is included.

5.1 Overview of Current FSMA Models

Modeling the magnetic shape memory effect has received a significant amount of attention over the past decade [138, 183, 226, 227, 228, 229, 230, 231]. Fundamentally, many of these models are focused on determining the induced strain resulting from an applied magnetic field and determining the magnetization of the FSMA material as functions of external force and magnetic field conditions. Typically, FSMA models fall into one of two categories: microscopic scale approach and a macroscopic scale approach [232]. Microscopic models view the shape change of the FSMA material as related to the crystallographic twinning of the microstructure. The twins themselves are the result of a martensitic transformation and are elastic [232, 233]. Macroscopic models view the magnetically induced shape change as magnetoplasticity. In general, most of the macroscopic constitutive models rely on the minimization of an energy function. The fundamental assumption of this approach is that there exists a complete conversion of magnetic into mechanical power.

One of the first micromechanical models was developed by James and Wuttig [183] in 1998 along with Tickle [156] in 1999. Essentially, a micromagnetic model was developed to predict magnetic field induced changes in the microstructure of the martensite variants and the subsequent magnetically induced strain. Their approach utilizes the constrained theory of magnetostriction. This theory was based on the minimization of Zeeman, magnetostatic, and mechanical energy arising from an applied load on a single crystal FSMA specimen. The exact magnetization and induced strain in the FSMA are determined from the predicted martensite variant distribution. Because the variant distribution is determined, the effect of the demagnetization field can be accounted for in the results. A comparison between the proposed model and actual material behavior, however, showed significant variations which raise questions regarding the validity of this approach despite the level of detail devoted to the prediction of the variant microstructure. Furthermore, the model itself is numerical and as a result, does not provide an intuitive grasp of the mechanism of the material behavior. This attribute makes this model difficult to utilize as a general FSMA analytical tool.

One of the first free-energy based models was developed by O'Handley in 1998 [138]. This free-energy model attempts to predict the magnetically induced strain for weak, strong, and intermediate anisotropy states. It is significant in that it that it highlights the importance of a large magnetocrystalline anisotropy and low twinning stress for initiating twin boundary motion in NiMnGa. Hirsinger and Lexcellent [234, 235, 236] extended O'Handley's model in 2003 by introducing an internal variable

into the free energy expression. This phenomenological model containing internal variables showed good correlation with the experimental data.

L'vov utilized a similar approach to O'Handley and proposed another free-energy based model [226]. In this model, the magnetically induced strain and the magnetization are also described as functions of variant volume fractions. L'vov included an analysis of the magnetic susceptibility and an equation for the temperature dependence of the magnetization of the material.

Likhachev and Ullakko developed a general, thermodynamics model of the magnetic field induced strain [237]. The significance of this model was that it could be applied to multi-dimensional cases containing multiple martensite variants. The basic mechanical state equation includes the effect of the magnetic field and was derived from a general Maxwell relation.

In sections 5.1.1 and 5.1.3, three prominent NiMnGa models are examined in detail. All three rely on the energy minimization approach and are basically thermodynamics based models. These models highlight many of the key developments in the formulation of NiMnGa phenomenological models. It should be noted, however, that there are many models under development and that these two are only samples of a larger body of work.

5.1.1 O'Handley et. al. [7, 138, 200, 238]

As mentioned previously, the model developed by O'Handley was one of the first free-energy based models used to describe the magnetically induced strain and magnetization in NiMnGa. Over the years, it has evolved to include the effects of both internal and external stress. Fundamentally, this 2-dimensional model predicts

the induced strain of an FSMA element on the macroscopic scale. The material is defined as having two martensite variants separated by one twin boundary. Magnetocrystalline anisotropy is represented by a constant, h_a and the model considers three cases associated the magnitude of this constant: weak, strong, and intermediate. The volume fraction of each variant is determined which then enables the calculation of both the induced strain and the magnetization. One of the main assumptions of this model is that both the induced strain and the magnetization are linearly dependent on the volume fractions of the martensite variants. An equation of the free energy density in the material was developed to determine the volume fractions in the material. Initially, this relation included terms for the Zeeman energy, magnetization energy of the reoriented variant, and the magnetic energy and elastic energy density. Later, an external mechanical energy term was introduced to account for the external stress on the material [238]. In this formulation, the Zeeman energy difference between variants was assumed to be driving the twin boundary motion in the material (strong anisotropy). Mechanically, the material was assumed to be linear, with the elastic energy density term included to model the internal resistance to twin boundary motion.

The free energy density in one martensite variant, *i*, is expressed by the following equation:

$$g_i = -\mu_0 M_i \cdot H + K_1 \cos^2 \theta_i + \sigma_{\text{int}} \cdot \varepsilon + \frac{1}{2} C \varepsilon^2 \tag{5.1}$$

where C is the effective stiffness, θ_i represents the angle between the magnetic field and the *easy* axis of the variant, and M_i is the magnetization of the variant. The

volume fraction of each variant is determined by minimizing eq. (5.1) for all martensite variants present in the material.

The effects of magnetocrystalline anisotropy are also included. For the case of strong anisotropy, the Zeeman energy difference was determined to be the driving force of the twin boundary motion. This driving force can be determined by the following equation:

$$f = \mu_0 M_s H\left[\cos\theta - \cos(\theta - \phi)\right] \tag{5.2}$$

where θ represents the angle between the applied magnetic field and *easy* axis of the first variant, and φ is the difference in angle between the variants. A further development implemented by Henry and O'Handley [7] included the addition of a simple hysteresis model between the magnetic field-strain response.

Some of the main outcomes of this modeling approach were that it shows the relationship between magnetic anisotropy and the FSMA mechanism. For maximum magnetically induced strain, a strong, magnetocrystalline anisotropy is desired. Furthermore, this model shows that transformation of the material into a single variant is an unlikely event.

5.1.2 Likhachev & Ullakko [174, 228, 230, 239]

The model developed by Likhachev and Ullakko is based on an exact thermodynamic consideration of both the magnetic and mechanical properties of the FSMA. It uses a direct derivation from a general Maxwell's relation and shows that the magnetic field induced deformation is directly related to the strain dependence of magnetization [230]. Both the induced strain and magnetization of the material are

modeled. The main premise of this model is that the effect of the magnetic field is equal to an additional mechanical stress:

$$\sigma_{mech}(\varepsilon) = \sigma_{mag}(h) \tag{5.3}$$

where σ_{mech} represents the mechanical stress as a function of strain and σ_{mag} represents the magnetic stress as a function of field. In accordance with general thermodynamic principles, both the mechanical and magnetic properties can be represented by the following state equations:

$$\sigma = \sigma(\varepsilon, h) \tag{5.4}$$

$$m = m(\varepsilon, h) \tag{5.5}$$

where σ represents the mechanical properties of the material and m represents the magnetization of the material. To obtain equations for (5.4) and (5.5), these quantities must be modeled after the appropriate thermodynamic potential. For instance:

$$\sigma(\varepsilon, h) = \frac{\delta}{\delta\varepsilon}\tilde{G}(\varepsilon, h), \quad m(\varepsilon, h) = \frac{\delta}{\delta h}\tilde{G}(\varepsilon, h) \tag{5.6}$$

where $\tilde{G}(\varepsilon, h) = G(\varepsilon, h) - hm(\varepsilon, h)$, and $G(\varepsilon, h)$ is the specific Gibbs free energy for fixed temperature and pressure conditions. Both of the relations in eq (5.6) must satisfy Maxwell's rule:

$$\frac{\delta}{\delta h}\sigma(\varepsilon, h) = -\frac{\delta}{\delta\varepsilon}m(\varepsilon, h) \tag{5.7}$$

Integration of eq. (5.7) over the magnetic field from 0 to h at a fixed strain condition and considering the case where σ=0, the magnetically induced strain can be determined from the following:

$$\sigma_0(\varepsilon) = \frac{\delta}{\delta\varepsilon}\int_0^h dhm(\varepsilon, h) \tag{5.8}$$

solving for strain:

$$\varepsilon^{msm}(h) = \left(\frac{\delta\sigma_0}{\delta\varepsilon}\right)^{-1}_{\varepsilon=0}\left(\frac{\delta}{\delta\varepsilon}\int_0^h dhm(\varepsilon, h)\right)_{\varepsilon=0} \tag{5.9}$$

A final equation, representing the effect of the magnetic field on the induced strain for NiMnGa tetragonal martensite can be derived from this general thermodynamics of solids approach. The magnetically induced strain in this case is:

$$\varepsilon^{msm}(h) = \frac{2}{3}\left(\varepsilon_0\frac{\delta\sigma_0}{\delta\varepsilon}\right)^{-1}_{\varepsilon=0}\left(\int_0^h dh(m_a(h) - m_t(h))\right) \tag{5.10}$$

where $m_a(h)$ and $m_t(h)$ are the specific magnetization functions for the axial and transverse variants respectively.

In the case of a simple, two-variant twinning geometry, the driving force of the twin boundary motion and the subsequent magnetically induced stress are:

$$f = \mu_0\int_0^h (m_a - m_t)dh \tag{5.11}$$

$$\sigma_{mag} = \frac{f}{\varepsilon_0} = \frac{\mu_0}{\varepsilon_0}\int_0^h (m_a - m_t)dh \tag{5.12}$$

where, ε_0 represents the maximum recoverable strain of the FSMA material.

5.1.3 Kiefer and Lagoudas [240, 241]

Similar to the model proposed by O'Handley [138], the model proposed by Kiefer and Lagoudas uses similar terms in the free energy expression. Energy associated with the magnetic shape memory effect, elastic strain energy, Zeeman energy, and magnetic anisotropy energy are included in this model as well as others. This model,

however, focuses on the influence of dissipative effects in the evolution of thermodynamic states, rather than the minimization of the free energy, which searches for equilibrium points in ideal processes [241]. This dissipative nature is accounted for by the introduction of internal state variables in the Gibbs free energy function. The effects of martensitic variant reorientation, rotation of the magnetization, and magnetic domain wall motion are incorporated.

Assuming that the non-variable magnetic domain volume fraction (α=1), the Gibbs free energy for this model is given by the following equation:

$$G = G(\sigma, H, \xi, \theta_i) = -\frac{1}{2}\sigma : S(\xi)\sigma - \frac{\mu_0}{\rho} M(\xi, \theta_i) \cdot H + G^{an}(\xi, \theta_i) + \frac{1}{\rho} f^{\xi}(\xi) + G_0 \tag{5.13}$$

where μ_0 is the permeability of free space and ρ is the mass density The independent variables include the Cauchy stress tensor, σ and the magnetic field intensity vector, H. The volume fraction, ξ and the magnetization rotation angle θ_i are internal state variables. The total Gibbs free energy presented in eq (5.13) represents a linear average of the contributions of each variant and corrected by the mixing term $f^{\xi}(\xi)$ and having a reference state value of G_0. Expressions for the effective elastic compliance, S, effective magnetization, M, and effective magnetic anisotropy energy G^{an} are:

$$S = S^{v_1} + \xi \Delta S = (1-\xi) S^{v_1} + \xi S^{v_2} \tag{5.14}$$

$$M = (1-\xi) M^{v_1} + \xi M^{v_2} = (1-\xi) M^{3} + \xi M^{4} \tag{5.15}$$

$$G^{an} = (1-\xi) G^{an, v_1} + \xi G^{an, v_2} = (1-\xi) G^{an,3}(\theta_3) + \xi G^{an,4}(\theta_4) \tag{5.16}$$

This work has shown to be quite versatile, and has been successfully integrated into other modeling efforts. Tan and Elahinia utilize the Kiefer and Lagoudas model for the development of a dynamics FSMA model [242]. Faidley and Dapino have developed a form of this model for their work in developing a model for NiMnGa with a collinear excitation field [178, 179].

5.1.4 Implementation of Current FSMA Models into Actuator Design

Each of the models presented here have a strong thermodynamics basis and tend to be quite useful for developing an understanding of the underlying physics of the FSMA actuation mechanism. In general, each of the models tends to show good agreement with the experimental data, producing very reliable predictions of the material behavior. However, there are some drawbacks inherent to each of these models. First, the effect of excitation frequency is not readily evident in the present body of work. As a result, most of these models have only been validated with quasi-static data. Henry and O'Handley [7] began to explore the dynamic excitation of the material and had only limited success. Furthermore, these thermodynamics based energy models are typically difficult to implement, especially in the process of actuator design. Furthermore, they tend to be enormously complex, requiring significant time and effort to adapt them to any given set of design requirements. Currently, there exists no simple, constitutive model that combines the effects of excitation frequency, mechanical and magnetic loading. In the present work, the development and implementation of a simple, FSMA model, characterized by experimental data is a key concern.

5.2 SMA Constitutive Models

Because of the close similarities that exist between the behavior of NiTi and NiMnGa, it is necessary to consider the possibility that existing quasi-static phenomenological models for NiTi can provide a basis for FSMA modeling. Currently, there are many existing SMA models based on combinations of thermodynamic, phenomenological, and statistical mechanics approaches. Of this wide variety of behavioral models, there exist several, well-known examples of constitutive models used to predict thermal SMA behavior. The Tanaka, [243] Liang and Rogers, [244] Brinson, [135] and Boyd and Lagoudas [245] models are four well documented, SMA constitutive models. All four are similar, describing the material behavior in terms of three state variables: stress, strain, and temperature for one-dimensional, quasi-static loading on the macro scale. Since the NiTi alloy behavior is highly sensitive to a host of external factors including but not limited to manufacturing processes, chemical composition, and mechanical and thermal training, all the models incorporate experimentally derived material parameters. Once the parameters are precisely determined, a particular model may be implemented and the material behavior successfully predicted. This approach highlights one of the key advantages of these models. Since they rely on a series of experimentally determined material parameters, implementation of these models is relatively straightforward. Since one of the main goals of this work was directed towards implementation of NiMnGa in actuators, emulation of this modeling approach was a natural choice.

The following section briefly describes the four aforementioned constitutive models developed to predict SMA behavior. An overview of each model's main contribution and key points is provided. On a final note, it is assumed that only uniaxial behavior of the material is studied. The scope of this work does not include lateral loading of the material.

5.2.1 The Tanaka Model

Developed in 1986, the Tanaka Model [246] represents one of the very first constitutive models proposed to capture the unique behavior of shape memory alloys. The basis of the model is thermo-mechanical and utilizes a formulation of the Second law of thermodynamics expressed in terms of the Helmholtz free energy. Fundamentally, the model assumes three state variables including, one dimensional strain, temperature, and martensite volume fraction. The global stress in the SMA is written as a function of these three state variables. Furthermore, the martensite volume fraction is a function of both the stress and the temperature. This complication facilitates the necessity of a recursive solution form for simultaneous determination of both the stress and martensite volume fraction (i.e. Newton-Raphson or similar method). The kinetics for the alloy transition from the low temperature, martensite phase to the high temperature austenite phase is expressed by an exponential function that describes the martensite volume fraction as a function of stress and temperature. A key point regarding this model is that it is limited to describing material behavior in response to a change in temperature only. The low-temperature, detwinning behavior of the alloy (the shape memory effect) is not included in the Tanaka's model.

The Tanaka model is now revisited in more detail. The constitutive equation is:

$$\sigma - \sigma_0 = E(\xi)(\varepsilon - \varepsilon_0) + \Omega(\xi - \xi_0) + \theta(T - T_0) \tag{5.17}$$

where the subscript 0 refers to the initial state of the SMA material. Fundamentally, this equation shows that the stress is the sum of three main parts: mechanical stress, stress resulting from phase transformation, and thermoelastic stress. The variables ε, T, and ξ represent strain, temperature and martensite volume fraction respectively. Furthermore, the Young's modulus E and the phase transformation coefficient Ω are functions of the martensite volume fraction, ξ. During heating, the SMA transforms from the martensite phase to the austenite phase, the martensite volume fraction varies from 1 (pure martensite condition) to 0 (pure austenite condition)

Many of the material's properties, including the Young's modulus, E, and the transformation coefficient, Ω, are determined by the content of martensite in the SMA. There exist distinct variations in these properties between the martensite and austenite states. The most common approach to representing the Young's modulus is to utilize a rule of mixtures formulation for the material comprised of mixed phases of martensite and austenite. The modulus of elasticity is determined from the following linear equation:

$$E(\xi) = E_A + \xi(E_M - E_A) \tag{5.18}$$

where E_M and E_A represent the modulus of elasticity for the martensite and austenite states respectively. The transformation coefficient, Ω, is expressed by applying block force and free strain conditions to the constitutive relation presented in equation 5.17. The resulting equation is as follows:

$$\Omega(\xi) = -\varepsilon_L E(\xi) \tag{5.19}$$

where ε_L is indicative of the maximum recoverable strain of the SMA. One of Tanaka's key contributions was the development of an evolutionary equation to describe the martensite volume fraction of the material. As mentioned previously, the equation has an exponential form and is a function of the stress and temperature. The equation for the austenite to martensite transformation is:

$$\xi = 1 - \exp\{a_M (M_S - T) + b_M \sigma\} \tag{5.20}$$

Similarly, the equation for the martensite to austenite transformation is:

$$\xi = \exp\{a_A (A_S - T) + b_A \sigma\} \tag{5.21}$$

where material dependent constants are defined according to the following relations:

$$a_A = \frac{\ln(0.01)}{A_S - A_F},\ b_A = \frac{a_A}{C_A} \tag{5.22}$$

$$a_M = \frac{\ln(0.01)}{M_S - M_F},\ b_M = \frac{a_M}{C_M} \tag{5.23}$$

The material coefficients E, θ, Ω, critical transformation temperatures A_s, A_f, M_s, M_f, and stress influence coefficients, C_A and C_M are all determined experimentally from the testing of SMA wires. Critical transformation temperatures A_s, A_f, M_s, and M_f, are obtained from heating samples in the stress free condition. The stress influence coefficients C_A and C_M are the slopes of the critical stress-temperatures plots for the boundaries of the austenite and martensite transformations respectively [153, 169].

5.2.2 The Liang and Rogers Model

At the most fundamental level, the Liang and Rogers model [244] utilizes the same constitutive relation as the Tanaka model. However, Liang and Rogers main

contribution was to replace the exponential martensite volume fraction equation with a cosine function. The austenite to martensite transformation for the martensite volume fraction is expressed by the following equation:

$$\xi = \frac{1-\xi_A}{2}\cos\{a_M(T - M_f) + b_M\sigma\} + \frac{1+\xi_A}{2} \tag{5.24}$$

Similarly, for the martensite to austenite transformation:

$$\xi = \frac{\xi_M}{2}\cos\{a_A(T - A_S) + b_A\sigma\} + 1 \tag{5.25}$$

where material dependent constants are defined according to the following relations:

$$a_A = \frac{\pi}{A_f - A_S},\ b_A = \frac{-a_A}{c_A} \tag{5.26}$$

$$a_M = \frac{\pi}{M_s - M_f},\ b_M = \frac{-a_M}{c_M} \tag{5.27}$$

Like Tanaka, the main drawback of this model is that it also does not include the strain-induced martensite transformation, or in other words, the shape memory effect.

5.2.3 Brinson Model

As stated earlier, the primary drawback of the Tanaka and Liang and Rogers models is that they are incapable of modeling the room temperature detwinning behavior of NiTi. In fact, both models are only capable of modeling the behavior of the SMA material that arises from a phase change during heating. This shortcoming is addressed in the Brinson model [203]. By separating the martensite volume fraction, ξ, into a stress preferred (detwinned) and temperature induced components the Brinson Model is capable of modeling the low temperature shape memory effect, as well as the pseudoelastic behavior that results from phase changes in the material.

Essentially, the Brinson model allows for modeling the shape memory effect below the A_s temperature.

The constitutive equation for the Brinson model is similar to both the Tanaka and Liang and Rogers models. For a set of non-constant coefficients, the resulting relation is:

$$\sigma - \sigma_0 = E(\xi)\varepsilon - E(\xi_0)\varepsilon_0 + \Omega(\xi)\xi_s - \Omega(\xi_0)\xi_{s0} + \theta(T - T_0) \tag{5.28}$$

As mentioned earlier, the martensite volume fraction is resolved into two components. The stress induced component refers to the amount of detwinned martensite present within the SMA sample, while the temperature induced component refers to the level of martensite occurring from the reversible phase transformation to austenite. The equation for the martensite volume fraction is as follows:

$$\xi = \xi_S + \xi_T \tag{5.29}$$

where ξ_S represents the stress-induced component and ξ_T represents the temperature induced component. Similar to the Liang and Rogers model, a modified cosine function is utilized to describe the martensite volume fraction.

Finally, by assuming constant material coefficients, the constitutive equation for the Brinson can be simplified to the following form:

$$\sigma - \sigma_0 = E(\xi)(\varepsilon - \varepsilon_0) + \Omega_s(\xi_s - \xi_{s0}) + \Omega_T(\xi_T - \xi_{T0}) + \theta(T - T_0) \tag{5.30}$$

where E is the Young's modulus as a function of the martensite volume fraction, ξ, Ω_s and Ω_T are stress and temperature induced transformation tensors respectively, and θ is related to the thermal coefficient of expansion. The initial conditions, σ_0, ε_0, ξ_{s0}, ξ_{t0}, and T_0, are included.

5.2.4 The Boyd and Lagoudas Model

The Tanaka, Liang and Rogers, and Brinson's model are mainly focused on one-dimensional shape memory alloy behavior. The Boyd and Lagoudas model however, represents a generalized, three-dimensional approach [245, 247]. Like the Tanaka model, the constitutive relation is determined by satisfaction of the second law of thermodynamics but unlike the Tanaka model, the Boyd and Lagoudas model uses a Gibbs free energy formulation instead of Helmholtz energy terms. The free energy of each phase of the shape memory material plus the free energy of mixing is summed to determine the specific Gibbs free energy. Strain is resolved into a mechanical component (ε_{ij}) and a transformation component (ε^{tr}_{ij}) which are functions of the martensite volume fraction:

$$\sigma_{ij} = C_{ijkl}\left[\varepsilon_{kl} - \varepsilon^{tr}_{kl} - \alpha_{kl}\left(T - T_0\right)\right] \tag{5.31}$$

From a dissipation potential, the evolutionary equation for the martensite volume fraction can be derived as follows:

$$\sigma^{eff}_{ij} + d^1 T - \rho b_1 \xi = Y^{**} + d^3_{ijkl}\sigma_{ij}\sigma_{kl} + d^4\sigma_{ij}\Delta T \tag{5.32}$$

where Y^{**} is the value of threshold stress, d^1T is related to the entropy reference state, d^3_{ijkl} and d^4_{ij} are parameters that are related to changing elastic moduli, ρ is the mass density, b_1 is a material constant and ΔT is the temperature difference.

Generally, this model is applicable to monolithic SMA structures while retaining the quality of being a true three-dimensional model. Furthermore, it was shown by Brinson and Huang [248] that the one dimensional form of this model is identical to the Tanaka model. However, even in its one dimensional form, the Boyd and

Lagoudas model retains the ability to model the low temperature martensite detwinning behavior.

As previously mentioned, there exist many models for shape memory alloy behavior. The Boyd and Lagoudas model is not the only thermodynamics model in existence. One such example is the model derived by Ivshin and Pence [249]. This model was formulated from a thermodynamic consideration of the kinetic relations for hysteresis of the phase fraction. One of the key features of this model is that it utilizes the austenite volume fraction as the primary variable instead of the martensite volume fraction. Nevertheless, the Boyd and Lagoudas model represents a fundamental, energy based, approach to modeling shape memory materials and is representative of a major category of shape memory alloy modeling.

5.2.5 SMA Model Applications to Analysis of NiMnGa

One approach to the development of a NiMnGa FSMA model is to look toward SMA models for inspiration. A wide variety of models exist but many of the main desirable qualities exist in the four models presented in sections 5.2.1-5.2.4. These models are all described in terms of a set of empirical constants that must be determined from experiments. As such, these constants represent actual, physical behavior of the SMA alloy. In fact, many of these constants can be derived from a few thermo-mechanical tests of the material [170, 210, 250]. As a result, these types of models are very useful in the process of actuator design. Provided that the physical constants are measured accurately, they can be highly reliable and effective at predicting SMA behavior. Furthermore, these models result in straightforward implementation which is a top criterion for NiMnGa model development. This is a

desired quality if the goal is to streamline the process of incorporation into existing actuator design algorithms. Free energy models, like the Boyd and Lagoudas model, although typically more comprehensive and generalized, are often difficult to implement in practical engineering problems. Furthermore, they also require an in-depth knowledge of the fundamental physics of the material. Currently, because FSMA materials are still relatively new, there is still a great deal of research required before the underlying physical issues are resolved. Therefore, the development of NiMnGa analytical tools will follow a similar, approach.

Of these four SMA constitutive models presented, the Brinson model in particular, is quite useful in predicting NiTi SMA behavior [86, 170]. However, if this model is to be used as a basis for FSMA modeling several key issues must be addressed. Among those issues:

1. The state variables must be reconsidered. Although strain is likely to remain a state variable in the FSMA model, temperature and martensite volume fraction may need to be revaluated. Magnetic field is a prime candidate for replacing the temperature variable. Martensite volume fraction however, may not have a place in FSMA modeling because of the material does not rely on a phase change to induce the shape memory effect.

2. New material constants must be defined. The resolution of issue #1 will likely lead to a redefined set of material parameters. Material constants like Young's Modulus, critical stresses, critical fields, and stress influence coefficients will likely reappear, albeit in a revised form.

3. A new constitutive relation must be developed. The final issue involves the incorporation of issues #1 and #2 to develop a general constitutive equation for NiMnGa actuation.

5.3 Development of a Quasi-static Model

It was recognized that the quasi-static behavior of FSMA shared many of the same characteristics attributed to thermal SMA behavior. Not only do they both achieve comparable levels of induced strain but both materials have a characteristically similar shape memory and pseudoelastic effects. On the surface, the main difference between FSMA and SMA is the type of activation field (magnetic versus thermal). Because of these similarities between the two materials, one viable approach is to take advantage of the existing SMA modeling efforts, using them for inspiration to develop a parallel quasi-static FSMA model.

Because it is capable of producing strains on the order of 6%, NiMnGa, one of the most widely known FSMA materials, has been considered for use in high stroke smart actuators for a range of applications [5, 168, 251, 252, 141]. However, the capabilities of the material are limited by the lack of a suitable set of analytical tools for predicting macroscopic actuator behavior. In terms of incorporating these tools into actuator design, these models are not adequately developed. To explore the full engineering potential of this material, a comprehensive, constitutive model is required so that FSMA behavior may be reliably predicted. At this time, a few micromechanical and thermodynamics based models are available, which predict the stress and strain states of NiMnGa in magnetic fields of up to 1.0 Tesla [174, 175, 238]. In practice, these models are not easy to implement and lack the quality of

straightforward implementation normally attributed to macromechanical constitutive models like those for NiTi thermal SMA. Several, well supported constitutive models, have been formulated for SMAs including the Tanaka, [243] Liang and Rogers [244], Brinson [203] and Boyd and Lagoudas [245] models. Since these models rely on experimentally determined material parameters, they are relatively easy to implement and serve as an important ingredient towards the development of SMA based intelligent systems. A macromechanical constitutive model, similar to those used to model NiTi, is what is required for NiMnGa. The subject of this section is the development of a phenomenological-based model, characterized by test data, developed in parallel to the Brinson model. The key issue to resolve with this approach is that the NiTi based model must be modified to accommodate strains induced by a magnetic field instead of a thermal field.

Model parameters were determined from quasi-static test data (Chapter 3) for NiMnGa rods subjected to uniaxial loading conditions. There are nine model parameters including fundamental threshold fields, fundamental critical stresses, Young's moduli in the stress and field preferred martensite configurations, stress-influence coefficients, and free strain. Furthermore, these parameters were functions of the applied magnetic field and applied axial stress. Most of the model parameters were obtained from a series of uniaxial compression tests of NiMnGa specimens subjected to constant applied magnetic fields. Once the parameters were identified, the model was implemented and compared with experimental data to evaluate its validity for all modes of NiMnGa behavior

5.3.1 Quasi-Static Model Formulation

In section 5.2.5, a set of three criteria were established regarding the relevant issues to be addressed for developing a NiMnGa model in parallel to the Brinson, SMA model. Each of these issues was addressed in turn, over the course of the NiMnGa model development.

The first issue involves redefining the state variables. Clearly, temperature must be replaced with a magnetic field input. Although research has shown that magnetic shape memory alloys like NiMnGa do possess a significant degree of thermal shape memory behavior [181], the scope of this study will be limited to magnetic field inputs only. Also, the fundamental mechanism driving magnetic shape memory alloys is different from thermal SMA. Strain is not recovered by martensite to austenite phase transitions but rather by the mechanism of twin boundary motion of the martensite. Therefore, if one is to be modeling magnetically induced strains only, choosing the martensite volume fraction as a state variable is not an option as it should always have a value of '1' over the course of magnetic excitation. Instead, since the twin boundary motion is essentially a detwinning phenomenon, the value of stress induced martensite will become a state variable. The mechanism of strain recovery for thermal SMA relies on a phase transition from the martensite to the austenite phase. In contrast, FSMA rely on transition from twinned (stress induced) to detwinned (field induced) martensite. Therefore, the twinned FSMA martensite is comparable to the martensite phase of SMA and the detwinned FSMA martensite is comparable to the austenite phase of thermal SMA.

The second issue to address involves redefining the material parameters that define the model. The eleven parameters used to define the Brinson model for SMA are as follows: 4 critical transformation temperatures (M_s M_f A_s A_f), 2 stress influence coefficients (C_A for austenite and C_M for martensite), 2 critical stresses for room temperature detwinning (σ^s_{cr} and σ^f_{cr}), 2 Young's moduli (E_M for martensite and E_A for austenite), and finally, a zero-stress, free strain parameter (ε_L). Likewise, the FSMA model is defined by a set of similar material parameters. The FSMA model has nine, experimentally determined constants including: 2 zero-stress, critical transformation fields (H_s and H_f), 2 stress influence coefficients (C_s for the start of twin boundary motion and C_f for the end of twin boundary motion), 2 critical stresses for zero-field detwinning ($\sigma_{cr,s}$ for the start and $\sigma_{cr,f}$ for the finish, 2 Young's Moduli (E_σ for stress-preferred martensite, E_H for field preferred martensite) and finally, a zero-stress, free strain ε_L. Effectively, this new set of parameters reassigns temperature to magnetic field based constants.

Now that the new material parameters and state variables have been reassigned, a new constitutive relation must be developed. The constitutive equation can be written in terms of magnetic quantities and assumes the following form:

$$\sigma - \sigma_0 = E(\xi_\sigma)(\varepsilon - \varepsilon_0) + \Omega(\xi_\sigma)(\xi_\sigma - \xi_{\sigma 0}) + \lambda(\xi_{\sigma 0})(H - H_0) \tag{5.33}$$

where σ_0, ε_0, $\xi_{\sigma 0}$, and H_0 represent the initial stress, strain, volume fraction of stress preferred martensite, and magnetic field intensity respectively. E, Ω, λ are constant material functions where E represents the Young's modulus of the FSMA, Ω is a transformation tensor, and λ is related to the magnetostriction of the material. To better capture nonlinear effects in the material behavior, these material functions need

not be linear and can be represented by higher order functions. In response to the necessity of redefining the state variables of the constitutive equation (eq. 5.30) these material functions are defined in relation to the volume fraction of stress preferred martensite, ξ_σ. In general, a magnetic field applied to the FSMA causes the volume fraction of stress preferred martensite to decrease resulting in the growth of field preferred martensite twins. As mentioned previously, this behavior is analogous to the phase transition from martensite to austenite in NiTi SMA. However, as also previously mentioned, strain recovery in thermal SMA occurs as a result of a phase transformation, while FSMA strain recovery occurs as a result of twin boundary motion in the martensite phase only. Therefore, the sum of the stress preferred martensite, ξ_σ, and field preferred martensite ξ_H must always be equal to unity.

$$\xi_\sigma + \xi_H = 1 \tag{5.34}$$

If it is assumed that the material is at the maximum free strain condition, $\varepsilon = \varepsilon_L$, with the material initially composed entirely of the field preferred variant, $\xi_{\sigma 0} = 0$, with the initial conditions of $\sigma_0 = \varepsilon_0 = H_0 = 0$, and final conditions of $\xi_\sigma = 1$, $\varepsilon = \varepsilon_L$, and $\sigma = H = 0$, the following relation can be obtained:

$$\Omega = -\varepsilon_L E \tag{5.35}$$

Using the constraint derived in eq. 5.35, the FSMA constitutive equation may be reduced to the following, simplified form,

$$\sigma = E(\xi_\sigma)(\varepsilon - \varepsilon_L \xi_\sigma) + \lambda(\xi_\sigma)(H - H_0) \tag{5.36}$$

where $E(\xi_\sigma)$ is the Young's modulus of the material as a function of the stress preferred martensite volume fraction, ε_L is the free-strain of the actuator, ξ_s is the

stress preferred volume fraction, λ is related to the magnetostriction of the material and H_0 is the initial external field applied to the material.

To account for variations in the mechanical properties between stress and field preferred martensite, a rule of mixtures formulation was used to quantify the Young's modulus of a martensite structure containing both field and stress-preferred twins. The linear function describing the Young's modulus, E is:

$$E(\xi_\sigma) = E_\sigma + \xi_\sigma (E_H - E_\sigma) \tag{5.37}$$

The phenomenological model for NiMnGa describes the material stress in terms of three state variables: stress-preferred martensite strain, and magnetic field that may be determined from testing the FSMA material over a range of constant, externally applied fields and observing the output stress and strain characteristics. In the following section (5.3.2) the process of identifying these parameters is discussed.

5.3.2 Parameter Identification

There are nine model parameters that must be quantified in order to characterize the quasi-static model. To determine the necessary constants for the quasi-static FSMA model, two types of tests were conducted, a constant stress test and a constant applied magnetic field test. Each of the tests was carried out in separate test rigs, built in house. Photographs of these test rigs appear in Figures 3.5, 3.7, and 3.9. All three of these test rigs utilize similar electromagnetic circuits for FSMA magnetic excitation. Details of the quasi-static testing are provided in Chapter 3. In this section, the results of the quasi-static testing are re-examined to determine and quantify the model parameters.

The first three parameters, E_σ, E_H, and ε_L, were obtained from direct examination of the stress-strain curves of the constant applied field tests discussed in chapter 3. In Figure 5.1, the Young's modulus for the field preferred variant, E_H, and the modulus for stress preferred variant, E_σ, are shown. Figure 5.1(a) shows the both moduli for the case of a constant 6 kOe applied field. Figure 5.1(b) shows both moduli for 3.5 kOe, 6 kOe, and 10 kOe applied fields. Based on these data, the Young's moduli appear to be constant with respect to the applied field. The value of the field preferred modulus, E_H, was measured to be 450 MPa while the modulus for the stress preferred variant, E_σ was measured to be 820 MPa.

The next model parameter to be determined is the free strain, ε_L. The free strain is defined as the maximum recoverable plastic strain that can be recovered with the application of a sufficient magnetic field. The ε_L parameter was determined from the zero applied field stress strain curve shown in Figure 5.2. Because there is no applied field acting upon the FSMA, there will be no MSM induced strain recovery when the load is removed. When the stress is reduced to zero, the actuator recovers a small amount of elastic strain. The remaining strain is plastic in nature but can be recovered when a sufficient external field is applied. The magnitude of plastic strain remaining in the material after the load has been removed in a zero field environment is 5.8%. This amount of residual strain is the free strain of the FSMA and represents the maximum strain capability of the material. This maximum capability is limited by the tetragonality of the *c/a* ratio of the martensite [181].

Many of the model parameters can be determined from the critical stress vs. applied field profiles shown in Figures 3.28 and 3.29. The final six parameters were

quantified by closely studying this relationship between the four critical transformation stresses and the applied field. Details regarding the method and experiments conducted to obtain this profile are provided in Section 3.5 By identifying the critical stresses over a range of field intensities, a critical stress profile, shown in Figure 5.3, can be developed for an iso-magnetic field. The beginning and end of the twin boundary motion during loading were denoted as σ_1 and σ_2, respectively. For twin boundary motion during recovery, σ_3 and σ_4 were similarly defined. These critical stress values are shown for the case of a 6 kOe applied field in Figure 5.1. Each curve of the critical stress behavior appeared to be linearly related to applied field below 7 kOe. For external fields larger than 7 kOe, the critical stresses began to level off, indicating the onset of magnetic saturation. Because the σ_1 and σ_3 curves were coincident and the σ_2 and σ_4 curves are parallel, it was sufficient to define, two, linear stress influence coefficients. The first stress influence coefficient, C_s, was defined as the slope of the σ_1 and σ_3 curves, or in other words, the variation of critical stress with applied field for the beginning of twin boundary motion. The second stress influence coefficient represented the critical stress behavior at the end of twin boundary motion, C_f, was determined from the slope of the σ_2 and σ_4 curves. Also, since at this stage, the model assumed to be linear, higher order effects like magnetic saturation, were neglected. The linear assumption will be revisited later. Each coefficient has units of MPa per kOe. Based on the experimental data, the values for C_s and C_f were measured to be 0.452 MPa/kOe and 0.488 MPa/kOe respectively.

The critical stress profile also contains two other features that lead to quantification of model parameters. Consider the profile shown in Figure 5.4. First, the points corresponding with zero applied field of the σ_1 and σ_2 curves are the two fundamental critical stresses $\sigma_{cr,s}$ and $\sigma_{cr,f}$. Along with the appropriate stress influence coefficients, these parameters were used to predict the critical stresses for any constant applied field during the mechanical loading cycle. These fundamental critical stresses were measured to be 0.284 MPa and 0.920 MPa for $\sigma_{cr,s}$ and $\sigma_{cr,f}$ respectively. The critical stresses of the reverse transition, σ_3 and σ_4, exist only above certain threshold fields. By noting the x-intercepts of these two curves, the two fundamental threshold fields may be identified. These threshold fields are similar in character to the martensite to austenite transformation temperatures for thermal SMA (A_s and A_f). For instance, consider Figure 5.5, the x-intercept of the σ_3 curve is 1.0 kOe. For applied fields greater than 1.0 kOe, the actuator will begin to revert back to the field preferred state when the load is removed. This field was the H_s parameter of the model. Likewise, the H_f field was defined by the x-intercept of the σ_4 curve, which was measured to be 3.5 kOe. Critical stresses for the unloading portion of the mechanical loading cycle were determined from these critical fields in combination with the stress influence coefficients. It was noted that the partial magnetic pseudoelastic effect occurred only for applied fields between H_s and H_f while complete pseudoelasticity occurred for fields greater than or equal to H_f. For applied fields below H_s, the zero-field behavior (magnetic SME) was the dominant strain recovery mechanism. Furthermore, it follows then that for field greater than H_f, 3.5 kOe, the main strain recovery mechanism will be magnetic pseudoelasticity.

The resulting constants determined from the entire set constant field experiments appears in Table 5.1. All of the parameter values represent the average of multiple sets of constant applied field, quasi-static loading tests.

5.4 Quasi-Static Model Validation

Once the material parameters were identified, the quasi-static model was implemented and validated with experimental data. In the model, stress was calculated in the actuator for a discrete number of strain steps. Once the stress reaches a predicted critical value, twin boundary motion occurs. As mentioned previously, these critical stresses are functions of applied magnetic field and can be determined from the corresponding combination of the parameters $\sigma_{cr,s}$, $\sigma_{cr,f}$, C_s, C_f, H_s, and H_f. During the region of twin boundary motion, a linear function was used to describe the transformation from the stress to field preferred martensite configurations.

5.4.1 Initial Model Validation

The first benchmark for a successful NiMnGa behavioral model was that it must be able to capture all of the major strain recovery mechanisms of the material including the magnetic shape memory effect, partial pseudoelasticity, and pseudoelasticity. In Figure 5.6, the result from the analytical model is compared to the experimental stress-strain curve for the zero field condition to show the model's effectiveness at capturing the magnetic shape memory effect. Figure 5.7 shows the results of the model compared to the stress-strain curve for a specimen exposed to a

constant 5 kOe field, demonstrating the model's ability to capture magnetic pseudoelastic behavior.

In general, the model shows good agreement with the experimental data in both Figures 5.6 and 5.7. Critical threshold stresses were predicted with a reasonable degree of accuracy and the model seemed to capture both the primary strain recovery mechanisms of the actuator. In the pseudoelastic region, there was a tendency of the model to slightly over-predict stresses during loading and slightly under-predict stresses during unloading. Generally, these inconsistencies are small and did not seriously undermine the accuracy of the analysis. The model did not, however, incorporate the smooth transitions between the field and stress preferred martensite configuration. This result was expected given that a piecewise linear model was assumed for the transition region between stress and field preferred martensite. However, further refinement of the model will be required in order to include these higher order effects.

For further validation, a comparison between the model and experimental data of non-standard strain recovery behavior was conducted. In Figure 5.8, the ability of the model to predict partial pseudoelasticity is shown for a 2 kOe applied magnetic field. Although the general shape of the NiMnGa behavior was reflected in the model, inconsistencies in stress calculation during the loading and unloading cycles were much more pronounced than they were in the cases shown in Figures 5.6 and 5.7. The model over-predicted the stresses during twin boundary motion by as much as 20% during the loading cycle for the partial pseudoelastic case shown in Figure 5.8.

Although the predicted stresses during unloading are better, there still exists a higher degree of model error than seen in the pseudoelastic analysis.

Figure 5.9 shows a comparison between the analytical model and a minor hysteretic loop at 6 kOe. As for all of the previous cases, the model is capable of predicting the stress-strain curve of a minor loop. For both partial pseudoelasticity and minor loops, the linearity of the model neglected higher order material behavior, which may be the cause of errors in the approximation of the stresses associated with twin boundary motion. These discrepancies lead to slightly less desirable predictions than in the cases of the SME and pseudoelasticity. Although useful for providing a general picture of actuator behavior, the linear model required further refinement before it could accurately predict material behavior for compositional intermediate states.

5.4.2 Refined Quasi-Static Model

One of the underlying assumptions of the quasi-static model was that all parameters were linearized. As a result, higher order effects such as magnetic saturation were neglected. This means that the analytical model over-predicts the critical stresses for large external fields close to magnetic saturation. Figure 5.10 demonstrates this limitation by comparing the model to the experimental stress-strain curve for an 8 kOe external field. Clearly, the model did not accurately capture the physical behavior of the material in this case. When the applied field is larger then 7 kOe, the NiMnGa element began to saturate. It was noted that beyond 7 kOe, the critical stresses shown in Figure 3.28, began to level off. This behavior was a clear indicator of magnetic saturation. At the onset of magnetic saturation, the material no

longer maintains a linear relationship between critical transformation stresses and applied field. Since the model initially uses linear stress-influence coefficients, they were insufficient for predicting critical stresses at or near magnetic saturation. What was now required is a new set of functions to replace the linearized coefficients C_s and C_f. These functions were obtained from the critical stress profile shown in Figure 5.11. When C_f and C_s are expanded from linear coefficients to simple, third order polynomials, they improve the ability of the model to predict critical stresses for any external magnetic field. The following expressions represent the nonlinear equations and conditions used to calculate critical transformation stresses in the NiMnGa.

For pseudoelastic behavior ($H_{app} > H_f$),

$$\sigma_1 = \sigma_3 = \left(-0.0002 * H_{app}^3 - 0.0289 * H_{app}^2 + 0.6678 * H_{app} - 0.5614\right) * 10^6 \quad (5.38)$$

$$\sigma_2 = \left(0.0005 * H^3{}_{app} - 0.0399 * H_{app}^2 + 0.699 * H_{app} + \sigma_{cr,f}\right) * 10^6 \quad (5.39)$$

$$\sigma_4 = \left(0.0024 * H_{app}^3 - 0.1024 * H_{app}^2 + 1.292 * H_{app} - 3.441\right) * 10^6 \quad (5.40)$$

where H_{app} represents the value of the applied magnetic field.

For the partial pseudoelastic behavior ($H_s > H_{app} > H_f$),

$$\sigma_4 = 0 \quad (5.41)$$

For shape memory behavior ($H_{app} < H_s$),

$$\sigma_3 = \sigma_4 = 0 \quad (5.42)$$

$$\sigma_1 = \sigma_{cr,s} \quad (5.43)$$

In Figure 5.12, the model is once again compared to the experimental stress-strain curve for an 8 kOe external field. In this case, however, the model was updated to include higher order critical stress functions. The critical stresses were not over-

predicted in the case presented in Figure 5.12 as they were in Figure 5.10 therefore, the model was able to compensate for the effects of magnetic saturation and yielded a better prediction of material behavior.

5.5 Development of a Dynamic NiMnGa Model

In order to predict the strain response for practical NiMnGa based actuators, a low-frequency model was required. Although the quasi-static model developed in the previous sections provided acceptable predictions of the stress-strain response of the FSMA element for a wide range of loading conditions, it was not capable of being directly transferred into a dynamic regime. One of the main assumptions of the Tanaka series of SMA models is that they assume instantaneous equilibrium of the material at all times during a mechanical cycle. This assumption however, may not be valid for dynamic excitation. However, the ability of material parameter based models like the one described above to predict material behavior is clearly quite good. What is needed in the case of dynamic FSMA excitation is a simple, parameter based model that takes into account the operating frequency in order to predict the strain response for a wide range of mechanical loading. This sections details the development of a low-frequency model derived from the experimental measurements of NiMnGa performed in Chapter 4. The model relies on a distinct set of material parameters so that it can represent actual material behavior and includes excitation frequency and stress as independent variables.

5.5.1 Formulation of the Low-Frequency Model

The proposed model must predict the induced strain-magnetic field behavior of the NiMnGa for dynamic excitation and varying levels of constant preload. Four, physical parameters, determined from experimental measurements were used to characterize the model. Each of the four parameters are functions of both stress and excitation frequency. To ensure that the model retained the ability to realistically capture the material behavior, care was taken to choose parameters that have physical meaning and could be measured experimentally. Consider a typical strain-field curve for NiMnGa (Figure 5.13). The first parameter, remnant strain, ε_R, was identified as the cross-over point between the positive and negative half cycles of excitation. Physically, remnant strain is the magnitude of strain remaining in the specimen when the magnetic field reaches zero during one cycle. The second parameter, B_c, is known as the activation field parameter. This parameter represents the activation field required to induce twin boundary motion for an increasing magnitude of magnetic field. A third parameter was determined from the slope of the induced strain-magnetic field curve for an increasing magnitude of field. The apparent slope, $K_{\varepsilon B}$, was assumed to be constant for increasing and decreasing magnitudes of magnetic field. Finally, a peak strain at magnetic saturation or peak saturation strain parameter was defined. The peak saturation strain, ε_{sat}, represents the magnitude of induced strain measured at the peak magnetic field. All four parameters, ε_R, B_c, $K_{\varepsilon B}$, and ε_{sat}, are shown in Figure 5.13. Note that these parameters are functions of both σ and excitation frequency (f_{ex}).

$$\varepsilon_R = f(\sigma, f_{ex}) \tag{5.44a}$$

$$B_C = f(\sigma, f_{ex}) \tag{5.44b}$$

$$K_{\varepsilon B} = f(\sigma, f_{ex}) \tag{5.44c}$$

$$\varepsilon_{sat} = f(\sigma, f_{ex}) \tag{5.44d}$$

To completely define the apparent shape of the material behavior, three additional points were required. These points B_1, B_2, and B_3 are also depicted in Figure 5.13 and are determined from the four model parameters. Effectively, these three points are dependant parameters. B_1 is similar in nature to a coercive field. In other words, it represents the magnitude of magnetic field required to remove the remnant strain. Although not related to the actual coercive field property of NiMnGa, B_1 is nevertheless similar in character. The next point, B_2 represents the magnetic field at which the peak saturation strain is achieved for an increasing magnetic field magnitude. The final point, B_3 represents the magnetic field at which the restoring force begins to overcome the effect of the applied field thereby inducing twin boundary motion. At B_3 stress preferred twins begin to grow at the expense of field preferred twins therefore beginning the process of strain recovery. Basically, B_3 represents the activation of twin boundary motion for a decreasing magnetic field magnitude.

Strain was calculated over discrete number of magnetic field steps by implementing a series of linear functions where the independent variable B represents the magnetic field. The parameters, ε_R, $K_{\varepsilon B}$, B_C, and ε_{sat} are functions of both stress and excitation frequency. The piecewise linear model was defined in the following manner for the positive half cycle of magnetic excitation.

For $B' > 0$, (5.45)

If $B < B_1$ then $\varepsilon = \varepsilon_R - K_{\varepsilon B}(B)$

If $B_1 < B < B_C$ then $\varepsilon = 0$

If $B_C < B < B_2$ then $\varepsilon = K_{\varepsilon B}(B - B_C)$

If $B > B_3$ then $\varepsilon = \varepsilon_{sat}$

For $B' < 0$, (5.46)

If $B > B_3$ then $\varepsilon = \varepsilon_{sat}$

If $0 < B < B_3$ then $\varepsilon = \varepsilon_R + B(K_{\varepsilon B})$

A similar set of relations was developed to model the material behavior over the negative half cycle of magnetic excitation.

5.5.2 Dynamic Model Parameter Identification

The aim of the proposed dynamic model was to provide a reliable analytical tool with the ability to predict the dynamic strain response for a specimen of NiMnGa acting under an AC magnetic field. Based on the information obtained from the dynamic characterization of the material, this model must necessarily be a function of pre-stress and excitation frequency. After the dynamic behavior of the FSMA was characterized, four model parameters were identified. These parameters include saturation strain, ε_{sat}, remnant strain, ε_R, zero-strain field, B_C, and the slope of the field induced strain $K_{\varepsilon B}$.

Figure 5.14 shows the behavior of the peak saturation strain, ε_{sat}, as a function of pre-stress for both 1 Hz and 2 Hz excitation frequencies. The data appeared to suggest a 'bell curve' trend with a maximum value of 5.1% occurring for 1.5 MPa of constant stress. For stresses below 0.8 MPa, the peak stain achieved by 1 and 2 Hz excitation was closely spaced. Beyond 0.8 MPa, the variation became larger,

showing a consistent 0.4% difference in peak strain between the two excitation frequencies and the trendline. Because only two excitation frequencies were studied, it was concluded that the effect of excitation frequency on this parameter could not be reliably determined. In the future, a more rigorous and thorough study of the effect of frequency on the peak strain is necessary to validate the model over a larger bandwidth. In Figure 5.15, the average peak strain for the 1 and 2 Hz excitation frequencies is shown. Although significant variation exists for larger magnitudes of constant stress (between 0.8 MPa and 1.4 MPa), the behavior of the ε_{sat} parameter showed a clear trend and provided a reasonable estimation of the peak strain. A third degree polynomial was fit to the data and the following equation was used to predict ε_{sat}:

$$\varepsilon_{sat}(\sigma,0) = -6.04\sigma^3 + 16.45\sigma^2 - 8.97\sigma + 2.02 \tag{5.47}$$

where σ represents the magnitude of constant stress.

The effect of preload on the remnant strain, ε_R, is shown in Figure 5.16. For each case observed, ε_R showed a strong dependence on stress. The characteristic shape of the data also followed a bell curve trend. For 1 Hz excitation, the peak remnant strain was 0.5% for a 1.17 MPa constant stress. For 2 Hz excitation, the peak remnant strain was 1.1% for a 1.42 MPa constant stress. This behavior suggested that not only does this parameter show a strong dependence on stress but also a pronounced dependence on excitation frequency. However, it is unusual to observe a 100% increase in strain this material as a result of a 1 Hz increase in the excitation frequency. A physical reason for this behavior could not be determined especially considering that only a limited range of excitation frequencies were tested.

Furthermore, a significant level of uncertainty exists in these measurements especially for stresses below 0.8 MPa. Below this stress level, the standard deviation in the 1 Hz and 2 Hz data was 0.040% while the standard deviation in the data sets above 0.8 MPa was 0.030%. Below 0.8 MPa a 0.040% standard deviation constitutes a significant variation in the data. The source of this uncertainty however, was most likely not related to the actual material behavior but rather a result of the testing environment. The magnitude of this parameter translates into a measurement of no more than 0.17 mm. This is close to the precision of the test equipment and therefore very sensitive to experimental error. As a result, a significant level of variation was expected. As in the case of the peak saturation strain parameter, since only two excitation frequencies were observed, a meaningful trend between remnant strain parameter and excitation frequency could not be determined. Therefore, the data sets for the 1 Hz excitation frequency were averaged with the data sets of the 2 Hz excitation frequency to determine a relationship between remnant strain and recovery stress. The following third order polynomial was used to predict the remnant strain for 1 Hz and 2 Hz excitation frequencies:

$$\varepsilon_R(\sigma,0) = -2.44\sigma^3 + 6.31\sigma^2 - 4.05\sigma + 0.81 \tag{5.48}$$

where σ is the magnitude of constant stress.

Figure 5.17 shows the relationship between $K_{\varepsilon B}$ and stress. Just as in the case of the peak saturation strain parameter, $K_{\varepsilon B}$ appeared to have a strong dependence on stress and was relatively independent of excitation frequency. Similarly, the largest variation between the two excitation frequencies occurred between 0.9 MPa and 1.33

MPa. However, despite the level of variation, the data suggested a clear trend. To model this parameter, the following third order polynomial was implemented:

$$K_{\varepsilon B}(\sigma,0) = -8.92\sigma^3 + 20.00\sigma^2 - 4.52\sigma + 1.25 \tag{5.49}$$

where σ is the magnitude of constant stress.

The zero-strain field, B_C, is shown in Figure 5.18. Although the data for the 1 Hz excitation appears to suggest a dependence on stress, this conclusion would be inaccurate. It was observed that the data for this parameter showed a pronounced level of variation, as much as 0.07 T for some data points. This was especially true of the 1 Hz case. The average value of the 1 Hz case was 0.584 T with a standard deviation of 0.062 T. The average value of the 2 Hz excitation case was 0.643 T with a standard deviation of 0.026 T. Although the level of precision in the 2 Hz data was clearly higher than that of the 1 Hz data, it was decided that the level of variation between the data points was small enough to allow both sets of data to be represented as constants equal to the average value of the data set. In other words, it was assumed that the value of B_C was independent of stress. This supposition qualitatively appeared to be the case in the 2 Hz data whose relatively flat curve clearly suggested that B_C was independent of stress. Furthermore, because of the limited range of frequencies investigated, it could not be concluded that this parameter had a pronounced dependence on excitation frequency. Additional tests including a larger range of excitation frequencies may establish a relationship between excitation frequency and the B_C parameter but in context with the current work, the value of this parameter was assumed to be constant. The average value of the combined data sets for the 1 Hz and 2 Hz cases was 0.623 T with a standard deviation of 0.050 T.

Therefore, the activation field parameter B_C was represented as a constant according to eq. (5.51).

$$B_C = 0.623 \tag{5.50}$$

Parameter identification yielded an unexpected result. Although the model was formulated with two independent variables in mind (excitation frequency and recovery stress) each of the four parameters was determined to be a function of recovery stress only. However, it cannot be concluded that excitation frequency does not have any effect on the material strain response because the range of frequencies tested was small. Based on the experimental data, it can only be concluded that for low frequencies (< 2 Hz) the strain response is a function of recovery stress only.

5.6 Dynamic Model Validation

Once the model parameters were identified, the dynamic model was implemented and compared to experimental data. For a given level of constant stress and excitation frequency, the four model parameters were calculated. Based on these values, the points B_1, B_2, and B_3 were determined from linear functions. Constant recovery stresses ranging from 0.33 MPa to 1.5 MPa were examined. To highlight the performance of the analytical model, three levels of constant stress, 0.42, 1.0, and 1.5 MPa were considered.

In Figure 5.19, the analytical model was compared to the experimental data for the case of 0.42 MPa constant stress at 1 Hz excitation in 5.19(a) and 2 Hz excitation in 5.19(b). Considering Figure 5.19(a), it was concluded that the model showed good correlation with the data as the magnetic field increases in magnitude. Furthermore, the amplitude of the strain response was also correctly predicted. Since the peak

saturation strain function was shown to be precise for stresses below 0.8 MPa, this result was expected. However, the correlation between the analysis and the data began to degrade when the magnetic field began decreasing in magnitude. The assumption of a constant $K_{\varepsilon B}$ also did not appear to apply in this instance, therefore the point B_3 was not correctly predicted. As a result, the model over-predicted the hysteresis in the strain-magnetic field loop. Figure 5.19(b) shows similar trends at 2 Hz excitation. In this case, two sets of data are presented in order to show the variation in material behavior for the same testing conditions. Although there was a slight variation in the peak saturation strain between the two data sets, the analytical model still appeared to be a good prediction of material behavior. Generally, the analytical model seemed to capture the form of the dynamic behavior of the material for stresses below 0.8 MPa.

Figure 5.20 compares the model to the experimental data for the case of a 1.0 MPa constant stress and 1 Hz excitation in 5.20(a) and 2 Hz excitation in 5.20(b). In contrast to the data shown in Figure 5.19, the accuracy of the model varies significantly between the 1 Hz and 2 Hz cases. The model in Figure 5.20(a) under-predicts the strain-magnetic field response for an increasing field and over-predicts the strain-magnetic field response for a decreasing magnetic field magnitude. Although the model accurately predicts the remnant strain in this case, the amplitude of the strain response is not well modeled. Once again, these discrepancies are traced to the behavior of the model parameters. For 1.0 MPa, there are large variations in the peak saturation strain which act as a significant source of error in the model. Similarly, the parameter ε_R is well represented at this stress level. For the 2 Hz

excitation case shown in Figure 5.20(b), the analysis showed a good correlation between the experimental data for an increasing magnitude of field and a reasonably accurate prediction of the peak saturation strain, ε_{sat}. However, just as in the case of 0.42 MPa constant stress, the data were not well modeled for a decreasing field magnitude. The reason for this discrepancy was traced to the assumption of constant $K_{\varepsilon B}$. While in the 1 Hz excitation case, this assumption appeared valid, it did not seem to apply to the case of the 2 Hz excitation. This dissimilarity in the predicted slope caused significant over-prediction in the hysteresis of the response.

Finally, Figure 5.21 provides a comparison between the proposed model and the experimental data for the case of a 1.5 MPa constant stress. The predictions for both 1 Hz excitation (Figure 5.21(a)) and 2 Hz excitation (Figure 5.21(b)) correlate with the test data. In Figure 5.21(a), even though the analysis continues to under-predict the material behavior for an increasing magnetic field magnitude and over-predict the material behavior for decreasing magnetic field magnitude, the error is significantly smaller than the two previous cases presented in Figures 5.20(a) and 5.19(a). In addition, the amplitude of the strain response was reasonably estimated and the analysis seemed to yield an accurate estimation of the remnant strain. Furthermore, the assumption of a constant $K_{\varepsilon B}$ for field both increasing and decreasing in magnitude appeared to be valid. The case of 2 Hz excitation depicted in Figure 5.21(b) also shows encouraging results. Peak saturation strain and remnant strain parameters follow the experimental data. Although the actual material behavior was still over-predicted for a decreasing magnetic field magnitude, the analysis and experimental data continued to show good correlation for increasing field

magnitudes. Similar to the case of 1 Hz excitation, the data presented in Figure 5.21(b) also appeared to support the validity of a constant $K_{\varepsilon B}$ assumption.

In summary, the model provided good predictions for very low ($\sigma < 0.6$) and very high ($\sigma > 1.33$ MPa) levels of constant stress. This result was expected because the individual model parameters show the least uncertainty in these stress regions. One of the key issues to resolve is the over-prediction of material behavior for a decreasing magnetic field. This problem can be traced back to the assumption of a constant $K_{\varepsilon B}$ for both increasing and decreasing magnetic field magnitudes. Although this assumption appeared to be valid at high levels of constant stress, at low levels, the slope for the increasing field was always greater than the slope of the decreasing magnetic field magnitude. As a result, the hysteresis predicted in the induced strain-magnetic field curves was much larger than the actual material behavior.

5.6.1 Low Frequency Model Evaluation

Although the model clearly requires further refinement to improve its accuracy, it does provide a reasonable prediction of material behavior while retaining the quality of straightforward implementation in addition providing physical insight into the actual material behavior. Even at it's least accurate (for the stress region 0.7 MPa $> \sigma >$ 1.33 MPa), the model is still able to track the material behavior, indicating its viability as a potential analytical approach.

Discrepancies between the dynamic model and experimental data for intermediate levels of stress arise from scatter in the measured behavior of the model parameters. It was concluded that further investigation into the behavior of the material parameters over a wider range of stresses and excitation frequencies is required to

improve the accuracy of the analysis. Although the model is currently constrained to low frequencies, the results are encouraging, and suggest further consideration as a potential approach for dynamic modeling of FSMA.

5.6.2 Low Frequency Model Limitations

Despite that a reasonable correlation exists between the calculated results and the test data, there are several issues that must be addressed in order to further improve the accuracy of the dynamic model. First, the accuracy of the model was highly sensitive to the measurement of the model parameters. Error in these measurements was directly transferred into the model. For moderate levels of stress, where the most experimental error was apparent, the model clearly demonstrates this supposition. Great consideration must be directed to ensuring, reliable measurements of the material constants in order to maintain a reasonable level of accuracy in the analytical results. Second, the apparent slope assumption for increasing and decreasing magnetic fields was not always correct. For example, the slope of the strain response at low stresses for an increasing magnetic field was generally much greater than the slope for a decreasing field. The current model assumes that the apparent slopes for increasing and decreasing magnetic fields are equal. For these stress levels, this assumption can lead to large over-predictions of strain when the field decreases in magnitude over the magnetic excitation. Next, dynamic tests were limited to low excitation frequencies. A full characterization of the material behavior over a more useful range of excitation frequencies (DC to 200 Hz for example) is necessary in order to improve the viability of the model. Because of the limited sample size, few meaningful conclusions regarding the effect of frequency can be drawn at this time.

Finally, the model in its current form does not include recovery stresses above 1.5 MPa. As a result, the model suggests that the induced strain always increases with recovery stress. The preliminary dynamic tests described in section 4.1 showed that beyond a certain optimum recovery stress, the induced strain began to actually decrease as recovery stress was increased. If the model in its current form were to attempt to predict the strain response for recovery stresses beyond 1.5 MPa, it would yield an inaccurate result. What is required are tests involving stress levels beyond 1.5 MPa in order to capture the behavior of the material when the influence of mechanical stress begins to constrain the magnetic shape memory effect.

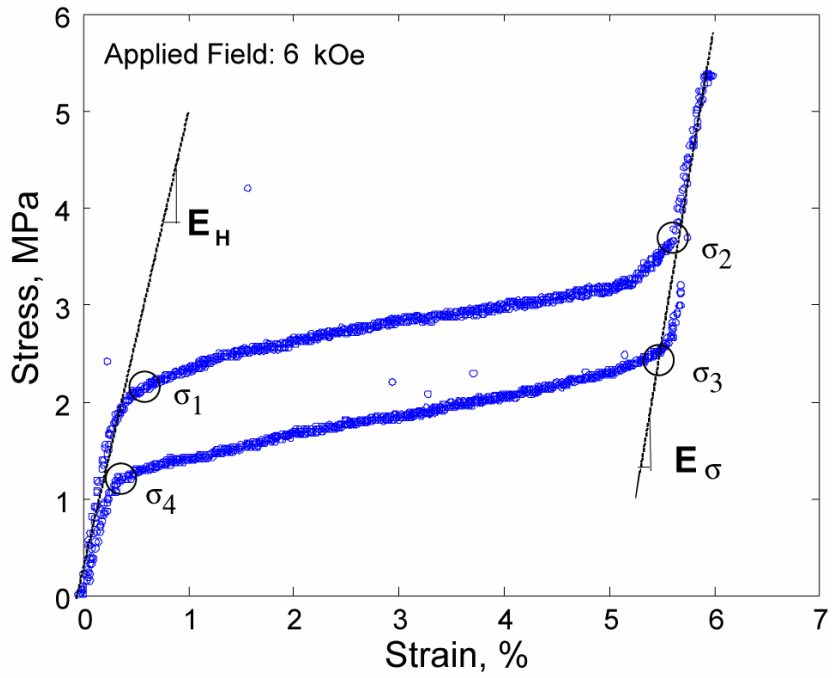

a) Young's Moduli for 6 kOe applied field

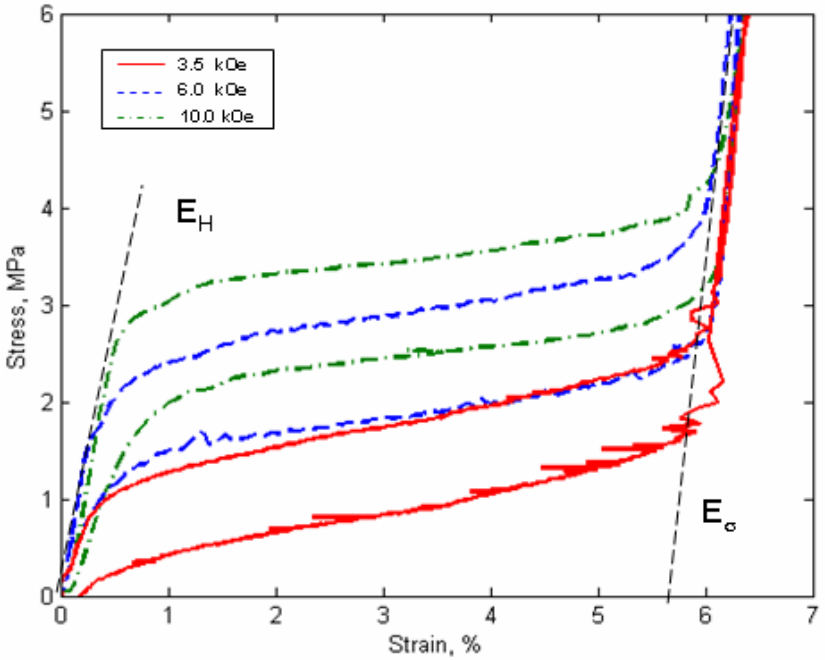

b) Young's Moduli for various applied magnetic field

Figure 5.1. Measurements of the field preferred (E_H) and stress preferred (E_σ) Young's moduli for NiMnGa

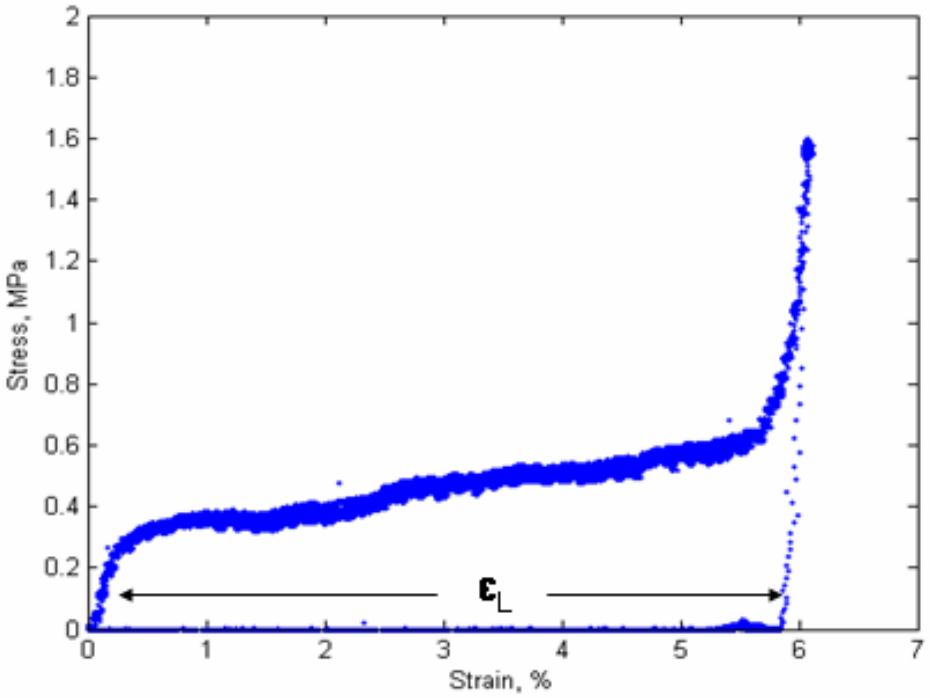

Figure 5.2. Measurement of the free strain, ε_L parameter

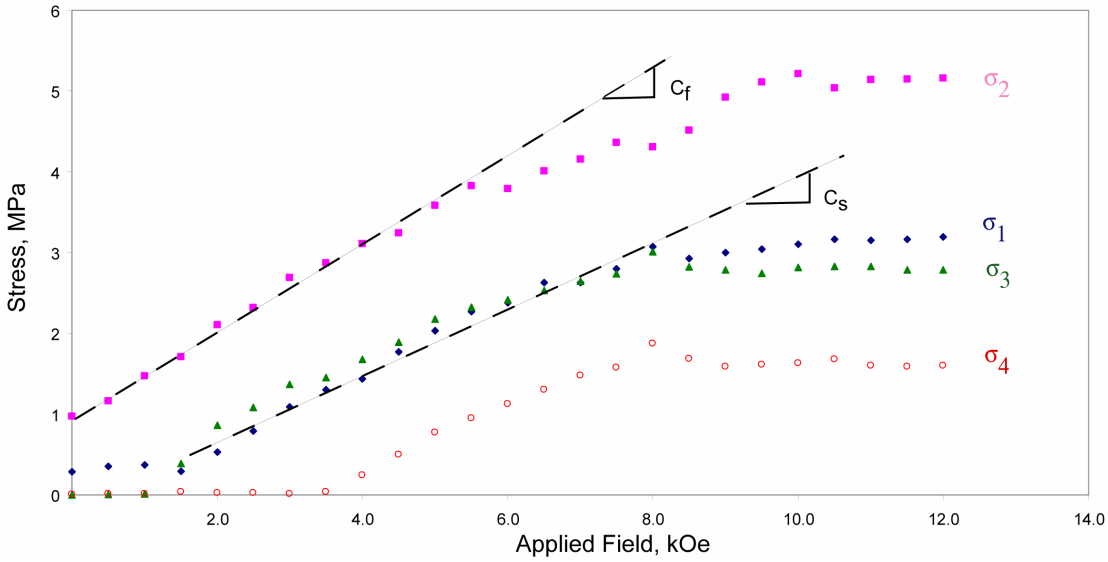

Figure 5.3 Measurement of the stress influence coefficients C_s and C_f from the critical stress vs. applied field profile

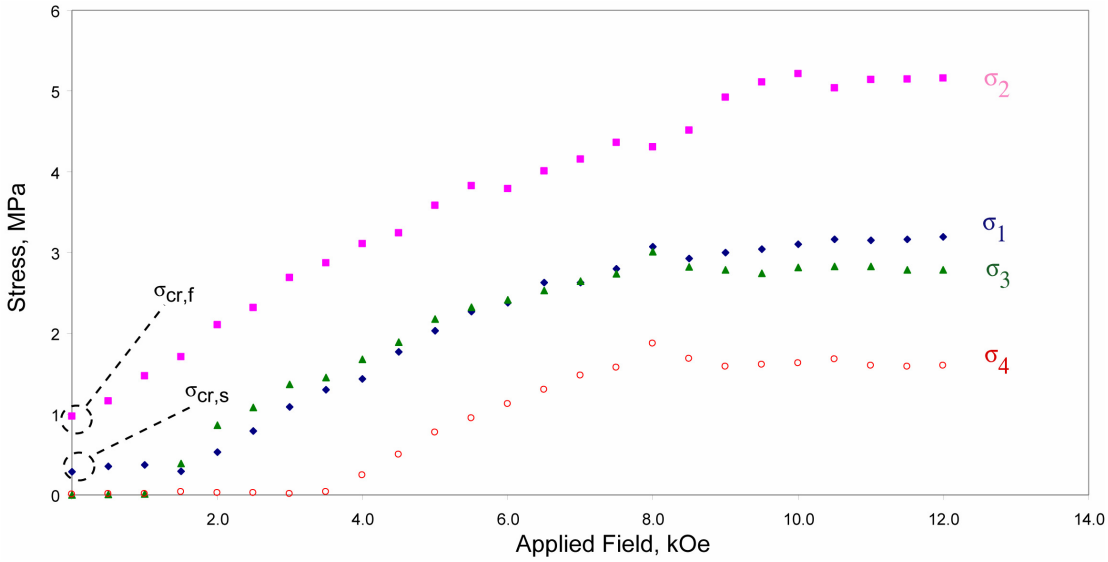

Figure 5.4 Measurement of the fundamental critical stresses $\sigma_{cr,s}$ and $\sigma_{cr,f}$ from the critical stress vs. applied field profile

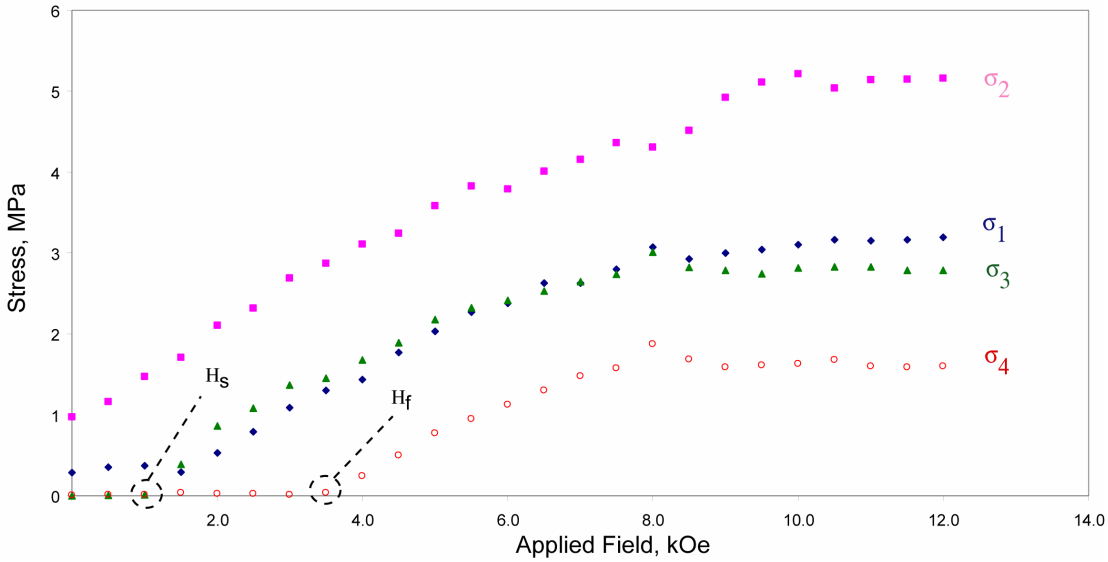

Figure 5.5 Measurement of the fundamental threshold fields H_s and H_f from the critical stress vs. applied field profile

Parameter	Value	Standard Deviation	Units
H_s	1.0	-	kOe
H_f	3.5	-	kOe
$\sigma_{cr,s}$	0.284	0.092	MPa
$\sigma_{cr,f}$	0.902	0.291	MPa
C_s	0.452	0.023	MPa/kOe
C_f	0.488	0.029	MPa/kOe
E_σ	820	16.59	MPa
E_H	450	17.01	MPa
ε_L	5.8	0.04	%

Table 5.1 Experimentally determined FSMA quasi-static model parameters

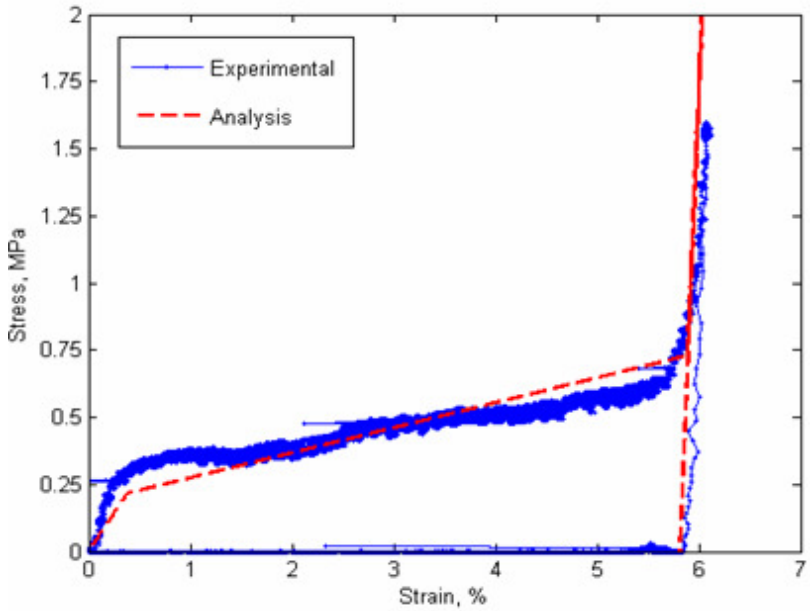

Figure 5.6 Comparison between analytical model and experiment for 0 kOe applied magnetic field (shape memory effect)

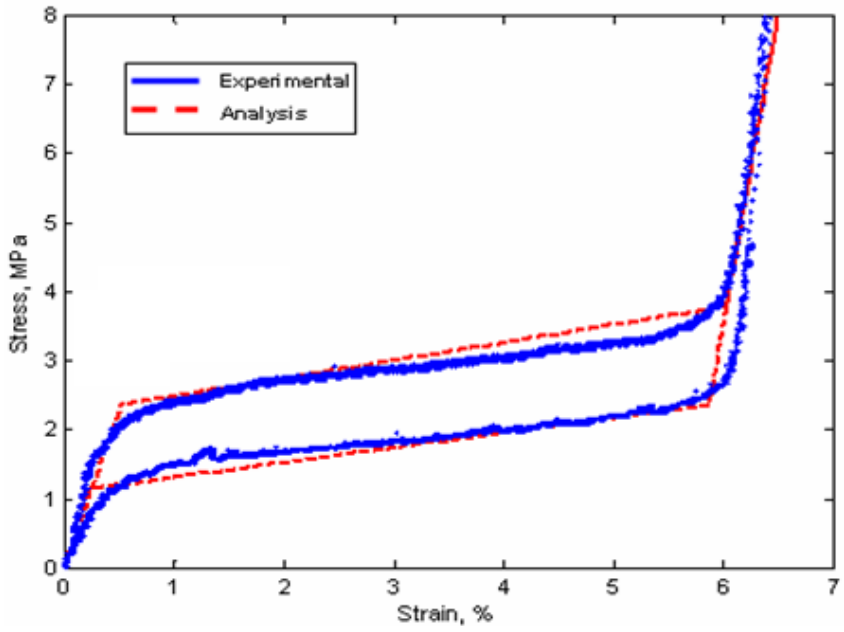

Figure 5.7 Comparison between analytical model and experiment for 5 kOe applied magnetic field (pseudoelastic behavior)

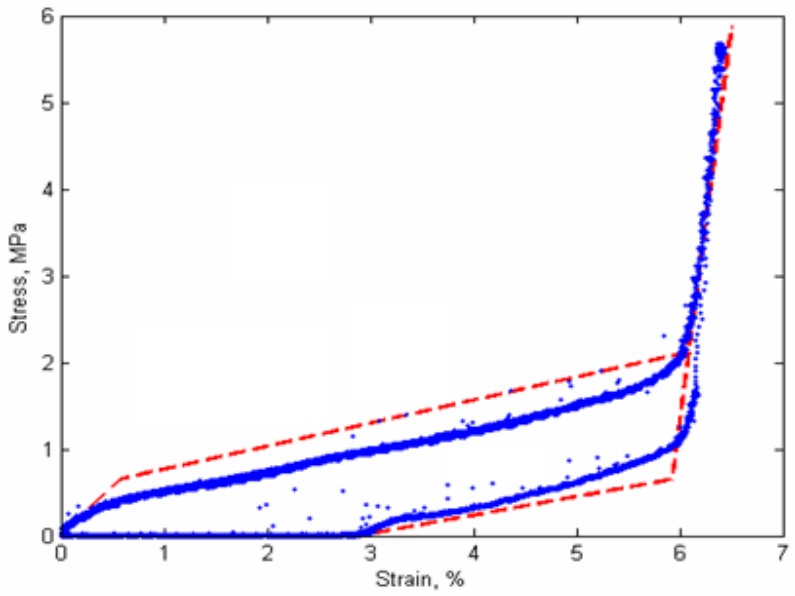

Figure 5.8 Comparison between analytical model and experiment for 2 kOe applied magnetic field (partial pseudoelastic behavior)

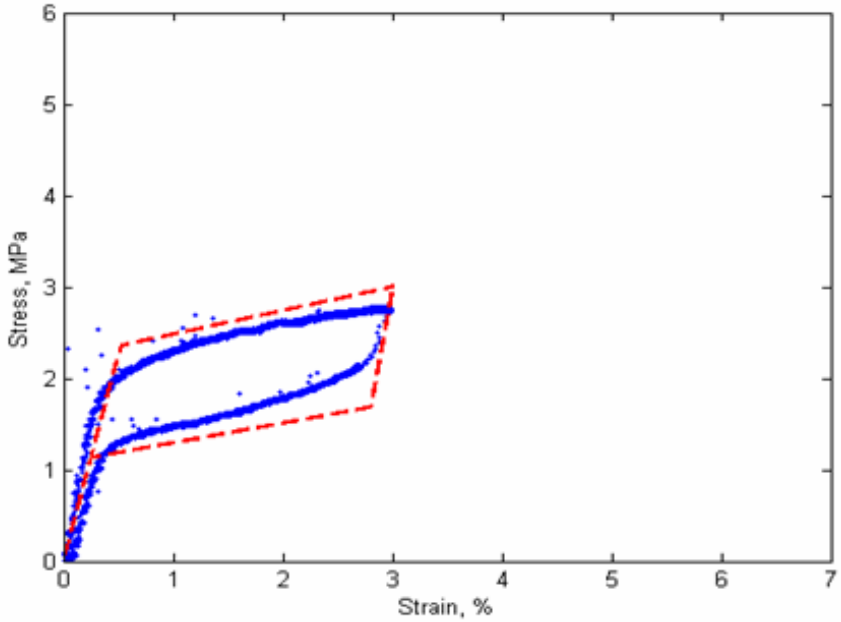

Figure 5.9 Comparison between analytical model and experiment for 6 kOe applied magnetic field (minor pseudoelastic loops)

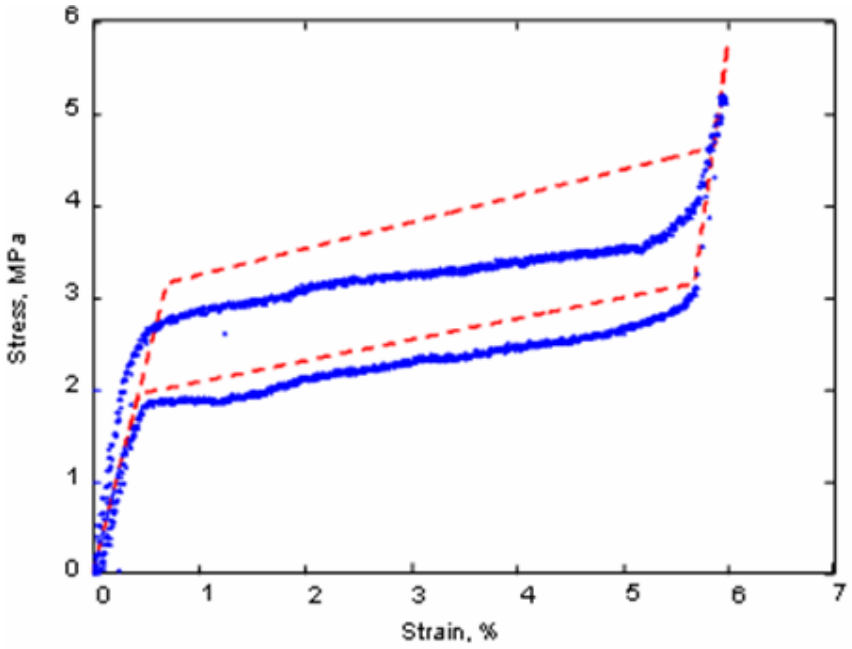

Figure 5.10 Effect of linearized model parameters on comparison between analytical model and experimental data for 8 kOe applied magnetic field

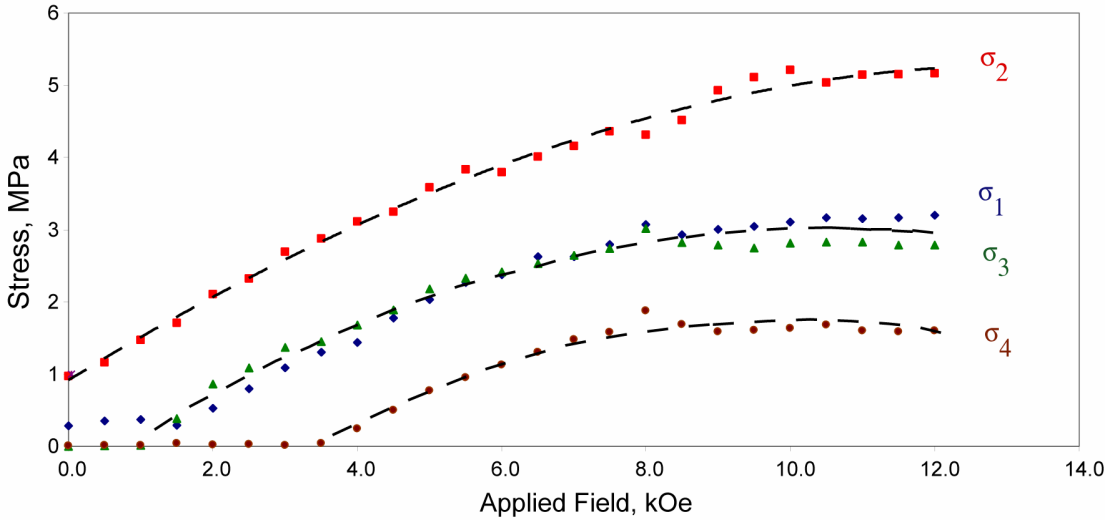

Figure 5.11 Third order trends in critical stress vs. applied field profile

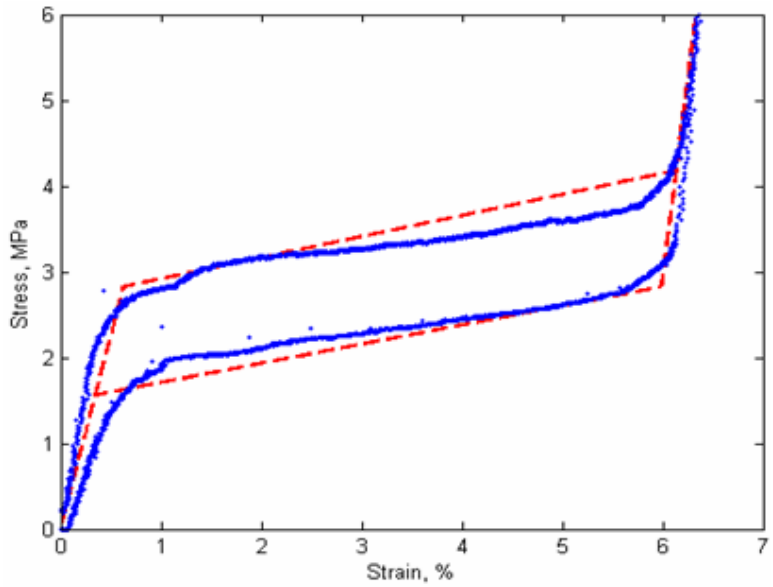

Figure 5.12 Comparison between experimental data and revised quasi-static model utilizing non-linear stress influence functions for 8 kOe applied field

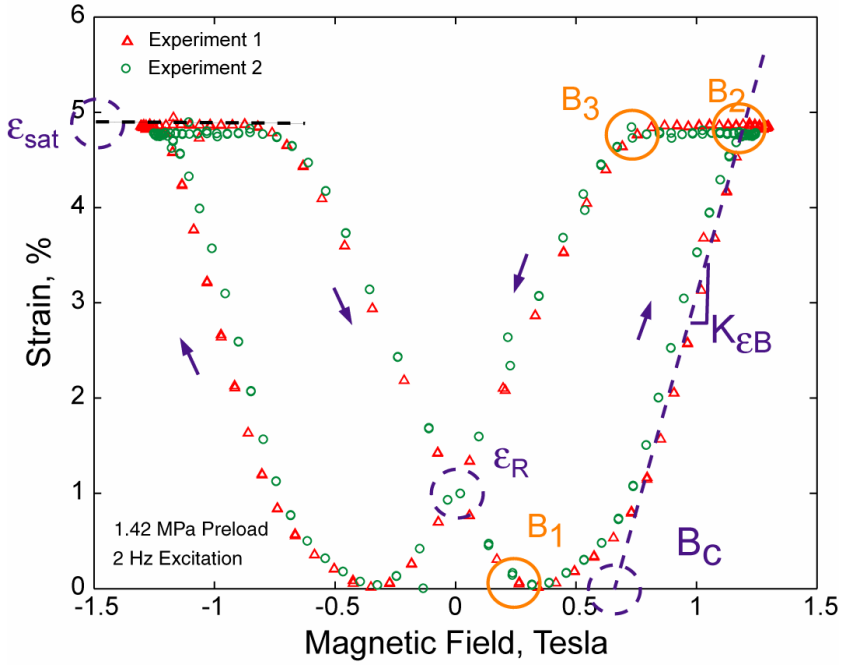

Figure 5.13 Typical strain dynamic strain response for 2Hz excitation and 1.42 MPa pre-stress depicting low-frequency FSMA model parameters

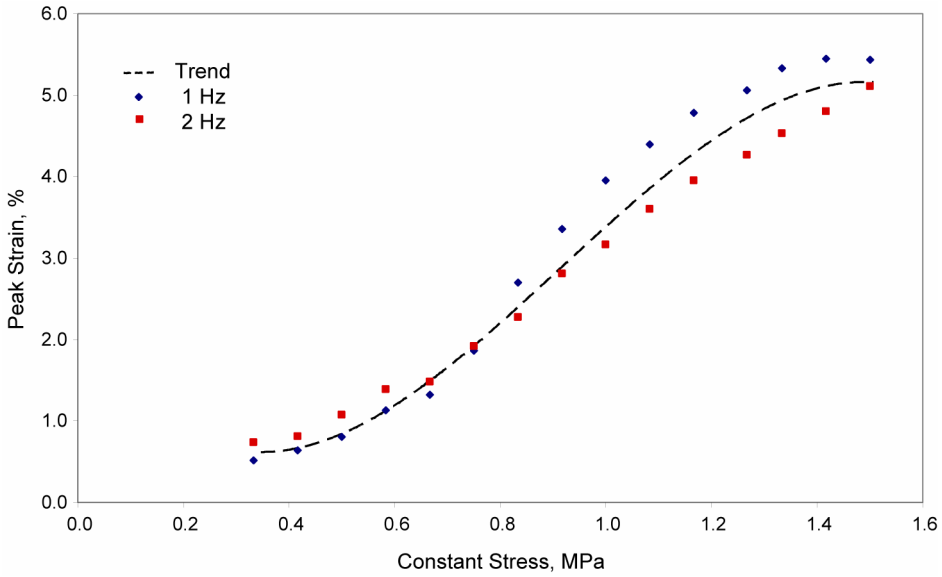

Figure 5.14 Peak strain parameter, ε_{sat}, for 1 Hz and 2 Hz excitation

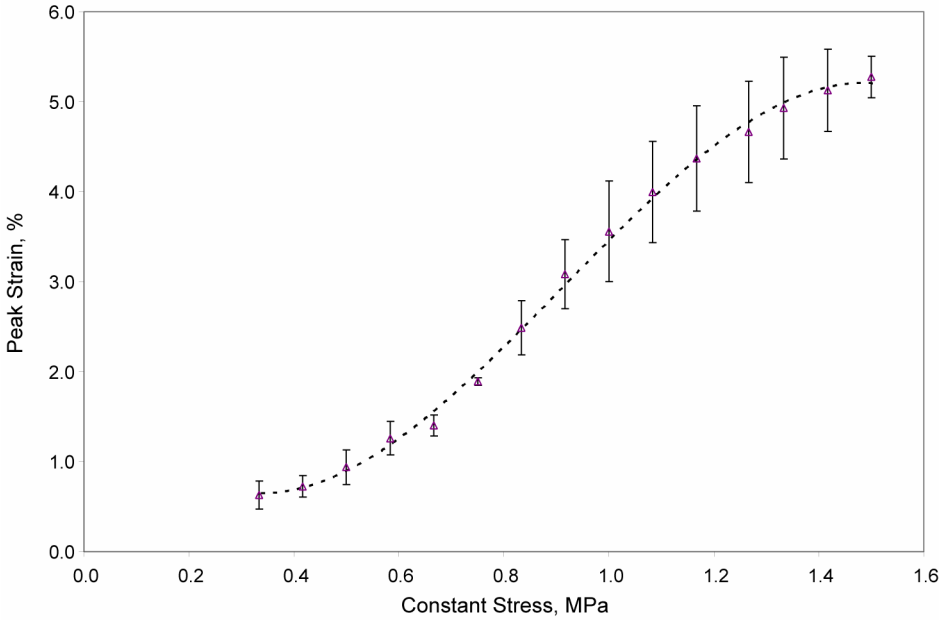

Figure 5.15 Combined peak strain function, ε_{sat}

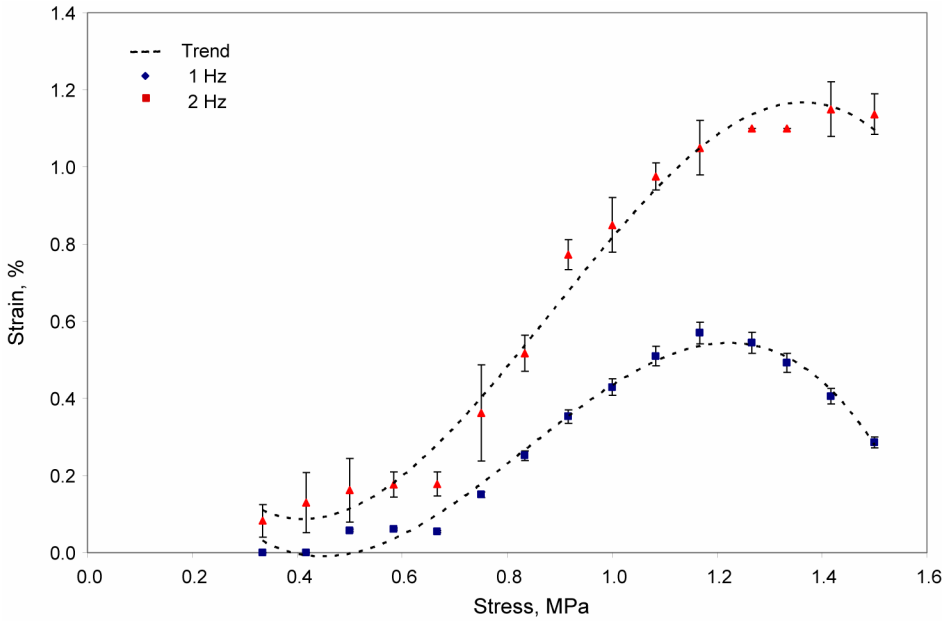

Figure 5.16 Remnant strain parameter, ε_R

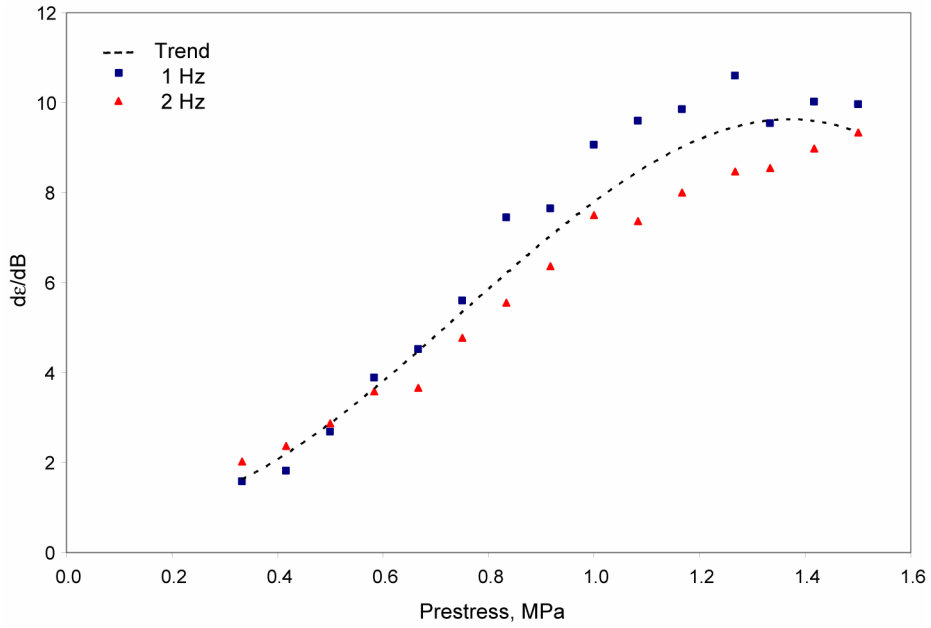

Figure 5.17 Apparent slope parameter, $K_{\varepsilon B}$ ($\delta\varepsilon/\delta B$)

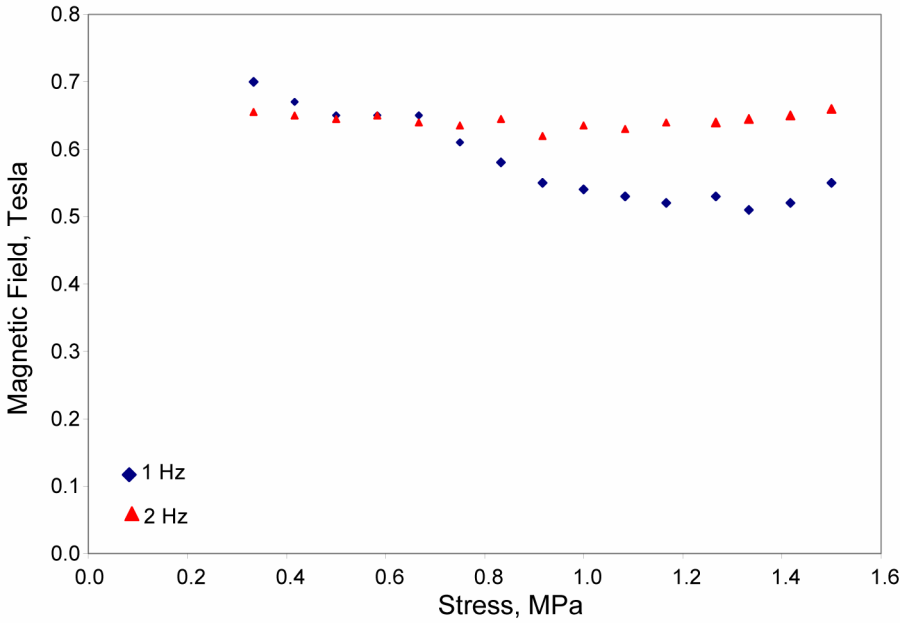

Figure 5.18 Activation field parameter, B_C

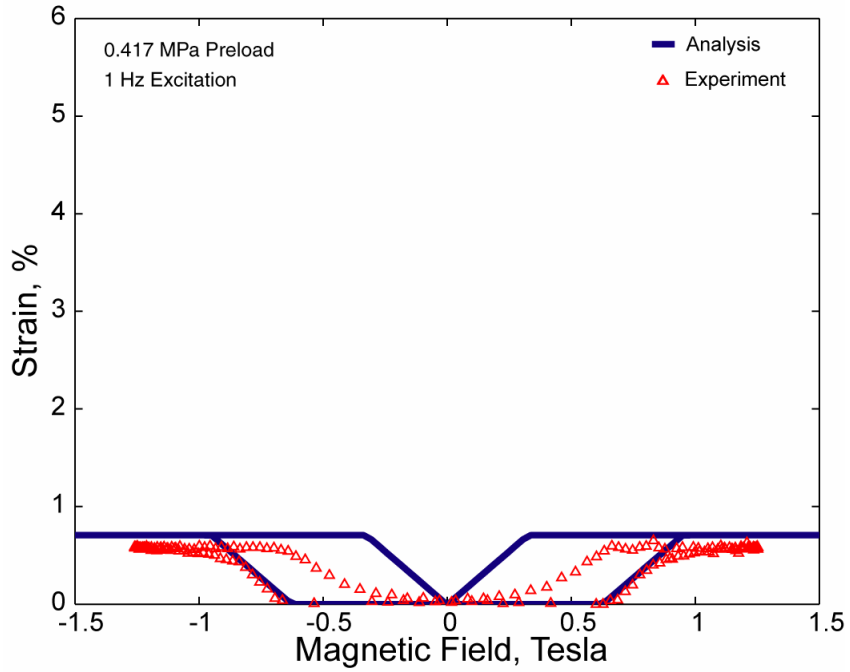

a) 1 Hz excitation

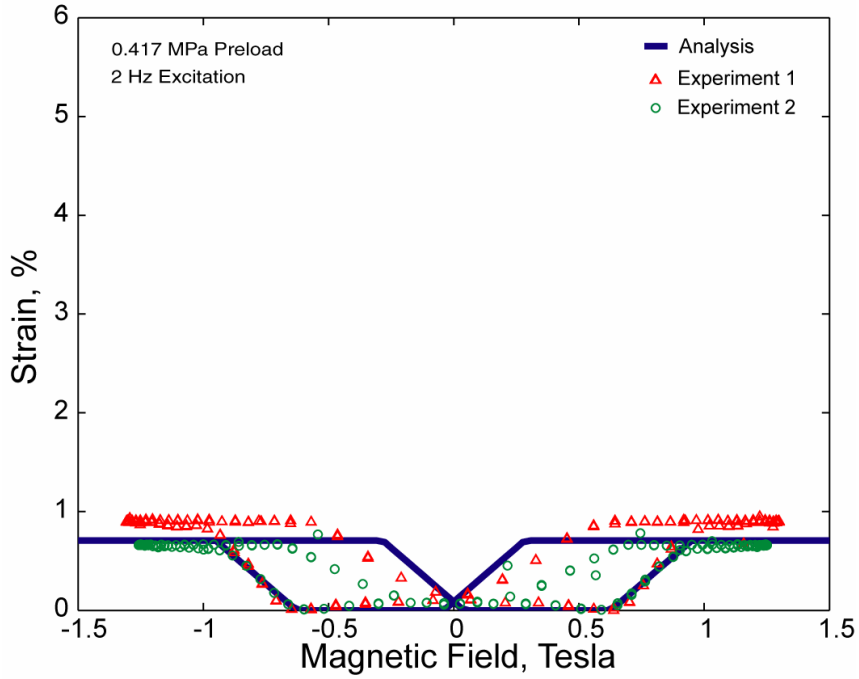

b) 2 Hz excitation

Figure 5.19 Comparison between low frequency model and experimental data for 0.42 MPa constant recovery stress

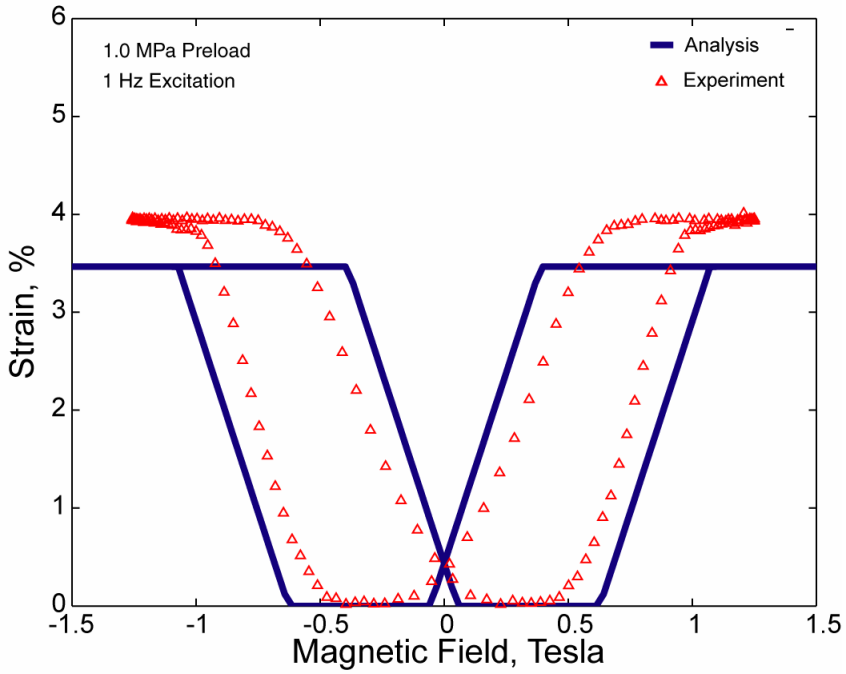

a) 1 Hz Excitation

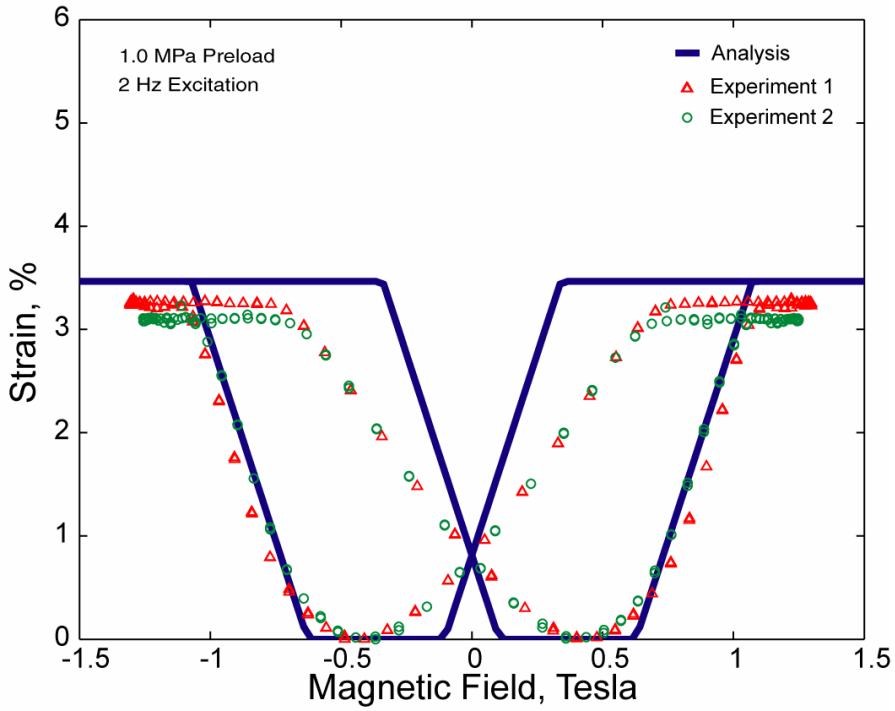

b) 2 Hz Excitation

Figure 5.20 Comparison between low frequency model and experimental data for 1.0 MPa constant recovery stress

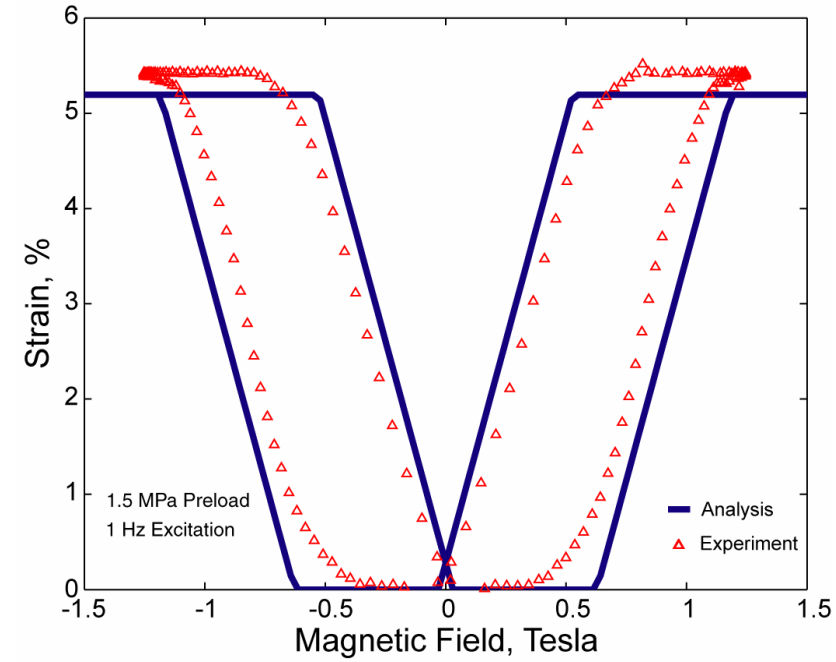

a) 1 Hz Excitation

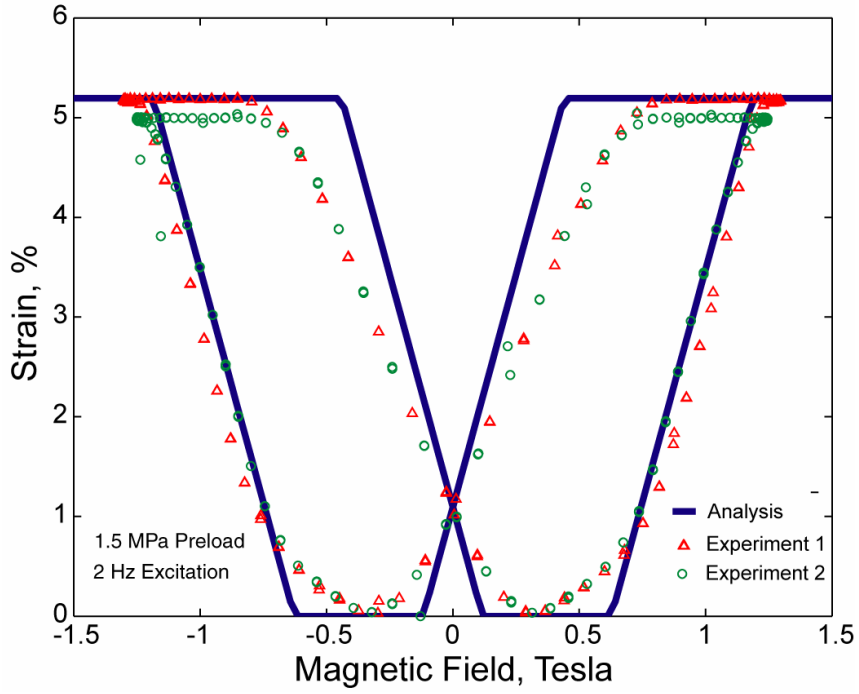

b) 2 Hz Excitation

Figure 5.21 Comparison between low frequency model and experimental data for 1.5 MPa constant recovery stress

Chapter 6: Design of NiMnGa TEF Actuators

The design of NiMnGa actuators for use on a trailing edge flap system for rotorcraft is the focus of this chapter. While previous chapters have been directed towards exploring the capabilities of the material itself, this chapter looks at the combination of the NiMnGa material and the magnetic circuit. One of the main themes of this chapter is the importance of the magnetic circuit. Most of the chapter is devoted towards developing an understanding of the phenomenon of magnetism in order to arrange the underlying principles into a set of actuator design tools.

In a practical sense, the majority of design effort will be directed towards the development of a compact, magnetic circuit capable of delivering the appropriate magnetic conditions to activate the NiMnGa element. The analysis presented here is intended to provide an acceptable estimate for parameters of a FSMA trailing edge flap actuator at the conceptual stage. A more detailed approach involving a higher level of analytical rigor, especially on the optimization of the magnetic circuit, is required to move from the conceptual to prototype stage. The main goal was to highlight the major design issues and to provide an understanding of the difficulties and trends associated with this particular actuator design problem.

The first section is primarily concerned with the development of the concept of magnetic circuits, discussing fundamental coil design principles and power requirements. A review of the basic concepts of magnetism useful for the design of FSMA actuators is provided in Appendix A. In the second section, a set of linearized

constitutive relations is defined for the purpose of providing an estimate of the transduction efficiency of NiMnGa. Section three provides a description of the step-by-step actuator design approach. In this section a conceptual, NiMnGa actuator is designed and optimized. The chapter concludes with a brief discussion on the performance of the conceptual actuator. A comparison of NiMnGa to Terfenol and piezoceramic materials and actuators is also included.

6.1 Magnetic Circuits

High permeability materials such as iron can be utilized to guide substantial amounts of magnetic flux through well-defined, geometrical paths. Networks accomplishing this aspect are known as magnetic circuits [254]. Magnetic circuits are utilized in a wide variety of applications including transformers, motors, loudspeakers and relays. In practice, these magnetic fields are generated by a network composed of a current carrying conductor wound around a high permeability core material of a specified geometry. The combination of the field inducing coil and high permeability core focuses magnetic flux on a region of interest, typically an air gap or some other material volume somewhere along the flux path. As mentioned earlier, magnetic and electrical circuits are closely related and therefore it is convenient to analyze magnetic circuits by considering an equivalent electrical circuit. The following sections provide information regarding this process.

The proceeding analysis focuses on the following magnetic circuit. Consider the simple magnetic circuit shown in Figure 6.1. The circuit consists of a coil of N turns, carrying a current I, wound over a core. The core serves as the circuit's flux return path and has a length l_f, a permeability μ_f, and a constant cross-sectional area A_f. The

effect of the corners is neglected in this simplified example. At a point along the flux path a small air gap of length l_g has been cut. The primary goal of this simple magnetic circuit is to produce a desired flux density across the air gap. To further simplify the analysis, the effects of magnetic 'fringing' are neglected also.

6.1.1 Magnetomotive Force and Reluctance

Just as electric circuits rely on electric potential, or V, to generate current, magnetic circuits rely on magnetomotive force (mmf) to generate flux. Essentially, magnetomotive force is the quantity of magnetic field force or "push" and is analogous to voltage in electrical circuits. MMF is dependant on both coil geometry and magnitude of current within the conductor. The following equation can be used to quantify mmf (V_m):

$$V_m = Ni \tag{6.1}$$

where N is the number of turns in the coil and i is the magnitude of current flowing through the coil. The units of mmf are Ampere-turns or Amp-turns.

The magnetic circuit can be analyzed by implementing a form of Ampere's law which states:

$$V_m = Ni = H_f l_f + H_g l_g \tag{6.2}$$

where the subscripts 'f' and 'g' refer to the flux return path and air gap respectively. Realizing that magnetic flux Φ, is analogous to electric current, it follows that the magnetic flux is conserved throughout the magnetic circuit and therefore constant at any cross section. Or in other words:

$$\Phi_f = \Phi_g = \Phi \tag{6.3}$$

Furthermore, since the flux path maintains a constant cross-sectional area:

$$B_f = B_g = B \tag{6.4}$$

Substitution of eq A.23 into eq 6.2 for the air gap and flux return allows the following relation to be written:

$$mmf = \frac{Bl_f}{\mu_f} + \frac{Bl_g}{\mu_g} \tag{6.5}$$

$$= \frac{\Phi l_f}{A\mu_f} + \frac{\Phi l_g}{A\mu_g} \tag{6.6}$$

$$= \Re_f \Phi + \Re_g \Phi \tag{6.7}$$

where $\Re$ is defined as the material reluctance. Reluctance is the quantitative measure of opposition to magnetic field through a given volume of space or material. It is analogous to resistance in electrical circuits and has the units of Amp-turns/Wb. It must be noted that reluctance is not a constant value. Due to the dependence of magnetic permeability on the external field intensity, reluctance varies accordingly. Generally, reluctance is defined for a volume by the following equation:

$$\Re = \frac{L}{\mu A} \tag{6.8}$$

where L is the length of the volume, A is the cross sectional area and μ is the volume's magnetic permeability.

6.1.2 Ohm's Law for Magnetism

It has been stated that there exists an analogy between electrical and magnetic quantities. As long as magnetic flux is confined to a flow within a well-defined path, this analogous behavior is valid. To determine the equivalent magnetic circuit, all

that is required is to identify the sources of mmf and determine the reluctances of the flux path.

An equivalent Ohm's law for magnetism may be defined. The sum of all mmf drops across the reluctances of the entire path is zero. Based on this magnetic equivalent to Ohm's law, the magnetomotive force (mmf) in a well-defined path can be expressed as:

$$V_m = \Re\Phi \tag{6.9}$$

In Figure 6.2, the equivalent magnetic circuit is shown. If the core material was composed out of low carbon steel, then μ_f is approximately 1000 times greater than μ_g. This means that almost all of the mmf is dropped across the air gap.

There are a few limitations about the magnetic equivalent of Ohm's law that should be noted. In eq. 6.9, the permeability of the core material is assumed to be constant. In reality, the permeability of the core changes depending on the level of flux passing through the cross-sectional area. These changes can be compensated for if the B-H curve of the material is known. However, if a non constant μ_f is assumed, then the magnetic equivalent of Ohm's law is nonlinear.

6.1.3 Power Consumption and Eddy Current losses

To determine the power consumption of a NiMnGa based actuator, the effective impedance of the system must be determined. This impedance of the system consists of an electrical impedance of the coils and the mechanical impedance of the actuator and load. The mechanical impedance is associated with the output work of the actuator, while the electrical impedance is indicative of the work required to generate

the magnetic excitation field. As the case with most smart actuators, the requirements of the power supply are determined by the electrical impedance of the coil.

Ideally, the electrical impedance of the coil consists of two parts. The first part of the impedance represents the finite resistance of the wire used in the windings of the coil. The second part of the impedance arises from the inductance of the coil. This component of the impedance is frequency dependent. Because large magnetic fields are required to actuate the NiMnGa element, the current within the coil must also necessarily be large. It is not uncommon for an actuator to require a coil current on the order of 2 to 3 amperes in order to maintain the necessary level of field across the FSMA element. One way to reduce the current requirement for the coil is to increase the number of turns in the coil. However, using this approach increases the inductance related impedance of the coil which dominates at high operating frequencies. Since the inductance of most FSMA based actuators is large, the power supply must be able to deliver high voltages, especially at high actuation frequencies.

The electrical impedance of the a coil, Z, at an excitation frequency ω, can be expressed by the following relation:

$$Z = R_l + j\omega L \tag{6.10}$$

where R_l is the resistance of the coil windings and L is the inductance of the coil. The resistance of the coil windings results in ohmic heating losses and is given by the following equation:

$$P_{heat} = i_c^2 R_l \tag{6.11}$$

where i_c is the total current passing through the coil. The voltage required for a given operating frequency ω is expressed as:

$$V_l = i_c \sqrt{R_l^2 + \varpi^2 L^2} \tag{6.12}$$

Clearly, eq 6.12 shows the frequency dependent nature of the required voltage. For a constant voltage (supplied by the power supply), as the operating frequency is increased, the effect of the inductance is to reduce the level of current within the coils. Therefore, if the voltage supplied by the power supply is not increased along with operating frequency, the level of magnetic field generated by the coil will drop. The inductance of the field generator is a major limiting factor in NiMnGa actuator design. In order to design an actuator capable of operating at a useful operating frequency, the requirements of the power supply are often quite high. Although the FSMA material may be capable of high-frequency operation, the power requirements required to generate a sufficient magnetic field at that operating frequency are difficult to achieve.

In addition to ohmic losses in the coil, another major source of power loss is due to eddy currents. Eddy currents arise from the effect of an alternating magnetic induction within a conductive medium, like iron. The time varying flux, generates an electromotive force (emf) around the cross section of the core as per Faraday's law. The magnetic fields generated by these currents oppose the change in flux density. In general, eddy currents are undesirable in FSMA actuator design because they produce additional ohmic (I^2R) losses. Because of their high conductivity, ferromagnetic materials are especially susceptible to eddy current losses. Figure 6.3(a), shows a schematic representation of eddy currents in a solid core.

One way to reduce the effect of eddy currents is to manufacture the core out of a series of thin lamina. As long as a thin insulating layer of insulating material

separates each lamina, the effect of eddy currents is significantly attenuated. Because of the layer of insulation, eddy currents are allowed to flow within the lamina but not between them. Since the induced emf in each lamination is proportional to the cross-sectional area and the resistance is proportional to the perimeter, the dissipated power is reduced. For a thin lamination, halving the width doubles the resistance and halves the current without altering the length of the current path. Figure 6.3b illustrates the phenomena of eddy currents in a laminated core. In general, eddy current losses are inversely proportional to the square of the number of laminations. In iron, eddy current losses are generally between 1 and 8 Watts per kilogram at 50 Hz and 1.5 T for good transformer steel. One minor drawback to using a laminated core is that the permeability of the core is slightly reduced. However, the reduction of magnetic permeability does not overshadow the significant reduction in eddy current losses.

As an example, consider Figure 6.4 which depicts a lamina if thickness h, width b, and length l [253]. The lamina is placed in a sinusoidally varying magnetic inductive field B, aligned perpendicular to the x-y plane. It is assumed in this analysis that eddy currents do not affect the level of flux density and the magnetic permeability of the lamina material is constant. The magnitude of the inductive field is expressed as:

$$B = B_0 \sin \omega t \tag{6.13}$$

where B_0 is the amplitude and ω is the circular frequency (rad/s). The changing magnetic induction produces a voltage in the laminate that results in a flow of current. Consider an elemental piece of the lamina of thickness h, width dz and length dx. A current element of thickness dy is shown in Figure 6.5, which is a part of a current

loop extending across the entire cross-section of the lamina depicted in Figure 6.4. The resistance of the element is given by:

$$dR = \rho \frac{1}{A} = 2\rho \frac{dx}{dydz} \tag{6.14}$$

where ρ is the resistivity of the material. The voltage produced is governed by the following equation:

$$dV = -\frac{d\phi}{dt} = -2\,ydxB_0\varpi \cos \varpi t \tag{6.15}$$

Therefore, the power dissipated in the element as a function of time is given by:

$$dP(t) = \frac{(dV)^2}{dR} = \frac{4y^2 B_0{}^2 \varpi^2 \cos^2 \varpi t}{2\rho} dydxdz \tag{6.16}$$

The average power dissipated, dP_d, is given by:

$$dP_d = \frac{\varpi}{2\pi} \int_0^{2\pi/\varpi} dP(t)dt \tag{6.17}$$

$$= \frac{B_0^2 \varpi^2}{3\rho} \frac{h^3}{8} dydx \tag{6.18}$$

The power dissipation per unit volume is determined by dividing the preceding equation by the volume of the element, *h dx dy*. The result indicates the eddy current loss per unit volume in the lamina which is:

$$P_d = \frac{B_0^2 \varpi^2 h^2}{24\rho} \tag{6.19}$$

Based on the result in eq (6.19), it is clear that the eddy current losses are also inversely proportional resistivity of the lamina material and directly proportional to the square of the lamina thickness. Consequently, the most effective way to minimize

eddy current losses is to design a flux return patch consisting of many thin lamina of high resistivity.

6.2 Constitutive Relations and Coupling Coefficient, k

FSMA materials, like all active materials, are essentially energy conversion devices. NiMnGa actuators convert magnetic energy into mechanical energy. The coupling coefficient, *k* is a measure of the efficiency of this energy conversion. This section focuses on defining and measuring *k* for NiMnGa FSMA.

6.2.1 Constitutive Relations and the Calculation of *k*

In Chapter 2, it was shown that the mechanism of field induced strain in NiMnGa is a non-linear function of the applied magnetic B-field. In fact, the relationship between the B-field and the induced strain can be expressed as a quadratic function. If the FSMA material is operated about a bias point, the induced strain can be assumed to vary linearly with the applied field. In this region, a set of linear constitutive relations can be written to model the behavior of the material. These relations are similar to those for piezoelectric materials [114, 214]. The linear coupled magneto-mechanical constitutive relations for a one dimensional FSMA material are:

$$\varepsilon = s^H \sigma + dH \tag{6.20}$$

$$B = d\sigma + \mu^\sigma H \tag{6.21}$$

where d (m/A) is the magneto-mechanical coupling coefficient corresponding to the slope of the linear region of the ε-H curve, and μ^σ is the magnetic permeability of the material at constant stress, corresponding to the slope of the B-H curve, s^H is the

compliance of the material along the direction of strain at a constant field intensity [222, 257]. There are three fundamental assumptions ascribed to these equations. The first, which has already been stated, assumes that the operation of the transducer is linear. Despite the fact that magnetic shape memory induced strains are non-linear in nature, it can be assumed that for small signal levels, approximately one third the maximum strain capability of the NiMnGa, eq (6.20) and eq (6.21) provide reasonable, linear approximations. The second assumption equates the magneto-mechanical coupling term 'd' in eq (6.20) to the magneto-mechanical coupling term 'd' in eq (6.21). Strictly speaking, these quantities are not equal. One represents the derivative of B with respect to stress at constant field strength (H), while the other represents the derivative of the strain, ε, with respect to the field strength (H) with the stress held constant. Although this assumption simplifies the coupled equations, it is often a poor approximation of the coupling term. Nevertheless, this approach provides a reasonable starting point to the analysis of a NiMnGa actuator. Finally, it is assumed that the quantities σ (stress), ε (strain), H and B are uniform throughout the NiMnGa element.

To determine the coupling coefficient, consider eq (6.20) and eq (6.21). H may be eliminated by considering eq (6.21):

$$H = \frac{B}{\mu^{\sigma}} - d\frac{\sigma}{\mu^{\sigma}} \tag{6.22}$$

Substituting eq (6.22) into eq (6.20) yields:

$$\varepsilon = s^{H}\sigma + d\left(\frac{B}{\mu^{\sigma}} - \frac{d\sigma}{\mu^{\sigma}}\right) \tag{6.23}$$

$$= s^H \left(1 - \frac{d^2}{\mu^\sigma s^H}\right)\sigma + d\frac{B}{\mu^\sigma} \tag{6.24}$$

$$= s^H \left(1 - k^2\right)\sigma + d\frac{B}{\mu^\sigma} \tag{6.25}$$

where k is the magneto-mechanical coupling coefficient and is given by:

$$k^2 = \frac{d^2}{s^H \mu^\sigma} \tag{6.26}$$

Alternatively, coupling coefficient can be estimated by the ratio of strain and magnetic energy by the following relation:

$$\frac{U_{mechanical}}{U_{magnetic}} = \frac{d^2}{s^H \mu^\sigma} = k^2 \tag{6.27}$$

As a consequence of eq (6.27), the magneto-mechanical coupling coefficient is basically an estimate of the energy conversion efficiency (transduction efficiency) of the material. This value places an upper bound on the magnitude of the mechanical power output of an NiMnGa actuator for a given magnetic input.

6.2.2 Measuring the Coupling Coefficient, *k*, in NiMnGa

In section 6.3.1, the coupling coefficient for NiMnGa was defined. Not only does the coupling coefficient provide an estimate of the efficiency of the actuator material, but it can also provide a means with which to compare NiMnGa with other active materials. This section focuses on measuring the coupling coefficient of NiMnGa from experimental data. Three quantities must be determined in order to calculate the value of k: the magneto-mechanical coupling term, d, the material compliance for constant field intensity, s^H, and the magnetic permeability for constant stress, μ^σ.

The material compliance was determined from data obtained from the quasi-static constant drive current testing detailed in section 3.5. For each applied field, the Young's modulus of material was measured. As an example, consider the stress-strain curve for a constant applied field of 8 kOe shown in Figure 6.6. The compliance of interest occurs over the transition region representing the twin boundary motion and subsequent induced strain of the FSMA. The modulus in this transition region, E_t, was measured for all applied fields. In Figure 6.7, the transition modulus as a function of the applied field intensity is shown. For applied fields below 2 kOe, the transition modulus appeared to be linearly related to the applied field. Beyond 2 kOe, this modulus was assumed to have a constant value. In order to best represent the capabilities of the FSMA material, the transition modulus, E_t, was estimated to be the average value between 2 kOe and 9 kOe. However, it was noted that since the standard deviation of the transition modulus in this region was significant (on the order of 2.45 MPa), implying that there exists a degree of uncertainty in this measurement. But in the context of this first order approximation, this level of uncertainty was deemed acceptable. The experimentally determined value for E_t was:

$$E_t = 26.97 MPa \tag{6.28}$$

It follows that the compliance of NiMnGa for constant field intensity, s^H is:

$$s^H = \frac{1}{E^t} \tag{6.29}$$

The magneto-mechanical coupling term was determined from the dynamic constant load tests detailed in section 4.3.2. First, the strain response had to be related to the magnetic field intensity. To convert the data from ε-B to ε-H, the

magnitude of the coil current for each case of constant stress testing was measured and multiplied by the number of turns in the coil and divided by the coil length as per eq. (A.14). This was done in order to determine the actual field intensity generated by the coil thereby directly relating the strain response to the magnetic energy delivered to the NiMnGa material. Figure 6.8 shows the strain response as a function of the applied field intensity for varying levels of constant stress and 1 Hz excitation frequency. To measure the magneto-mechanical coupling coefficient, the slope of the strain response was measured and is denoted on Figure 6.8 as 'd_1'. However, it was noted that according to the data presented in Figure 6.8, the value of 'd_1' is not constant for all stress levels. In fact, below 0.917 MPa, the value of 'd_1' appeared to vary according to the level of applied stress. Figure 6.9 shows 'd_1' as a function of applied stress. Based on this data, 'd_1' appears to be quadratically related to the constant recovery stress below 0.917 MPa and constant above 0.917 MPa. For the purposes of estimating the magneto-mechanical coupling, the value of 'd_1' above 0.917 MPa was used.

$$d = d_1 = 1.703E-07\left(m/A\right) \tag{6.30}$$

The final term required for calculating the coupling coefficient is the magnetic permeability for constant stress, or μ^{σ}. Because it was not possible to directly determine this value from experiment, the permeability was obtained from the manufacturer, Adaptamat [135]. The manufacturer lists the relative permeability (μ_r value) as ranging from 1.5 to 40. The relation of B to H in a magnetic circuit and its components is not constant, therefore the magnetic permeability of the FSMA element will not a constant, but inherently a function of the magnetic field. As a

result, both cases were included in the calculation of the coupling coefficient in order to illustrate the impact of magnetic permeability on the calculation. Furthermore, this approach will serve a means to provide an upper and lower boundary for the value of the coupling coefficient.

To quantify the coupling coefficient for NiMnGa, the experimentally determined parameters were substituted in eq (6.26) and solved for k. In Figure 6.10, the magnitude of k is shown as a function of the constant recovery stress. Two cases, one associated with a relative permeability of 1.5 and one associated with a relative permeability of 40 are shown. As expected, the behavior of k shares the same characteristic behavior of the magneto-mechanical coupling term d. The maximum value of k for both values of permeability occurs for recovery stresses above 0.917 MPa. Furthermore, as the magnetic permeability increases, the magnitude of the coupling coefficient decreases. Assuming that k is measured for a constant recovery stress greater than or equal to a 0.917 MPa, the range of the coupling coefficient is as follows:

$$0.125_{(\mu^{\sigma}=40)} > k > 0.644_{(\mu^{\sigma}=1.5)} \tag{6.31}$$

One of the reoccurring themes evident in the behavior of NiMnGa is that many of its properties are dependent on the level of recovery stress. The coupling coefficient was also shown to be a strong function of the recovery stress. This result further highlights the importance of being aware of the recovery forces acting on the FSMA element when designing actuators. Furthermore, it was interesting to note that increasing the relative magnetic permeability of the material effectively decreases the transduction efficiency of the material as an energy conversion device.

6.2.3 Coupling Coefficient, Permeability and NiMnGa Magnetic Circuits.

One of the main disadvantages of NiMnGa is associated with the large magnetic fields (B-field) required to induce twin boundary motion. As a result, when designing FSMA actuators, it is necessary to optimize the magnetic circuit for flux generation. Consider a magnetic circuit (shown in Figure 6.11) containing a flux return path, air gap, and NiMnGa element each associated with a reluctance $\Re_f$, $\Re_g$, and $\Re_{fsma}$ respectively. To activate twin boundary motion, the FSMA element requires a flux density B_{act}. In order to examine the effect of permeability on efficiency and required power, two magnetic permeabilities will be considered μ_{high}^{σ} and μ_{low}^{σ} where $\mu_{high}^{\sigma} >> \mu_{low}^{\sigma}$.

Writing the magnetic equivalent of Ohm's law for the magnetic circuit results in the following:

$$\Phi = \frac{V_m}{\Re_f + \Re_g + \Re_{fsma}} \tag{6.32}$$

To simplify the analysis, it is assumed that the air gap is very small. Since the relative permeability of air is much smaller than iron, (typically μ_r = 1000-3000 for iron and μ_r = 1 for air) the reluctance of a large air gap will potentially be three orders of magnitude larger than the reluctance of the iron core. In order to compensate for this difference in relative permeability, the length of the air gap must be at least 5-6 orders of magnitude smaller than the length of the flux return path. This will be necessary in order to ensure that the reluctance of the air gap is several orders of magnitude smaller than the reluctance of the flux return path. Then it becomes

reasonable to assume that the reluctance of the air gap in eq (6.55) becomes negligible when compared to the reluctance of the flux return path and the FSMA element. Rewriting eq (6.32):

$$\Phi = \frac{V_m}{\Re_f + \Re_{fsma}} \tag{6. 33}$$

Substituting eq (A.24) and the required flux for twin boundary activation of the FSMA material allows eq (6.33) to be rewritten as follows:

$$B_{act} A_{fsma} = \frac{N i_{req}}{\Re_f + \Re_{fsma}} \tag{6.34}$$

where i_{req} represents the magnitude of required coil current and N the number of turns in the coil (a fixed parameter). Solving eq (6.34) for i allows the required coil current for FSMA actuation to be determined.

$$i_{req} = \frac{B_{act} A_{fsma}}{N} \left(\Re_f + \Re_{fsma} \right) \tag{6.35}$$

where N, i, A_{fsma}, and B_{act} are constants.

1) Case 1 $\mu^{\sigma} = \mu^{\sigma}_{high}$

   In this case, the permeability of the FSMA is large. According to eq (6.8), a high magnetic permeability has the effect of reducing the reluctance of the FSMA. Therefore, the required coil current, i_{req}, is small.

2) Case 1 $\mu^{\sigma} = \mu^{\sigma}_{low}$

In this case the permeability of the FSMA is small. According to eq (6.8) a small magnetic permeability has the effect of increasing the reluctance of the FSMA. Therefore, the required coil current, i_{req}, is large.

So, for a small magnetic permeability, the required coil current to induce twin boundary motion is larger than the required current for a large magnetic permeability. Consequently, the required coil power for the small permeability case is larger than the case where magnetic permeability is large. Intuitively, this result makes sense. A larger magnetic permeability means that the material accepts more magnetic flux which in turn means that a smaller mmf is required to induce twin boundary motion. However this result seems to be at odds with the result determined in eq (6.31) where a small magnetic permeability produces higher transduction efficiency. Based on the available evidence, it was concluded that although a high material permeability is desirable to minimize the required coil power, it also decreases the transduction efficiency of the energy conversion. In other words, the design of the magnetic circuit for FSMA actuators may require a trade off between required power and efficiency.

In practice, in order to avoid magnetic saturation in the flux path, the generation of large flux densities often requires the flux return paths to have sizeable cross-sectional areas and subsequently large volumes of high permeability materials. Given that high permeability materials are typically very heavy, NiMnGa based actuators also tend to be very heavy devices with the majority of the mass concentrated on the flux return path.

6.3 FSMA Actuator Design

This section focuses on the design of a conceptual NiMnGa actuator for driving trailing edge flaps on the rotor blade of a model MD 900 Explorer helicopter. First, a set of actuator requirements specific to the MD 900 rotor system are defined. Then the algorithm for the coil design is outlined. Once a conceptual design is determined, it will be compared to other active materials in order to assess the capabilities of an NiMnGa based actuator.

6.3.1 Sizing NiMnGa Element for Trailing Edge Flap Actuator

Based on the aeromechanics analysis presented by Shen and Chopra [136, 137] the following set of actuator requirements were determined.

R1. Actuator force requirement: 40-60 N

R2. Actuator stroke requirement: 0.5 - 2.0 mm

R3. Actuator size constraint: 5 cm maximum height

R4. Actuator bandwidth: maximum operating frequency: 50 Hz

It is important to point out the **R3** exists as a physical constraint of the D-spar of the helicopter blade. In the development of the conceptual NiMnGa actuator it was assumed that the actuator was imbedded within the D-spar. If the actuator was located aft of the D-spar than the maximum height requirement may be reduced.

The requirements **R1** and **R2** are used to determine the physical dimensions of the NiMnGa element. To determine the cross-sectional area of the FSMA material, it **R1** was used. Solving eq (6.20) for σ yields:

$$\sigma = \frac{(\varepsilon - dH)}{s^H} \tag{6.36}$$

The force requirement defined by **R1** was then substituted into eq (6.36) and then solved for the cross-sectional area. The cross-sectional area was determined by the following equation:

$$A = \mathbf{R1}\frac{s^H}{(\varepsilon - dH)} \tag{6.37}$$

Once the cross-sectional area had been determined, the length and height of the FSMA element were determined. It should be noted that this method of sizing the FSMA element was meant only as a first order approximation. Eq (6.37) was developed from a linearized equation and is valid only for low signal levels (approximately one third the maximum strain capability. In practice, a more rigorous method of sizing must be implemented in order to precisely size the NiMnGa element. This first order analysis was meant to find the minimum requirements for a conceptual NiMnGa based actuator. Although all of the assumptions in sizing may not be valid in practice, they nevertheless provide a reasonable starting point for actuator design.

To calculate the length of the FSMA element, a desired induced strain of 1.7% was chosen. Although the NiMnGa material was capable of 5% strain, the maximum induced strain could not be used in this case. The derivation of eq (6.20) assumes that the FSMA element was operating in a linear region. Because the FSMA strain response is nonlinear, the underlying assumption was that a linear or near-linear response could be achieved at low signal levels. The linear region in this case was defined as operation about a bias point of 3% strain with a peak-to-peak amplitude of

no more than one third the maximum induced strain capability. In the case of magnetostrictive transducers, another non-linear material, this approach yields a good first approximation [222]. Since **R2** called for a maximum stroke of 2 mm, a total length of approximately 118 mm was required in order for the NiMnGa element to achieve the required stroke for 1.7% induced strain.

The remaining two requirements **R3** and **R4** are utilized to size the entire actuator and calculate the required power respectively. In Table 6.1, the NiMnGa element dimensions and sizing constants for the conceptual actuator are shown.

6.3.2 Designing NiMnGa TEF Actuators

Once the FSMA element was sized, a magnetic circuit was designed. Using a spread sheet, a series of circuit configurations were calculated and then evaluated based on mass and power consumption. The core of the magnetic circuit consists of a laminated E-frame shape of transformer grade steel. The dimensions of the actuator are depicted in Figure 6.12(a) and Figure 6.12(b). Since the core was a laminated structure, the eddy current losses were assumed to be small and neglected for this first order analysis.

The algorithm for designing the coil and actuator dimensions consists of nine basic steps.

1.) Calculate the cross sectional area of the flux return path. The parameters t_1 and l_c should match the corresponding dimensions of the active material plus an additional 10-20% to account for fringing in the air gap. This can be represented by a 'fringing factor' F, that is expressed as a percentage of the

length of the active material. Including the fringing factor ensures that the field across the poles of the field generator is close to uniform. For an FSMA bar of width w_s and length l_s:

$$t_1 = w_s(1+F)/2 \tag{6.38}$$

$$l_c = l_s(1+F) \tag{6.39}$$

2.) Determine the length of the solenoid l_o. The length of the solenoid is based on the dimension l_1, which can be chosen based on other specifications such as overall actuator dimensions.

$$l_o = k(l_1 - t_1/2) \tag{6.40}$$

Assume that k is between 0.6 and 0.9 to account for the gap between the poles or tapering of the central arms. The gap between the faces of the middle arms of the E-frame is fixed by the thickness of the FSMA element, t_s, with as little air gap as possible.

3.) Estimate the required *mmf*. Because the geometry of the flux return path is not known at this point, in this initial calculation it is assumed that the *mmf* required is dependent only upon the reluctances of the air gap and FSMA sample. The effect of the flux return path is neglected for now but will be added in a later step to serve as a check on the initial estimate. This assumption is only valid if the permeability of the flux return is large, and its reluctance is small compared to that of the sample and the air gap. The *mmf* is given by:

$$mmf = B_a A_c \left(\Re_a + \Re_s \right) \tag{6.41}$$

where B_a is the required magnetic flux density, A_c is the core cross-section (given by l_c x $2t_1$) and $\Re_a$ and $\Re_s$ are the reluctances of the air gap and the FSMA sample respectively.

4.) Assume the coil geometry. Choose the total number of turns, N_{tot}, and a wire gauge. From these parameters, the number of turns per layer N_t, and the number of layers in the coil N_l can be determined. The remaining calculations are performed for several values of N_{tot} so that the optimum value can be identified. This procedure is much simpler to implement than finding a closed form solution for the optimum number of turns. For a wire diameter d_w:

$$N_t = \frac{l_o}{d_w} \tag{6.42}$$

$$N_l = \frac{N_{tot}}{2N_t} = \frac{t_2 - t_1}{d_w} \tag{6.43}$$

In eq (6.42) and eq (6.43), any imperfections in winding the wire are neglected. This assumption becomes more accurate as the wire diameter decreases.

5.) Find the remaining dimensions of the flux return path. To minimize the mass of the flux return, it is assumed that the coil will fill all the empty space in the E-frame. Using the value of N_l, the remaining dimensions of the E-frame, t_2 and l_2 are calculated.

$$t_2 = N_l d_w + t_1 \tag{6.44}$$

$$l_2 = 3t_1 + 2N_l d_w \tag{6.45}$$

6.) Determine the electrical properties of the circuit. Now that the geometry of the E-frame has been determined, the length of the wire in the coil, l_w, and the resistance of the coil can be calculated. In addition, since the geometry of both the coil and the E-frame are now known, the inductance of the coil can also be calculated. The length of the wire is given by:

$$l_w = N_{tot}\left(2l_c + 4t_2\right) \tag{6.46}$$

For a wire of cross-sectional area A_w, with a resistivity ρ_w, and a flux return path of permeability μ_c, the resistance of the coil R_w and the inductance L_w are:

$$R_w = \frac{N_{tot}\rho_w}{A_w}\left(2l_c + 4t_2\right) \tag{6.47}$$

$$L_w = \frac{N_{tot}^2 \mu_c l_c t_1}{l_2 + 4l_1} \tag{6.48}$$

7.) Determine the magnitude of the power required by the coil. The current flowing in the coil i_w, is determined by dividing the *mmf* by the assumed number of turns.

$$i_w = \frac{mmf}{N_{tot}} \tag{6.49}$$

From the required current and the calculated coil impedance, the power required, P_w, at a given operating frequency can now be determined.

$$P_w = i_w^2 \sqrt{R_w^2 + L_w^2} \tag{6.50}$$

Note that the heat produced by the coil, P_d, is purely due to ohmic heating and is given by:

$$P_d = i_w^2 R_w \tag{6.51}$$

8.) Determine the mass of the magnetic field generator. Provided that the densities of the material used in the flux return and in the wire are known, the mass of the magnetic field generator can be calculated. The mass of the flux return M_a and coil M_w are given by:

$$M_a = 2\rho_c l_c \left[4t_1 \left(l_1 - \frac{t_1}{2} \right) + t_1 (l_2 + t_1) \right] \tag{6.52}$$

$$M_c = \rho_w l_w A_w \tag{6.53}$$

where ρ_c is the density of the material of the flux return and ρ_w is the density of the material of the wire. The total mass of the magnetic field generator is:

$$M_{tot} = M_c + M_w \tag{6.54}$$

9.) Determine the actual *mmf* produced. Now that all the parameters are known, the reluctance of the flux return path can be determined and included into the *mmf* calculation. If it is small then the initial assumption is valid and the reluctance of the flux return can be neglected. If the reluctance is large then it must be included into the calculation of *mmf*. Comparing the predicted mmf to the required mmf, in this manner gives an indication of the accuracy of the coil design. Since the number of turns, N_{tot} is fixed for each design the current

in the coil must be increased to compensate for the increase in *mmf*. Once the true current in the coil is known it can be substituted into the power equation and the actual required power of the coil can be determined.

10.) The coil impedance, required power and total mass is calculated for each assumed value of N_{tot}. From these calculations, based on important requirements such as maximum driving frequency (minimum L_w), minimum total power, minimum heating of the coil (minimum R_w), and minimum total mass, the optimum coil geometry can be chosen.

The following section details the choices made to select the optimum magnetic circuit for the NiMnGa actuator.

6.3.3 A Conceptual NiMnGa actuator

Once the NiMnGa element was sized, the next task was to design a magnetic circuit capable of meeting the actuator requirements discussed in section 6.4.1. The design algorithm outlined in the previous section was used to generate coil designs. In order to find an optimum design, hundreds of conceptual actuators and their associated parameters were calculated via a spreadsheet. The independent parameters of the actuator design were associated with coil geometry, i.e. the number of turns in the coil, *N*, and the wire gauge of the coil windings. By varying both *N*, and the wire gauge, a wide range of actuator parameters could be calculated. Each actuator configuration was forced to conform to the **R3** and **R4** requirements discussed in section 6.4.1. By utilizing this approach, every actuator configuration was capable of

meeting all the trailing edge flap system design requirements. As a result, an optimum configuration could be identified by plotting specific quantities as functions of the wire gauge and number of turns.

The two main considerations for the design of a conceptual NiMnGa actuator were required power and mass. Both of these qualities should be made as low as possible for the final actuator design to maximize the performance. Coil heating arising from ohmic losses should also be minimized. As a practical consideration, cooling an on-blade TEF actuator would be a difficult task. Water cooled coils are out of the question and forced convection within an aerodynamic surface (rotor blade) would be problematic. Coil heating is not desirable for two main reasons. First, if the coil generates too much heat, it can potentially damage the FSMA element by causing a phase transition from martensite to austenite therefore eliminating the magnetic shape memory properties of the material. Second, if the coil becomes too hot, the insulation on the copper windings could potentially burn resulting in a short-circuit condition, and causing coil failure. Both problems lead to a potentially catastrophic failure of the actuator, therefore it was necessary to minimize ohmic losses.

In Figure 6.13, the required current for achieving a 1 T inductive field was plotted against the wire gauge. Based on this information, increasing the number of turns, N, decreases the required current in the coil. In fact, according to Figure 6.13, doubling the number of turns reduces the required current by half. This result was intuitive given that the mmf required to generate the desired inductive field depends on the number of turns and current only. At this point in the design process, it appeared that

configurations with the maximum number of turns should receive the most consideration.

In Figure 6.14, the heat generated as a function of wire gauge and coil turns is shown. For each value of N, the heat generated by the coil tends to increase as the wire gauge becomes smaller (increasing wire gauge). Furthermore, for a constant wire gauge, coil heat increases as the number of turns decreases. From a heat generation perspective, it appeared that a coil with a small wire gauge (larger wire diameter) and large number of turns was desired. This supposition did not hold true when the actuator mass was taken into consideration. In Figure 6.15, the total actuator mass as a function of the wire gauge and number of turns is shown. As the wire gauge was increased, the total mass of the actuator decreased. It was also noted that mass increased as the number of coil turns increased. Therefore, in terms of mass, it was observed that the lightest coils were those with small wire diameter (high wire gauge) and low number of turns. Clearly, there exists a trade off between heat generation and actuator mass. From a practical application perspective, it was decided that optimizing for heat generation should take slight precedence over actuator mass. Heat dissipation from a source consisting of tightly wound coils in the confined allowable space within a rotor blade presents a difficult technical barrier. In order to ensure that the active material element does not lose its actuation capabilities as a result these thermal conditions, a cooling system would be required. It was reasoned that any mass savings gained from sacrificing minimum heat generation capability would by lost when actuator cooling systems were added to the design.

The total power consumption of the actuator as a function of wire gauge and number of turns is shown in Figure 6.16. Based on this information, power consumption was minimized for large number of turns and large wire diameters (small wire gauge).

Since power generation and coil heating are minimized for a large number of turns only cases where N = 1000 were considered for the final design. Table 6.2 shows the relevant actuator parameters for each design configuration. The final configuration was determined by evaluating the configurations as a function of wire diameter. Configurations that exceeded the height constraint of 5 cm defined in **R3** were rejected. It was decided that a wire gauge of 20 provided the best trade between coil heating, total mass, and required power. The finalized actuator parameters and actuator specifications are shown in Table 6.3 and Table 6.4 respectively.

6.4 FSMA Conceptual Actuator Performance

Once the conceptual actuator was designed, an approximation of the general performance parameters was performed. Quantities such as power density and efficiency were estimated so that the actuator could be compared to other, similar actuator systems.

6.4.1 Estimation and Evaluation of Performance Parameters

The power density of the conceptual actuator was calculated. First, the total power output $P_{o,}$ was determined from the trailing edge flap requirements (section 6.4.1) and the following equation:

$$P_o = F \times D \times f \tag{6.55}$$

where F was the peak value of force as prescribed by **R1**, D was the maximum stroke as prescribed in **R2**, and f was the operating frequency stipulated by **R4**. Once the power was calculated, the power densities by weight (Q^w) and by volume (Q^v) were calculated by the following equations:

$$Q^w = P_0 / M_a \tag{6.56}$$

$$Q^v = P_0 / V_a \tag{6.57}$$

where M_a was the total mass of the actuator and V_a was the total volume of the actuator.

The overall efficiency of the actuator was also determined. Overall efficiency was defined as the total output power divided by the required electrical power. The equation for overall efficiency was:

$$Q_{eff} = P_o / P_w \tag{6.58}$$

where P_0 was the power output of the actuator and P_w was the total required electrical power to drive the magnetic circuit.

In Table 6.5, the performance parameters of the conceptual actuator are shown. The power density of the actuator by volume Q^v, was determined to be 625 kW/m^3. This value was several orders of magnitude less than the power density calculated for the NiMnGa element (section 4.4.2). Clearly, the power density determined for the actuator reflects the influence of the large magnetic circuit volume. In general, FSMA actuators require relatively large magnetic circuit volumes in order to operate. In fact, the volume of the NiMnGa element accounted for only 4.16% of the total actuator volume (actuator volume: 5.06e^{-4} m^3 vs. element volume: 2.19e^{-5} m^3). The fact that the material requires a much larger magnetic circuit volume to activate the

twin boundary motion significantly diminishes its attractiveness for use in this particular application. The overall efficiency of 1.89% seemed to be quite low. In section 6.3.2, the maximum transduction efficiency estimate (k) of the material was determined to by 0.7 or 70%, nearly 35 times higher than the overall efficiency of the actuator. The low value of overall efficiency was indicative of the large power requirements of the coil. Because the magnetic requirements of the material are large, the coil geometry must include a large number of windings (maximum N). Unfortunately, this increases the inductance of the electrical circuit which results in a substantially larger electrical impedance, especially at high frequencies. Effectively, the optimum coil geometry for a field generation perspective was not favorable in terms of power minimization. As a result, the efficiency of the actuator was expected to be very low. Furthermore, because of the simplifying assumptions in the design process, the power requirements for the conceptual actuator were under-predicted. Effects such as eddy current and mechanical losses were not included. Therefore, the actual overall efficiency of a prototype NiMnGa actuator may actually be less than what was determined from the present analysis.

6.4.2 Comparison of NiMnGa to Other Active Materials

The performance of the conceptual NiMnGa actuator and the material characteristics of the NiMnGa element were compared to piezo-electric and magnetostrictive materials. The parameters for the magnetostrictive material were obtained from measurements performed by Calkins and Flatau [222, 258], Butler [259], and Dapino and Flatau [260]. Piezoelectric characteristics were obtained from

experiments performed by Near [261] and from the Mide technology corporation [262].

In Table 6.6, the material properties of Terfenol-D are compared to the experimentally determined material properties of NiMnGa. It was noted that Terfenol was about three orders of magnitude stiffer than NiMnGa. Although NiMnGa seemed to be a softer material, its magneto-mechanical coupling factor of the FSMA was much larger than that of Terfenol. The difference in magneto-mechanical ('*d*') coupling factor was expected due to the large potential magnitude of induced strain capable of being generated by NiMnGa. Both materials show similar coupling coefficients indicating that the level of transduction efficiency in NiMnGa is comparable to Terfenol. Basically, terfenol is a large force, small strain producing material while NiMnGa is a small force, large strain producing material. Furthermore, both materials require large magnetic circuits for actuation. Many of the same design challenges inherent to NiMnGa actuators are also shared by magnetostrictive materials like Terfenol.

Typical values of the coupling coefficients of piezoceramics and NiMnGa are shown in Table 6.7. Qualitatively, based on the data presented in Table 6.7, piezoceramics and NiMnGa materials share comparable values of the coupling coefficient. This indicated that the transduction efficiency of piezoceramics was very close to that of the NiMnGa alloy.

In Table 6.8, properties of various piezoceramic actuators are compared to the properties of the NiMnGa conceptual actuator. Information on the piezoelectric devices was obtained from experiments performed by Near [261]. According to

Table 6.8, the NiMnGa actuator outperformed piezoelectric actuators on only one category: displacement. The NiMnGa consumed 150% of the power of the multilayer actuator but produced approximately 800 times the displacement. Furthermore, the NiMnGa actuator produced the least force and was attributed with the lowest overall efficiency. Similar to the case when NiMnGa is compared to Terfenol, the NiMnGa was a high stroke, low force device while the piezoelectric devices tended to be high force, low stroke devices. Clearly, if an application requires a large amount of strain, then NiMnGa actuators may be most appropriate. However, the cost of this strain generating capability of NiMnGa based actuators included substantially higher power requirements and very low overall efficiencies when compared to similar piezoelectric devices.

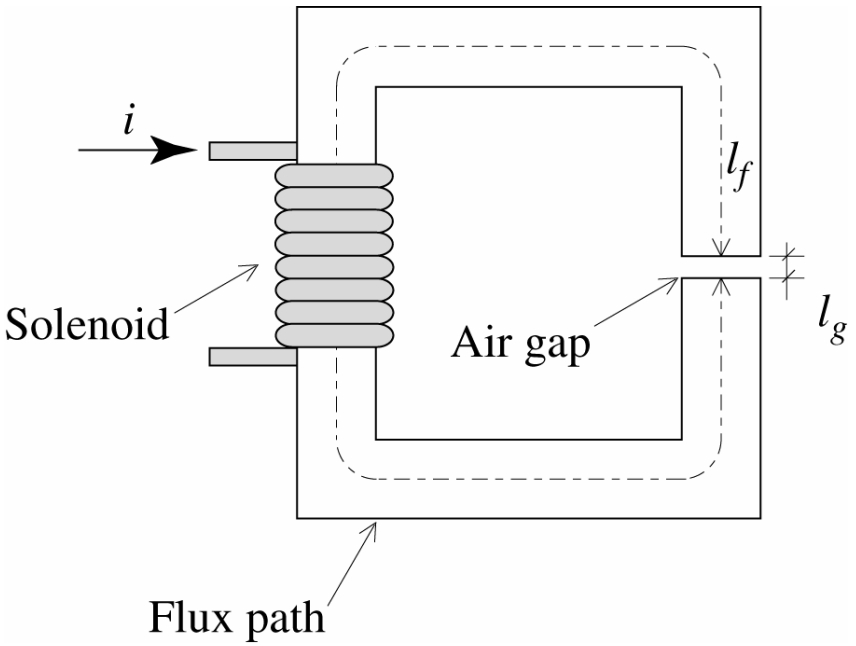

Figure 6.1 Schematic of a simple magnetic circuit

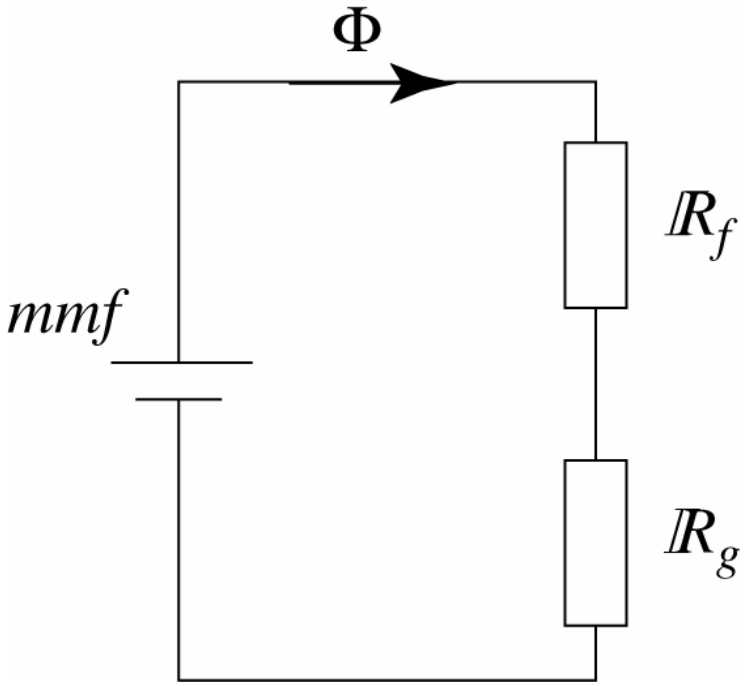

Figure 6.2 Equivalent magnetic circuit

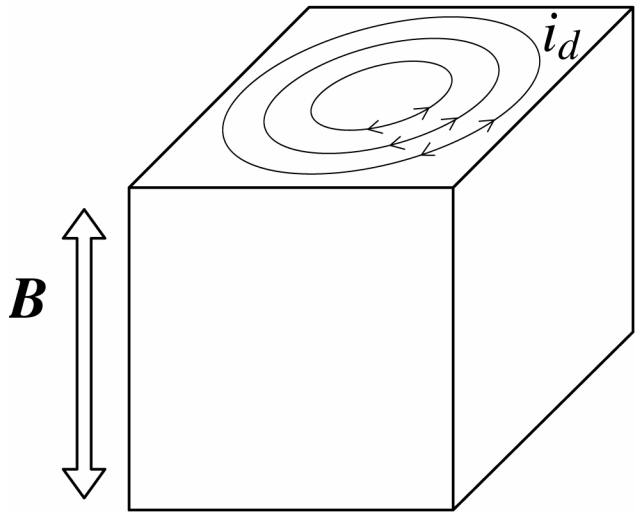

a) Eddy currents in a solid core

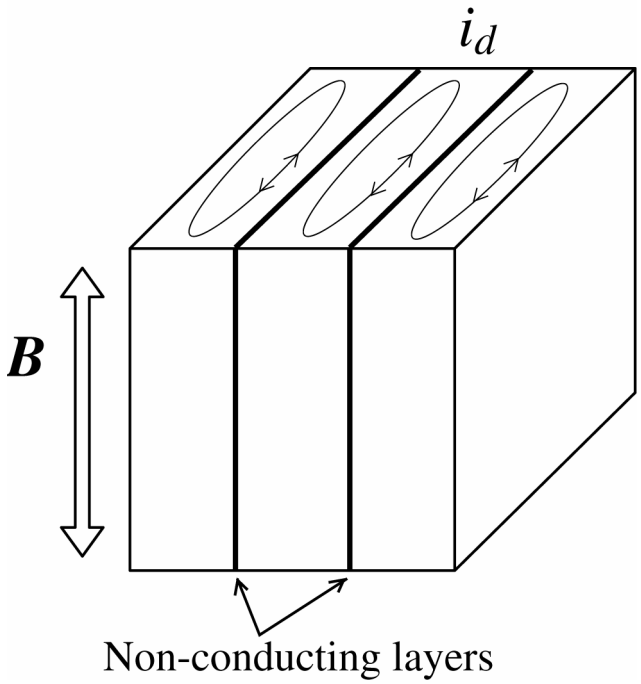

b) Eddy currents in a laminated core

Figure 6.3 Eddy currents arising from an alternating magnetic field

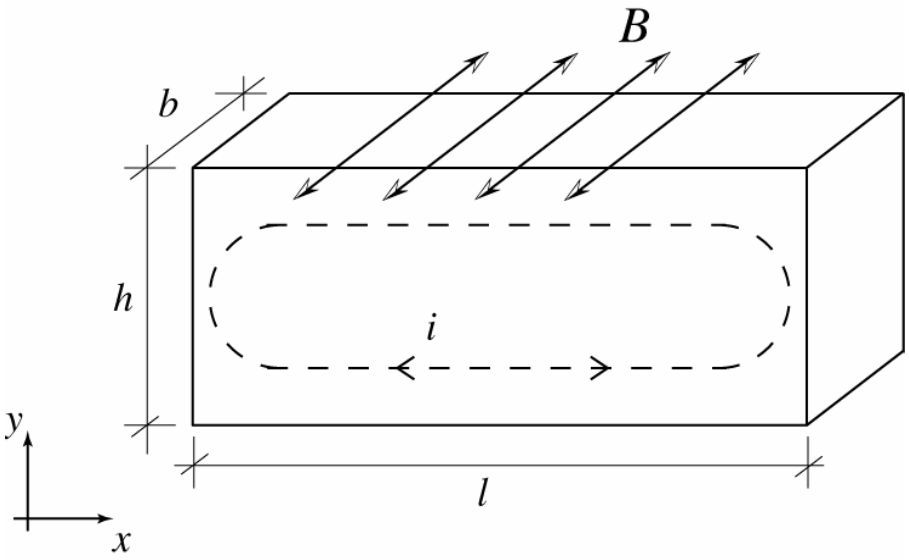

Figure 6.4 Eddy currents in a lamina

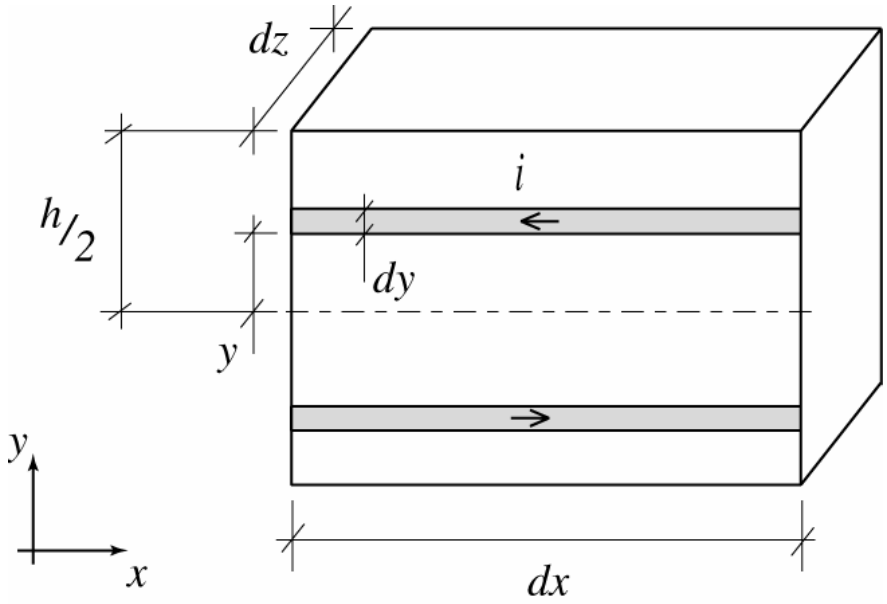

Figure 6.5 Differential lamina element and associated current loop

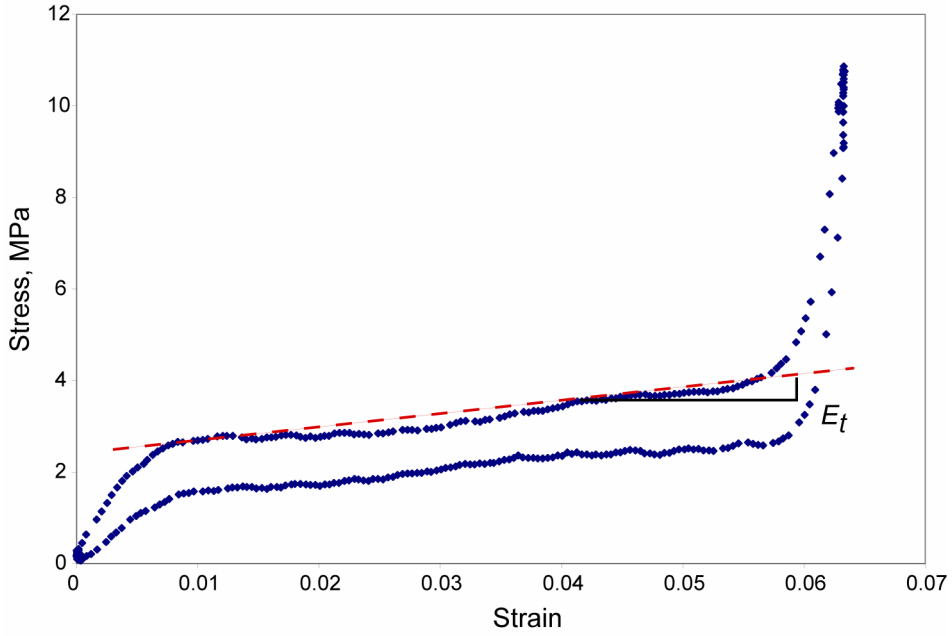

Figure 6.6 Measurement of E_t, from stress-strain curve for 8 kOe constant field intensity

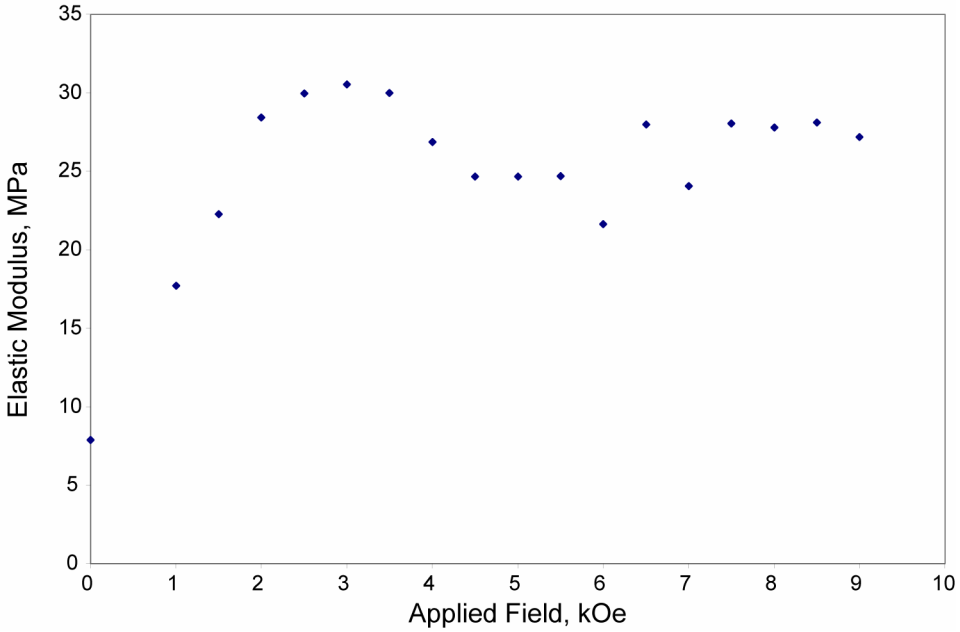

Figure 6.7 Effect of field intensity on transition modulus, E_t

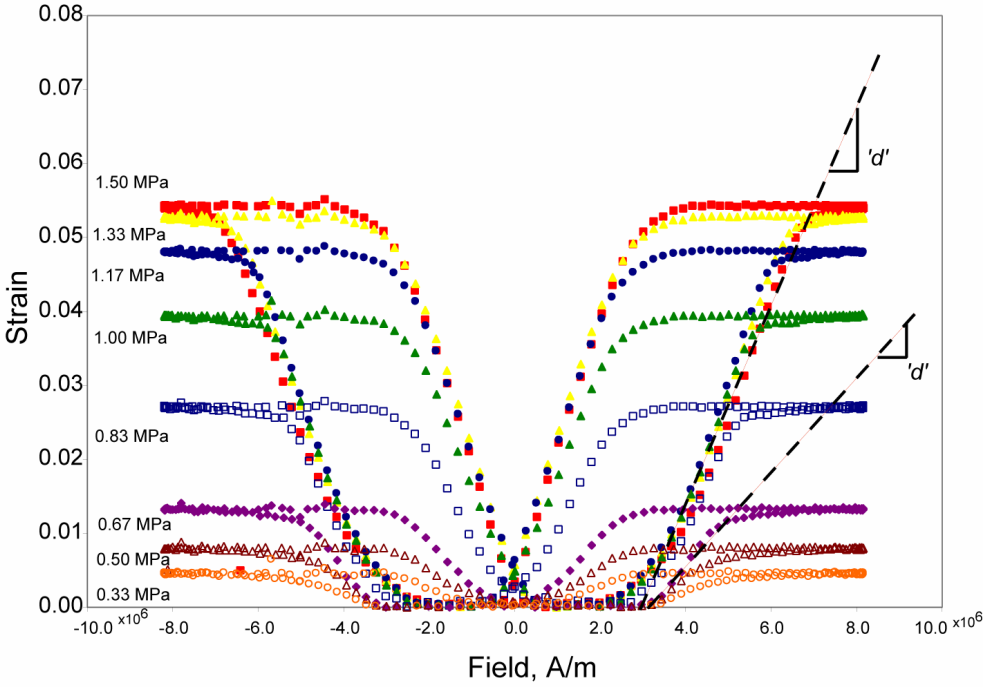

Figure 6.8 Measuring magneto-mechanical coupling, '*d*' in NiMnGa

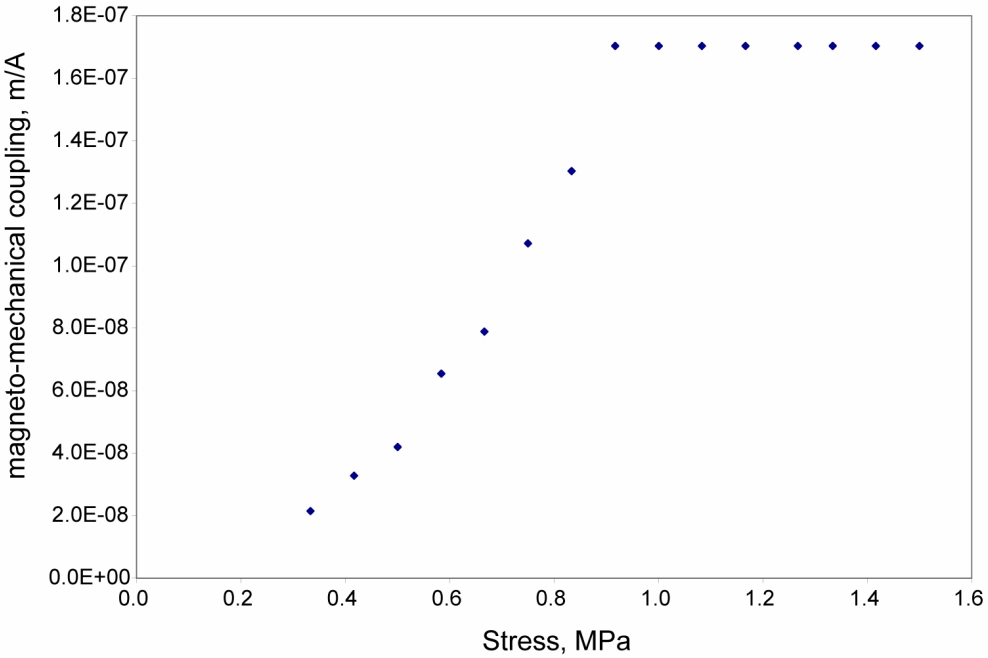

Figure 6.9 Effect of recovery stress on magneto-mechanical coupling, '*d*' in NiMnGa

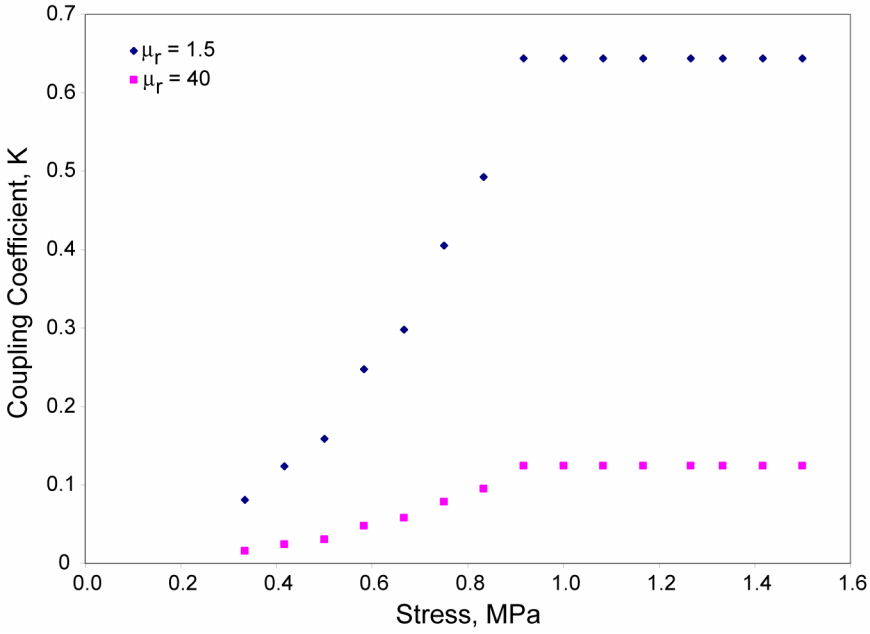

Figure 6.10 Effect of recovery stress on the coupling coefficient, *k*

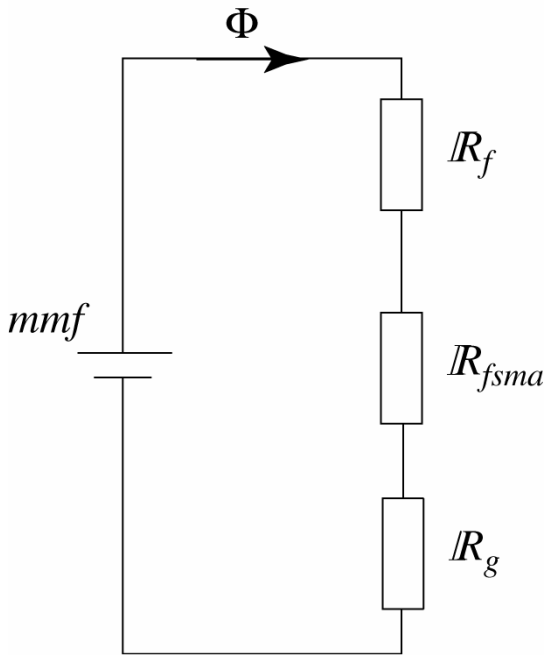

Figure 6.11 Magnetic circuit for a simple NiMnGa actuator

CONSTANT	VALUE	UNIT
Length	118	mm
Width	2	mm
Height	9.3	mm
Mass	18.3	g
E_t	26.97	MPa
H	800	kA/m
ε	0.05	
d	1.703E-07	m/A
Force req.	60	N

Table 6.1 NiMnGa actuator element dimensions and sizing constants

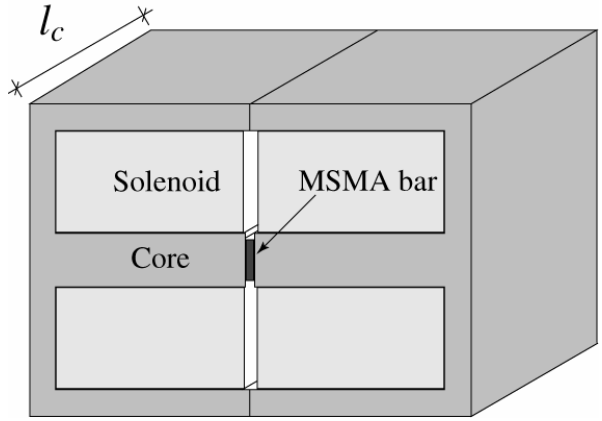

a) Conceptual NiMnGa based actuator: ¾ view

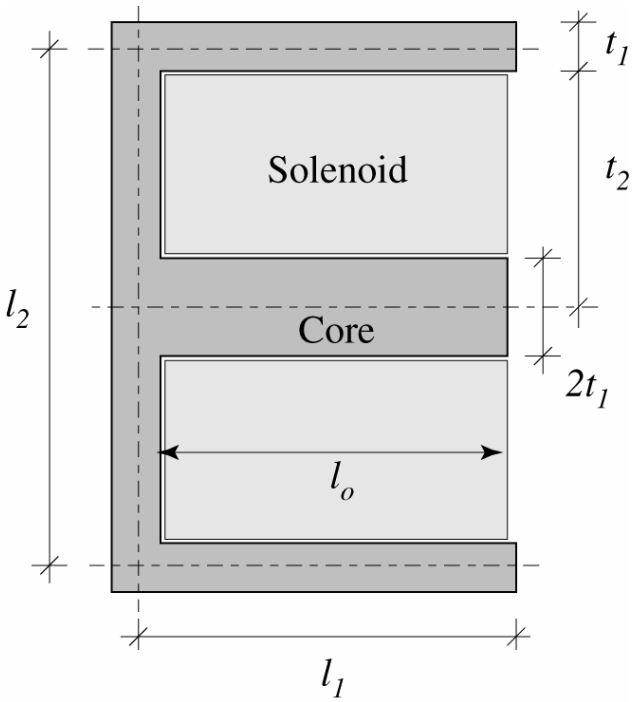

b) Conceptual NiMnGa based actuator: front view

Figure 6.12 E-frame dimensions for conceptual NiMnGa TEF actuator

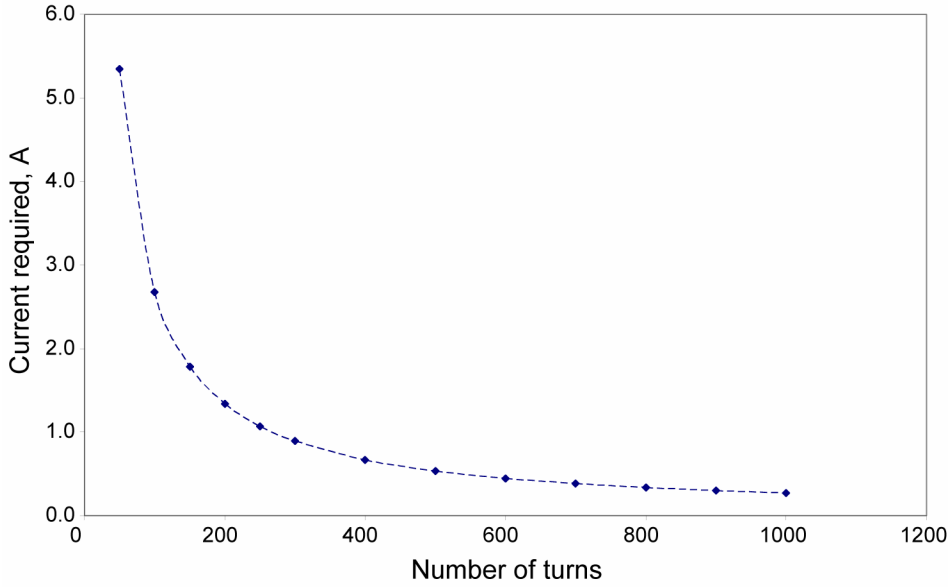

Figure 6.13 Required current vs. number of coil turns

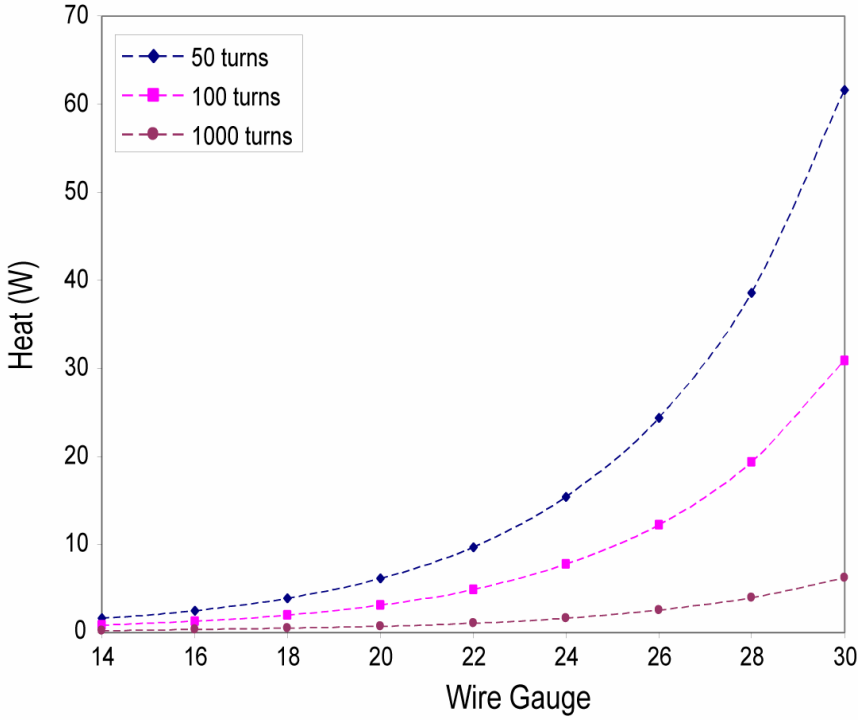

Figure 6.14 Heat generation as a function of coil wire gauge

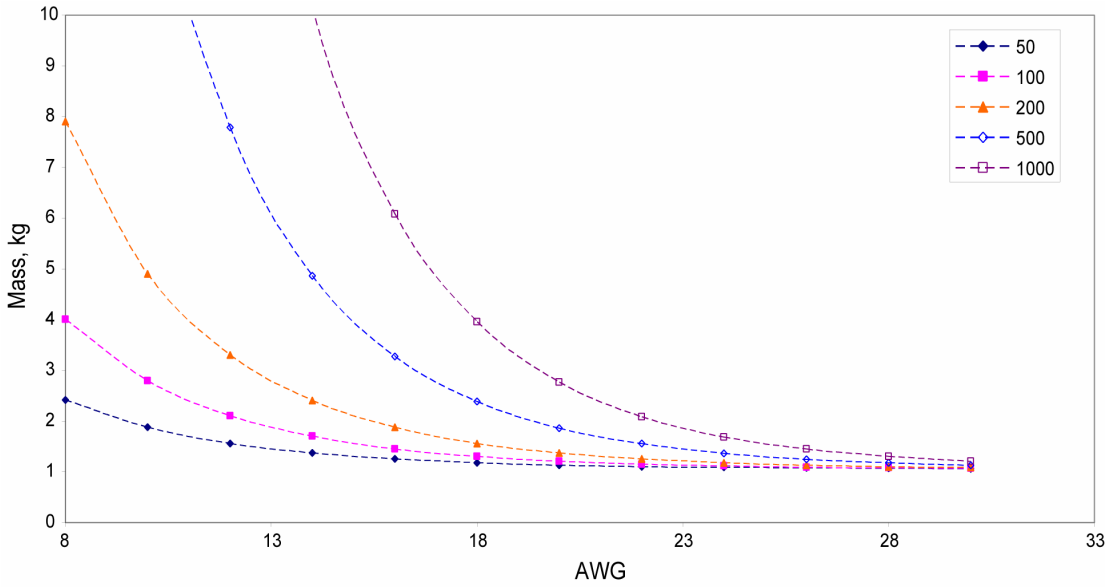

Figure 6.15 Total actuator mass as a function of wire gauge

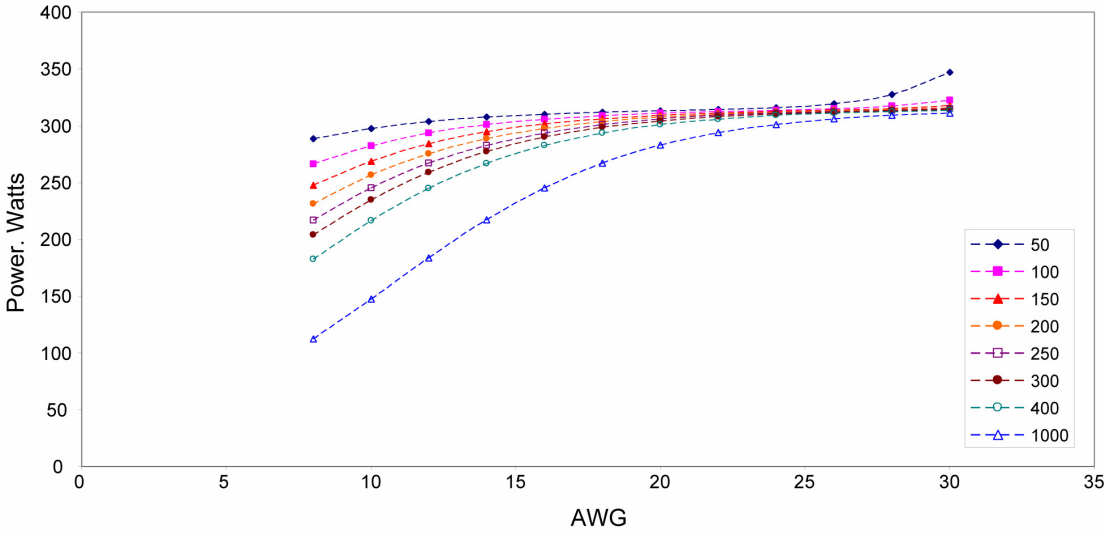

Figure 6.16 Required power as a function of wire gauge

AWG		14	16	18	20	22	24	26	28	30
Wire diameter, mm		0.001629	0.001291	0.001025	0.000812	0.000644	0.000510	0.000405	0.000322	0.000255
N_c	turns	20.6	25.9	32.7	41.3	52.0	65.6	82.6	104.1	131.5
N_t	turns	24.3	19.3	15.3	12.1	9.6	7.6	6.1	4.8	3.8
t_2	mm	0.045	0.030	0.021	0.015	0.012	0.009	0.008	0.007	0.007
L_2	mm	0.096	0.067	0.048	0.036	0.029	0.025	0.022	0.020	0.019
l_w	m	463.016	404.147	367.354	343.904	329.334	320.111	314.371	310.741	308.431
R_w	ohms	3.831	5.320	7.669	11.459	17.427	26.984	42.003	65.902	104.460
L_w	mH	19.329	21.841	23.771	25.190	26.161	26.814	27.238	27.513	27.691
P_{act}	watts	251.401	279.461	301.049	316.928	327.790	335.114	339.867	342.969	345.020
P_{ohm}	watts	0.274	0.380	0.548	0.819	1.246	1.929	3.003	4.711	7.468
R_{core}	A-turn/Wb	12934	11446	10517	9924	9556	9323	9178	9087	9028
I_w	amps	0.26738	0.26738	0.26738	0.26738	0.26738	0.26738	0.26738	0.26738	0.26738
mmf_{act}	A-turns	287.750	285.407	283.943	283.010	282.431	282.064	281.835	281.691	281.599
actuator	kg	1.548	1.366	1.252	1.180	1.135	1.106	1.088	1.077	1.070
coil	kg	8.593	4.714	2.702	1.585	0.956	0.583	0.361	0.225	0.140
total	kg	10.141	6.080	3.954	2.764	2.090	1.689	1.450	1.302	1.210

Table 6.2 Actuator configurations as a function of wire gauge

AWG		14	16	18	**20**	22	24	26	28	30
Wire diameter, mm		0.001629	0.001291	0.001025	**0.000812**	0.000644	0.000510	0.000405	0.000322	0.000255
N_c	turns	20.6	25.9	32.7	**41.3**	52.0	65.6	82.6	104.1	131.5
N_t	turns	24.3	19.3	15.3	**12.1**	9.6	7.6	6.1	4.8	3.8
t_2	mm	0.045	0.030	0.021	**0.015**	0.012	0.009	0.008	0.007	0.007
L_2	mm	0.096	0.067	0.048	**0.036**	0.029	0.025	0.022	0.020	0.019
l_w	m	463.016	404.147	367.354	**343.904**	329.334	320.111	314.371	310.741	308.431
R_w	ohms	3.831	5.320	7.669	**11.459**	17.427	26.984	42.003	65.902	104.460
L_w	mH	19.329	21.841	23.771	**25.190**	26.161	26.814	27.238	27.513	27.691
P_{act}	watts	251.401	279.461	301.049	**316.928**	327.790	335.114	339.867	342.969	345.020
P_{ohm}	watts	0.274	0.380	0.548	**0.819**	1.246	1.929	3.003	4.711	7.468
R_{core}	A-turn/Wb	12934	11446	10517	**9924**	9556	9323	9178	9087	9028
I_w	amps	0.26738	0.26738	0.26738	**0.26738**	0.26738	0.26738	0.26738	0.26738	0.26738
mmf_{act}	A-turns	287.750	285.407	283.943	**283.010**	282.431	282.064	281.835	281.691	281.599
actuator	kg	1.548	1.366	1.252	**1.180**	1.135	1.106	1.088	1.077	1.070
coil	kg	8.593	4.714	2.702	**1.585**	0.956	0.583	0.361	0.225	0.140
total	kg	10.141	6.080	3.954	**2.764**	2.090	1.689	1.450	1.302	1.210

Table 6.3 Finalized actuator configuration

CONSTANT	VALUE	UNIT
Max. Stroke	2	mm
Max Force	60	N
Operating f	50	Hz
Peak Field	1.0	Tesla
Length	142	mm
Width	85.6	mm
Height	41.6	mm
Mass	2.764	kg
Req. Power	317	Watts
Ohmic Losses	0.82	Watts

Table 6.4 Conceptual NiMnGa actuator specifications

CONSTANT	VALUE	UNIT
P_o	6	Watts
P_w	317	Watts
Q^w	2.17	W/kg
Q^v	625	kW/m^3
Q_{eff}	1.89	%

Table 6.5 Performance Parameters of NiMnGa

CONSTANT	UNIT	TERFENOL [260]	TERFENOL [259]	TERFENOL [222]	FSMA
Young's Modulus, E^H	GPa	50-60	25-30	60	0.027
Permeability, μ^σ	Tm/A	2.2-6.7 e-6	11.56 e-9	2.2e-6	1.9-50 e-5
Magneto-mechanical coupling, d	(m/A)	4.5 e-9	15 e-9	4.5 e-9	1.7 e-7
Coupling Coefficient, k		0.35-0.5	0.7-0.75	0.4	0.13-0.64

Table 6.6 Comparison of NiMnGa FSMA properties to Terfenol-D

MATERIAL	PROPERTY	VALUE
Piezoceramics [262]		
	k_{33}	0.7-0.73
	k_{31}	0.3-0.4
NiMnGa		
	k	0.13-0.64

Table 6.7 Comparison of typical piezoceramic coupling coefficients with NiMnGa

DEVICE	MAX. FORCE	DISPLACEMENT	REQ. ELECTRICAL POWER @ 5O HZ	EFFICIENCY
	N	μm	Watts	%
Bimorph	90	500	0.75	7.9
Rainbow	500	1000	1.75	5.4
Patch Actuator	100	10	0.25	7.1
Tubular Actuator	1000	10	0.55	10.5
Multilayer Actuator	35000	25	205	21.1
NiMnGa Actuator	60	20000	317	1.89

Table 6.8 Comparison of piezoelectric actuators to NiMnGa conceptual actuator

Chapter 7: Summary and Conclusions

The properties of NiMnGa magnetic shape memory alloy were investigated for the purpose of developing a NiMnGa based actuator to drive trailing edge flaps on rotorcraft. The trailing edge flap (TEF) system is a component of a smart rotor, and its inherent multi-functionality allows it to be used for both primary rotor control and vibration suppression; and quite capable of replacing the conventional swashplate. Aeromechanics analyses of the system have shown that the TEF system requires compact, moderate-force, high stroke actuators in order to achieve adequate control authority. These requirements make for the presentation of a strong case for the incorporation of active materials into TEF actuator concepts. In chapter 1, details of the technical issues involved with the incorporation of several active material based systems in rotorcraft are discussed. Ideally, successfully integrating trailing edge flaps on a smart rotor concept will require active materials which are capable of delivering relatively high levels of dynamic stroke. Because of the unique characteristics of the FSMA material (i.e. high dynamic stroke, wide operating bandwidth), NiMnGa based actuators have several advantages over other active material based actuators in that they have the potential to be used in compact actuator concepts without requiring heavy, mechanically complex, stroke amplification mechanisms.

The first aspect of the current research (Chapters 3 & 4) was focused on the characterization of NiMnGa specimens. Fundamentally, the goal was to observe the material behavior for a broad range of mechanical and magnetic loading conditions.

Testing was divided into two major categories: quasi-static and dynamic. Both categories involved extensive testing the samples in a wide range of operating environments including constant strain, constant stress, constant recovery spring stiffness, and constant applied magnetic field. As a result of these tests, basic properties such as block force, free strain, damping, and magneto-mechanical coupling were determined and an understanding of the underlying physics behind the material response for both quasi-static and dynamic excitation was also developed.

The second aspect of the research (Chapter 5) focused on the modeling of NiMnGa behavior. A quasi-static model utilizing the same basic principles as the Brinson model for thermal SMA was proposed to predict the stress-strain response of NiMnGa elements as a function of applied stress and magnetic field. When compared to experimental data, the analysis correlated with all of the main strain recovery mechanisms (magnetic shape memory effect, magnetic pseudoelasticity), and was capable of accommodating the effects of magnetic saturation. Additionally a low-frequency dynamic model was proposed to predict the strain response of a NiMnGa element in a time varying magnetic field was proposed. This model was based upon a set of experimentally measured parameters and was designed to predict the strain response as a function of recovery stress, magnetic field, and excitation frequency. This model showed good correlation with most of the data, but had difficulty accurately predicting material behavior for moderate stress levels.

The third and final aspect was focused on the design of a conceptual NiMnGa actuator for use on a TEF system (Chapter 6). Methodologies for both FSMA element sizing and a first approximation magnetic coil design were presented. Based

on these methods, a series of conceptual actuators were designed and then down-selected to determine an optimum configuration. Once selected, the performance properties of the actuator were estimated and then compared to other active material based actuators to evaluate the quality of the concept.

7.1 Key Points

Over the course of this study, several key elements regarding NiMnGa materials and actuators became evident. The following list highlights the key findings in this work:

i. **NiMnGa Behavior:** There were several recurring themes that presented themselves over the course of the material characterization. First, and foremost, the driving force behind the magnetic shape memory alloy strain mechanism is the interaction between the external magnetic field and the microstructure of the material itself. While the magnetic field induces twin boundary motion in the material, this effect only occurs because of the magnetocrystalline anisotropy of the material. Clearly, the fundamental behavior of the bulk specimen is largely dependent on the quality of the microstructure of the specimen. Chemical composition, method of crystal growth, sample purity, and post production treatments (cutting, polishing, etc.), and temperature are just a few of the factors that exert a major influence on the behavior of this material. Consequently, designers of applications for NiMnGa cannot ignore the quality and composition of the microstructure of the material and expect to utilize its full potential. Second, the applied stress field works in opposition to the

effect of the magnetic field. As a result, applied magnetic fields raise the threshold for mechanically induced twin boundary motion and vice versa. Furthermore, many of the properties of the material are dependent upon the level of recovery stress acting on the sample. Peak strain, residual strain, power density and damping capability are just some of the material parameters that are directly related to the level of recovery stress. Clearly, NiMnGa applications must include a careful consideration of recovery force in order to maximize the material performance.

ii. **NiMnGa Modeling:** In general, modeling techniques for NiMnGa and other similar FSMA materials can take advantage of the large body of work devoted to the modeling of conventional thermal SMA materials. It was shown in this work that by using a parallel approach, and drawing direct analogies between magnetic and thermal specific quantities, the behavior of NiMnGa could be effectively modeled by adapting an accepted SMA model. However, certain exceptions must be made to accommodate specific effects, like magnetic saturation and strain recovery through twin boundary motion rather than temperature induced phase transformation.

iii. **NiMnGa Performance:** Dynamic tests and the observation of the effects of strain rate suggest that the FSMA material responds quickly to changes in the magnetic field environment. This statement is supported in the literature which reports NiMnGa actuation at frequencies in the kHz range [6]. In fact, the maximum excitation frequency (50 Hz) was not

determined to be a material limitation but rather a limit of the magnetic circuit. One of the major points to understand about NiMnGa is that its performance is directly coupled to the quality of the driving magnetic circuit. Furthermore, measurements of the energy density of NiMnGa showed that it was comparable to piezoelectrics. The difference between the two materials is that while piezos are a high force, low stroke material, NiMnGa is a low force, high stroke material. In other words, NiMnGa trades force for strain generation capability.

iv. **Actuator Design:** Applications utilizing NiMnGa require a carefully designed magnetic circuit. To make the material practical for use on rotorcraft, the power requirements should be reduced by at least a factor of 10. However, it is unlikely that a magnetic circuit optimized for minimum power consumption could realistically reduce the required power by such a significant level. Nevertheless, the material performance is directly linked to the quality of the magnetic circuit. This aspect of the material is also a source of other disadvantages. First, because of the orientation of the magnetic field in relation to direction of strain, it is difficult to measure the magnetic environment *inside* the material. Second, the required magnetic circuit accounts for 99.35% of the mass of the actuator (total actuator mass 2.764 kg vs. NiMnGa mass of 0.018 kg). This can potentially negate any weight savings gains this material may provide. Furthermore, the requirement of the magnetic circuit makes it difficult to minimize the volume of the actuator. As a result, a compact NiMnGa

actuator is largely dependent on the ability to design a compact magnetic circuit. However, it must be stated that it is likely that designing a lightweight, compact actuator with low electrical power requirements which delivers a 6 to 10 kOe field over frequency bandwidth suitable for providing sufficient flap control authority is not physically possible.

v. **Role of FSMA:** In general, NiMnGa can be characterized as a low-force, high stroke, dynamic material. Compared to other active materials like piezoelectrics and magnetostrictives, FSMA trade force generation capability for strain generation. Similarly, NiMnGa provides the strain producing capability of a thermal SMA like NiTi, with the operating bandwidth of a magnetostrictive. However, these qualities have several associated drawbacks. Because of the substantial field requirement for inducing twin boundary motion, these materials require substantial amounts of electrical power to operate. The coil design process presented in this work was intended to show the ideal minimum power requirements of a conceptual actuator. Even with these simplifying assumptions, it is evident that FSMA are power intensive materials. In most cases, limits in the material performance are determined by the limitations associated with either the magnetic circuit or the supporting electronics.

7.2 Feasibility of NiMnGa Actuators on the Smart Rotor

It has been shown in the current work that the NiMnGa ferromagnetic shape memory alloy is capable of fulfilling the performance requirements (discussed in section 6.4.1) for driving trailing edge flaps on rotorcraft. But the question of

whether or not FSMA are better suited for this application than other active materials is difficult to answer at this point. Magnetic shape memory alloys offer many advantages over other active materials. However these advantages can be less worthwhile, especially in an application that imposes strict volumetric, weight, and power constraints, such as those inherent to driving a TEF system. To answer the question of the feasibility of NiMnGa for trailing edge flap actuation, it is important to consider the advantages and disadvantages of the material.

7.2.1 Advantages of NiMnGa Based Actuators

The main advantage of NiMnGa is its ability to deliver large levels of dynamic stroke over a wide range of excitation frequencies. This single advantage is the main reason for arguing that NiMnGa is better suited for TEF actuation than other active materials. One of the main assumptions associated with choosing an active material for TEF actuation is that it has a high energy density. Although, NiMnGa, piezoceramics, and magnetostrictive materials have similar energy densities it is difficult to state that these materials would be equally suited for the application. In fact, it is not enough that the active material has a high energy density. The ability to produce the required amount of stroke without the aid of amplification takes precedence. Otherwise, a high force, low stroke material based design (piezoelectrics for instance) is burdened with the additional requirement of a stroke amplification mechanism. If the goal is to develop a mechanically simple, compact actuator design, then it is important to choose materials that have superior stroke generating capability.

7.2.2 Limitations of NiMnGa Actuators

The ability of the NiMnGa alloy to produce relatively large levels of dynamic stroke, as compared to other active materials, is balanced by several inherent limitations. In general, these limitations are connected to the large field requirements necessary to induce the twin boundary motion and the subsequent induced strain. Completely inducing twin boundary motion in the entire specimen typically requires a magnetic field on the order of 1 Tesla, a significant magnetic requirement. To generate this level of magnetic field, a large coil is often required. For an application requiring a compact actuator design, like driving TEFs on rotorcraft, a heavy, bulky coil is potentially as large a problem as requiring a stroke amplification mechanism. For a practical application, it must be determined whether or not it is better to have a heavy coil embedded in a rotor blade or a heavy, complex stroke amplification mechanism.

Another limitation associated with the field requirement is the level of electrical power required to energize the coil. The required magnetic field depends on the current supplied to the coil. Consequently, the ohmic power requirements alone tend to be quite high. Furthermore, for dynamic applications, the inductance of the coil begins to dominate the coil impedance, which further increases the electrical requirements. To reduce the magnitude of the required current necessary to generate the magnetic field, coil geometries often include a large number of turns. Although this strategy can reduce the required current, it also increases the inductance of the coil, which also increases the electrical requirements.

A final limitation associated with NiMnGa driven TEFs is associated with the method of power delivery. The current requirements for energizing the drive coil can, in general, be expected to be quite high. Therefore, the rotor system must be equipped with an electrical slip-ring, large enough to be able to deliver sufficient power to the actuator. This requirement incurs additional weight penalties.

7.2.3 Overcoming Challenges Associated with NiMnGa

Considering both the advantages and disadvantages of using FSMA materials for trailing edge flap actuation, two fundamental conclusions can be drawn regarding the results of the current research. First, it can be stated that the FSMA material itself does indeed possess all of the necessary attributes for trailing edge flap actuation and is capable of meeting the force, stroke, and frequency requirements. However, when one considers the influence of the magnetic field generator, the system becomes less practical. The operation of the material requires a level of magnetic field which demands relatively high mass magnetic circuits and substantial electrical power requirements. As a result, it can be stated that secondly, the implementation of an FSMA system on an integrated smart rotor system is not practical at this time. This system will become feasible only if certain technical issues can be resolved.

One of the main technical challenges associated with NiMnGa materials and actuators is associated with the high magnetic field requirement. Short of altering the fundamental chemical composition of the material itself, it is difficult to reduce this requirement. However, there are two strategies that could be implemented to overcome the problem associates with the magnetic field requirement:

1. **Permanent Magnets:** The incorporation of permanent magnets within the driving magnetic circuit provides an effective way of introducing a bias field into the system. Through the use of bias fields, not only can the material be configured for bi-directional actuation but, the magnitude of the time-varying field can be substantially reduced. Reducing the required current for the time-varying field by half reduces the electrical power (ohmic) by a factor of four. However, it must be noted that the effective use of permanent magnets within the magnetic circuit requires a clever design. Integration of permanent magnets into the magnetic circuit is not a trivial matter. The difficulty associated with this approach arises from the necessity to place the magnets in such a manner as to overall gain the benefits of the bias field without causing substantial increases in the reluctance of the magnetic circuit.
2. **Optimized LRC Circuit:** Fundamentally, the magnetic coil responsible for energizing the alloy is an LRC circuit. If this circuit is designed for a resonance condition, then not only can the required power for the coil be reduced, but the size of the support electronics can also be minimized. However, there are several practical problems associated with this approach. First, the process of tuning of the circuit for specific resonance frequency may yield non-physical values for the LRC components, thus limiting the practicality of the approach. Although there are several techniques involving op-amp networks that can address this situation, they can provide only limited results. Furthermore, this LRC circuit

optimization approach assumes that the system is tuned to one specific operating condition and therefore, is likely to perform poorly at operating frequencies which are outside of a narrow frequency bandwidth. In such cases, this approach would not be practical for a vibration control application which requires effective operation over a range of operating frequencies.

7.3 Future Research Directions

There are several avenues of interest that provide impetus for further research in the area of utilizing magnetic shape memory alloys in actuators for driving trailing edge flaps on a smart rotor concept. The following is a list of suggested topics for future research.

i. **Extend Dynamic Testing:** In the context of the current research, limitations in the test equipment prevented testing at excitation frequencies above 5 Hz and constant recovery stresses above 1.5 MPa. Both of these limitations were associated with the inability of the test rig's PID controller to compensate for the change in material stiffness near the end of the region of twin boundary motion. Tests involving higher excitation frequencies and stresses should be performed in order to observe the dynamic behavior of NiMnGa in the case where the recovery stress begins to overcome the magnetic anisotropy of the material. Furthermore, a key limitation in the current work was that because an inexpensive and reliable source of NiMnGa was lacking, it was only feasible to conduct tests on a small sample population. As the availability

of the material increases, tests aimed at determining the consistency of the material response over a large sample population should be conducted.

ii. **Modeling:** In the context of the current work, many of the governing equations were linearized. As a result, material behavior near the onset of conclusion of twin boundary motion was not well modeled. The smooth transitions of the actual material behavior are not reflected in the analysis. One possible avenue of further study would be to carefully observe what is happening near the transition regions and then develop an improved set of relationships to model the data. Furthermore, effects such as magnetic saturation were incorporated into the model by performing many tests on a few samples of FSMA material, then through regression, determining a suitable function to reflect that behavior. The weakness inherent to this approach is that the model is determined from a small sampling of the material population and may only be applicable to that population. A better approach would be to conduct tests on a broader sample size, including samples of various geometries. Unfortunately, due to the recent discovery of the material, the availability of NiMnGa at this time is neither reliable nor economically conducive to this approach. In the future, if the material becomes easier to acquire, a broader testing approach would be required.

iii. **Bias Fields:** Actuator configurations utilizing permanent magnets for the generation of a bias field must be explored. Permanent magnets offer a potentially effective method for reducing both the size and power

requirements of the magnetic circuit. Work directed at determining clever, and effective magnetic circuits incorporating permanent magnets should be a major issue.

iv. **Actuator Design and Testing:** The current study was limited to determining conceptual NiMnGa based actuators. The next step involves the design and fabrication of a prototype actuator to test on a model rotor in the vacuum chamber and wind tunnel. Substantial effort should be placed on the design of the next generation magnetic circuit. The analysis presented here was meant to be a first approximation of the *minimum* requirements of the drive coil. An analysis involving a more detailed approach (magnetic FEM, etc.) in the design of the magnetic circuit and more rigorous optimization procedure is required to produce magnetic circuit that minimizes the required power and emphasizes a compact construction.

Appendix A : Overview of Basic concepts in Magnetism

Magnetism is a well know branch of science that has it's origins in ancient Greece. As early as 600 B.C., Greek philosophers were aware of the magnetic properties of natural ferric ferrite (Fe_3O_4) stones, more commonly called lodestones. Through the centuries, the phenomenon of magnetism has been well-documented and remains one of the cornerstones of modern science. As such, it is impossible to provide a comprehensive background of magnetism in this current work without filling several volumes. Details on all of the topics discussed in this section may be found in virtually any basic physics textbook or similar resource [253, 254, 255, 256]. This brief overview will be directed at describing the aspects of magnetic theory that are useful for designing electromagnetic circuits for FSMA actuators.

A.1 Magnetic Flux, Induction and the Biot-Savart law

Magnetic flux, typically represented by the symbol Φ, represents the total quantity of field effects or 'substance' of the field. When relating magnetic quantities to electrical quantities, flux and current are analogous. In other words, flux is the rate in which a charged particle crosses a surface perpendicular to the 'flow'. Often, flux is denoted by the units 'weber' (Wb) or Tm^2 (Tesla-meter^2). One weber is the flux induced by a current varying at a uniform rate of one amp per second (A/s). Flux changing uniformly at a rate of 1 Wb/s induces 1 volt of electric potential. The vector quantity **B**, magnetic flux density, represents the amount of field flux concentrated in a given area. The units of flux density are Tesla (T) or Wb per meter^2 (Wb/m^2). A magnetic field of 1 Tesla is defined as the field required to exert a force

of 1 N on a charge of 1 Coulomb moving at a velocity of 1 m/sec. Physically, the magnitude of a one Tesla, inductive field can be obtained by noting the magnetic field of the earth near the surface is approximately 0.5 x 10^{-4} T [253]. Typical laboratory magnets can produce fields of up to 2.5 T.

The magnetic flux, Φ for a given surface is defined as:

$$\Phi = \int_A \mathbf{B} dA \tag{A.1}$$

with units in webers. For a given region, eq (A.1) provides the total amount of magnetic flux.

For a given current distribution, the Biot-Savart law allows for the direct calculation of the B-fields generated. Although the Biot-Savart law may be derived from Maxwell's relations, it is most convenient to derive it from the concept of magnetic vector potential.

Fundamentally, magnetic fields are produced as a result of the motion of electric charges. The Biot-Savart law is a fundamental relation of electromagnetism and can be used to calculate the magnetic induction around a current carrying conductor of any given geometry. Consider Figure A.1. At a point P, a conductor element of length *ds* carrying a steady current *i* generates a magnetic induction given by the following vector quantity:

$$d\mathbf{B} = \frac{\mu_0}{4\pi} \frac{\mathbf{i} \times \hat{\mathbf{r}}}{r^2} ds \tag{A.2}$$

where r is the distance of the point P from the conductor, and $\hat{r}$ is the unit vector pointing from the element to P. The quantity μ_0 is known as the permeability of free space and is given by:

$$\mu_0 = 4\pi \times 10^{-7} \text{ Tm/A or N/A}^2 \qquad \text{(A.3)}$$

The result of the vector cross product in eq. (A.2), d**B**, lies in a plane perpendicular to the *ds* axis. On the axis of the differential element of the conductor, d**B,** becomes zero. The maximum magnetic induction always occurs in the plane perpendicular to the differential conductor element axis. Qualitatively, the sense of the quantity B, in response to a current in a conductor, is governed by the right hand rule.

The Biot-Savart law allows the magnetic flux density or induction to be calculated for a uniform current carrying filament or conductor. In this work, three geometries of current carrying conductors will be examined. Since theses geometries are commonly used in practice, they will provide useful insight into the design of magnetic circuits, a necessary step for FSMA actuator development. A review of an infinite uniform conductor, a single circular coil, and a solenoid is provided. In practice, the solenoid is the most common configuration used to generate inductive fields.

First, consider a uniform, straight conductor of infinite length coincident with the x-axis. A current *i* is allowed to pass through this conductor. Figure A.2 illustrates this geometry. At a point P a distance '*a*' from the *x*-axis, the differential magnetic induction is given by the following equation:

$$dB = \frac{\mu_0}{4\pi} i \frac{dx \sin\theta}{r^2} \qquad \text{(A.4)}$$

$$= \frac{\mu_0}{4\pi} \frac{i}{a} \sin\theta d\vartheta \qquad \text{(A.5)}$$

When eq (A.5) is integrated over the angle θ, the total magnetic induction B, is given by:

$$B = -\frac{\mu_0}{4\pi}\frac{i}{a}\int_{\pi}^{0}\sin\theta d\theta = \frac{\mu_0}{4\pi}\frac{2i}{a} \tag{A.6}$$

In this case, the flux lines, or lines of induction, are concentric circles set in a plane perpendicular to the axis of the conductor. The directional 'sense' of these lines is governed by the right hand rule.

Next, the case of the single, circular coil is considered. In Figure A.3, a single turn circular coil of radius R, carrying a current *i*, lying in the x-z plane is shown. At a point P on the coil's y-axis and distance l, from the center, the magnetic induction is given by the following:

$$B = \int_0^{2\pi R}\frac{\mu_0}{4\pi}i\frac{ds}{r^2}\sin\alpha \tag{A.7}$$

$$= \frac{\mu_0}{4\pi}i\frac{\sin\alpha}{r^2}\int_0^{2\pi R} ds \tag{A.8}$$

$$= \frac{\mu_0}{2}\frac{iR}{r^2}\sin\alpha \tag{A.9}$$

At the center of the coil, where α = 90°, the magnetic flux density becomes:

$$B = \frac{\mu_0}{2}\frac{i}{R} \tag{A.10}$$

Close to the center of the loop, the lines of constant magnetic induction are nearly parallel. A uniform flux density along the central axis can be created by taking advantage of this phenomenon and stacking a large number of tightly packed loops together. This tight package of current carrying loops is known as a solenoid.

The final and most useful geometry from an FSMA actuator perspective is the solenoid. Technically, a solenoid is constructed by winding insulated wire around a straight, central axis many times, thereby creating a large number of helical turns. For a number of turns, N, wound in an air-core solenoid of length L, it can be shown that the flux density at any point on the solenoid axis is:

$$B = \mu_0 \frac{Ni}{L} = \mu_0 ni \tag{A.11}$$

where the quantity *n* represents the number of turns per unit length. It is important to point out that the flux density is independent of the solenoid radius. The result in eq (A.11) is meant for a thin solenoid of finite length. The flux density of a thick, solenoid requires a more detailed treatment of the Biot-Savart law and associated constraints. In practice, eq (A.11) works well for an initial estimation of the flux density in a solenoid.

One important property of the solenoid is that as the length increases, the inductive field at the center becomes more and more uniform. Consider the solenoid in Figure A.4. Typically, near the lengthwise center of the solenoid, the flux density is assumed to be uniform. However, near the ends of the solenoid, this assumption is often not valid. A 'fringing' effect occurs near the ends of the solenoid that has the effect of reducing the flux density at these points. In practice an empirical, 'fringing' factor can be utilized in order to quantify the fractional length over which the flux density is not uniform. As a rule of thumb, a fringing factor of 10% is adequate for most solenoid applications. Physically, this means that the magnetic field within a solenoid can be assumed constant everywhere except within a distance from the edge equal to 10% of the total solenoid length.

Sometimes a coil is wrapped around a core material such as iron to take advantage of its higher permeability. This is a standard method for increasing the flux generation capability of the solenoid. However, core materials such as iron saturate at some finite level of field (~1.6 T for iron) while air cores do not. Magnetic saturation is a limitation occurring in inductors having a ferromagnetic (or ferrimagnetic) core. Basically a ferromagnetic material is said to be saturated when an increases in the field intensity, H, produce progressively smaller increases in the flux density B. To account for a core material in eq (A.11), substitute μ_c for μ_0. In this event, μ_c represents the permeability of the core material. An important property of the solenoid is the inductance, L_s. For a solenoid with N turns, of length L, cross-sectional area A, and core permeability, μ_c, the inductance is determined by the following relation:

$$L_s = \frac{\mu_c}{L} N^2 A \tag{A.12}$$

A.2 Field Intensity and the B-H Curve

From eq. (A.11) it is shown that the magnitude of the flux density is also a function of the permeability of the core material. However, it is possible to define a quantity called the magnetic field intensity, **H**, that is independent of the core material and depends linearly on the magnitude of current alone. Typically, it is convenient to express the strength of the magnetic field in terms of **H** instead of **B**. In free space, the relationship of **B** and **H** is defined by:

$$\mathbf{B}_0 = \mu_0 \mathbf{H} \tag{A.13}$$

where $\mathbf{B}_0$ is the flux density in free space and μ_0 is the permeability of free space. The units of H are amps per meter (A/m) or sometimes written as Henries (H). A straight conductor of length 1 m, carrying a current of 1 amp generates a tangential magnetic field of strength $1/4\pi$ A/m at a distance of 1 m.

In practical applications, the required field intensity is generated by means of a series of tightly packed, current carrying loops, or in other words, a coil. The shape of the coils is dictated by the geometry of the required field, but is normally designed to produce a uniform field over the region of interest. The magnitude of field intensity inside a solenoid having '*n*' turns per meter and carrying a current of *i* amps is given by:

$$H = ni \tag{A.14}$$

From eq (A.14) it follows that the units of H are Amp-turns per meter (A.turns/m).

One other important effect related to current carrying conductors is described by Faraday's law. Faraday's laws states that a varying magnetic field produces a voltage in a conductor. The magnitude of this voltage is given by:

$$V_i\left('emf'\right) = -N\frac{d\phi}{dt} \tag{A.15}$$

No matter how the magnetic field is changed, Faraday's law states that this voltage will be generated. When an emf is generated by a change in magnetic flux according to Faraday's law, the polarity of the induced emf is such that it produces a current whose magnetic field opposes the change which produces it. The induced magnetic field inside any loop of wire always acts to keep the magnetic flux in the loop

constant. The 'minus' sign in Faraday's law denotes the effect of Lenz's law. Fundamentally, Lenz's Law is based on the principle of conservation of energy.

The relationship between B and H can be examined by consulting a B-H curve. The B-H curve in Figure A.5 describes the behavior of a material in a cyclically varying magnetic field. Qualitatively, the hysteresis in Figure A.5 is common to ferromagnetic materials. When the field intensity is zero, the magnetic induction does not also go to zero. The level of persistent magnetic induction remaining in the material when the field intensity is brought to zero is known as the 'remnant induction', or B_r. Furthermore, the magnetic flux density saturates at the point B_s. At this point, all the magnetic moments in the material are aligned with the direction of the field intensity and no further rearrangement is possible. In practice, saturation occurs over the region of the B-H curve where the magnitude of B begins to 'level off' for an increasing field intensity, H. As more flux is forced into the same cross-sectional area of a ferromagnetic material, fewer atoms are available within that material to align their electrons with the additional field intensity. It is important to note that saturation only occurs in ferromagnetic core electromagnets. Air core electromagnets do not saturate. For pure iron, B_r is 2 T and B_s is 2.15 T. The area enclosed by the B-H curve is equivalent to the work done in magnetizing the material. In other words, the area is the stored magnetic energy per unit volume, V_m. This quantity is expressed as:

$$V_m = \frac{1}{2}\int BdH \tag{A.16}$$

The permeability of a material can be measured from the B-H curve. The magnetic permeability, μ, is a specific measure of a material's acceptance of magnetic flux. Magnetic permeability is the slope of the B-H curve and is defined as follows:

$$\mu = {dB}/{dH} \tag{A.17}$$

where the units of μ are Wb/A.m or H/m.

Based on the value of μ, a material may be classified as diamagnetic ($\mu < \mu_0$), paramagnetic ($\mu > \mu_0$), or ferromagnetic ($\mu >> \mu_0$). In the case of ferromagnetic materials, the value of μ is not constant but depends on the magnitude of the applied field intensity.

A.3 Magnetism in Matter

The magnetic flux density inside a given material originates from a collection of small current loops or magnetic dipole moments. The magnetization vector, **M**, is defined as the net dipole moment per unit volume at each point throughout the magnetic material. The units of magnetization are the same as field intensity (**H**), and are typically listed as A/m. For any material, on the atomic level, the magnetic dipoles are randomly oriented and in the absence of an external field, the magnetization of that material is zero. This concept is illustrated in Figure A.6. When the material is placed in an inductive field, the magnetic moments in the material reorient themselves preferentially along the direction of the applied field. This phenomenon results in a net internal magnetic induction or magnetization, **M**. A material in this state is magnetized. A region in which the magnetic dipoles are oriented in the same direction is known as a magnetic domain. Ferromagnetic materials contain a large number of magnetic domains, randomly oriented in an

unmagnetized sample. These domains are easily aligned by external magnetic fields resulting in a net magnetization. However, this magnetization is partly retained upon removal of the magnetic field. This phenomenon is identified by the level of hysteresis on the B-H curve of the material.

The net magnetic induction in a material is the vector sum of the externally applied magnetic field intensity and the magnetization (**H** and **M**). This phenomenon is represented by the following equation:

$$\mathbf{B} = \mathbf{B}_0 + \mu_0 \mathbf{M} \tag{6.18}$$

where $\mu_0\mathbf{M}$ is the contribution of the internal magnetization and $\mathbf{B}_0$ is the flux density in free space. In linearly isotropic materials, **M** is proportional to the applied field H by a factor know as susceptibility, χ_m. Magnetic susceptibility is a dimensionless parameter and is defined by the following equation:

$$\chi_m = \frac{\|\mathbf{M}\|}{\|\mathbf{H}\|} \tag{6.19}$$

Substituting eq A.13 and eq. A.19 into eq A.18 results in:

$$\mathbf{B} = \mu_0 \mathbf{H} + \mu_0 \mathbf{M} \tag{A.20}$$

$$= \mu_0 (1 + \chi_m)\mathbf{H} \tag{A.21}$$

$$= \mu_0 \mu_r \mathbf{H} \tag{A.22}$$

$$= \mu_c \mathbf{H} \tag{A.23}$$

where $\mu_r = 1 + \chi_m$ is the relative permeability of the material and μ_c is the magnetic permeability of the material. For pure iron, the relative permeability, μ_r is as high as 5000. The susceptibility of a material is not a constant parameter.

A.4 Demagnetization

For a material exposed to an external magnetic field, the magnetic dipoles of that material rotate to align with the direction of that field. This gives rise to a net magnetization vector **M** inside the material. In response to this magnetization, the material creates poles within itself which in turn generates a magnetic field intensity. This field intensity is in opposition to the external field and is known as the demagnetization field or H_d. The effect of the demagnetization field is to reduce the field intensity *inside* the material. Figure A.7 shows the demagnetization field for a material exposed to an external magnetic field. In practice, the magnitude of the demagnetization field is quantified by the following equation:

$$H_d = N_d M \tag{A.24}$$

where N_d is an empirical factor determined by the geometry of the specimen (i.e. sphere, ellipsoid, long slender rod, etc.). In practice, a general rule of thumb is that the higher the aspect ratio of the specimen, the lower the demagnetization field tends to be. For very high aspect ratio specimens, the demagnetization field is often neglected. However, in the case of NiMnGa FSMA, due to the orthogonal orientation of the excitation field and direction of strain, the apparent aspect ratio of the specimen is very low leading to a significant demagnetization field.

.

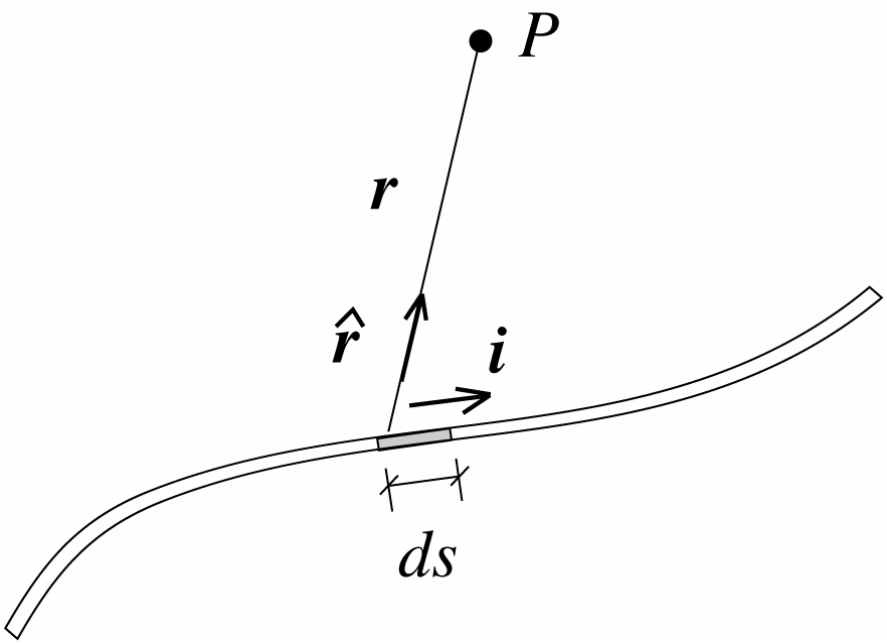

Figure A.1 Magnetic field produced by a current carrying element

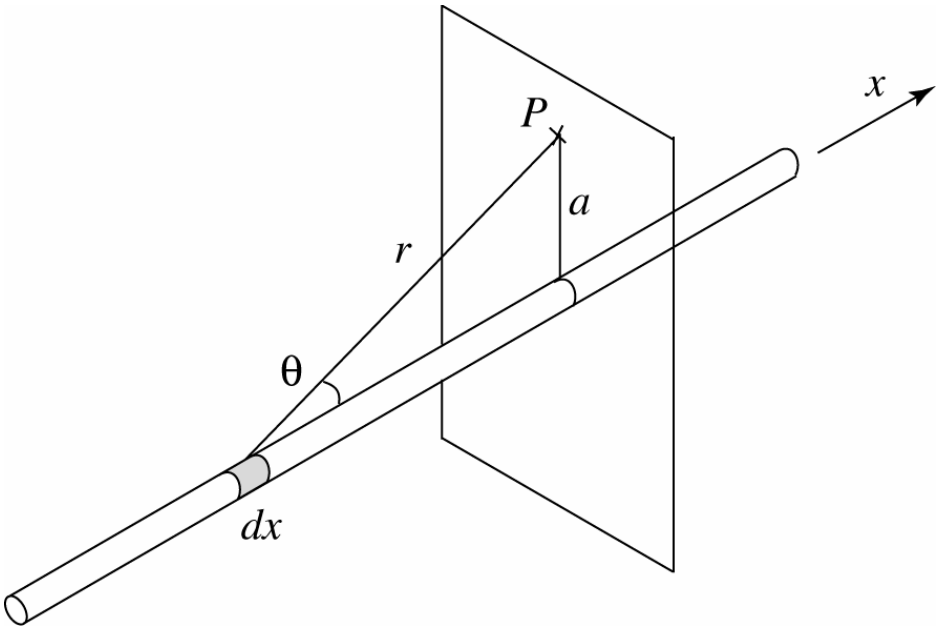

a) Application of the Biot-Savart law

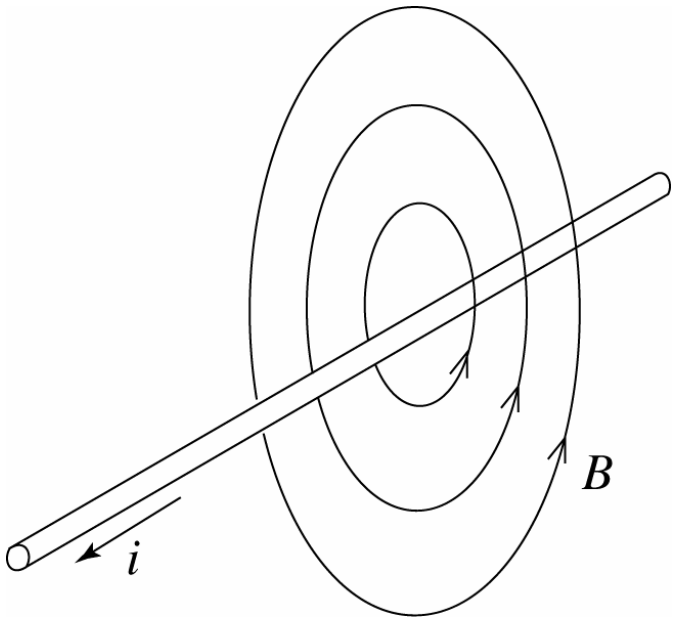

b) Direction of magnetic induction

Figure A.2 Magnetic induction due to a uniform, straight, current carrying conductor of infinite length

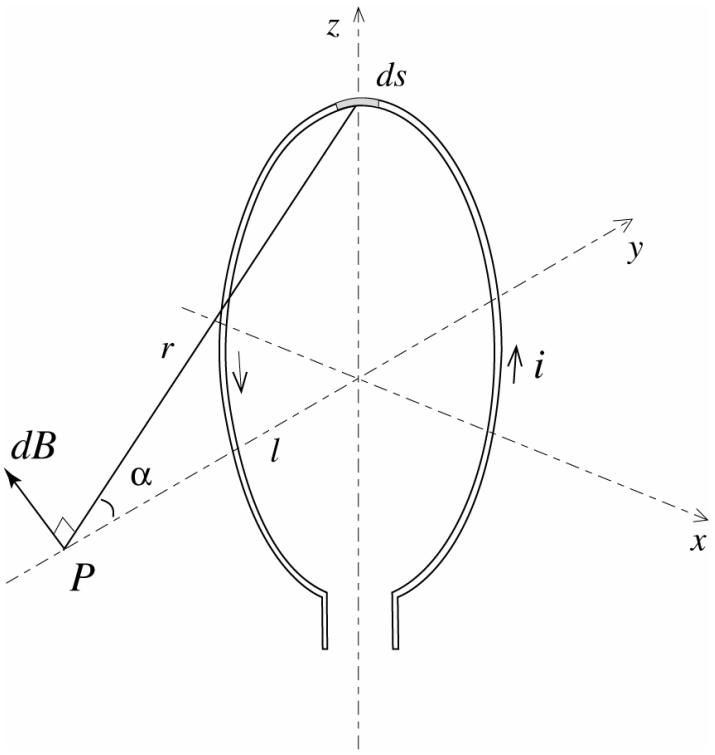

a) Application of the Biot-Savart law

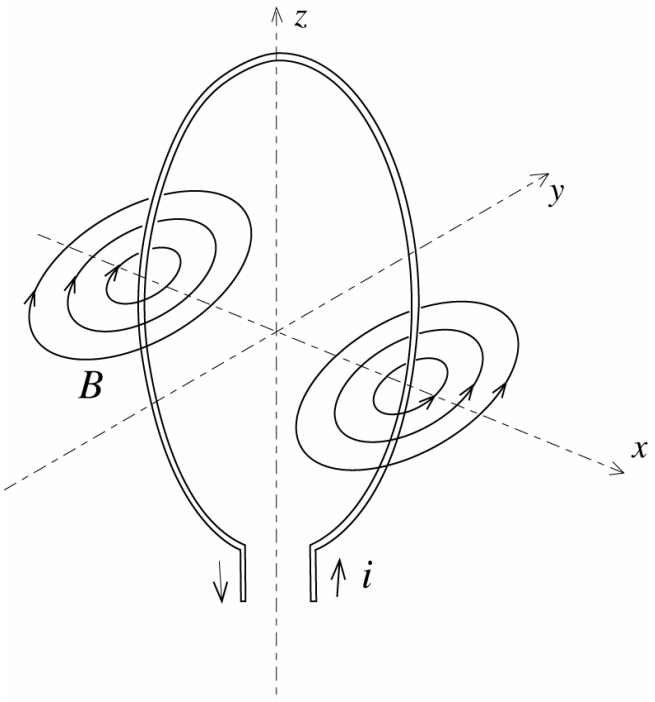

b) Direction of magnetic induction

Figure A.3 Magnetic induction due to a current carrying loop

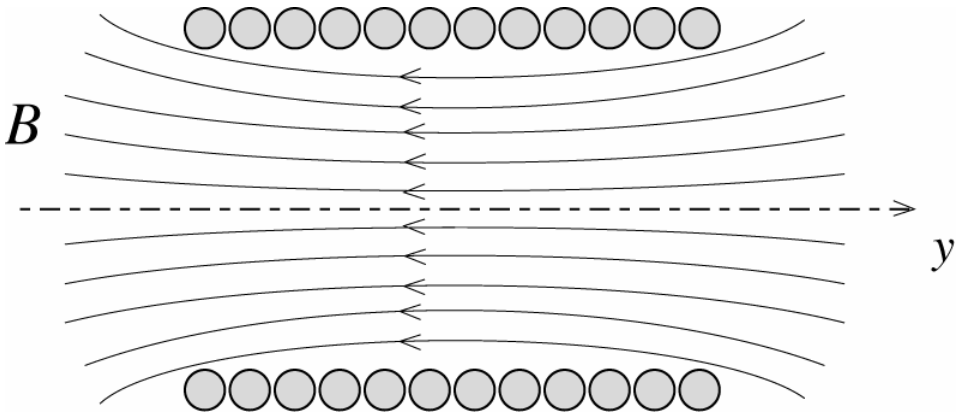

a) Solenoid (side view)

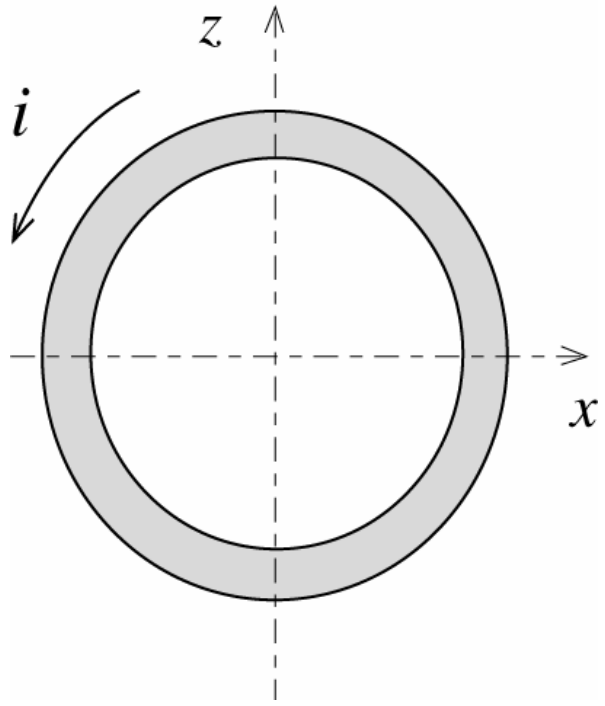

b) Solenoid (front view)

Figure A.4 Magnetic induction due to a current carrying solenoid

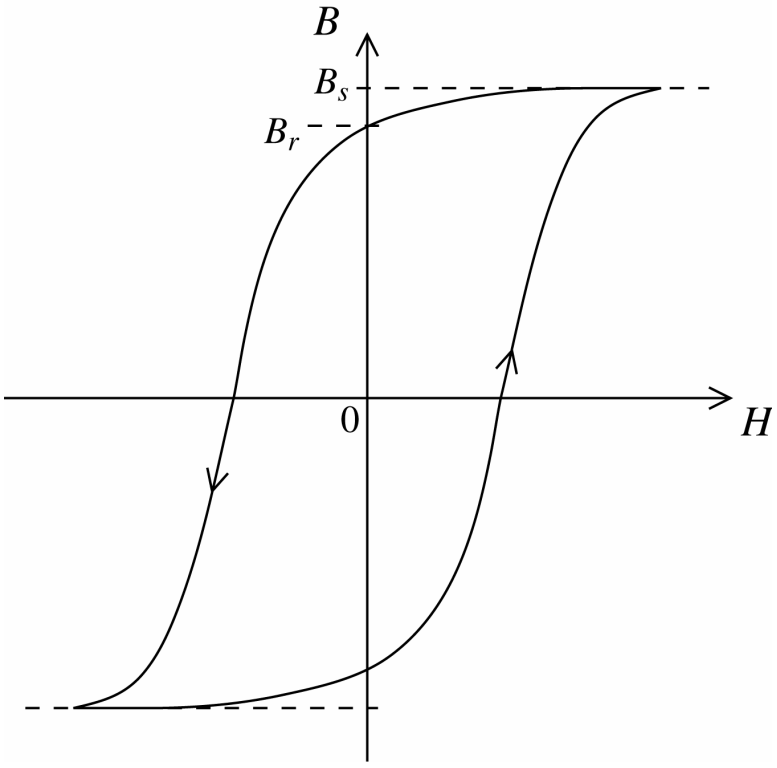

Figure A.5 Typical B-H curve for a ferromagnetic material

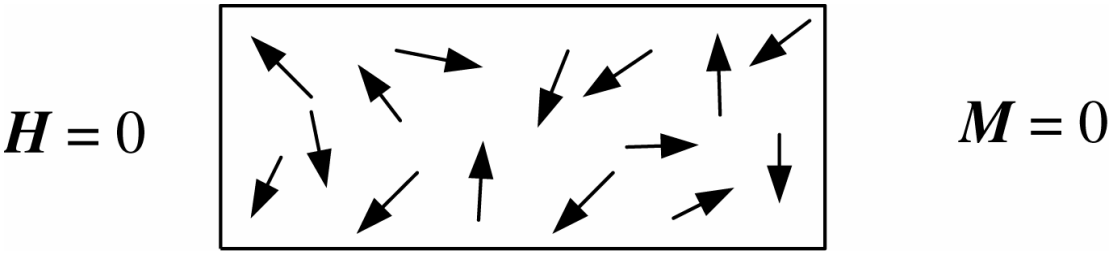

a) Magnetic moments with no applied field

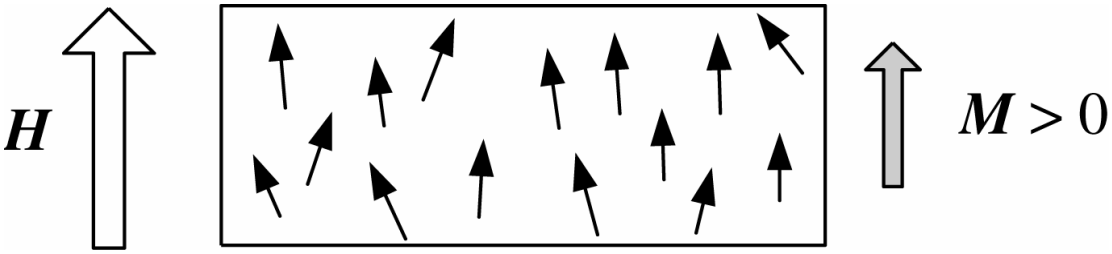

b) Reorientation of magnetic moments with applied field

Figure A.6 Effect of external field on a ferromagnetic material

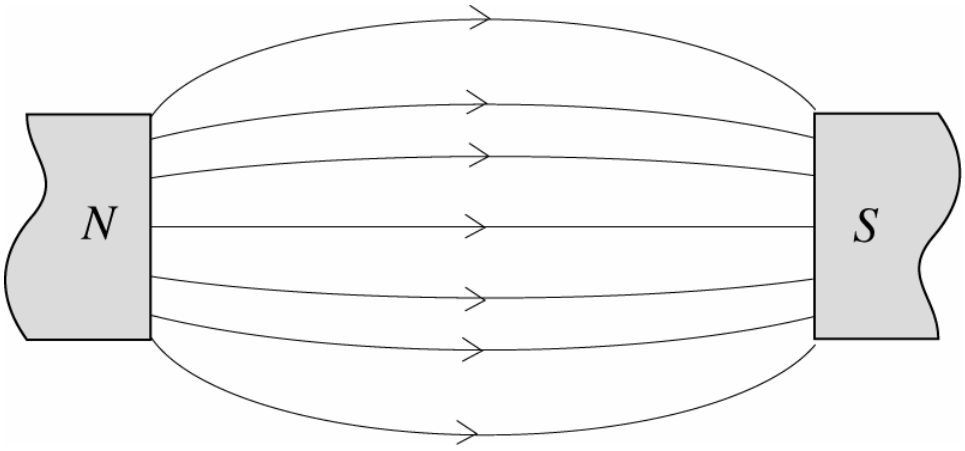

a) Magnetic field occurring between two poles

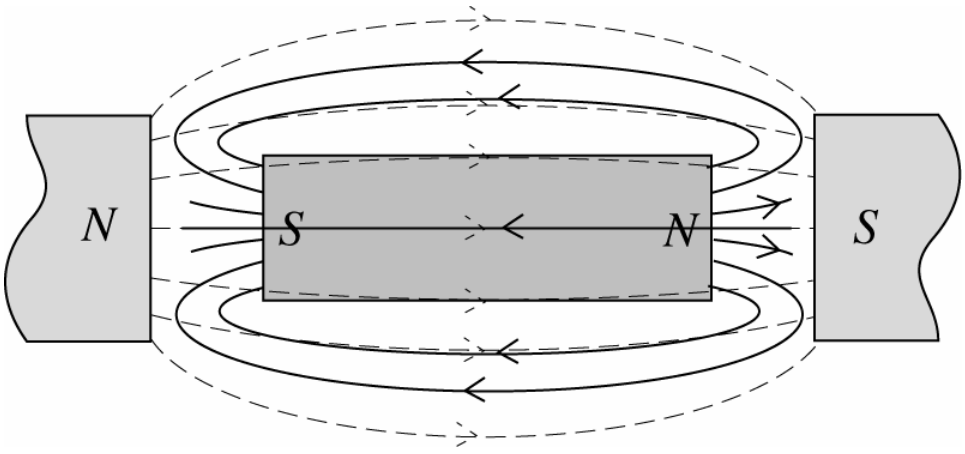

b) Effect of introducing a ferromagnetic material between two poles

Figure A.7 The demagnetization effect

Bibliography

[1] R.W. Prouty. *Helicopter performance, stability and performance*. Robert E. Kriege Publishing Company, Inc., Malabar, FL, 1990.

[2] R. Olson. Reducing helicopter costs. *Vertiflite*, 39(1):10–16, January/February 1993.

[3] E.A. Fradenburgh. The first 50 years were fine ... but what should we do for an encore? *Journal of the American Helicopter Society*, 40(1):3–19, January 1995. The 1994 Alexander A. Nikolsky Lecture.

[4] Inderjit Chopra. "Status of application of smart structures technology to rotorcraft systems" *Journal of the American Helicopter Society*, 45(4):228–252, October 2000.

[5] K. Ullakko, A. Likhachev, O. Heczko, A. Sozinov, T. Jokinen, K. Forsman, I. Aaltio, "Magnetic Shape Memory (MSM) – A New Way to Generate Motion in Electromechanical Devices," *ICEM 2000*, 1195-1199, August (2000)

[6] M. Marioni, D.C. Bono, R.C. O'Handley, S.M. Allen, "Pulsed magnetic field actuation of single crystalline ferromagnetic shape memory alloy NiMnGa," *Proceedings of SPIE*, 4699, 191-194 (2002).

[7] C. Henry, J. Feuchtwanger, D. Bono, M. Marioni, P. Tello, M. Richard, S. Allen, R. O'Handley, "AC performance and modeling of ferromagnetic shape memory actuators," *Proceedings of SPIE*, vol. 4333, pp. 151-162, (2001).

[8] Wayne Johnson. *Helicopter theory*. Dover Publications, Inc., New York, NY, 1980.

[9] Andreas Paul Friedrich Bernhard. *Smart Helicopter Rotor with Active Blade Tips*. PhD thesis, University of Maryland, College Park, MD 20742 USA, February 2000.

[10] G. Reichert. Helicopter vibration control - a survey. *Vertica*, 5(1):1–20, 1981.

[11] R.G. Loewy. Helicopter vibrations, a technological perspective. *Journal of the American Helicopter Society*, 29(4):3–20, October 1984.

[12] Braun, D., "Development of Antiresonance Force Isolators for Helicopter Vibration Reduction," *Journal of the American Helicopter Society*, Sept., 1980, pp. 37-44.

[13] Roget, B. and Chopra, I., "T railing Edge Flap Control Methodology for Vibration Reduction of Helicopter With Dissimilar Blades."*Proceedings of the 42nd AIAA/ASME/AHS Adaptive Structures Forum*, Seattle, WA, April 16-18, 2001.

[14] Alfred Gessow and Garry C. Myers, Jr. *Aerodynamics of the helicopter*. College Park Press, College Park, MD, 1985.

[15] Lewicki, D.G., and Coy, J.J., "Vibration Characteristics of OH-58A Helicopter Main Rotor Transmission," *NASA TechnicalPaper 2705*, 1987.

[16] C.W. Ellis and R. Jones. Application of an absorber to reduce helicopter vibration levels. *Journal of the American Helicopter Society*, 8(3):30–38, July 1963.

[17] E. P. Schuett. Application of passive helicopter rotor isolation for alleviation of rotor induced vibration. *Journal of the American Helicopter Society*, 14(2):34–48, April 1969.

[18] K. B. Amer and J. R. Neff. Vertical-plane pendulum absorbers for minimizing helicopter vibratory loads. *Journal of the American Helicopter Society*, 19(4):44–48, October 1974.

[19] Hawles, D.R., "Liquid Inertia Vibration Eliminator," *Proceedings of the 36th American Helicopter Society Forum* , May, 1980.

[20] Smith, M.R., "The Model 427 Pylon Isolation System," *Proceedings of the 55th American Helicopter Society Forum* , May, 1999.

[21] Braun, D., "Development of Antiresonance Force Isolators for Helicopter Vibration Reduction," *Journal of the American Helicopter Society*, Sept., 1980, pp. 37-44.

[22] A.E. Staple. An evaluation of active control of structural response as a means of reducing helicopter vibration. In *15th European Rotorcraft Forum*, pages 51.1–51.18, Amsterdam, The Netherlands, September 1989.

[23] A.E. Staple and D.M. Wells. Development and testing of an active control of structural response system for the EH101 helicopter. In *16th European Rotorcraft Forum*, Glasgow, Scotland, September 1990.

[24] W.A. Welsh, P.C. von Hardenberg, P.W. von Hardenberg, and A.E. Staple. Test and evaluation of fuselage vibration utilizing active control of structural response (acsr) optimized to ads-27. In *46th American Helicopter Society Forum*, pages 21–37, Washington, DC, May 1990.

[25] Mitsuhiro Aso and Shun-ichi Bandoh. The development of the total vibration reduction (TVR) system. In *55th American Helicopter Society Forum*, pages 202–208, Montreal, Canada, May 1999.

[26] Bernhard, A., "Sikorsky," Private Communication, 22nd May, 2002.

[27] T. Millott and W. Welsch. Helicopter active noise and vibration reduction. In *25th European Rotorcraft Forum*, Rome, Italy, September 1999. Paper G-23.

[28] P.R. Payne. Higher harmonic rotor control. *Aircraft Engineering*, 30(354):222–226, August 1958.

[29] I. Chopra and J. C. McCloud III. A numerical simulation study of open-loop, closed loop and adaptive multicyclic control systems. *Journal of the American Helicopter Society*, 28(1):311–325, October 1983.

[30] K. Nguyen and I. Chopra. Application of higher harmonic control to rotors operating at high speed and thrust. *Journal of the American Helicopter Society*, 35(3):78–89, July 1990.

[31] K. Nguyen and I. Chopra. Application of higher harmonic control (HHC) to hingeless rotors. *Vertica*, 14(4):545–556, October 1990.

[32] K. Nguyen and I. Chopra. Effects of higher harmonic control on rotor performance and control loads. *Journal of Aircraft*, 29(3), May/June 1992.

[33] C.E. Hammond. Wind tunnel results showing rotor vibratory loads reduction using higher harmonic blade pitch. *Journal of the American Helicopter Society*, 28(1):10–15, January 1983. 275.

[34] E.R. Wood, R.W. Powers, C.H. Cline, and C.E. Hammond. On developing and flight testing higher harmonic flight control system. *Journal of the American Helicopter Society*, 30(1):3–20, January 1985.

[35] W. Miao, S.B.R. Kottapali, and H.M Frye. Flight demonstration of higher harmonic control (HHC) on the S-76. In *42nd American Helicopter Society Forum*, Washington DC, June 1986.

[36] M. Polychroniadis and M. Achache. Higher harmonic control: flight tests of an experimental system on an sa 349 research gazelle. In *42nd American Helicopter Society Forum*, Washington DC, June 1986.

[37] J. Shaw, N. Albion, E.J. Hanker, and R.S Teal. Higher harmonic control: wind tunnel demonstration of fully effective vibratory hub forces suppression. *Journal of the American Helicopter Society*, 34(1):14–25, January 1989.

[38] M. Kretz. Relaxation of rotor limitations by feedback control. *Proceedings of the 33rd Annual Forum of the American Helicopter Society*, 1977.

[39] K.F. Guinn. Individual blade control independent of a swashplate. *Journal of the American Helicopter Society*, 27(3):25–32, July 1982.

[40] N. D. Ham. A simple system for helicopter individual-blade-control using modal decomposition. *Vertica*, 4(1/2):23–28, 1980.

[41] N. D. Ham. Helicopter individual blade control and its applications. In *39th American Helicopter Society Forum*, St. Louis, MO, May 1983.

[42] N. D. Ham. Helicopter-individual blade control research at mit 1977-1985. *Vertica*, 11(1/2):109–122, 1987.

[43] D. Teves, V. Kl¨oppel, and P. Richter. Development of active control technology in the rotating system, flight testing and theoretical investigations. In *18th European Rotorcraft Forum*, September 1992.

[44] P. Richter and A. Blaas. Full scale wind tunnel investigation of an individual blade control system for the bo-105 hingeless rotor. In *19th European Rotorcraft Forum*, Cernobbio, Italy, pp. 276, 1993 September.

[45] S.A. Jacklin, A. Blaas, D. Teves, and R. Kube. Reduction in helicopter BVI noise, vibration and power consumption through individual blade control. In *51st Annual Forum of the American Helicopter Society*, Fort Worth, TX, May 1995.

[46] P. Lorber, C. Park, D. Polak, J. O'Neill, and W. A. Welsh. Active rotor experiments at Mach scale using root pitch IBC. *Presented at the American Helicopter Society 57th Annual Forum,Washington DC*, May 9-11 2001.

[47] N. D. Ham. Helicopter gust alleviation, attitude stabilization and vibration reduction using individual blade control through a conventional swashplate. In *11th European Rotorcraft Forum*, London, UK, September 1985.

[48] T.R. Quackenbush. Testing of a stall flutter suppression system for helicopter rotors using individual blade control. *Journal of the American Helicopter Society*, 29(3):38–4, 1984.

[49] D. Morbitzer, U.T.P. Arnold, and M. M¨uller. Vibration and noise reduction through individual blade control, experimental and theoretical results. In *24th European Rotorcraft Forum*, Marseilles, France, September 1998. Paper TE-10.

[50] Epps, J.J., "Methodology for In-Flight Tracking of Helicopter Rotor Blades Using Shape Memory Alloy Actuators," *Proceedings of the 56th American Helicopter Society Forum* , May, 2000.

[51] Singh, K., "Design of an Improved Shape Memory Alloy Actuator for Helicopter Blade Tracking." *Proceedings of SPIE Conference on Smart Structures and Intelligent Systems*, San Diego, CA, 2002.

[52] Judah H. Milgram. *A comprehensive aeroelastic analysis of helicopter main rotors with trailing edge flaps for vibration reduction*. PhD thesis, University of Maryland, Aerospace Department, College Park, MD, January 1997.

[53] Friedrich K. Straub. A feasibility study of using smart materials for rotor control. *Smart Materials and Structures*, 5(1):1–10, February 1996.

[54] J.L. McCloud, III. An analytical study of a multicyclic controllable twist rotor. In *31st American Helicopter Society Forum*, Washington, DC, May 1975.

[55] A. Z. Lemnios and F. K. Dunn. Theoretical study of multicyclic control of a controllable twist rotor. Technical Reports NASA-CR-151959, NASA, April 1976.

[56] J.L. McCloud, III and A.L. Weisbrich. Wind tunnel test results of a full-scale multicyclic controllable twist rotor. In *34th American Helicopter Society Forum*, Washington, DC, May 1978.

[57] Inderjit Chopra and John. L McCloud, III. A numerical simulation study of open-loop, closed-loop and adaptive multicyclic control systems. *Journal of the American Helicopter Society*, 28(1):311–325, January 1983.

[58] S. Dawson and F. K. Straub. Design, validation and testing of a model rotor with tip mounted active flaps. *Proceedings of the 50th Annual Forum of the American Helicopter Society, Washington DC*, May 1994.

[59] F. K. Straub. Active flap control for vibration reduction and performance improvement. *Proceedings of the 51st Annual Forum of the American Helicopter Society, Fort Worth, TX*, May 1995.

[60] S. Dawson, A. Hassan, and Friedrich K. Straub. Wind tunnel test of an active flap rotor: BVI noise and vibration reduction. In *51st American Helicopter Society Forum*, pages 631–648, Fort Worth, TX, May 1995.

[61] A. P. F. Bernhard, J. O'Neill, F. Kohlhepp, W. Welsh, and P. Lorber. Active Rotor Control (ARC) of a mach-scale trailing edge flap rotor. *Presented at the American Helicopter Society 57th Annual Forum, Washington DC*, May 9-11 2001.

[62] T.A. Millott and P.P. Friedmann. Vibration reduction in helicopter rotors using an actively controlled partial span trailing edge flap located on the blade. Technical Report NASA-CR-4611, NASA, June 1994.

[63] T.A. Millott and P.P. Friedmann. Vibration reduction in rotorcraft using the actively controlled trailing edge flap and issues related to practical implementation. In *54th American Helicopter Society Forum*, Washington, DC, May 1998.

[64] T.A. Millott and P.P. Friedmann. Vibration reduction in rotorcraft using active control: a comparison of various approaches. *Journal of Guidance, Control and Dynamics*, 18(4):664–673, August 1995.

[65] Judah Milgram and Inderjit Chopra. A parametric design study for actively controlled flaps. *Journal of the American Helicopter Society*, 43(2):110–119, April 1998.

[66] Shen, J., and Chopra, I., "Actuation Requirements for a Swashplateless Helicopter Control System with Trailing-Edge Flaps," 2002 AIAA SDM Conference, Denver, Co, April 2002.

[67] Shen, J., and Chopra, I., "A Parametric Design Study for a Swashplateless Rotor with Trailing-Edge Flaps," 2002 AHS Annual Forum, Montreal, Canada, June 2002.

[68] Shen, J., and Chopra, I., "Ultralight Helicopter with Trailing-Edge Flaps for Primary Control," Proceedings for American Helicopter Society International Meeting on Advanced Technology and Life Saving Activities, Tochigi, Japan, November, 2002.

[69] Eric F. Prechtl and Steven R. Hall. An x-frame actuator servo-flap actuation system for rotor control. In *SPIE symposium on smart structures and materials, conference on smart structures and integrated systems*, pages 309–320, San Diego, CA, March 1998.

[70] Eric F. Prechtl and Steven R. Hall. Design of a high efficiency, large stroke, electromechanical actuator. *Smart Materials and Structures*, 8(1):13–30, February 1999.

[71] Eric F. Prechtl and Steven R. Hall. Preliminary testing of a Mach-scaled active rotor blade with trailing-edge servo flap. In *SPIE symposium on smart structures and materials, conference on smart structures and integrated systems*, pages 14–21, Newport Beach, CA, March 1999.

[72] Eric F. Prechtl and Steven R. Hall. Hover testing of a Mach-scaled rotor with an active trailing edge flap. In *8th Army Research Office (ARO) workshop on the aeroelasticity of rotorcraft systems*, State College, PA, October 1999.

[73] Eric F. Prechtl. *Design and Implementation of a Piezoelectric Servo-Flap Actuation System for Helicopter Rotor Individual Blade Control*. PhD thesis, Massachusetts Institute of Technology, Department of Aeronautics and Astronautics, Cambridge, MA, February 2000.

[74] Robert Ormiston. Aeroelastic considerations for rotorcraft primary control with on-blade elevons. *Presented at the American Helicopter Society 57th Annual Forum, Washington DC*, May 9-11 2001.

[75] I. Chopra. Review of current status of smart structures and integrated systems. *SPIE Smart Structures and Integrated Systems*, 2717:20–62, 1996.

[76] I. Chopra. Status of application of smart structures technology to rotorcraft systems. *Presented at the Innovations in Rotorcraft Technology, Royal Aeronautical Society, London*, 2717:20–62, June 1997.

[77] Daniel J. Jendritza and Hartmut Jonocha, editors. *Adaptronics and Smart Structures*. Springer Verlag GmbH, 1999.

[78] B.K. Wada, J.L. Fanson, and E.F. Crawley. Adaptive structures. *Journal of Intelligent Material Systems and Structures*, 1(2):157–174, April 1990.

[79] Patricia W. Stevens and Edward C. Smith. Active interrogation of helicopter rotor faults using trailing edge flap actuation. *Presented at the American Helicopter Society 57th Annual Forum, Washington DC*, May 9-11 2001.

[80] E.F. Crawley. Intelligent structures for aerospace: a technology overview and assessment. *AIAA Journal*, 32(8):1689–1699, August 1994.

[81] Andrew J. Moskalik and Diann Brei. Force-deflection behavior of piezoelectric c-block actuator arrays. *Smart Materials and Structures*, 8(5):531–543, October 1999.

[82] M.W. Hooker. Properties and performance of RAINBOW piezoelectric actuator stacks. In *SPIE symposium on smart structures and materials, conference on industrial and commercial applications of smart structures technologies*, pages 413–420, San Diego, CA, March 1997.

[83] THUNDER actuators. Face International Corporation, http://www.faceinternational.com, Norfolk, VA, 1999.

[84] K.M. Mossi and R.P. Bishop. Characterization of different types of high-performance THUNDER actuators. In *SPIE symposium on smart structures and materials, conference on smart materials technologies*, pages 43–52, Newport Beach, CA, March 1999.

[85] Jeanette Epps and Inderjit Chopra. Shape memory alloy actuators for in-flight tracking of helicopter rotor blades. *Smart Materials and Structures*, 10(1):104–111, 2001.

[86] Jeanette J. Epps. *In-Flight Tracking of Helicopter Rotor Blades with Tabs Using Shape Memory Alloys*. PhD thesis, University of Maryland, College Park, MD 20742 USA, 2000.

[87] Harsha Prahlad and Inderjit Chopra. Design of a variable twist tilt-rotor blade using shape memory alloy (SMA) actuators. In *Proceedings of SPIEs Annual Symposium on Smart Structures and Materials, Newport Beach, CA*, volume 4327, pages 46–59, 2001.

[88] Jayanth N. Kudva, Brian P. Sanders, Jennifer L. Pinkerton-Florance, and Ephrahim Garcia. Overview of the DARPA/AFRL/NASA Smart Wing Phase II program. *Proceedings of the 8th SPIE Conference on Smart Structures and Materials: Industrial and Commercial Applications of Smart Structures Technologies, Newport Beach, CA*, 4332:383–389, March 2001.

[89] Jayanth N. Kudva, Christopher A. Martin, Lewis B. Scherer, Peter A. Jardine, Anna-Maria Rivas McGowan, Renee C. Lake, George P. Sendeckyi, and Brian P. Sanders. Overview of the DARPA/AFRL/NASA Smart Wing program. *Proceedings of the 6th SPIE Conference on Smart Structures and Materials: Industrial and Commercial Applications of Smart Structures Technologies, Newport Beach, CA*, 3674:230–236, March 1999.

[90] K. Ullakko, P. Jakovenko, V.G. Gavriljuk, "New developments in actuator materials as reflected in magnetically controlled shape memory alloys and high-strength shape memory steels", Proceedings of SPIE Conf. on Smart Structures and Materials, 2715, pp. 42-50 (1996).

[91] Peter Che-Hung Chen. *Development of a smart rotor with induced-strain actuation of blade twist*. PhD thesis, University of Maryland, Aerospace Department, College Park, MD, 1996.

[92] Peter C. Chen and Inderjit Chopra. Hover test of a smart rotor with induced strain actuation of blade twist. *AIAA Journal*, 35(1):6–16, January 1997.

[93] Peter C. Chen and Inderjit Chopra. Wind tunnel test of a smart rotor model with individual blade twist control. *Journal of Intelligent Material Systems and Structures*, 8(5):414–425, May 1997.

[94] Aaron A. Bent and Nesbitt W. Hagood. Anisotropic actuation with piezoelectric fiber composites. *Journal of Intelligent Material Systems and Structures*, 6(3):338–349, 1995.

[95] John P. Rodgers and Nesbitt W. Hagood. Manufacture of adaptive composite plates incorporating piezoelectric fiber composite plies. In *36th AIAA/ASME/ASCE/AHS/ASC Structures, Structural Dynamics and Materials Conference and AIAA/ASME Adaptive Structures Forum*, pages 2824– 2835, New Orleans, LA, April 1995.

[96] John P. Rodgers, Aaron A. Bent, and Nesbitt W. Hagood. Characterization of interdigitated electrode piezoelectric fiber composites under high electrical and mechanical loading. In *SPIE symposium on smart structures and materials, conference on smart structures and integrated systems*, pages 642–659, San Diego, CA, March 1996.

[97] John P. Rodgers. *Development of an integral twist-actuated rotor blade for individual blade control*. PhD thesis, Massachusetts Institute of Technology, Department of Aeronautics and Astronautics, Cambridge, MA, October 1998.

[98] W. Keats Wilkie, Matthew L. Wilbur, Paul H. Mirick, Carlos E.S. Cesnik, and SangJoon Shin. Aeroelastic analysis of the NASA/ARMY/MIT active twist rotor. In *55th American Helicopter Society Forum*, Montreal, Canada, May 1999.

[99] Carlos E.S. Cesnik, SangJoon Shin, W. Keats Wilkie, Matthew L. Wilbur, and Paul H. Mirick. Modeling, design and testing of the NASA/ARMY/MIT active twist rotor prototype blade. In *55th American Helicopter Society Forum*, Montreal, Canada, May 1999.

[100] Matthew L. Wilbur, W. Keats Wilkie, William T. Yeager, Renee C. Lake, Chester Langston, Carlos E.S. Cesnik, and SangJoon Shin. Hover testing of the NASA/ARL/MIT active twist rotor. In *8th Army Research Office (ARO) workshop on the aeroelasticity of rotorcraft systems*, State College, PA, October 1999.

[101] CurtisWalz and Inderjit Chopra. “Design and testing of a helicopter rotor model with smart trailing edge flaps”. In *35th AIAA/ASME/ASCE/AHS/ASC structures, structural dynamics and materials conference and AIAA/ASME/AHS adaptive structures forum*, Hilton Head, SC, April 1994.

[102] Oren Ben-Zeev and Inderjit Chopra. “Advances in the development of an intelligent helicopter rotor employing smart trailing edge flaps”. *Smart Materials and Structures*, 5(1):11–25, February 1996.

[103] Nikhil A. Koratkar and Inderjit Chopra. “Analysis and testing of a Froude scaled rotor with piezoelectric bender actuated trailing-edge flaps”. *Journal of Intelligent Material Systems and Structures*, 8(7):555–70, July 1997.

[104] Nikhil A. Koratkar and Inderjit Chopra. “Analysis and testing of a Mach scaled helicopter rotor in hover with piezoelectric bender actuated trailing-edge flaps”. In *SPIE symposium on smart structures and materials, conference on smart structures and integrated systems*, pages 266–290, San Diego, CA, March 1998.

[105] Nikhil A. Koratkar and Inderjit Chopra. “Analysis and testing of a Mach scaled rotor model with piezoelectric bender actuated trailing-edge flaps”. In *40th AIAA/ASME/ASCE/AHS/ASC structures, structural dynamics and materials conference and AIAA/ASME/AHS adaptive structures forum*, pages 2380–2402, St. Louis, MO, April 1999.

[106] Nikhil A. Koratkar and Inderjit Chopra. “Design, fabrication and testing of a Mach scaled-rotor model with trailing edge flaps”. In *55th American Helicopter Society Forum*, pages 558–578, Montreal, Canada, May 1999.

[107] Nikhil A. Koratkar and Inderjit Chopra. “Hover testing of a Mach-scaled rotor with trailing-edge flaps”. In *SPIE symposium on smart structures and materials, conference on smart structures and integrated systems*, Newport Beach, CA, March 2000.

[108] Nikhil A. Koratkar and Inderjit Chopra. Windtunnel testing of a Mach-scaled rotor with trailingedge flaps. In *56th American Helicopter Society Forum*, Virginia Beach, VA, May 2000.

[109] Nikhil Ashok Koratkar. *Smart Helicopter Rotor with Piezoelectric Bender Actuated Trailing-Edge Flaps*. PhD thesis, University of Maryland, College Park, MD 20742 USA, 2000.

[110] Andreas P.F. Bernhard and Inderjit Chopra. Development of a smart moving blade tip activated by a piezo-induced bending-torsion coupled beam. In *SPIE symposium on smart structures and materials, conference on smart structures and integrated systems*, pages 63–79, San Diego, CA, February 1996.

[111] Andreas P.F. Bernhard and Inderjit Chopra. “Hover testing of an active rotor blade tip and structural analysis of the actuator beam.” In *39th AIAA/ASME/ASCE/AHS/ASC structures, structural dynamics and materials conference and AIAA/ASME/AHS Adaptive structures forum*, pages 3299–3325, Longbeach, CA, April 1998.

[112] Andreas P.F. Bernhard and Inderjit Chopra. Hover testing of active rotor blade-tips using a piezo-induced bending-torsion coupled beam. *Journal of Intelligent Material Systems and Structures*, 9(12):963–974, December 1998.

[113] C.M. Bothwell, Ramesh Chandra, and Inderjit Chopra. Torsional actuation with extensiontorsional composite coupling and magnetostrictive actuators. *AIAA Journal*, 33(4):723–729, April 1995.

[114] Jayant Sirohi, and Inderjit Chopra, *Piezoelectric Hydraulic Hybrid Actuator for a Potential Smart Rotor Application*, PhD thesis, University of Maryland, College Park, MD 20742 USA, 2002.

[115] Friedrich K. Straub and R.J. King. Application of smart materials to helicopter rotor active control. In *SPIE symposium on smart structures and materials, conference on industrial and commercial applications of smart structures technologies*, pages 66–77, San Diego, CA, March 1996.

[116] Friedrich K. Straub, M.A. Ealey, and M.L. Schetky. Application of smart materials to helicopter rotor active control. In *SPIE symposium on smart structures and materials, conference on industrial and commercial applications of smart structures technologies*, pages 99–113, February, CA, March 1997.

[117] Friedrich K. Straub, Hieu T. Ngo, V. Anand, and D.B. Domzalski. Development of a piezoelectric actuator for trailing-edge flap control of rotor blades. In *SPIE symposium on smart structures and materials, conference on smart structures and integrated systems*, pages 2–13, Newport Beach, CA, March 1999.

[118] Friedrich K. Straub and Bruce D. Charles. Comprehensive modeling of rotors with trailing edge flaps. In *55th American Helicopter Society Forum*, Montreal, Canada, May 1999.

[119] Friedrich K. Straub. Development of a full scale smart rotor system. In *8th Army Research Office (ARO) workshop on the aeroelasticity of rotorcraft systems*, State College, PA, October 1999.

[120] Friedrich K. Straub. Smart rotor technology developments - challenges and payoffs. In *The 12th International Conference on Adaptive Structures Technology*, University of Maryland, College Park, MD, October 2001.

[121] D. Schimke, Peter J¨anker, A. Blaas, R. Kube, G. Schewe, and Ch. Keßler. Individual blade control by servo-flap and blade root control, a collaborative research and development programme. In *23rd European Rotorcraft Forum*, pages 46.1–46.16, Dresden, Germany, September 1997.

[122] D. Schimke, Peter J¨anker, V. Wendt, and B. Junker. Wind tunnel evaluation of a full scale piezoelectric flap control unit. In *24th European Rotorcraft Forum*, Marseilles, France, September 1998. Paper TE-02.

[123] P. J¨anker, V. Kl¨oppel, F. Hermle, T. Lorkowski, S. Storm, M. Christmann, and M. Wettemann. Development and evaluation of a hybrid piezoelectric actuator for advanced flap control technology. In *25th European Rotorcraft Forum*, Rome, Italy, September 1999. Paper G-21.

[124] B.G. van der Wall R. Kube, A. B¨uter, U. Ehlert, W. Geissler, M. Raffel, and G. Schewe. A multi concept approach for development of adaptive rotor systems. In *8th Army Research Office (ARO) workshop on the aeroelasticity of rotorcraft systems*, State College, PA, October 1999.

[125] T. Lorkowski, P. J¨anker, F. Hermle, , S. Storm, M. Christmann, and M. Wettemann. Development of a piezoelectrically actuated leading edge flap for dynamic stall delay. In *25th European Rotorcraft Forum*, Rome, Italy, September 1999. Paper G-20.

[126] Francois Toulmay, Valentin Kloppel, Francois Lorin, Bernhard Enenki, and Jacques Gaffiero. Active blade flaps - the needs and current capabilites. *Presented at the American Helicopter Society 57th Annual Forum, Washington DC*, May 9-11 2001.

[127] Taeoh Lee and Inderjit Chopra. Design and static testing of a trailing-edge flap actuator with piezostacks for a rotor blade. In *SPIE symposium on smart structures and materials, conference on smart structures and integrated systems*, pages 321–332, San Diego, CA, March 1998.

[128] Taeoh Lee and Inderjit Chopra. Development and validation of a refined piezostack-actuated trailing-edge flap actuator for a helicopter rotor. In *SPIE symposium on smart structures and materials, conference on smart structures and integrated systems*, Newport Beach, CA, March 1999.

[129] T. Lee, I. Chopra, "*Design of a High Displacement Smart Trailing-Edge Flap Actuator Incorporating Dual Stage Mechanical Stroke Amplifier for Rotors*," Ph.D. dissertation, University of Maryland, Department of Aerospace Engineering, College Park, MD, 1999.

[130] D. A. Fink, T. J. Hawkey, M. Gaudreau, B. Wellman, and R. A. Ormiston. An electromagnetic actuator for individual blade control. *Presented at the American Helicopter Society 57th Annual Forum, Virginia Beach, Virginia*, May 2000.

[131] D. A. Fink, T. J. Hawkey, M. Gaudreau, B. Wellman, and R. A. Ormiston. An electromagnetic actuator for individual blade control. *AHS National*

Specialists' Meeting "Improving Rotorcraft Acceptance Through Active Controls Technology, Bridgeport, Connecticut, October 2000.

[132] Matthew Tarascio, Marc Gervais, Tim Gowen, Jun Ma, Kiran Singh, Gaurav Gopalan, Kristi Kleinhesselink, Yong sheng Zhao, and Inderjit Chopra. Raven SAR Rotorcaft. Technical report, Alfred Gessow Rotorcraft Center, University of Maryland, College Park, MD 20742, 2001. In response to the 2001 Annual AHS International Student Design Competition - Graduate Category.

[133] Jason Pereira, Felipe Bohorquez, Mustapha Chehab, Ronald Couch, Tracy Duvall, Jacob Park, Beerinder Singh, and Inderjit Chopra. 406-UM TerpRanger Light Helicopter Upgrade Program. Technical report, Alfred Gessow Rotorcraft Center, University of Maryland, College Park, MD 20742, 2002. In response to the 2002 Annual AHS International Student Design Competition - Graduate Category.

[134] A.J. du Plessis, A.W. Jessiman, C.J. Muller, M.C. van Schoor, "Latching valve control using ferromagnetic shape memory alloys", *Smart Structures and Materials 2003: Industrial and Commercial Applications of Smart Structures Technologies, Proceedings of SPIE,* 5054, pp. 320-331, 2003.

[135] website: www.adaptamat.com

[136] J. Shen, and I. Chopra, "Actuation requirements for a swashplateless helicopter control system with trailing-edge flaps," *2002 AIAA SDM Conference*, Denver, Co, April 2002.

[137] J. Shen, and I. Chopra, "A parametric design study for a swashplateless rotor with trailing-edge flaps," *2002 AHS Annual Forum*, Montreal, Canada, June 2002.

[138] R.C. O'Handley, "Model for Strain in Magnetic Shape Memory Alloys," *Journal of Applied Physics*, 83, 6, 3263-3270 (1998).

[139] R. Couch, I. Chopra, "Experimental Characterization of NiMnGa Ferromagnetic Shape Memory Alloy Rods Under Dynamic Magnetic Fields", *Proceedings of SPIE*, San Diego, March 2003.

[140] J. Tellinen, I. Soursa, A. Jaaskelainen, I. Aaltio, K. Ullakko, "Basic Properties of Magnetic Shape Memory Actuators," Proceedings of Actuator 2002, Bremen Germany (2002).

[141] P. Mullner, V.A. Chernenko, G. Kostorz, "Stress-Induced Twin Rearrangement

Resulting in Change of Magnetization in a NiMnGa Ferromagnetic Martensite,"
Scripta Materialia, 49, 129-133, (2003).

[142] S.Y. Chu, R. Gallagher, M. De Graef, M.E. Henry, *IEEE Transactions on Magnetics*, 37, 2666-2668 (2001).

[143] S.J. Murray, M. Marioni, S.M. Allen, R.C. O'Handley, T. Lograsso, *App. Phys. Lett.,* 77, 886-888 (2002).

[144] O. Heczko, A. Sozinov, K. Ullakko, *IEEE Transactions on Magnetics*, 36, 3266-3268 (2000).

[145] A. Sozinov, Y. Ezer, G. Kimmel, P. Yakovenko, D. Giller, Y. Wolfus, Y. Yeshurun, K. Ullakko, V.K. Lindroos, *J. Phys IV* (France), 11, 311-316 (2001).

[146] A. Sozinov, A.A. Likhachev, N. Lanska, K. Ullakko, V.K. Lindroos, *Proceedings of SPIE*, 4699, 195-205 (2002).

[147] A. Sozinov, A. Likhachev, N. Lanska, K. Ullakko, *Applied Phys. Lett*, 80, 1746-1748 (2002).

[148] V.V. Martynov, V.V. Kokorin, *J. Phys. III*, 2, 739 (1992).

[149] A. Sozinov, A.A. Likhachev, K. Ullakko, *Proceedings of SPIE*, 4333 189-196 (2001).

[150] A. Sozinov, A. Likhachev, N. Lanska, K. Ullakko, V. Lindroos, "Crystal Structure, Magnetic Anisotropy and Mechanical Properties of Seven-Layered Martensite in NiMnGa," *Proceedings of SPIE*, 4699, 195-205 (2002).

[151] A. Sozinov, A.A. Likhachev, N. Lanska, O. Soderberg, K. Ullakko, V.K. Lindroos, *Proceedings of SPIE*, 5053, 586-594 (2003).

[152] M. Marioni, D.C. Bono, R.C. O'Handley, S.M. Allen, "Pulsed magnetic field actuation of single crystalline ferromagnetic shape memory alloy NiMnGa," *Proceedings of SPIE*, 4699, 191-194 (2002).

[153] L.M. Cheng, S.P. Farrell, R. Ham-Su, C.V. Hyatt, *Proc. of SPIE*, 5387, 137 (2004).

[154] K. Ullakko, J.K. Huang,, C. Kantner, R.C. O'Handley, T. Lograsso, *App. Physics Letters*, 69, 1966 (1996).

[155] S.J. Murray, "Magneto-mechanical properties and applications of Ni-Mn-Ga ferromagnetic shape memoy alloy," Ph.D. Thesis, MIT, Boston, MA, 2000.

[156] R. Tickle, R.D. James, T. Shield, M. Wuttig, V.V. Kokorin, "Ferromagnetic shape memory in NiMnGa system", *IEEE Trans. Magn.*, 35, 4301 (1999).

[157] W.H. Wang, G.H. Wu, J.L. Chen, C.H. Yu, Z. Wang, Y.F. Zheng, L.C. Zhao, W.S. Zhan, *J. Phys. Condens. Matter*, 12, 6287 (2000).

[158] V.A. Chernenko, E. Cesari, V.V. Kokorin, I.N. Vitenko, *Scr. Metall. Mater.*, 33, 1239 (1995).

[159] V.V. Kokorin, V.V. Martynov, V.A. Chernenko, *Scr. Metall. Mater.*, 26, 125 (1995).

[160] V.V. Martynov, V.V. Kokorin, *J. Phys. III*, 2, 739 (1992).

[161] G.H. Wu, C.H. Yu, L.Q. Meng, J.L. Chen, F.M. Yang, S.R. Qi, W.S. Zhan, Z. Wang, Y.F. Zheng, L.C. Zhao, *Appl. Phys. Lett.*, 75, 2990 (1999).

[162] R. O'Handley, *Modern Magnetic Materials: Principles and Applications*, New York: Wiley, 2000.

[163] Y. Enomoto, *J. Phys: Condens. Matter.,* 1, 5527-5530 (1989).

[164] J.W. Christian, *Metall. Trans.*, A 13, 509 (1982).

[165] A.G. Khachturyan, *Theory of Structural Transformations in Solids,* New York: Wiley, 1983.

[166] D.I. Paul, "Ferromagnetic Shape Memory Alloys: Theory of Interactions," *Bringing Materials Research Together: 2004,* website: http://mpc-web.mit.edu/about_mpc/ar2004/paul.pdf

[167] D.I. Paul, J. Marquiss, D. Quattrochi, "Theory of Magnetization: Twin Boundary Interaction in Ferromagnetic Shape Memory Alloys," *Journal of Applied Physics,* 93, 8, 4561-4565 (2003).

[168] I. Soursa, J. Tellinen, E. Pagounis, I. Aaltio, K. Ullakko, "Applications of Magnetic Shape Memory Actuators,"*Proceedings of Actuator 2002*, Bremen Germany (2002).

[169] I. Chopra, "Review of State of Art of Smart Structures and Integrated Systems," *AIAA Journal*, 40, No. 11, 2145-2187 (2002).

[170] Harsha Prahlad and Inderjit Chopra, *Development of Smart Torsional Actuators for Active Twist Tilt Rotor (VTTR) Blades*, PhD thesis, University of Maryland, College Park, MD 20742 USA, April 2002.

[171] K.H. Buschow, F.R, De Boer, *Physics of Magnetism and Magnetic Materials*, Springer, 2003 190 pp.

[172] Dunlop, D. J., Magnetic properties of fine-particle hematite, *Ann. Géophys.*, 27, 269-293, 1971.

[173] K. Ullakko, J.K. Huang, R.C. O'Handley, *Scr. Metall. Mater.,* 36, 1133 (1997).

[174] A. Likhachev, K. Ullakko, "Magnetic Field Controlled Twin Boundary Motion and Giant Magneto-Mechanical Effects in Ni-Mn-Ga Shape Memory Alloy," *Physics Letters A*, 275, 142-151 (2000).

[175] P. Mullner, V.A. Chernenko, M. Wollgarten, G. Kostorz, "Large Cyclic Deformation of a NiMnGa Shape Memory Alloy Induced by Magnetic Fields," *J. of Appl. Physics*, 92 (11), 6708-6713 (2002).

[176] K. Ullakko, J.K. Huang, C. Kantner, R.C. O'Handley, V. Kokorin, "Large Magnetic Field Induced Strains in Ni_2MnGa Single Crystals," *Appl. Phys. Lett.*, 69 (13), 1966-1968 (1996).

[177] A. Sozinov, A. Likhachev, N. Lanska, K. Ullakko, V. Lindroos, "Crystal Structure, Magnetic Anisotropy and Mechanical Properties of Seven-Layered Martensite in NiMnGa," *Proceedings of SPIE*, 4699, 195-205 (2002).

[178] L.E. Faidley, M.J. Dapino, G.N. Washington, T.A. Lograsso, R.C. Smith, "Dynamic Response in the DC-20 kHz Range and Delta-E Effect in Ferromagnetic Shape Memory NiMnGa, *Proceedings of IMECE'03*, Washington, D.C. (2003).

[179] L. Faidley, M. Dapino, G. Washington, T. Lograsso, R. Smith, "Analytical and Experimental issues in NiMnGa Transducers," *Proceedings of SPIE*, March (2003).

[180] A.A. Cherechukin, I.E.Dikshtein, D.I. Ermakov, et. al., "Shape Memory Effect due to Magnetic Field-Induced Thermoelastic Martensitic Transformation in Polycrystalline Ni-Mn-Fe-Ga Alloy," *Physics Letters A,* 291, 175-183 (2001).

[181] N. Glavatska, G. Mogylny, I. Glavatskiy, V. Gavriljuk, "Temperature stability of martensite and magnetic field induced strain in NiMnGa", *Scripta Materialia*, 46, 605-610 (2002).

[182] K. Ullakko, *J. of Mater. Eng. Perform.*, 5, 405 (1996).

[183] R.D. James, M. Wuttig, *Philos Mag A,* A77, 1273 (1998).

[184] A. Sozinov, A.A. Likhachev, N. Lanska, K. Ullakko, V.K. Lindroos, *Proceedings of SPIE*, 4699, 195-205 (2002).

[185] J. Pons, V.A. Chernenko, R. Santamarta, E. Cesari, *Acta Mat.*, 48, 3027-3038 (2000).

[186] A. Malla, M. Dapino, T. Lograsso, D. Schlagel, "Effect of Composition on the Magnetic and Elastic Properities of Shape-Memory NiMnGa," *Proceedings of SPIE*, March (2003).

[187] A.N. Vasilev, A.D. Bozhko, V.V. Khovailo, I.E. Dikshtein, V.G. Shavrov, V.D. Buchlnikov, M. Matumoto, S. Suzuki, T. Takagi, J Tani, *Phys. Rev. B*, 59, 1113 (1999).

[188] A.D. Bozhko, A.N. Vasilev, V.V. Khovailo, I.E. Dikshtein, V.V.Kiledov, S.M. Seletski, A.A. Tulaikova, A.A. Cherechukin, V.G. Shavrov, V.D. Buchelnikov, *JTEP*, 88, 954 (1999).

[189] S.K. Wu, S.T. Yang, *Materials Letters*, 57, 4291 4296 (2003).

[190] P.J. Webster, K.R.A. Ziebeck, S.L. Town, M.S. Peak, *Philos. Mag.,* B 49, 295 (1984).

[191] H. Warlimont, L. Delaey, R.V. Krishnan, H. Tas, *J. of Mater. Sci.*, 9, 1545 (1974).

[192] K.Hiroyuki, K. Sasaki, "Straining of Magnetic Shape Memory Martensite by Uniform Magnetic Field," *Scripta Materialia*, 48, 31-35 (2003).

[193] V.A.Chernenko, V.V. Kokorin, *Proceedings of the International Conference on Martensitic Transformation,* Monterey, 1992, p.1205.

[194] G. Airoldi, B. Rivolta, C. Turco, *ICOMAT-86*, Jpn. Inst Metal., 691 (1987).

[195] H.C. Lin, S.K. Wu, *Scripta Metall. Mater.*, 25, 1295 (1991).

[196] W.J. Beuler, R.C. Wiley, F.E. Wang, "Nickel-Based Alloys," U.S Patent 3,174,851,23, March 1965.

[197] K.Ullakko, J.K Huang, V.V. Kokorin, R.C. O'Handley, "Magnetically controlled shape memory effect in NiMnGa Intermetallics", *Scr.Mater.*, 36, 1133 (1997).

[198] S.J. Murray, M. Farinelli, C. Kantner, J.K. Huang, S.M. Allen, R.C. O'Handley, *J. Appl. Phys.*, 83, 7297 (1998).

[199] R.Tickle, R.D. James, *J. Magn. Magnetic Mater.*, 195, 627 (1999).

[200] R.C. O'Handley, S.J. Murray, M. Marioni, H. Nembach, S.M. Allen, "Phenomenology of giant magnetic-field-induced strain in ferromagnetic shape memory alloys", *J. Appl. Phys.*, 87, 4712 (2000).

[201] Y. Ma, S. Awaji, K. Watanabe, M. Matsumoto, N. Kobayashi, *Appl. Phys. Lett.*, 76, 37 (2000).

[202] Website: http://www.irm.umn.edu/hg2m/hg2m_c/hg2m_c.html, magnetic anisotropy

[203] Brinson, L.C., "One-Dimensional Constitutive Behavior of Shape Memory Alloys: Thermomechanical Derivation with Non-Constant Material Functions and Redefined Martensite Internal Variable", *Journal of Intelligent Material Systems and Structures*, vol. 4, pp. 229-242, April 1993.

[204] H. Prahlad, I. Chopra, "Comparative Evaluation of Shape Memory Alloy Constitutive Models and Experimental Data," *Journal of Intelligent Material Systems and Structures*, vol 12. No 6, pp. 386-396 (2001).

[205] H. Prahlad, I. Chopra, "Development of a Strain-Rate Dependent Model of Uniaxial Loading of SMA Wires," *12th International Conference on Adaptive Structures and Technologies,* CRC Press, Boca Raton, FL, 2001.

[206] Perkin Elmer, website: www.perkinelmer.com.

[207] Igus Corporation, website: www.igus.com.

[208] Instron Corporation, website: www.instron.com.

[209] J. Atulasimha, A. Flatau, I. Chopra, R. Kellog, "Effect of stoichiometry sensing behavior of iron-gallium", *Proceedings of SPIE Smart Structures and Materials Conference*, San Diego, March 2004.

[210] H. Prahlad, I. Chopra, "Experimental Characterization of NiTi Shape Memory Alloy Wires Under Uniaxial Loading Conditions", *Journal of Intelligent Systems and Structures*, vol 11, No.4, pp. 272-282, 2000.

[211] J. Epps, I. Chopra, "Comparative Evaluation of Shape Memory Alloy Constitutive Models with Experimental Test Data", *Proceedings of AIAA/ASME/ASCE/AHS/ASC 38th Structures, Structural Dynamics, and*

Materials Conference and Adaptive Structures Forum, AIAA, Reston, VA, 1997.

[212] Y. Ezer, A. Sozinov, G. Kimmel, V. Etelaniemi, A. D'Anci, et. al., "Magnetic Shape Memory (MSM) effect in textured pocrystalline Ni_2MnGa", *Proc. SPIE 1999*, vol 3675, pp.244-251 (July 1999).

[213] V.A. Chernenko, V.A. L'vov, E. Cesari, J. Pons, A.A. Rudenko, et. al., "Stress-strain behaviour of NiMnGa alloys: experiment and modeling", *Materials Science and Engineering A*, Article in Press.

[214] ANSI/IEEE. *IEEE Standard on Piezoelectricity*, 1987. Std. 176.

[215] *Morgan Matroc Inc. Piezoceramic Databook*, Morgan Matroc Electroceramic Div., Bedford, OH, 1993.

[216] J. L. Butler. *Application Manual for the Design of ETREMA Terfenol-D Magnetostrictive Transducer*, ETREMA Products, Edge Technologies, 1988.

[217] J. R. Pratt, S. C. Oueini, and A. H. Nayfeh. Terfenol-d nonlinear vibration absorber. *Journal of Intelligent Material Systems andStructures*, 10(1):29-35, January 1999.

[218] M. Moet, A. E. Clark, M. Wun-Fogle, J. Linberg, J. Teter, and E. McLaughlin. Characterization of terfenol-d for magnetostrictive transducers. *Journal of the Acoustical Society of America*, 89(3):1448-1455, 1991.

[219] I. Soursa. *"Performance and modeling of magnetic shape memory actuators and sensors,"* PhD dissertation, Helsinki University of Technology, Department of Electrical and Communications Engineering, May 2005.

[220] I. Soursa, J. Tellinen, I. Aaltio, K. Ullakko, "MSM-sensor," Patent FI 20030333, (Pending), 2003.

[221] F. T. Calkins, A. B. Flatau, and M. J. Dapino. Overview of magnetostrictive sensor technology. *AIAA-99-1551, Proceedings of AIAA/ASME/ASCE/AHS/ASC Structures, Structural Dynamics, and Materials Conference, St. Louis, MO*, April 1999.

[222] F.T. Calkins, A. Flatau "Terfenol-D Sensor Design and Optimization," Aerospace Engineering and Engineering Mechanics Department, Iowa State University, 1997.

[223] R.D. James, and D. Kinderlehrer , *J. Appl. Phys*., 76, 7012 (1994).

[224] R. Couch, I. Chopra, "Quasi Static Modelling of NiMnGa Magnetic Shape Memory Alloy," *Proceedings of SPIE*, San Diego, March 2004.

[225] R. Couch, I. Chopra, "A quasi-static model for NiMnGa magnetic shape memory alloy," *Proceedings of SPIE*, San Diego, March 2005.

[226] V.A. L'vov, Gomonaj E.V., V.A. Chernenko, "A phenomenological model of ferromagnetic martensite", *Journal of Physics: Condensed Matter*, vol 10, No.21, pp.4587-4596.

[227] V.A. Chernenko, V.A. L'vov, E. Cesari, *Journal of Magnetism and Magnetic Materials*, 196-197 (1999) 859.

[228] A.A. Likhachev, and K. Ullakko, "The model development and experimental investigation of giant magneto-mechanical effects in NiMnGa", *J. Mag. Mater.*, 226-230, pp. 1541-1543 (2001).

[229] V.A. L'vov, S. Zagorodnyuk, V.A. Chernenko, T. Takagi, *Mater. Trans.* JIM 43 (2002) 876.

[230] A.A. Likhachev, and K. Ullakko, "Quantitative model of large magnetostrain effect in ferromagnetic shape memory alloys", *Europhys. J.*, B14, 263-267 (2000).

[231] N.I. Glavatska, A.A. Rudenko, I.N. Glavatskiy, V.A. L'vov, "Statistical model of magnetostrain effect in martensite," *Journal of Magnetism and Magnetic Materials*, 265(2), pp.142-151, 2003.

[232] P. Mullner, V.A. Chernenko, G. Kostorz, "A microscopic approach to the magnetic-field-induced deformation of martensite (magnetoplasticity)", *Journal of Magnetism and Magnetic Materials*, vol. 267, no. 3, pp. 325-334 (2003).

[233] N.I. Vlasova, *Journal of Magnetism and Magnetic Materials*, vol 222, pp. 138, (2000).

[234] L. Hirsinger, C. Lexcellent, "Internal variable model for magneto-mechanical behaviour of ferromagnetic shape memory alloys NiMnGa," *Journal de Physique IV*, 112, pp.977-980, 2003.

[235] L. Hirsinger, C. Lexcellent, "Modelling detwinning of martensite platelets under magnetic and (or) stress actions on Ni_2MnGa," *Journal of Magnetism and Magnetic Materials*, 254, pp.275-277, 2003.

[236] L. Hirsinger, C. Lexcellent, "Ni_2MnGa shape memory alloys: modeling of magneto-mechanical behavior," *Journal of Applied Electromagnetics and Mechanics*," 19, pp.473-477, 2004.

[237] A.A. Likhachev, and K. Ullakko, "Quantitative model of large magnetostrain effect in ferromagnetic shape memory alloys", *Europhys. J.*, B2, 1 (1999).

[238] S.J. Murray, R.C. O'Handley, S.M. Allen, "Model for discontinuous actuation of ferromagnetic shape memory alloys under stress", *J. of Appl. Phys*, vol 89(2), pp. 1295-1301 (2001).

[239] A.A. Likhachev, A. Sozinov, K. Ullakko, "Magnetic forces controlling magnetic shape memory in NiMnGa and their practical measurement from the mechanical testing experiments in constant magnetic fields," *Proceedings of SPIE*, vol 5387, pp. 128-136, (2004).

[240] B. Kiefer and D.C. Lagoudas, "Phenomenological modeling of ferromagnetic shape memory alloys", *Smart Structures and Materials 2004: Active Materials: Behavior and Mechanics Proceedings of SPIE,* 5387, pp 164-176 (2004).

[241] B. Kiefer and D.C. Lagoudas, "Modeling of the magnetic field induced martensitic variant reorientation and associated magnetic shape memory effect in FSMAs", *Proceedings of SPIE,* 5761, pp 454-465 (2005).

[242] H. Tan, M. Elahinia, "Dynamics modeling of ferromagnetic shape memory alloys (FSMA) actuators", *Proceedings of SPIE Conference on Smart Structures and Materials* , San Diego, March 2006.

[243] K. Tanaka, "A Thermo-mechanical Sketch of Shape Memory Effect: One-Dimensional Tensile Behavior", *Res Mechanica*., vol. 18, no. 3, pp. 251-263, 1986.

[244] Rogers, C.A., Liang, C., "One-dimensional Thermomechanical Constitutive Relations for Shape Memory Material", *Journal of Intelligent Materials and Structures*, vol. 1., pp.207-234, April 1990.

[245] J.G. Boyd, D.C. Lagoudas, "A thermodynamic constitutive model for the shape memory materials Part I. monolithic shape memory alloys", *International Journal of Plasticity,* 12(6):805, 1996.

[246] K. Tanaka, F. Nishimura, H. Matsui, H. Tobushi, P.H. Lin, "Phenomenological Analysis of Plateaus on Stress-Strain Hysteresis in TiNi Shape Memory Alloy Wires", *Mechanics of Materials, An International Journal*, vol. 24, no. 1, pp. 19-30, 1996.

[247] J.G. Boyd, D.C. Lagoudas, "A thermodynamic constitutive model for shape memory materials Part II . The SMA composite material", *International Journal of Plasticity*, 12(7):843-873, 1996.

[248] L.C. Brinson, M. Huang, "Simplification and comparisons of shape memory alloy constitutive models", *Journal of Intelligent Material Systems and Structures*, vol 7, No. 1, pp. 108-114, 1996.

[249] Y. Ivshin, T.J. Pence, "A Thermo Mechanical Model for One Variant Shape Memory Material", *Journal of Intelligent Material Systems and Structures*, vol. 5, No. 4, pp. 455-473, 1994.

[250] L.C. Brinson, M. Huang, "Simplification and Comparisons of Shape Memory Alloy Constitutive Models," *Journal of Intelligent Material Systems and Structures*, vol. 7, no. 1, pp. 108-114 (1996).

[251] R. Couch, J. Sirohi, I. Chopra, "Development of a Quasi-Static Model of NiMnGa Magnetic Shape Memory Alloy," *Proceedings of ICAST*, Bar Harbor, October 2004.

[252] R. Couch, J. Sirohi, I. Chopra, "Testing and Modeling of NiMnGa Ferromagnetic Shape Memory Alloy for Static and Dynamic Loading Conditions," *Proceedings of SPIE*, San Diego, February 2006.

[253] R.A. Serway, "*Physics for Scientists and Engineers."* Saunders College Publishing, 1983.

[254] K.R. Demarest, "*Engineering Electromagnetics,"* Prentice Hall, Inc., 1998.

[255] S.E. Schwarz, "*Electromagnetics for Engineers*," Saunders College Publishing, 1990.

[256] H.E. Burke, "*Handbook of Magnetic Phenomenon*," Van Nostrand Reinhold Company, Inc. 1986.

[257] A. Clark, "Magnetostrictive rare earth-Fe_2 compounds," *Ferromagnetic Materials Volume 1*, North-Holland Pub., 1980.

[258] F. Calkins, M. Dapino, A. Flatau "Effect of prestress on the dynamic performance of a Terfenol-D transducer," *Proceedings of SPIE 1997,* vol 3041, no. 23, San Diego, CA, March 1997.

[259] J. Butler, "Application Manual for the Design of ETREMA Terfenol-D magnetostrictive transducers," EDGE Technologies, Inc., Ames, Iowa, 1988.

[260] M. Dapino, F. Calkins, A.Flatau, and D. Hall, “Measured Terfenol-D material properties under varied applied magnetic field levels,” *Proceedings of SPIE 1996 Symposium on Smart Structures and Materials*, #2717-66, San Diego, CA, March 1996.

[261] C.D. Near, “Piezoelectric Actuator Technology,” *Proceedings of SPIE*, vol.2717, pp. 246-258, 1996.

[262] Mide Technology Corporation Website, www.mide.com/quickpack_poweract/qp_piezo_material_properties.html